SYNTHESIS AND CHARACTERIZATION OF POROUS CARBON COMPOSITE DERIVED FROM BIOMASS WASTE FOR SUPERCAPACITOR APPLICATION

SIM CHENG KIM

FACULTY OF SCIENCE
UNIVERSITI MALAYA
KUALA LUMPUR

2020

SYNTHESIS AND CHARACTERIZATION OF POROUS CARBON COMPOSITE DERIVED FROM BIOMASS WASTE FOR SUPERCAPACITOR APPLICATION

SIM CHENG KIM

THESIS SUBMITTED IN FULFILMENT OF THE REQUIREMENTS FOR THE DEGREE OF DOCTOR OF PHILOSOPHY

INSTITUTE OF BIOLOGICAL SCIENCES
FACULTY OF SCIENCE
UNIVERSITI MALAYA
KUALA LUMPUR

2020

UNIVERSITI MALAYA

ORIGINAL LITERARY WORK DECLARATION

Name of Candidate: **SIM CHENG KIM**

Matric No: **SHC160028**

Name of Degree: **DOCTOR OF PHILOSOPHY**

Title of Project Paper/Research Report/Dissertation/Thesis ("this Work"):

SYNTHESIS AND CHARACTERIZATION OF POROUS CARBON COMPOSITE DERIVED FROM BIOMASS WASTE FOR SUPERCAPACITOR APPLICATION

Field of Study

ENVIRONMENTAL SCIENCE MANAGEMENT

I do solemnly and sincerely declare that:

(1) I am the sole author/writer of this Work;
(2) This Work is original;
(3) Any use of any work in which copyright exists was done by way of fair dealing and for permitted purposes and any excerpt or extract from, or reference to or reproduction of any copyright work has been disclosed expressly and sufficiently and the title of the Work and its authorship have been acknowledged in this Work;
(4) I do not have any actual knowledge nor do I ought reasonably to know that the making of this work constitutes an infringement of any copyright work;
(5) I hereby assign all and every rights in the copyright to this Work to the University of Malaya ("UM"), who henceforth shall be owner of the copyright in this Work and that any reproduction or use in any form or by any means whatsoever is prohibited without the written consent of UM having been first had and obtained;
(6) I am fully aware that if in the course of making this Work I have infringed any copyright whether intentionally or otherwise, I may be subject to legal action or any other action as may be determined by UM.

Candidate's Signature Date:

Subscribed and solemnly declared before,

Witness's Signature Date:

Name:

Designation:

SYNTHESIS AND CHARACTERIZATION OF POROUS CARBON COMPOSITE DERIVED FROM BIOMASS WASTE FOR SUPERCAPACITOR APPLICATION

ABSTRACT

Energy storage devices have gradually dominated human daily activities and indispensable to economy development such as supercapacitor and battery. There are few factors determining the performance of supercapacitor and active material is one of the crucial. Therefore, biomass such as pineapple peel (PP) and green waste (GW) were preferred and prior mixed with manganese and tin carbonate to synthesize carbon composite (PP/GW-ZMO and PP/GW-ZTO) via combustion. Brunauer–Emmett–Teller (BET) was employed to study the textural properties with the highest specific surface area obtained in PP-C (1765.92 m^2g^{-1}) and GW-C (1613.92 m^2g^{-1}). The existence of composite materials was examined using x-ray diffraction (XRD), energy-dispersive x-ray spectroscopy (EDX) and transmission electron microscopy (TEM). Field emission scanning electron microscopy (FESEM) results indicated weight ratio of composite materials have altered the morphology structure. Electrochemical studies implied that carbon composite materials derived from GW exhibited better specific capacitance such as GW-ZMO1 and GW-ZTO1 achieved 123 Fg^{-1} and 104 Fg^{-1} at 0.3 Ag^{-1}, respectively. Symmetrical cells were fabricated to examine the device's performance. Stability test implied that devices fabricated from both porous carbon and carbon composites were steady after 5000 cycles at 0.3 Ag^{-1} with capacitance retention more than 85 %. Nevertheless, PP-C exhibited poor durability which it dropped drastically to almost null specific capacitance while PP-ZMO1, PP-ZTO1, GW-ZMO1 and GW-ZTO1 retained 65 %, 88 %, 79 % and 106 %, accordingly after 900 cycles of varies current densities.

Keywords: biomass, carbon composite, supercapacitor, specific capacitance

SINTESIS DAN PENCIRIAN KOMPOSIT KARBON BERLIANG YANG DIHASILKAN DARIPADA SISA BIOMAS UNTUK APLIKASI SUPERKAPASITOR

ABSTRAK

Peranti penyimpan tenaga telah menguasai aktiviti-aktiviti manusia secara perlahan dan sangat penting dalam perkembangan ekonomi. Prestasi kapasitor ditentukan daripada pelbagai faktor dan bahan aktif elektrod adalah antara yang memainkan peranan penting. Oleh itu, biomas seperti kulit nenas (PP) dan sisa hijau (GW) dipilih dan bercampur dengan mangan dan timah karbonat untuk menghasilkan komposit karbon (PP/GW-ZMO dan PP/GW-ZTO) melalui proses pembakaran. Brunauer-Emmett-Teller (BET) digunakan untuk mengkaji sifat tekstur dengan kawasan permukaan tertinggi yang diperolehi dalam PP-C (1765.92 m^2g^{-1}) dan GW-C (1613.92 m^2g^{-1}). Kewujudan bahan komposit diperiksa dengan menggunakan XRD, spektroskopi sinar-x penyebaran tenaga (EDX) dan mikroskop elektron penghantaran (TEM). Mikroskop elektron (FESEM) menunjukkan nisbah berat bahan komposit mengubah struktur morfologi. Kajian elektrokimia menunjukkan bahawa bahan komposit karbon yang diperoleh daripada GW mempamerkan kapasitan spesifik yang lebih baik seperti GW-ZMO1 dan GW-ZTO1 telah mencapai 123 Fg^{-1} dan 104 Fg^{-1} pada 0.3 Ag^{-1}. Sel simetri direka untuk mengkaji prestasi peranti. Ujian kestabilan menunjukkan peranti yang dibuat dari karbon dan komposit karbon adalah stabil selepas 5000 kitaran pada 0.3 Ag^{-1} dengan pengekalan kapasitan lebih daripada 85 %. Walau bagaimanapun, PP-C mempamerkan ketahanan yang lemah di mana ia menurun secara mendadak ke kapasitan hampir kosong manakala PP-ZMO1, PP-ZTO1, GW-ZMO1 dan GW-ZTO1 mengekalkan 65 %, 88 %, 79 % dan 106 % masing-masing selepas 900 kitaran pada ketumpatan arus yang berbeza.

Kata kunci: biomas, karbon komposit, kapasitor, kapasitan spesifik

ACKNOWLEDGEMENTS

First of all, I would like to convey my special gratitude and appreciation to my supervisors Associate Professor Dr. Noor Zalina Mahmood and Professor Dr. Siti Rohana Majid for their tremendous guidance, motivation, inspiration and enthusiasm during my research life. Thank you for the advice which allow me to think critically which is very valuable to both my research and future career life.

My sincere thanks to Ministry of Higher Education, Malaysia who has awarded me the MyPhD scholarship that sponsored my whole research expenses. Other than that, I also would like to thank my fellow labmates who have made my research life more exciting and fun. The friendship and memories are also the one which let me grow stronger whenever there is any unsuccessful in doing experiment. My acknowledgement goes to all the operators and officers of Universiti Malaya as without the assistance from them, I would not be able to complete my PhD works.

Finally, my deepest gratitude goes towards my beloved parents, husband and siblings. Words cannot express my appreciation for their countless love and spiritual support. Finally, I thank to my Buddha, for assisting me to get through all the obstacles and I will keep on learning from you in all ways.

TABLE OF CONTENTS

LIST OF FIGURES

LIST OF TABLES

LIST OF SYMBOLS AND ABBREVIATIONS

Δi	:	Average of discharge current
Δt	:	Discharge time
ΔV	:	Voltage change
0-D	:	Zero-dimensional
1-D	:	One-dimensional
2-D	:	Two-dimensional
2E	:	Two-electrode
3-D	:	Three-dimensional
3E	:	Three-electrode
AC	:	Activated carbon
Ag/AgCl	:	Silver/silver chloride
$AlCl_3$	:	Aluminium chloride
BET	:	Brunauer-Emmet-Teller
BJH	:	Barrett-Joyner-Halenda
C/ZMO	:	Carbon/zinc dimanganese oxide
C/ZnO	:	Carbon/zinc oxide
C/ZTO	:	Carbon/zinc tin oxide
CA	:	Carbon aerogel
CH_5NO_3	:	Ammonium bicarbonate
CNF	:	Carbon nanofibers

CO_2	:	Carbon dioxide
C_{sp}	:	Specific capacitance
CV	:	Cyclic voltammetry
DTG	:	Differential thermogravimetric
E	:	Energy density
EDLC	:	Electrical double-layer capacitors
EDX	:	Energy dispersive x-ray spectroscopy
EIS	:	Electrochemical impedance spectroscopy
ESR	:	Equivalent series resistance
$FeCl_3$	:	Iron (III) chloride
FESEM	:	Field emission scanning electron microscopy
GCD	:	Galvanostatic charge-discharge
GHG	:	Greenhouse gases
GO	:	Graphene oxide
GW	:	Green waste
GW-C	:	Green waste porous carbon
GW-ZMO	:	Green waste-based carbon/zinc dimanganese oxide composite
GW-ZTO	:	Green waste-based carbon/zinc tin oxide composite
H_2SO_4	:	Sulphuric acid
H_3PO_4	:	Phosphoric acid
HCl	:	Hydrochloric acid

HRTEM	:	High resolution transmission electron microscopy
IEO	:	International energy outlook
IR	:	Internal resistance
K^+	:	Potassium ion
K_2CO_3	:	Potassium carbonate
KOH	:	Potassium hydroxide
Li	:	Lithium
M_{ac}	:	Mass of active material
Mn	:	Manganese
$MnCO_3$	:	manganese carbonate
$MnSO_4.H_2O$	:	Manganese (II) sulphate, monohydrate
MWCNT	:	Multi-wall carbon nanotubes
N_2	:	Nitrogen
Na_2CO_3	:	Sodium carbonate
NaOH	:	Sodium hydroxide
NMP	:	N-methyl-2-pyrrolidone
O	:	Oxide
OECD	:	Organization of economic cooperation and development
P	:	Power density
P/P_0	:	Relative pressure
PP	:	Pineapple peel

PP-C	:	Pineapple peel porous carbon
PP-ZMO	:	Pineapple peel-based carbon/zinc dimanganese oxide composite
PP-ZTO	:	Pineapple peel-based carbon/zinc tin oxide composite
Pt	:	Platinum
PvdF	:	Polyvinylidene fluoride
R_{ct}	:	Charge transfer resistance
rGO	:	Reduced graphene oxide
R_s	:	Bulk electrolyte resistance
$SnCO_3$	:	Stannous carbonate
STP	:	Standard temperature and pressure
TG	:	Thermogravimetric
TGA	:	Thermogravimetric analysis
TMOs	:	Transition metal oxides
XRD	:	X-ray diffraction
ZMO	:	Zinc dimanganese
Zn	:	Zinc
$ZnCl_2$	:	Zinc chloride
$ZnMn_2O_4$	:	Zinc dimanganese
ZnO	:	Zinc oxide
ZTO	:	Zinc tin oxide

CHAPTER 1: INTRODUCTION

1.1 Energy consumption

Over the years, environmental issues such as climate change, waste disposal, overpopulation, deforestation, land and water scarcity etc. has been on the rise. According to Mark Tercek, president of The Nature Conservancy (2017), there are more than 9 billion people that will consume and stay in this planet indicating that there will be high demand on energy, food and water.

Fossil fuels, the natural and most important fuels in providing energy for different applications such vehicles, electricity, construction and cooking, though, its burning is also the main factor of climate change due to the releasing of greenhouse gases (GHG). On the other hand, it is inevitably that humankind activities and socio-economic development is very much depending on the usage of fossil fuel for energy purpose.

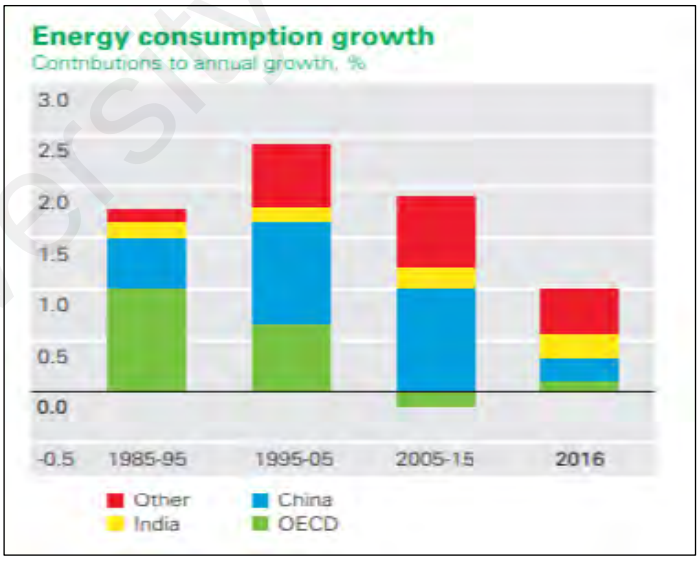

Figure 1.1: Energy consumption growth (%) for Organization of Economic Cooperation and Development (OECD), China, India and other countries (BP Statistical Review of World Energy, 2017)

According to the report of BP Statistical Review of World Energy (2017), energy consumption growth as shown in Figure 1.1 implies that developing countries used up the highest energy for the past 10 years. However, it showed a drop in the year of 2016 which is mainly driven by advanced technologies with energy efficient features in addition with supply from renewable energy which is cleaner and lower carbon energy sources.

Other than that, International Energy Outlook (2017) also reported a world energy consumption as displayed in Figure 1.2(a) between OECD and non-OECD countries. The bar chart implying that consumption of energy in non-OECD is predicted to be increased and Asia will be the highest demand among other regions which is mainly due to the high economic and rapid population growth as well as the increased access to marketed energy that made up a rise of 41% of energy consumption in non-OECD while only 9% in OECD countries between 2015 to 2040.

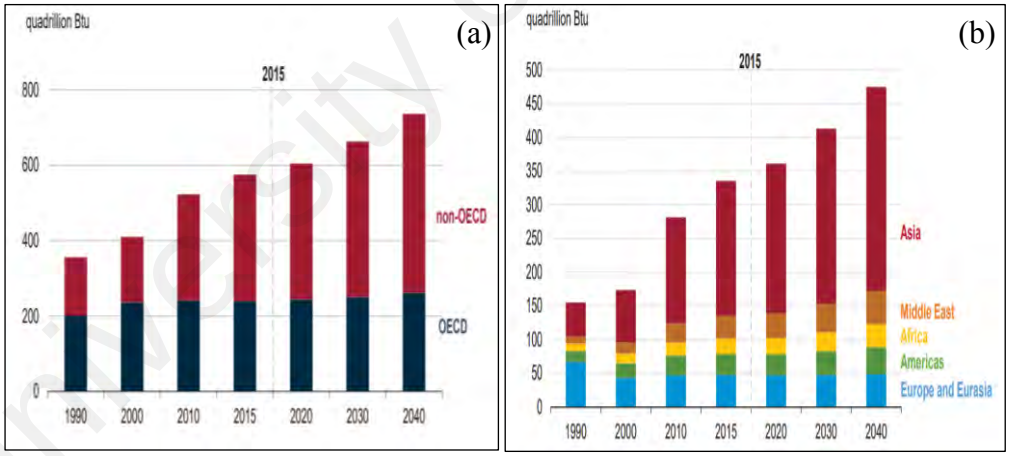

Figure 1.2: Forecast of world energy consumption for (a) OECD and non-OECD countries and (b) non-OECD by region (International Energy Outlook, 2017)

Therefore, renewable energy is the main concern and core focus of researchers for future energy source. Renewable energy can be originated from the sources such as wind, tide, sunshine and waste where large amount of the energy can be generated. In this sense, the energy storage devices which are important in storing and transferring the energy to

various applications plays the essential role. Batteries and supercapacitors are the most common energy storage devices. Among all types of devices, supercapacitor attracted the most attention from researchers due to its remarkable characteristics of high power density, moderate energy density, flexibility and long cycle stability which is accounted to be one of the most promising sustainable energy storage in future (Zhang et al., 2009; Yang et al., 2015).

Supercapacitor is fabricated by two electrodes with a separator between them. To acquire a good performance of supercapacitor, the active material of electrodes plays a major role in terms of its textural properties such as surface area, pore size and pore volume. Majority of supercapacitor electrodes are using activated carbon as the source of active materials owing to its high surface area, conductivity, low cost and abundance. Hence, it is important to obtain raw materials for activated carbon which is eco-friendly and cost effectiveness.

1.2 Rationale and importance of this study

Rapid development of economy, growth of human population with prompt progress of urbanization consequently lead to the thousand tons of solid wastes annually originated from industrial and households (Dai et al., 2018). In view of significant increase on solid waste volume, different types of pollution are created such as air, water, soil and aesthetic are impacted, not to mention human health. Additionally, the limitation of land has urged for immediate action on solid waste management including biomass waste. As an example, study has reported that pineapple has been applied in food industry for desserts, juice, cocktail, jam, salad and can food processing (Foo & Hameed, 2012). The massive cultivation of pineapple has driven a potential problem towards waste management. On the other hand, the current city landscaping which focus on green planting has resulting in bulky green wastes due to the trimming activities to keep the city clean, neat and

attractive. Therefore, it is crucial to reduce the solid waste generation in a way that is not harmful to the environment but into high-value product.

Biomass, an organic matter, for instance wood or wood waste, food waste, agricultural crops and waste materials, animal manure and human sewage exists as natural resource with abundant quantity and environmentally friendly in nature. This type of solid waste consists of carbonaceous component which can be converted into carbon and further utilize as electrode active material. Biomass-derived activated carbon appeared to be the potential candidate as sustainable and economy material for to be applied in the devices and energy storage systems such as batteries, fuel cell and supercapacitors (Cao & Yang, 2018; Kesavan et al., 2019).

On the other hand, accelerate innovative in technology such as portable electronics products, hybrid electric vehicle and electric vehicle requesting high demand on rechargeable energy storage system (Zhu et al., 2018b). This has illustrated the importance of supercapacitors development to meet the current technology issues in storage capacity and rate capability. These issues have restricted the usage in commercialization as compared to Li-ion battery. Thus, a research is desired to enhance the energy density of supercapacitor to cater the current application requirement. In view of this, one step biomass-derived carbon composite is synthesized by combusting technique. It is believed that with the utilization of biomass raw material and incorporation of additives, the sustainability and better performance of the energy storage system can be achieved meanwhile resulting in win-win situation whereby the waste management issue can be dealt with and meanwhile design a renewable efficient energy storage system.

Additionally, according to the reported document in 2012, 4.28 million tons of porous carbon is consumed, and the worldwide demand is believed to rise 10 % annually

(McQuillan et al., 2018; Zanella et al., 2014). Study done by Research T. M. (2013) accounted that 1,204,500 tons of porous carbon is demanded globally just in 2012. Considering the fact that porous carbon is in high demand, careful tailoring of porous carbon by various synthesis methods is essential to fulfil the needs in various application such as water treatment, clean gas emission, sensor, chemical recovery and not to mention the energy storage device.

1.3 Objectives

There are three objectives to be achieved in this research to solve the problem statement mentioned above. The objectives are listed as follow:

i. To identify the textural properties of the biomass-derived porous carbon and carbon-based composite
ii. To determine the electrochemical behaviour of biomass-derived electrode materials
iii. To study the rate capability and stability of symmetrical cells using the optimized samples

1.4 Structure of thesis

The thesis comprises of 9 chapters such as introduction, literature review, methodology, results, discussion, conclusion and future recommendation

Chapter 1 comprises of the introduction and background on environmental issues mainly energy consumption and the importance of supercapacitor. This chapter also explain the significance of the study along with the objectives.

In chapter 2, the review on carbon composite and supercapacitor is reported. Study on the synthesis of carbon composite and its raw materials together with electrochemical performance is stated.

Chapter 3 will describe the methodology used in the study which encompasses the process on pre-treatment of the raw materials to synthesis of pure activated carbon, transition metal oxide and carbon composite and applied in supercapacitor. The characterization of the textural properties and electrochemical performance are discussed in this chapter too.

The 4th to 7th chapters will explain all the findings in this study. For instance, Chapter 4 covered the results of porous carbon derived from pineapple peel (PP) and green waste (GW). Additionally, binary ZnO/carbon composite systems are outlined in Chapter 5 followed with ternary carbon composite such as zinc dimanganese (ZMO)/carbon and zinc tin oxide (ZTO)/carbon composites in Chapter 6 and 7 respectively. All the physical characterizations and electrochemical performances of respective materials are inclusive in every chapters.

Chapter 8 consists of discussion on the relationship between pore properties and electrochemical performance. The effect of carbon to composite ratio towards the physical properties and specific capacitance is explained in this chapter.

Chapter 9 is the last chapter of this thesis in which the conclusions of the study will be stated and recommendations for future study will be stated.

CHAPTER 2: LITERATURE REVIEW

2.1 Introduction

Carbons existed in many forms and have been used as active material for supercapacitor applications. Activated carbon (AC), a type of porous carbon which is extensively used as electrode material in supercapacitor due to its high surface area. Utilizing biomass as raw material for AC has been very common where there are lots of literature reviews. Although activated carbon has been showed as a good material for supercapacitor, it has capacitance limitation at around 100 Fg^{-1} even with high surface area (~3000 m^2g^{-1}) (Barbieri et al., 2005; Tran & Jeong, 2017). Therefore, incorporation of guest materials such as transition metal oxide and conducting polymer as carbon composite are predicted to provide synergistic effect to enhance both the power and energy density.

In this chapter, types of carbon and carbon composite with various types of transition metal oxides will be discussed and further explaining on the synthesize methods as well as the characterization part. Since the synthesized carbon composite will be used for supercapacitor application, the history of supercapacitor and its electrochemical performance will be discussed according to types of carbon and metal oxide incorporation.

2.2 Carbon

The word “carbon” is originally translated from the Latin word “carbo” which is defined as charcoal and usually use as the source for combustion. The first case that has been recorded on the usage of wood char was for the smokeless fuel and reduction of copper, zinc and tin ores to produce bronze by Eygptians and Sumerians in 3750 BCE (González-García, 2018).

Carbon is one of the elements fall under Group 14 in the periodic table. In the universe, it is the 4th most abundant chemical element by mass, 15th richest element in the Earth's crust, and 2nd abundant element by mass in human body (around 20 % after oxygen) (Bondavalli, 2018). It exists in many forms such as in gas and solid. In gas, it is found in carbon dioxide (CO_2) or methane (CH_4) while in solid form, it can be categorized into crystalline and amorphous structure. Diamond and graphite are categorized under crystalline form whereas activated carbon, carbon nanotube, mesoporous carbon fall under the umbrella of amorphous structure with different degrees of hardness such as diamond is the hardest while softest as in graphite. Nonetheless, no matter if it exists in hard or soft structure, they are all made up of same carbon atoms, and only with different arrangements of carbon atom that resulting in different molecules (Saucerman, 2004). This can be seen solely in carbon nanostructure which is categorized into different dimensional that will be discussed as followed (Zhi et al., 2013):

(a) <u>Zero-dimensional (0-D) carbon nanoparticles</u>

This type of carbon always refers to sphere particles with the feature ratio close to 1. It mainly consists of AC, carbon nanosphere and mesoporous carbon. Carbon falls under this group used to exhibit high surface area (~3000 m^2g^{-1}). Moreover, the pore structure can be tailored according to its suitability as metal oxides supporting backbone for supercapacitor electrode.

(b) <u>One-dimensional (1-D) carbon nanostructure</u>

This group comprises carbon nanotubes (CNT), carbon nanofibers (CNF) and carbon nanocoils which possess fiber-shaped with high aspect ratio. This type of materials owns to have outstanding electronic properties that facilitate the ions movements during electrochemical reactions.

(c) Two-dimensional (2-D) nanosheets

The nanostructure of this group is defined as sheet-shaped materials such as graphene, graphene oxide (GO) or reduced graphene oxide (rGO). Their characteristics of strong mechanical strength and good electronic conductivity serve them as a promising candidate for supercapacitor electrode.

(d) Three-dimensional (3-D) porous architectures

Carbon nanofoams or sponges and graphite are made up of low dimensional building blocks. This structure provides large area of electrolyte-electrode interface and ease the electron pathway.

In order to have a better picture, the diagram displays in Figure 2.1 illustrated the structure of carbon with different dimensional.

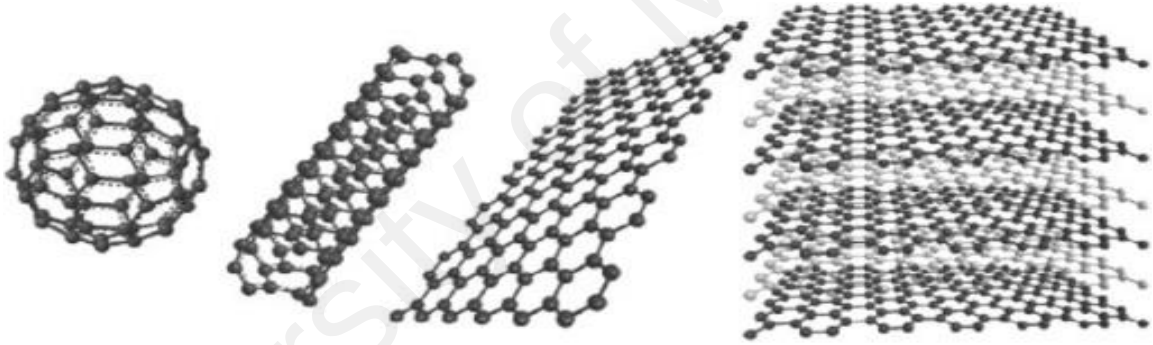

(a) (b) (c) (d)

Figure 2.1: Forms of sp2-bonded carbon (a) 0-D, (b) 1-D, (c) 2-D and (d) 3-D (Zhou et al., 2014)

2.2.1 Activated carbon

Activated carbon is a high porosity carbonaceous material with well-developed internal pore structure which can be categorized into micropore (< 2 nm), mesopore (2-50 nm) and macropore (> 50 nm) as shown Figure 2.2. It has been studied over the 20th century, additionally, the development of activated carbon is growing even rapidly during the second half of the last century mainly due to the environmental concern and regulations particularly on water resources, air pollution, clean gas application, chemical

and metal removal and more importantly the energy storage/conversion (González-García, 2018; Purnomo et al., 2018) which having high impact on human regular activities.

The outstanding characteristics of activated carbon such as high surface area, large pore volume, strong mechanical support, facile synthesis method, high thermal and chemical stability (Guan et al., 2018; Xia et al., 2010; Zhai et al., 2011) are the core reasons that researchers investigate extensively for the past decade. However, few factors have been considered prior to the choice of precursors, for instance, ease of accessibility, carbon rich component, low cost, abundance, sustainable and environmentally friendly (Adeyi, 2010; Hernandez et al., 2007; Kazmierczak-Razna et al., 2017; Yahya et al., 2015). Hence, agricultural wastes and woody biomass became the exclusive choice to fit the requirements as it can be cultivated through short rotation period with high volume of biomass leftover. Nevertheless, the biomass waste is always an unwanted by-product rendered it to be cheap and most importantly, the chemical constituents claimed to have high carbon content and low ash contents (0.2–10 wt%) (Ao et al., 2018; Danish & Ahmad, 2018).

Majority of the biomass contain three main components which are cellulose, hemicellulose and lignin. Cellulose composes of partly crystalline polysaccharides with at least 3000 glucose units. The only difference in hemicellulose is the quantity of saccharide units. Both cellulose and hemicellulose have in average of 44.4 wt.% carbon, 49.4 wt.% oxygen and 6.2 wt.% hydrogen. Lignin on the other hand is complex as it is linked by C-O-C and C-C bonds to form a 3-D polymer of phenylpropane units which allows it to have higher carbon content (62 wt.%) and lower oxygen content (32 wt.%). Besides that, lignin also acts as the backbone of lignocellulosic materials with the linkage between cellulose and hemicellulose by ether and C-C bond (Jibril et al., 2008).

As discussed above different components exhibited various polysaccharides chains, hence, ratio of these elements within the individual biomass varies. This is important as different ratios will consequently influence the thermal degradation rate and temperature as well as the reactions involved during their decompositions (Cagnon et al., 2009). Study reported that properties of the activated carbon is very much rely on the nature and structure of the precursor (Cagnon et al., 2009). Study reported that precursor with higher lignin content (grape seeds, cherry stones) will contribute to more macropore structure while raw materials with more cellulose (apricot stones, almond shells) assists in developing microporous structure (Demiral et al., 2011; Ioannidou & Zabaniotou, 2007) .

Until now, many researchers reported on the usage of agro biomass to produce activated carbon. Herein, we can claim that utilization of biomass has achieved the recognition from both researchers and society as a promising precursor for AC. Table 1 listed out the biomass that have been selected to produce AC.

Table 2.1: List of precursor materials from agricultural wastes for AC.

Agro-waste	Reference	Agro-waste	Reference
Palm shell	(Maarof et al., 2017)	Corn stalk	(Li et al., 2018)
Coconut shell	(Sun et al., 2017)	Corn cob	(Bagheri & Abedi, 2011)
Almond shell	(Nabais et al., 2011)		
Walnut shell	(Liu et al., 2017)	Avocado seed	(Rodrigues et al., 2011)
Durian shell	(Tham et al., 2011)		
Peanut shells	(Georgin et al., 2016)	Tomato stems	(Fu et al., 2017)
Bamboo	(Zhang et al., 2018a)	Sugarcane bagasse	(Gonçalves et al., 2016)
Olive bagasse	(Demiral et al., 2011)		
Olive stone	(Moreno et al., 2014)	Wheat straw	(Ma, 2017)
Tea leave	(Wong et al., 2018)	Chestnut shell	(Chen et al., 2018a)
Rice husk	(Yu et al., 2018)	Cotton stalk	(Nahil & Williams, 2012)
Banana peel	(Zhang et al., 2016b)		
Grape stalk	(Ozdemir et al., 2014)	Pomegranate seed	(Ahmad et al., 2014)

2.2.2 Parameters affecting AC textural properties

Numerous studies have been conducted to study the porosity of AC. It has been discussed that surface area and pore structure development are strongly connected to the techniques and experimental conditions such as the carbonization and activation steps which include carbonization temperature, rate of heating, holding time, gas flowing rate, activating agents, impregnation ratio etc (Danish & Ahmad, 2018).

2.2.2.1 Synthesis technique

Activated carbon is usually synthesized via conventional or microwave heating. In conventional heating, it mainly refers to physical activation, chemical activation and physiochemical activation. Physical activation utilizes oxidizing gas such as carbon dioxide, oxygen or steam to activate the raw material which can be carried out in one or two steps either during or after carbonization (Demiral et al., 2011). Chemical activation on the other is conducted by impregnation of the raw materials followed by the carbonization. The chemical activating agent can be in alkali metals (e.g. KOH, K_2CO_3, NaOH, and Na_2CO_3), alkaline earth metals (e.g. $AlCl_3$, $FeCl_3$, and $ZnCl_2$) and some acids (e.g. H_3PO_4 and H_2SO_4) (Nayak et al., 2017). Physiochemical activation on the other hand is the combination of both physical and chemical activation. Various activation methods have its own advantages and weakness which are listed in Table 2.2.

Table 2.2: Pros and cons of different activation methods (Ao et al., 2018).

Conventional methods	Advantages	Disadvantages
Physical activation	✓ Environmentally benign ✓ No precise requirements for the materials processing	✓ High activation temperature ✓ Long holding time ✓ Less carbon yield ✓ Low quality of ACs ✓ Consume high energy

Table 2.2, continued.

Conventional methods	Advantages	Disadvantages
Chemical activation	✓ Lower carbonization and activation temperatures ✓ Shorter carbonization and activation times ✓ Lower energy consumption ✓ Inhibition of tar formation due to reaction of activating agent ✓ Higher carbon yields	✓ Severe corrosion to the equipment ✓ Strict requirements on washing to remove chemical residue ✓ Adverse effects towards environment & public health
Physiochemical activation	✓ Applicable to unremoved chemical even after washing ✓ Promote pore formation ✓ Develop unique textural and chemical characteristics of ACs	✓ More complex process ✓ High cost

Microwave heating is about dielectric heating at certain frequencies which depend on the dipolar and interfacial polarization effects (Ao et al., 2018). It is rapid, selective and energy-saving approach without direct interaction with the substance (Duan et al., 2011). Heat generation is the only difference between microwave and conventional heating. This is attributed to the microwave energy generated transforms to heat energy which allow the heat to penetrate all over the materials consequently, fasten the processing time and enhance the total quality of the produced (Baytar et al., 2018). However, higher microwave radiation levels will destruct the pore structures and reduce adsorption capacities (Deng et al., 2010).

2.2.2.2 Activating agent

The effect on activating agent is only occurred in the chemical and physiochemical activation methods. There are many types of activating agents such as sulphuric acid

(H_2SO_4), zinc chloride ($ZnCl_2$), potassium hydroxide (KOH), sodium hydroxide (NaOH), sodium carbonate (Na_2CO_3), phosphoric acid (H_3PO_4), potassium carbonate (K_2CO_3) etc. However, $ZnCl_2$, KOH and H_3PO_4 are the reagent that are more commonly been used (Molina-Sabio & Rodríguez-Reinoso, 2004; Uçar et al., 2009). Different activating agents have claimed to produce different pore structures.

The effect of olive residues chemically activated in both KOH and H_3PO_4 was investigated (Elmouwahidi et al., 2017). The results implying that AC produced from KOH possessed pore structure of microporosity and very low mesoporosity while H_3PO_4 illustrated typical mesoporous materials. This is tally with the report which claimed that KOH give rise to a widening of micropore width, $ZnCl_2$ additionally develops small mesoporosity and H_3PO_4 produces a more heterogeneous pore size distribution (Molina-Sabio & Rodríguez-Reinoso, 2004). This synthesized AC further influences the application as supercapacitor with larger micropores, higher mesopore volume and surface phosphorus group enhance both the specific capacitance and cycling stability. This is attributed to the polyphosphate which reduce the hydrophobicity surface subsequently increased capacitance and metaphosphate assisted in stability (Hulicova-Jurcakova et al., 2009).

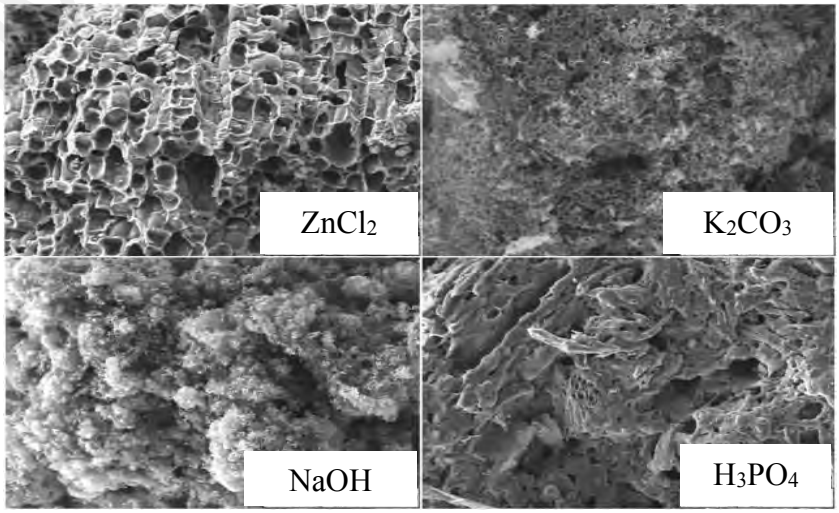

Figure 2.2: SEM images of AC impregnated with various activating agents (Kılıç et al., 2012)

Another study was conducted to investigate the effect of $ZnCl_2$, K_2CO_3, NaOH and H_3PO_4 on *Euphorbia rigida*, a type of plant (Kılıç et al., 2012). Various impregnation ratio of individual reagent is carried out resulting in high impregnation ratio leads to low AC yield in a sequence of 29.5 - 17.8 % ($ZnCl_2$), 13.3 - 9.7 % (K_2CO_3), 13.4 - 4.1 % (NaOH) and 29.0 - 16.8 % (H_3PO_4). Among the reagents, $ZnCl_2$ shows the highest yield. In terms of surface area: 2613 m^2g^{-1} from 75 % K_2CO_3, 1115 m^2g^{-1} from 75 % $ZnCl_2$, 790 m^2g^{-1} from 100 % H_3PO_4 and 396 m^2g^{-1} from 100 % NaOH. For morphology as illustrated in Figure 2.2, honeycomb-like porosity is observed in sample impregnated with $ZnCl_2$ and H_3PO_4 while spongy-like in K_2CO_3. The reagents of NaOH, however, lead to surface deformation and negligible pore formation. Based on the results obtained, it stated that $ZnCl_2$ can produce AC with high surface area. This is further confirmed by Liu and his co-researchers (2016) that claimed $ZnCl_2$ is one of the widely recognized chemical agent that promotes the degradation of carbonaceous material during calcination. As it acts as Lewis acid, it inhibits the formation of tar which subsequently enhance the carbon yield and specific surface area (Liu et al., 2016).

2.2.2.3 Carbonization/activation temperature and time

Carbonization/activation temperature and time play a great role in determining the carbon yield and most importantly the specific surface area. Activated carbon derived from *Arundo donax*, a giant cane is studied with effect of carbonization temperature, time and impregnation ratio (Üner & Bayrak, 2018). It is observed that the increased of carbonization temperature and time has reduced the carbon yield. For instance, a sample was applied with temperature from 300 to 700 ºC of same duration, the carbon yield reduced from 46.16 to 33.29 %. In contrary, with same heating temperature but holding time increased from 30 to 180 mins, the carbon yield resulted in from 46.16 to 42.84 %. Here, we can claim that heating temperature have more significant effect as compared to

carbonization time. This is mainly due to more volatile compounds are released at higher temperature.

Other than carbon yield, pore structure and specific surface area are affected. The study reported that increased carbonization time allow more amount of N_2 adsorbed as sufficient time is provided for thermal energy activates the interactions between *raw material* and $ZnCl_2$ (Üner & Bayrak, 2018). This directly enhance the specific surface area and pore volume. However, longer carbonization time will lead to adverse effect as the pore wall will be burnt resulting in the collapse of structure (Qin et al., 2018).

Temperature has significant influence on the development of porous network of the AC and should be high enough to evaporate all the moisture and volatile matters to form pores (Kwaghger & Ibrahim, 2013). Higher temperature will cause enlargement in pore size such as increment of mesoporosity and reduction in micropore (Prahas et al., 2008). There is also optimum temperature for AC to avoid shrinkage in activated carbon structure leading to decreased in surface area. For instance, Üner & Bayrak (2018) observed a reduction in surface area from temperature of 400 - 700 ºC after they achieved highest surface area at 400 ºC. Figure 2.3 depicts the pore structure prepared from varies temperatures.

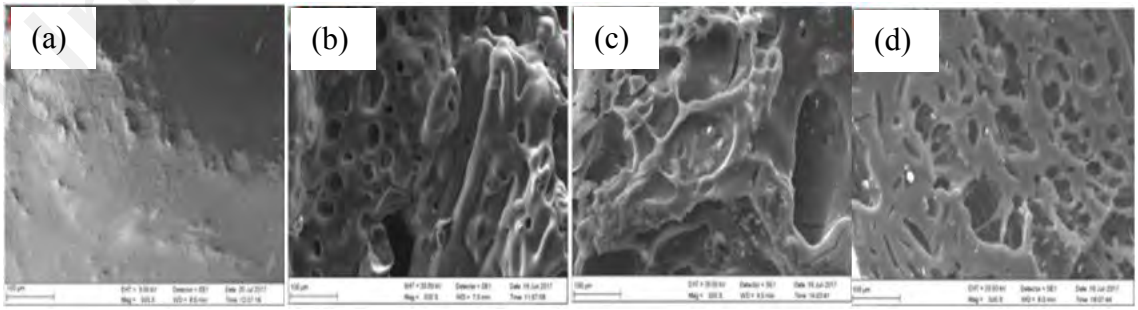

Figure 2.3: SEM image of (a) raw material, activated carbon at various carbonization temperatures of (b) 300, (c) 400 and (d) 500 °C (Üner & Bayrak, 2018)

Looking into both surface area and carbon yield, $ZnCl_2$ has been selected as the activating agent as it provides the highest carbon yield with high surface area (Deng et al., 2009). Besides that, long activation time and high activation temperature will cause adverse effect to the raw material, thus, up to 1 hour holding time with 500 ºC is decided in this research to synthesize good textural properties of AC.

2.2.3 Application of activated carbon

Activated carbon is well-known to its tailored pore size through different synthesis methods. Therefore, it has been selected to be applied in various applications such as water purification, air filtration, colour and chemical removal, electrode materials for supercapacitors and enhancement on the fertility of agricultural soil (Pallarés et al., 2018). However, only application as supercapacitor will be focussed to fit the research purpose.

Activated carbon is selected as an electrode material for supercapacitor mainly due to its high porosity as recognized globally. The micropore and mesopore of the activated carbon play an important character in determining the performance of the supercapacitor. It is reported that micropores consists of charges accumulation while mesopores assists in providing pathway for adsorption and ionic transportation (Frackowiak et al., 2006). Thus, the good combination of micropore and mesopore is critical in delivering excellent performance of the supercapacitor.

Supercapacitor has been a unique role in bridging the gap of battery and capacitor. As known, battery is able to store large energy but relatively low in delivering energy. On the other hand, capacitor is rapid in transporting power though the energy storage cannot last long (Chang & Zainal, 2019). Supercapacitor are famous due to the outstanding performance such as fast energy delivering, excellent cycle stability and rapid charge/discharge (Frackowiak et al., 2006; Zeng et al., 2019). It is generally classified

into three types of capacitors such as double-layer capacitors, pseudocapacitors and hybrid capacitors as illustrated in Figure 2.4.

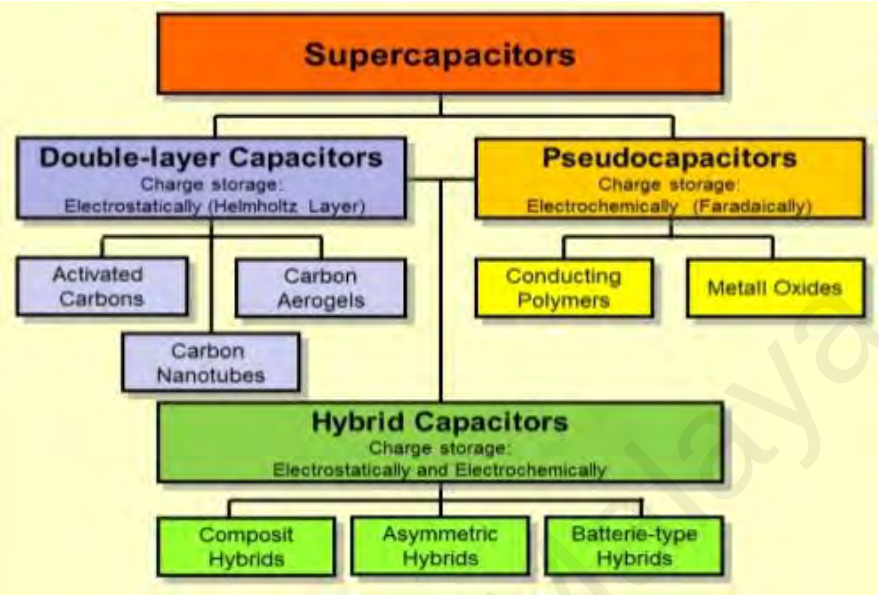

Figure 2.4: Classification of supercapacitor (Gidwani et al., 2014)

As depicted in Figure 2.4, electrical double-layer capacitors (EDLC) can be made up with AC, CNT or carbon aerogel (CA) which will further be discussed in this section. Pseudocapacitors consist of either conducting polymer or metal oxide type of electrode materials which usually exhibit redox reaction during charging/discharging. Lastly, the hybrid capacitors are composite hybrids, asymmetric hybrids or battery-type hybrids whereby the first referring to the electrode containing both carbon and metal oxide/conducting materials which will be explained in detail at later sections. Asymmetric hybrids are two electrodes comprising different elements such as one of the electrodes is carbon material while another electrode is metal oxide/conducting polymer. Battery-type hybrids, on the other hand denoting the electrode which its behaviour reacts alike to the battery due to the elements used such as lithium-ion battery.

The typical EDLC is composed of two electrode films and a separator which serve as an electrolyte. The energy storage process in EDLC is based on the concept of accumulation of electrostatic charge from the reversible ion adsorption/desorption and

arrangement of solvated molecules at the interface between electrode and electrolyte to form electric double layer (Lee et al., 2018a). As depicted in Figure 2.5, the ions are attracted to opposite charge and reverse to relax position when it is discharged.

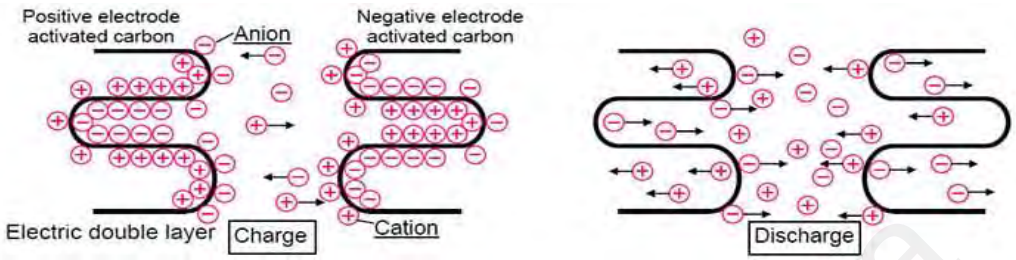

Figure 2.5: Energy storage mechanism in typical EDLC (Shandle, 2019)

The capacitive performance of the EDLC is usually analysed by cyclic voltammetry (CV) and galvanostatic charge-discharge (GCD). Liu and his colleagues (2016) haves studied the capacitive behaviour of the AC produced from willow leaves using $ZnCl_2$ as activating agent. A 6 M KOH is employed as the electrolyte medium, from the CV curves in Figure 2.6(a), a rectangular shape is observed indicating the typical EDLC behaviour and mirror image of the of the GCD curves implying rapid and reversible charge-discharge characteristic. The Nyquist plots show different width of the semicircle indicating different charge transfer resistance which mainly due to varies carbonization temperatures in which higher temperature will tends to favour ion migration into the electrode active sites.

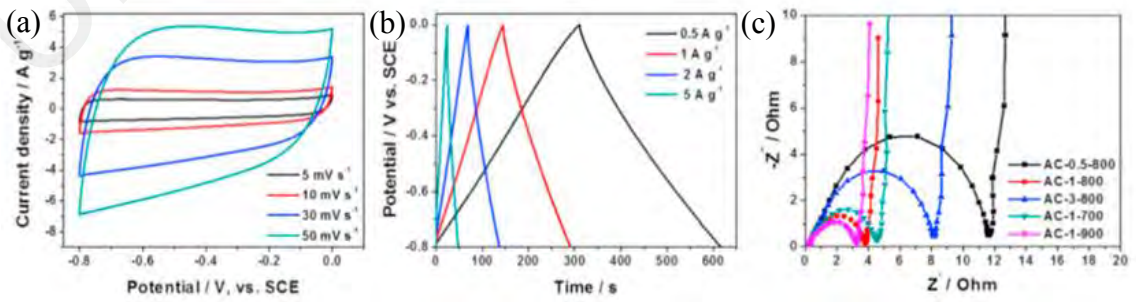

Figure 2.6: (a) Cyclic voltammetry curves, (b) Galvanostatic charge-discharge curves and (c) Nyquist plots of activated carbon (Liu et al., 2016)

There have been numerous studies carried out regarding on the usage of biomass as electrode materials for EDLC which showed promising results. Listed in Table 2.3 are the results of specific capacitance in different electrolyte medium utilizing agricultural waste as precursor for electrode materials.

Table 2.3: List of specific capacitances from porous carbon derived from agricultural waste (Abioye & Ani, 2015).

Material	Activating method	S_{BET} ($m^2\ g^{-1}$)	Specific capacitance ($F\ g^{-1}$)	Electrolyte	Cell configuration
Sugarcane bagasse	MW-$ZnCl_2$	1416	138	$EMImBF_4$	2E
Peanut shell	MW-$ZnCl_2$	1552	199	1 M Et_4NBF_4/PC	2E
Rice husks	MW-$ZnCl_2$	1527	194	1 M Et_4NBF_4/PC	2E
Argan seed shells	KOH	2062	355	1 M H_2SO_4	3E
Waste tea leaves	KOH	2841	330	2 M KOH	3E
Oil palm empty fruit brunch	KOH+CO_2	1704	149	1 M H_2SO_4	2E
Waste coffee beans	$ZnCl_2$	1019	368	1 M H_2SO_4	2E, 3E
	$ZnCl_2$	1021	100	$TEABF_4$/AN	3E
Coffee endocarp	CO_2	1038	167	1 M H_2SO_4	3E
	KOH	361	69	1 M H_2SO_4	3E
DDGS	KOH	2959	260	6 M KOH	2E
Sunflower seed shell	KOH	1162	244	30 wt% KOH	2E
	CO_2+KOH	2509	311	30 wt% KOH	2E
Apricot shell	NaOH	2335	339	6 M NaOH	2E
Sugarcane bagasse	$ZnCl_2$	1788	300	1 M H_2SO_4	2E, 3E
Cassava peel waste	KOH+CO_2	1352	153	0.5 M H_2SO_4	3E
Camellia oleifera shell	$ZnCl_2$	1935	374	1 M H_2SO_4	3E
		1935	266	6 M KOH	3E
Corn grains	KOH	3199	257	6 M KOH	2E

2.3 Carbon composite

Carbon composite material is referring to the material made from carbon and other constituents which can be conducting polymer or transition metal oxides (TMOs). As this study is conducted based on TMOs, thus, only TMOs related literature review will be discussed. TMOs can be categorized into noble and base TMOs in which noble TMOs are RuO_2, IrO_2, etc., while base TMOs have been developing from monometallic oxides (such as NiO, ZnO_2, MnO_2, SnO_2, Co_3O_4, Fe_3O_4, and Mn_3O_4) to single phase bimetallic oxides to single-phase bimetallic oxides (such as $NiCo_2O_4$, $MnCo_2O_4$, $NiMoO_4$, $NiFe_2O_4$, $ZnMn_2O_4$ and $CoMn_2O_4$) (Wu et al., 2016).

As carbon composite materials involve TMOs, thus, the characteristics of supercapacitor energy storage mechanism consists of both pseudo and EDLC capacitance behavior. EDLC storage mechanism has been discussed in earlier section (Figure 2.5), hence, the storage mechanism of pseudo-capacitance is displayed in Figure 2.7. Pseudo-capacitance originated from the electron-transfer mechanisms of the TMOs and electrolyte ions such as during charging, intercalation of ions will be occurred and TMOs experience oxidation while in discharging, de-intercalation of the ions will lead to reduction.

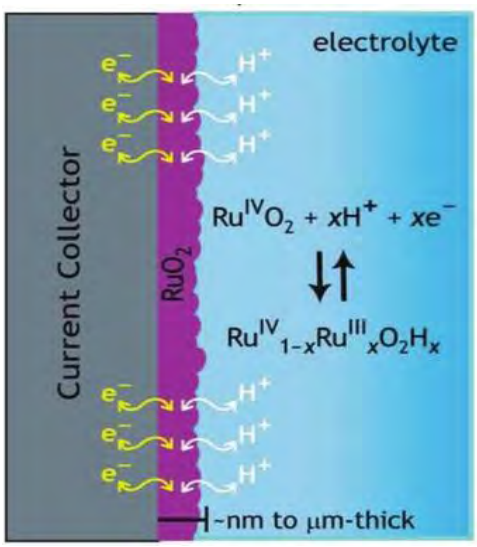

Figure 2.7: Energy storage mechanism of pseudocapacitor (Shahzad et al., 2019)

Carbon-based composites are selected due to its unique characteristics which usually possess homogeneous microstructure and well-distributed metal nanoparticles that exhibited better performance for supercapacitor (Yan et al., 2019a). Further discussion will be focused on the composite of carbon/monometallic TMO such as carbon/zinc oxide (C/ZnO) and carbon bimetallic TMO including carbon/zinc dimanganese oxide, $ZnMn_2O_4$ (C/ZMO) and carbon/zinc tin oxide, $ZnSnO_3$ (C/ZTO).

2.3.1 Carbon/zinc oxide (C/ZnO) composite

Zinc oxide nanostructure are accredited with its outstanding optical and electrical properties which allows it to be applied in various field such as solar cells, gas sensors, and electrochemical supercapacitors (Sasirekha et al., 2018). Moreover, ZnO exhibits strong chemical/thermal stability, good electrochemical performance, eco-friendly in nature and low-cost granted it to be selected by researchers in supercapacitor application (Lee et al., 2018b). According to the studies conducted, ZnO can be appeared in various nanostructures, for instance, microspheres, nanoflowers, nanosheets and nanofibers (Ashar et al., 2016; Diallo et al., 2015; Lee et al., 2018b). On the other hand, ZnO also have drawbacks which are the formation of dendrite growth leading to low rate capability and poor repeatability during the consecutive cycling process (Selvakumar et al., 2010). Therefore, various composites including carbon or other metal oxides are utilized to overcome these limitations (Xiao et al., 2017).

In the later discussion, the physical characterization of various carbon/ZnO composite synthesized by different methods which leads to different morphologies will be included. Further performance in application as supercapacitor will also be studied.

2.3.1.1 Microwave technique

Selvakumar and his co-researchers have produced ZnO material via microwave assisted synthesis method with different microwave power. AC/ZnO composite material is obtained by the addition of activated carbon with synthesized ZnO in different ratios during electrode fabrication (Selvakumar et al., 2010). The XRD spectrum below showed the peaks are indexed to the wurtzite single phase ZnO (JCPDS Card No. 36-1451) with no impurities peak.

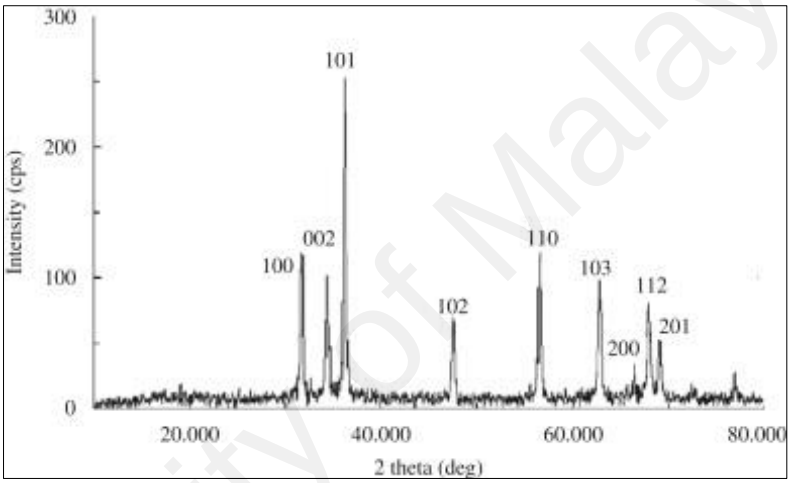

Figure 2.8: XRD spectrum of ZnO (Selvakumar et al., 2010)

As textural properties of the ZnO is not analysed, therefore, cyclic voltammetry test for ZnO with different microwave power in 0.1 M Na_2SO_4 at a scan rate of 50 mVs^{-1} is carried out to investigate its performance. The result illustrated that higher microwave power tends to change the surface features materials causing poor cyclic voltammetry response. Hence, only ZnO with microwave power (75 W) is mixed with AC for further electrochemical performance. Figure 2.9(b) shows that ratio of 1:1 of (ZnO:AC) achieved the maximum energy storage capability of 160 Fg^{-1}. The nearly rectangular shape of CV curve indicating good capacitive behaviour and synchronization of the double-layer and pseudo-capacitive behaviour.

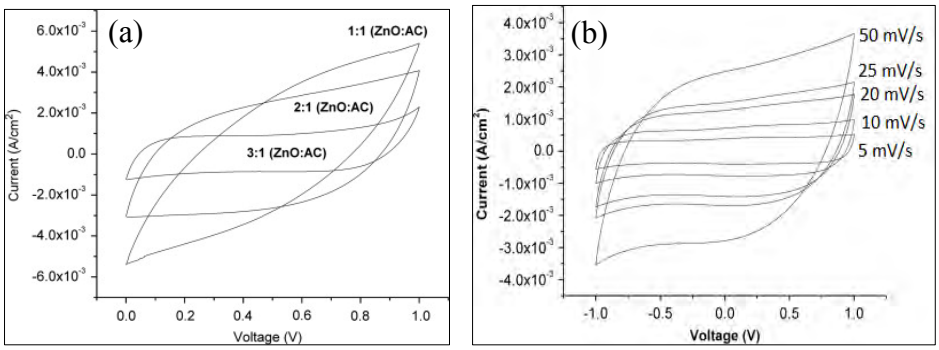

Figure 2.9: Cyclic voltammetry of (a) different ratios of ZnO:AC and (b) various scan rates of sample ZnO:AC (1:1) (Selvakumar et al., 2010)

2.3.1.2 Chemical activation-precipitation dual method

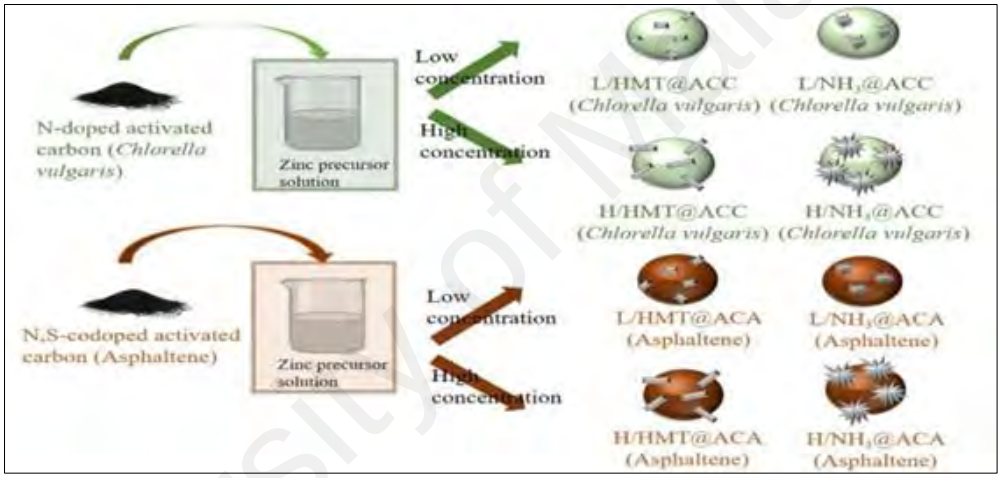

Figure 2.10: Schematic diagram of synthesizing AC:ZnO composites derived from *Chlorella vulgaris* and asphaltene using chemical activated-precipitation method (Lee et al., 2018b)

Another study has been conducted to produce AC:ZnO composite using two steps chemical activation-precipitation method (Lee et al., 2018b). The AC is synthesized by furnace under N_2 flow from two types of precursor namely *Chlorella vulgaris* and asphaltene. ZnO is introduced by the addition of prepared ACs into individual zinc precursor aqueous solution consisting zinc nitrate hexahydrate : hexamethylenetetramine (HMT) and zinc acetate dihydrate : ammonia (NH_3) as illustrated in Figure 2.10. This

study is about the influence of concentration and types of zinc precursor towards the surface morphology which directly affecting the supercapacitor performance.

The SEM images depict that with high concentration of zinc precursor, the nanostructure of ZnO tends to fill the porous structure of the AC which led to drastic reduction in surface area. Besides that, with dissimilar zinc precursors, the shape of ZnO also perform differently which are rod shape with zinc nitrate hexahydrate and flower shape with zinc acetate dihydrate. These morphologies strongly affect the electrochemical performance mainly due to flower structure favours the redox process interaction at the interface of ZnO and electrolyte as compared to rod shape ZnO particles (Lee et al., 2017).

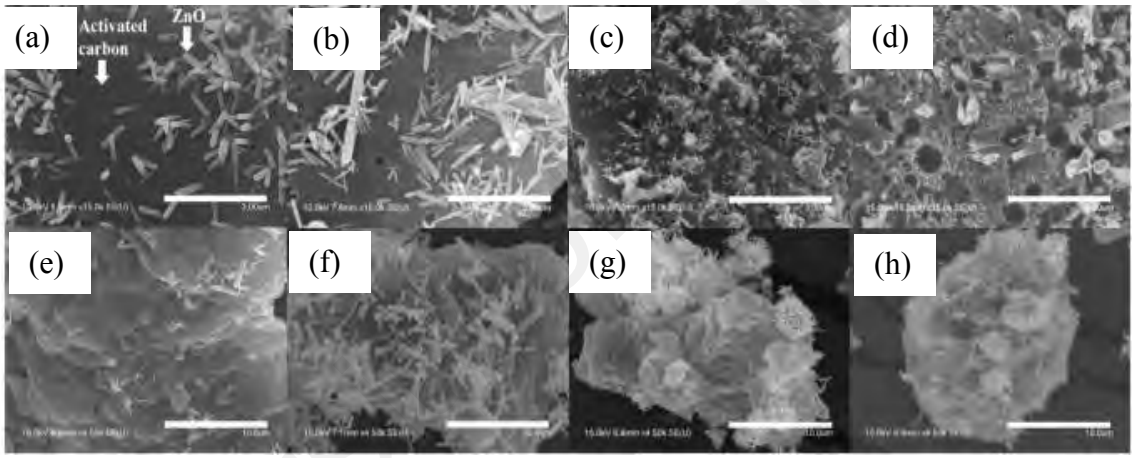

Figure 2.11: SEM images of (a) L/HMT@ACC, (b) H/HMT@ACC, (c) L/NH_3@ACC, and (d) H/NH_3@ACC, (e) L/HMT@ACA, (f) H/HMT@ACA, (g) L/NH_3@ACA and (h) H/NH_3@ACA (Lee et al., 2018b)

The electrochemical properties of the composites are carried out whereby highest specific capacitance of 155 Fg^{-1} is obtained from L/HMT@ACA while 106 Fg^{-1} for L/HMT@ACC at 0.5 Ag^{-1} employing Na_2SO_4 from -1 to 0 V. The promising results can be justified with few explanations. First is attributed to the higher specific area and mesopore volume. Then it comes to the structure of ZnO which provides electrically conductive pathway to ease the electron transport during electrochemical process. Lastly,

with low concentration of ZnO, porosity from AC and ZnO structure allow rapid penetration of electrolyte ion and facilitation of ion/electron transport.

2.3.1.3 Sol-gel method

Sol-gel method is carried to synthesize AC/ZnO by utilizing zinc acetate and sucrose as precursor (Sasirekha et al., 2018). This method is known to be environmentally friendly due to lesser toxic employed which involved only zinc acetate, sucrose and solvent eventually reduced the hazardous waste during preparation. The sample can be indexed to hexagonal structured ZnO as illustrated in Figure 2.12(a). Sol-gel method produced ZnO in irregular granular shape and depicted in Figure 2.12(b).

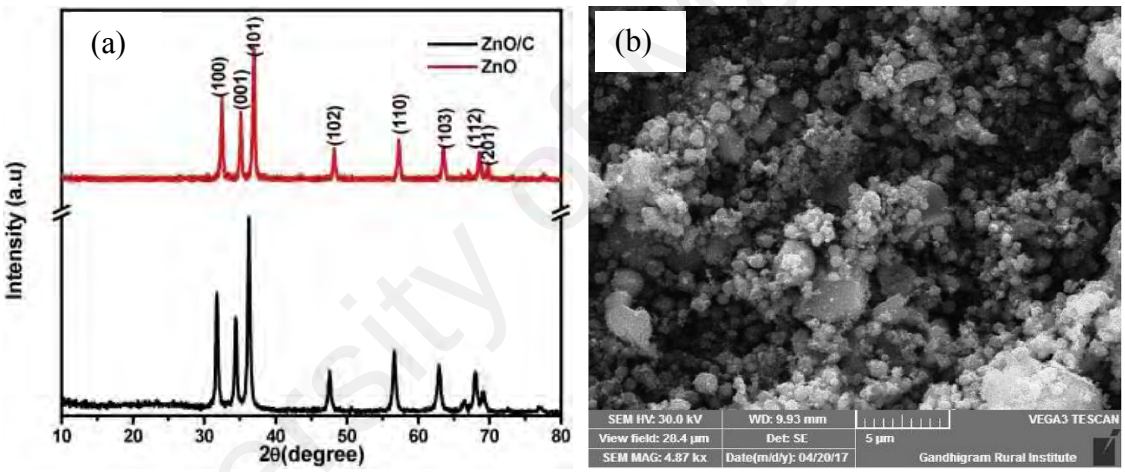

Figure 2.12: (a) XRD patterns of ZnO and AC/ZnO nanocomposite (b) SEM image of AC/ZnO composite (Sasirekha et al., 2018)

At a scan rate of 25 mVs^{-1}, the highest specific capacity of 177.81 Fg^{-1} is achieved with quasi-rectangular shape of CV curve. Electrochemical results showed that AC/ZnO nanoparticles material has better performance in energy storage mainly due to the spherical shaped of the ZnO while carbon assisted in better ion intercalation/deintercalation of the electrode material.

2.3.1.4 Co-precipitation method

Carbon aerogel has strong chemical stability and high conductivity, however, up to now only one research is conducted for CA/ZnO composite for supercapacitor. A study is carried out utilizing $ZnCl_2$ to produce ZnO by co-precipitation method (Kalpana et al., 2006). Carbon aerogel is mixed physically with the prepared ZnO of different ratio such as CA/ZnO (1:1) and (1:2) and pasted on the nickel foam which served as current collector. Here, the cubical shape of the CA/ZnO composite is synthesized as shown in Figure 2.13(a) and (b).

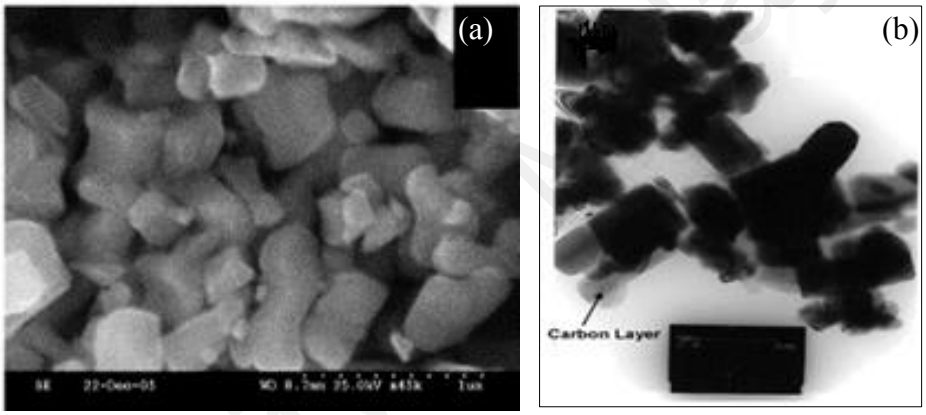

Figure 2.13: (a) SEM and (b) TEM images of CA/ZnO (1:2) composite (Kalpana et al., 2006)

The fabricated supercapacitor is further examined in 6 M KOH electrolyte. Results obtained implying that higher ratio of ZnO having better energy storage performance which is 25 Fg^{-1} at 10 mVs^{-1} due to the conductivity and dispersion of ZnO matrix enhanced by the CA and the high porosity of CA provide better route for the transport of electrolyte ions into the composite matrix. Additionally, CA also plays a major role in stabilizing the crystal lattice of ZnO which it might undergo transformation during cycling process of ZnO. Other than that, high R_{ct} of 180 Ω is observed suggesting that CA is not favorable for long cycling test which it is reasonable that only 500 cycles is conducted for this study.

A multi-wall carbon nanotube (MWCNT) is attracted due to its unique network and high electrical conductivity; however, it requires harsh treatment and toxic solvent (H_2SO_4, HNO_3, and H_2O_2) during synthesizing process (Lee et al., 2018c). Lee and co-researchers (2018c) employed co-precipitation method to produce MWCNT/ZnO with spherical and flower shape of ZnO. Spherical shape of MWCNT/ZnO composite is generated through the solution mixture of MWCNT with zinc nitrate hexahydrate and HMT while flower shape can be created with the mixing of MWCNT, zinc acetate dihydrate and NH_3. This study focussed on the mixture duration time for 30 and 60 mins at 90 ºC. It is observed that longer reaction time leading to larger particle of ZnO while flower-like increasing the amount of petal radially as illustrated in Figure 2.14. This has strongly influenced the surface area as larger particles of ZnO tend to block the pores on MWCNT.

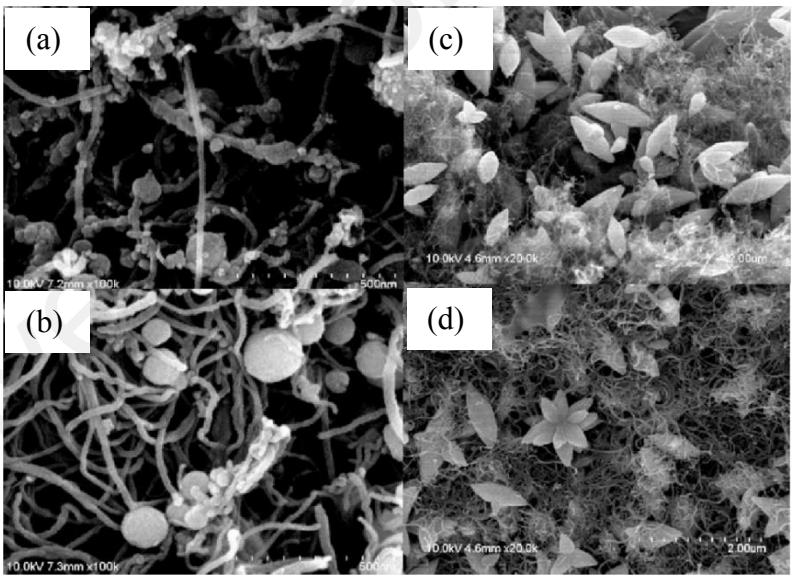

Figure 2.14: FESEM images of (a) HMT/ZnO_MWNT30, (b) HMT/ZnO_MWNT60, (c) NH_3/ZnO_MWNT30 and (d) NH_3/ZnO_MWNT60 (Lee et al., 2018c)

The capacitive performance of the composite materials is tested in 1 M tetraethylammonium tetrafluoroborate. Results indicated that the addition of ZnO to MWCNT has enhanced the capacitance i.e. 10.9, 40.1, 22.7, 24.7, and 14.1 Fg^{-1} for

MWNT, HMT/ZnO_MWNT30, HMT/ZnO_MWNT60, NH_3/ZnO_MWNT30 and NH_3/ZnO_MWNT60 samples. Herein, it also implied that longer reaction time contributed to the capacitance reduction mainly due to accumulation of ZnO has ruined the surface structure and obstructed the protons and electrons to be adsorbed on the surface of the electrode. Therefore, it is important to manage the reaction time and zinc precursor during preparation.

2.3.2 Carbon/zinc dimanganese (C/ZMO) composite

Spinel structure manganese oxides such as $LiMn_2O_4$ (Abdollahifar et al., 2019), $CoMn_2O_4$ (Chen et al., 2019a), $NiMn_2O_4$ (Ray et al., 2019), $ZnMn_2O_4$ (Bhagwan et al., 2018; Chen et al., 2019b) have been studied as material for either supercapacitor or battery usage. However, among these, ZMO attracted the attention of researcher as it possesses low working potential, environmental benign and high energy density (Senthilkumar et al., 2019). ZMO has been studied to perform in many morphologies, for instance, nanoparticles, nanoplates, nanorods and microspheres as tabulated in Table 2.4.

Table 2.4: A summary of different morphologies of ZMO accompanied with individual technique (Yan et al., 2019b).

Methods	**Materials**
Electrospinning	$ZnMn_2O_4$ nanorod
Annealing MnOOH and $Zn(OH)_2$ at 700 °C	Loaf-like $ZnMn_2O_4$ nanorod
Hydrothermal method	Cubic $ZnMn_2O_4$
Reduction/ion exchange/re-crystallization	$ZnMn_2O_4$ nanosheet
Electrospinning	Crumpled $ZnMn_2O_4$ nanosheet
“Escape-by-crafty-scheme” method	$ZnMn_2O_4$ nanoplate
Self-sacrificial template formation	Ultrathin $ZnMn_2O_4$ nanosheet
Solvothermal method	Flower-like $ZnMn_2O_4$ microspheres
Auto-computation method	Flower-like $ZnMn_2O_4$ microspheres

Literature reviews also can be found on ZMO being synthesized using different methods such as sol-gel, solvothermal, co-precipitation, wet-chemical and combustion which to be applied in both supercapacitor or Li-ion battery. Here, different electrochemical performances in terms of specific capacitance and stability are listed in Table 2.5.

Table 2.5: Electrochemical performance of ZMO prepared by various methods.

Material	**Method**	**Electrolyte medium**	**Specific capacitance**	**Stability**	**Reference**
Hetarolite ZMO	Hydrothermal	1 M KCl	675 Fg^{-1} at 5 mVs^{-1}	61.7 %, 1000 cycles	(Senthilkumar et al., 2019)
ZMO Nanosheet	Cathodic electro-deposition	0.5 M Na_2SO_4	457 Fg^{-1} at 1 Ag^{-1}	92.5 %, 4000 cycles	(Barkhordari et al., 2019)
ZMO	Surfactant	0.5 M Na_2SO_4	191 Fg^{-1} at 5 mVs^{-1}	98.4 %, 1000 cycles	(Zhu et al., 2018a)
ZMO Nanofiber	Electro-spinning	1 M Na_2SO_4	240 (±5) Fg^{-1} at 1 Ag^{-1}	~98 %, 2000 cycles	(Bhagwan et al., 2018)
Hierarchi-cal porous ZMO	Sucrose-assisted combustion	6 M KOH	411.75 Fg^{-1} at 1 Ag^{-1}	88.3 %, 4000 cycles	(Huang et al., 2017)
Porous ZMO	Hydrothermal coupled with calcination	2 M KOH	155(±2) Fg^{-1} at 2 mVs^{-1}	~99 %, 1100 cycles	(Guo et al., 2015)
Porous ZMO	Calcination	1 M Na_2SO_4	1093 Fg^{-1}	~96 %, 5000 cycles	(Gao et al., 2015)
ZMO	Urea combustion	2 M KOH	160(±5) Fg^{-1} at 3 mVs^{-1}	~100 %, 500 cycles	(Sahoo & Sharma, 2015b)

As seen from the above table, reports on synthesized ZMO used as supercapacitor are limited due to much of the literature reviews are stated on the application as Li-ion batteries, not to mention the combination of carbon with ZMO. Thus, reports with different techniques in producing C/ZMO are discussed as followed.

2.3.2.1 Combustion method

This method is widely used due to inexpensive precursor, high yield, able to produce large-scale, easy constructing, simple equipment and most importantly rapid crystallisation (Abdollahifar et al., 2018) which is also the reason being selected in this research. This method has employed manganese nitrate, $Mn(NO_3)_2$ and zinc nitrate, $Zn(NO_3)_2$ as precursor for the synthesis of ZMO while polyethylene glycol (PEG) polymers served to produce carbon source. PEG with different molecular weight denoted as PEG-2 and PEG-6 are first dissolved separately and added dropwise individually to the homogeneous solution containing $Mn(NO_3)_2$ and $Zn(NO_3)_2$. The mixture is further added with urea and combusted at muffle furnace at 370 (±10) °C.

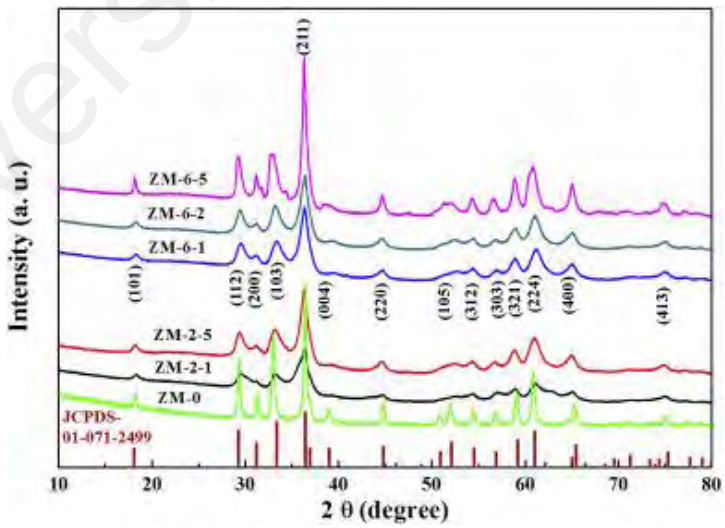

Figure 2.15: XRD pattern of C/ZMO composite (Abdollahifar et al., 2018)

The results obtained from the XRD obviously shown the patterns that agreed with tetragonal $ZnMn_2O_4$ (JCPDS No. 01-071-2477). However, the patterns have displayed

peak with different intensities and broadening implying varies crystallite sizes. Additionally, it also showed that without the addition of PEG, high intensity peaks of $ZnMn_2O_4$ is revealed. Thus, it is proved that PEG has the ability in suppressing crystallite growth during synthesis process which in turn increasing carbon residue.

Besides that, it is observed that different molecular weights of PEG but similar quantity of usage have influence on the pore size. This also implied that varies quantity and types of raw material in producing carbon leads to diverse pore structure which is important during electrochemical reactions mainly due to appropriate pore size and volume enhance the diffusion of electrolyte ions at the interface of electrode-electrolyte. Thus, understanding the parameters allow pore structure tailoring to be constructed which is essential to produce materials according the application requirements.

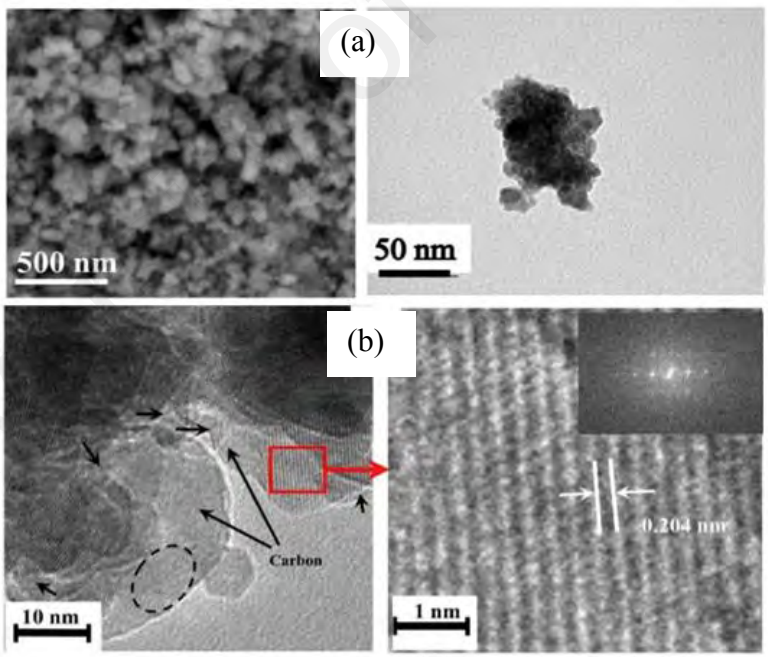

Figure 2.16: (a) SEM and (b) TEM images of C/ZMO composite (Abdollahifar et al., 2018)

According to the Figure 2.16(a), it can be seen that combustion method resulting in agglomerates particles to produce interconnected nano-porous hierarchical structures.

Figure 2.16(b), on the other hand, has revealed that high crystallinity can be achieved by this method with the lattice fridge obtained from TEM image.

The electrochemical performance is analysed in three-electrode system employing 1.75 M Na_2SO_4 electrolyte. The selected potential window is 0.1-1.0 V as potential range below 0.1 V causing the loss of Mn from the electrode through disproportionation reaction of Mn^{3+} to produce soluble Mn^{2+} (Weng et al., 2015) and turning the electrolyte to brownish colour in prolong cycle. Figure 2.17(a) has depicted the CV curves with nearly rectangular shape which is originated from the carbon the source implying ideal capacitive behaviour. Capacitance in the range of 75-105 Fg^{-1} is achieved compared to pure ZMO which is only 38 Fg^{-1}. Much of the capacitance value is contributed by carbon as ZMO is a poor electronic conductor, with the presence of carbon coating, conductivity within the secondary particles is enhanced subsequently increase the utilization of the oxide nano-crystallite. Furthermore, stability over 10000 cycles are conducted and showed superior capacitance retention, proving C/ZMO a promising active material as supercapacitor. However, most studies lack of the information on the durability of the materials over long cycling test, thus, in this research has covered and will discuss in later chapter.

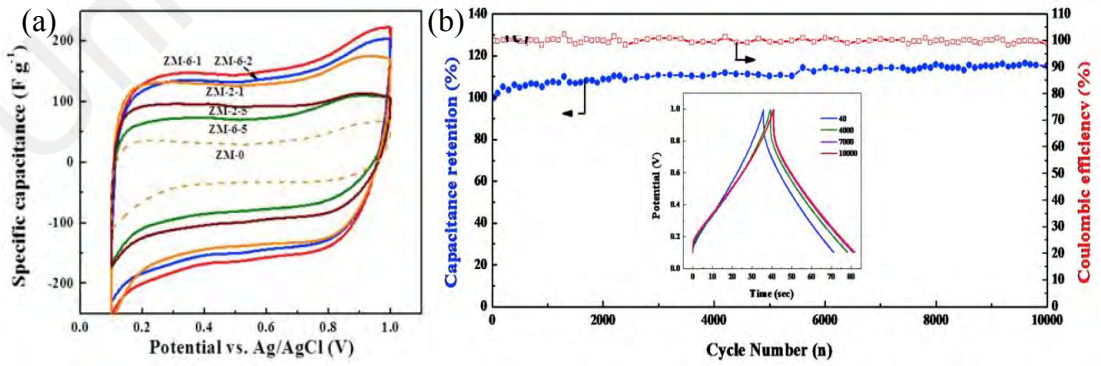

Figure 2.17: (a) Cyclic voltammetry and (b) stability test of C/ZMO composites (Abdollahifar et al., 2018)

2.3.2.2 Hydrothermal method

Guan and his colleagues (2016) have carried out the first hydrothermal synthesis of C/ZMO using $Mn(NO_3)_2$ and $Zn(NO_3)_2$. Solution contained these two chemicals along with nickel foam is autoclaved at 180 °C for 4 hours to obtain light green products attached on the nickel foam. This prepared nickel foam is then placed into the Teflon-lined with 1 M glucose solution to be heated at 180 °C for 8 hours. In order to obtain carbon, the nickel foam is heated in a tube furnace under Argon gas atmosphere at 700 °C for 3 hours while the intermediate sample is calcined in air for 3 hours at 300 °C to achieve ZMO growth on the nickel foam.

Sandwiched-like morphology is observed under the SEM image and evenly distributed on the nickel foam substrate. Figure 2.18(b) clearly shown that ZMO nanoparticles are well encapsulated with the graphitized carbon layer. The XRD pattern further confirming that ZMO is achievable with this method in which the pattern is consistent with $ZnMn_2O_4$ (JCPDS No. 71-2499).

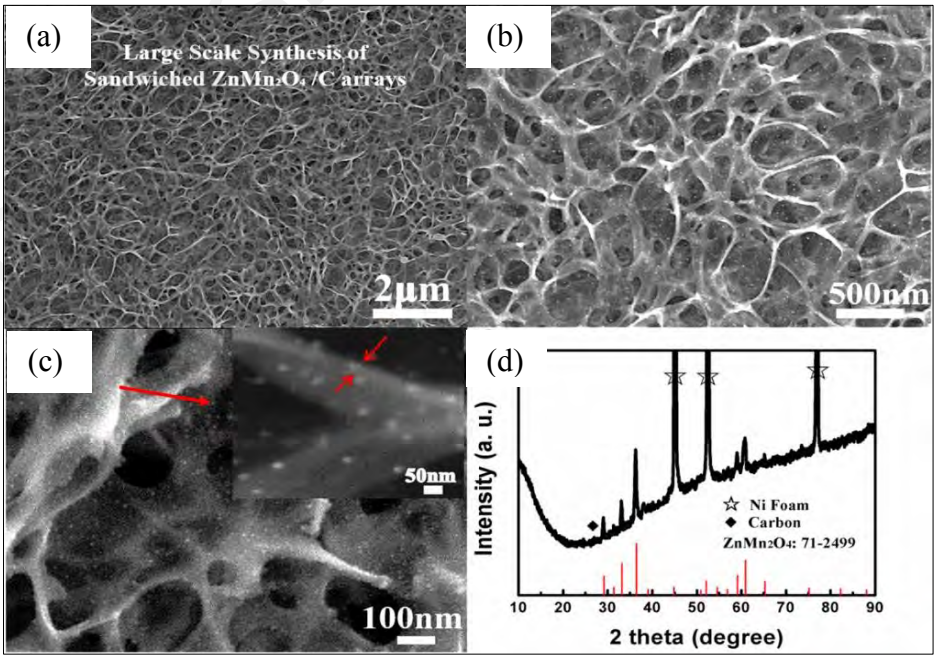

Figure 2.18: (a-c) SEM images of C/ZMO with different magnifications and (d) XRD pattern of C/ZMO (Guan et al., 2016)

A series of electrochemical tests by Guan and his co-reserachers (2016) were conducted in 1 M KOH electrolyte as shown in Figure 2.19. Two redox peaks can be observed from the CV curve which is attributed to ZMO. As the scan rates higher, the redox peaks are moved, this can be explained with electric polarization and some irreversible reactions (Han et al., 2013). Specific capacitance is calculated based on CD discharge curve with 1786 Fg^{-1} is obtained at 1 Ag^{-1}. High stability also observed even high current density is applied indicating sandwiched-like morphology provides strong mechanical strength.

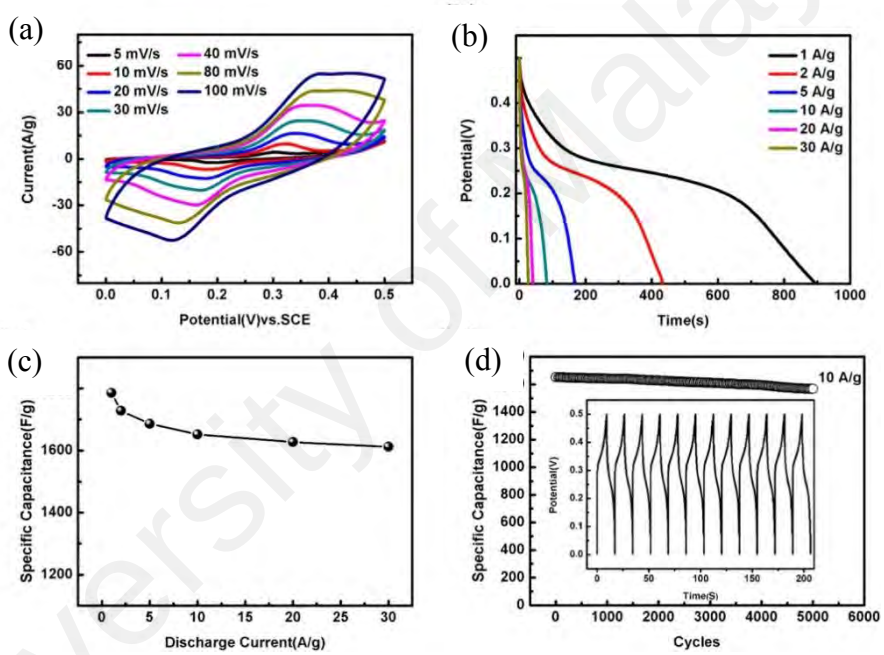

Figure 2.19: (a) CV vs scan rates, (b) GCD curves, (c) specific capacitance vs current densities and (d) stability test of C/ZMO (Guan et al., 2016)

2.3.2.3 Metal-organic frameworks-derived method

Metal-organic frameworks (MOFs) is quite a new methodology as to previous discussed approaches. This method provides perfect templates to construct different nanostructures and its unique characteristics such as tailored nanostructure, shorter electron and ion diffusion route and miscellaneous compositions have attracted the attention of researchers to choose for the preparation of nanomaterials for supercapacitor

application recently (Zhu et al., 2018c). Here, organic linkers i.e. 1, 3, 5-benzenetricarboxylic acid is used and manganese acetate tetrahydrate ($C_4H_4MnO_4 \cdot 4H_2O$) and zinc acetate dehydrate ($C_4H_4ZnO_4 \cdot 2H_2O$) acted as precursor for ZMO. The mixture is first exposed to carbonization at 500 °C in N_2 condition and further heated at 300 °C in air to synthesize spinel structure of ZMO. Eventually, ZMO/C nanorod (ZMCN) is generated while ZMO nanorod (ZMON) is only pyrolyzed in air for 2 hours at 450 ºC. As shown in Figure 2.20, the nanorod is rough which due to the evaporation of gaseous molecules and decomposition of organic linkers during heat treatment.

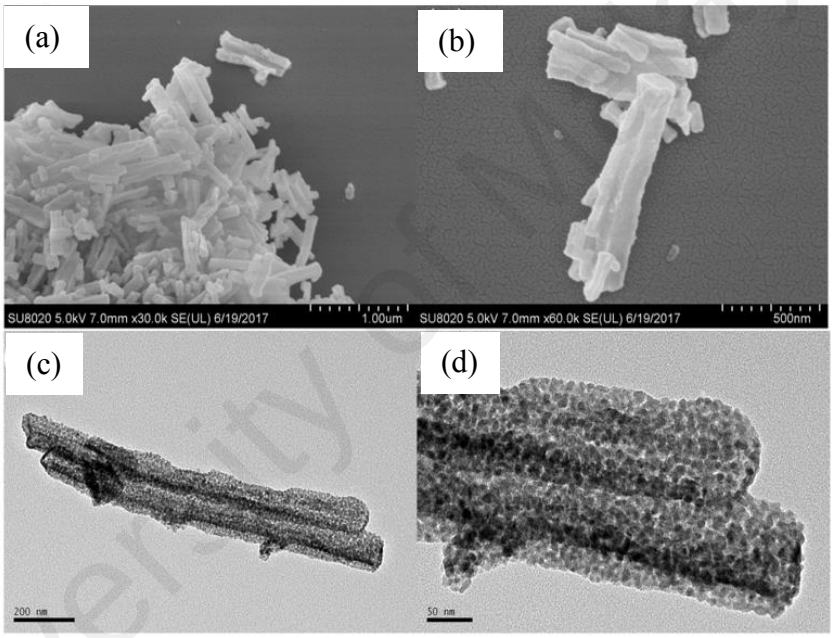

Figure 2.20: (a,b) FESEM and (c,d) TEM images of ZMCN (Zhu et al., 2018c)

According to the electrochemical results illustrated in Figure 2.21, it is obvious that ZMCN exhibited higher capacitive value. The almost rectangular shape and insignificant redox peaks in the CV curves implying rapid successive surface of redox process. Highest capacitance obtained from ZMCN and ZMON is 589 Fg^{-1} and 217.5 Fg^{-1} respectively. Undeniable that with the existence of porous and interconnected carbon, specific capacitance and stability is enhanced, this can be explained with more active sites are provided and shorter ions transfer pathway.

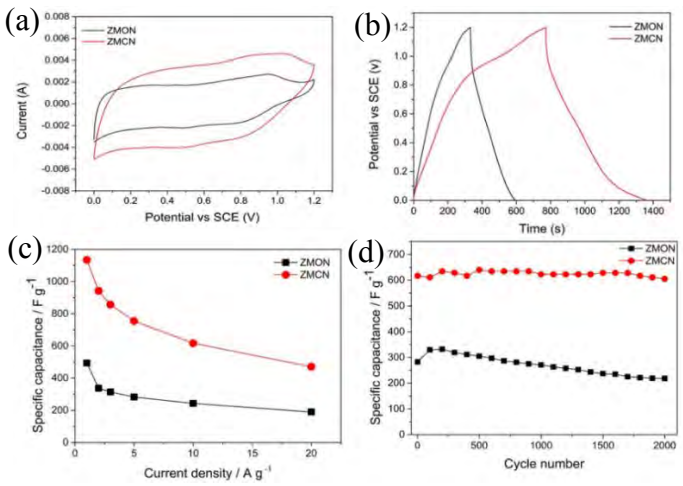

Figure 2.21: (a) CV at 10 mVs^{-1}, (b) GCD at 1 Ag^{-1}, (c) specific capacitance vs current densities and (d) stability test of ZMCN and ZMON (Zhu et al., 2018c)

2.3.3 Carbon/zinc tin oxide (C/ZTO) composite

Zinc tin oxide (ZTO) system consists of zinc stannate or meta-stannate ($ZnSnO_3$) and zinc ortho-stannate (Zn_2SnO_4) in which the front is a perovskite type of oxide that forms face-centered-cubic closed structure in which every ZnO_6 octahedron shares a face with SnO_6 octahedron in the crystal (Hoel et al., 2010) while the later forms an inverse spinel structure as shown in Figure 2.22. ZTO can be synthesized easily through solid-state reaction in which $ZnSnO_3$ can be obtained and stable in the temperature range of 350 - 750 ºC, however, temperature higher than 750 ºC can lead to decomposition by forming $ZnSnO_4$ and SnO_2 (Chen et al., 2012).

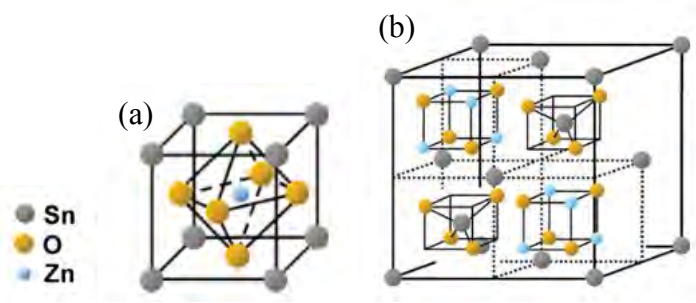

Figure 2.22: Crystal structure of (a) perovskite and (b) inverse spinel ZTO (Bora et al., 2015)

This type of structure is a typical non-centrosymmetric oxide, thus exhibiting outstanding impulsive polarization and piezoelectric strain characteristics which are important for different applications (Bora et al., 2015). ZTO also considered as multifunctional materials (Chen et al., 2012) which is one of the reasons attracted considerable attention for the past few years coupled with its simple synthesis method, abundance and chemically properties (Han et al., 2014; Zhang et al., 2019) have added credit for itself. However, ZTO also encounter problem such as low capacitance retention which is attributed to pulverization and agglomeration during cycling test.

As this research is concerned about $ZnSnO_3$, thus, report regarding Zn_2SnO_4 will not be included here. Due to its unique characteristics, ZTO has been widely used gas sensors, solar cells, thin-film transistor, piezoelectric generator and Li-ion battery (Yan et al., 2019c). To the best of my knowledge, there is yet research reporting the utilization of ZTO as supercapacitor application. Hence, literature review here only covers the types of synthesis method and its physical characterization with related electrochemical performance for C/ZTO composite material.

2.3.3.1 Hydrothermal method

The design of sandwiched-like C/ZTO has been carried out by Luo and his co-researchers (2016) utilizing $ZnSn(OH)_6$ as precursor for ZTO and glucose as carbon source. The mixture of $ZnSn(OH)_6$ and glucose were hydrothermal at 180 ºC for 6 hours and further heated 2 hours at 540 ºC in argon atmosphere. The synthesized material is evaluated using XRD, SEM and TEM. As illustrated in Figure 2.23(a), XRD pattern shown both broad and crystalline peaks whereby the broad peaks indicating the amorphous characteristic while crystalline peaks can be assigned to ZTO (JCPDS No. 28-1486). SEM and TEM images also clearly display that ZTO is successfully synthesized within carbon. Crystal lattice is not depicted indicates the amorphous properties of ZTO.

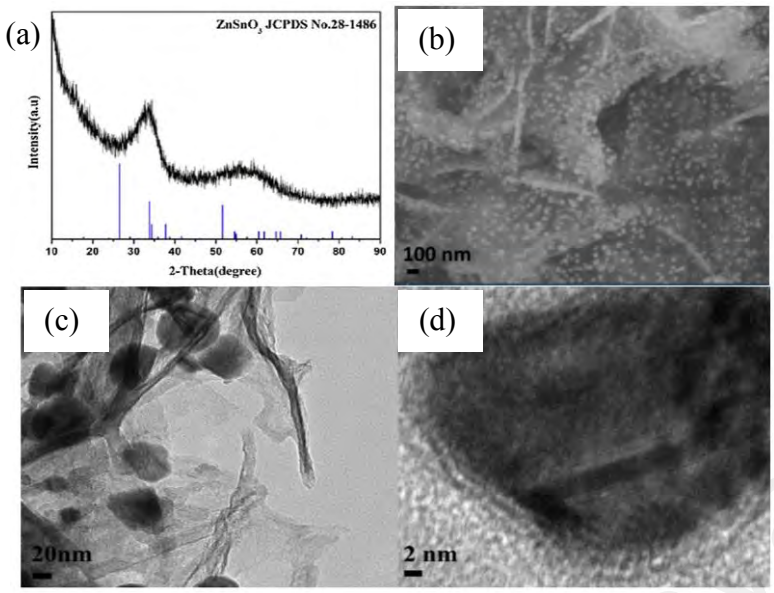

Figure 2.23: (a) XRD pattern, (b) SEM, (c) TEM and (d) HRTEM images of C/ZTO (Luo et al., 2016)

Another study to produce C/ZTO is also carried out via hydrothermal (Xie et al., 2014), however, with a different approach whereby, ZTO is prior synthesized with varies temperature and mixed with glucose followed by hydrothermal at 180 ºC for 7 hours. The product is further calcined in argon condition at 450 ºC for 4 hours. As depicted in Figure 2.24(a), the XRD pattern reported is similar to the previous study. Due to the different methodology steps, cubical shape of ZTO is produced with surface modification by carbon elements as shown in Figure 2.24(b) and (c). With effect of this carbon coating, the specific surface area is greatly enhanced which is beneficial to the electrochemical performance.

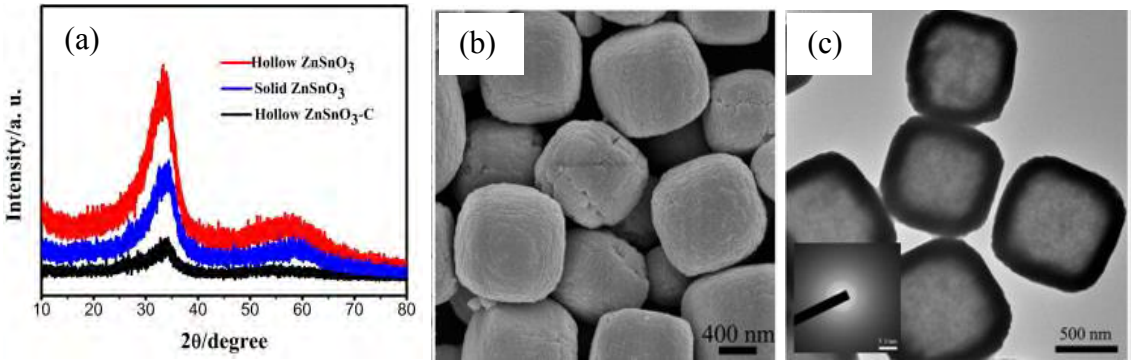

Figure 2.24: (a) XRD pattern, (b) SEM and (c) TEM images of C/ZTO (Xie et al., 2014)

Despite materials from both studies are applied in batteries instead of supercapacitor, the electrochemical behaviour still can be observed. The result of C/ZTO always showed better performance as compared to ZTO alone. First, more active sites are available to take part in the electrochemical reaction which increase the specific capacitance. Moreover, the inner crack of the hollow microcubes able to reduce the severe volume change during intercalation/deintercalation process and shorter pathway for ion diffusion have undeniable enhance the cyclability. Besides that, carbon which acts as conducting material assists in preventing agglomeration and pulverization which improve structural stability. Lastly, the amorphous characteristic of ZTO allows a more homogenous volume change to maintain the electrodes structural integrity (Li et al., 2012; Luo et al., 2016; Xie et al., 2014).

2.3.3.2 Aqueous solution method

Alam and his colleagues (2015) have conducted study by using zinc acetate dihydrate and tin chloride dihydrate as precursor for ZTO. These chemicals are then dissolved individually and mixed together with NaOH added by drop wise. The mixture then stirred continuously at 160 ºC for 24 hours for reaction to occur. The composite was then prepared by the addition of MWCNT with prepared ZTO. This kind of treatment is indeed requiring minimal skill and inexpensive equipment to accomplish. However, it still involves many steps unlike this study which synthesize carbon/ZTO composite in one combustion step.

According to the XRD pattern illustrated in Figure 2.25(a), the pattern of synthesized materials is consistent to ZTO (JCPDS No. 11-0274) with a broad peak indicating the amorphous structure of MWCNTs. The FESEM image also ensures MWCNTs and ZTO are present in the synthesized composite material. As this study was applied as

piezoelectric power generation, therefore, only physical characterizations of the material are included.

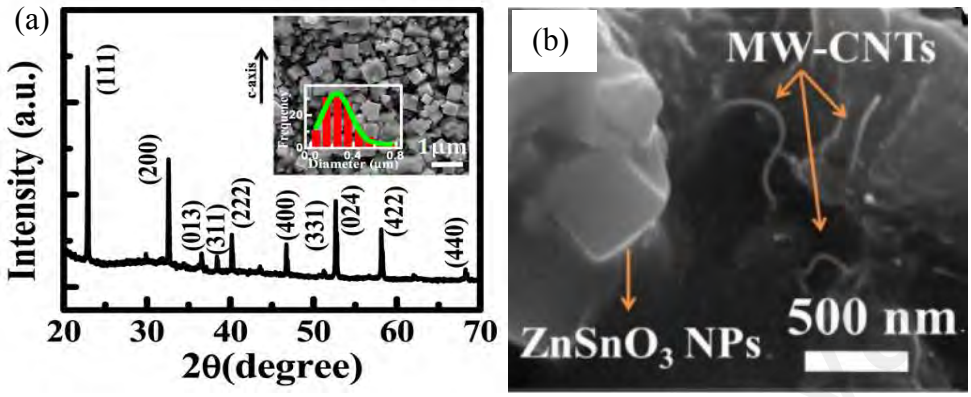

Figure 2.25: (a) XRD pattern and (b) FESEM image of MWCNTs/ZTO (Alam et al., 2015)

2.4 Summary

- In biomass, both cellulose and hemicellulose having averagely 44.4 wt.% carbon meanwhile, lignin on the other hand have higher carbon content (62 wt.%) and lower oxygen content (32 wt.%).
- Activating agent such as $ZnCl_2$ develops small mesoporosity, provides the highest yield and promotes the degradation of carbonaceous material during calcination.
- Good combination of micropore and mesopore is critical in delivering excellent performance of the supercapacitor
- Carbon-based composites electrode is selected due to its unique characteristics which usually possess homogeneous microstructure and well-distributed metal nanoparticles exhibited better performance for supercapacitor
- C/ZnO composite is claimed to have different morphologies by varies precursor such as rod shape with zinc nitrate hexahydrate and flower shape with zinc acetate dihydrate. Moreover, longer reaction time also led to larger particle of ZnO while flower shape increased by the amount of petal radially.

- ZMO has been synthesized using different methods such as sol-gel, solvothermal, co-precipitation, wet-chemical and combustion. Among all kind of methods, combustion gained the most attraction due to inexpensive precursor, high yield, able to produce large-scale, easy constructing, simple equipment and most importantly rapid crystallisation. This method also assisted in agglomeration of particles to produce interconnected nano-porous hierarchical structures.
- ZTO has been widely used gas sensors, solar cells, thin-film transistor, piezoelectric generator and Li-ion battery, however, there is still none research reporting in the application as supercapacitor.
- There are also no reports studying on the rate capability in long cycling test for carbon-based composite materials in which this assessment is carried out in this study.

CHAPTER 3: METHODOLOGY

3.1 Introduction

Pineapple has become one of the new sources for the wealth of country mainly due to its increasing export value which is increase from RM155 million a year to RM320 million by 2020 in Malaysia (Othman, 2017). Looking at this, undeniable that it will lead to the rise in waste volume as pineapple waste such as the peel, crown and stem made up 40-50 % of the fresh fruit (Abdullah & Mat, 2017). The pineapple peel (PP) mainly consists of carbohydrates such as cellulose, hemicellulose, and lignin (Khedkar et al., 2018) that contributed to the synthesis of carbon materials. Other than pineapple peel, green waste (GW) such as fallen/trimming leaves, grass clippings, branch cutting mostly due to urban landscaping maintenance (Zhang & Sun, 2018b) has placed an urgent management solution too attributed to its bulky volume. Similarly, green waste also contains the same composition as fibre comprise cellulose, hemicellulose and lignin which can acts as carbon source (Biswal et al., 2013; Jagadeesan & Eswaramoorthy, 2010). Therefore, both wastes have been chosen not only for its beneficial composition but also its high accessible of reaching it around the world.

In this study, both PP and GW were utilized as carbon source while for the carbon composite materials; manganese carbonate ($MnCO_3$) and stannous carbonate ($SnCO_3$) are incorporated to both PP and GW which will further used in supercapacitor application. This chapter will explain the steps including pre-treatment of the raw materials, synthesis of carbon composite and further discuss on the behavior of synthesis materials for electrochemical performance. Nitrogen adsorption test was analyzed to study the textural properties of the samples. Surface morphology is studied under the field emission scanning electron microscopy (FESEM) while microscopic structure via transmission electron microscopy (TEM). FESEM equipped with energy dispersive X-ray spectroscopy (EDX) tool assisted in determining the element of the samples. The nature

(amorphous/crystalline) of the samples is studied using x-ray diffraction (XRD). The electrochemical performance of the samples is further examined by cyclic voltammetry (CV) and galvanostatic charge-discharge (GCD) will the resistance of the samples is conducted via electrochemical impedance spectroscopy (EIS).

3.2 Materials

Pineapple peel was collected from the fruit stall while green waste was obtained from waste collection site at University of Malaya. Ammonium bicarbonate (CH_5NO_3) was procured from Sigma-Aldrich. Manganese (II) sulphate, monohydrate ($MnSO_4.H_2O$) and stannous sulphate ($SnSO_4$) were obtained from Ajax Finechem. The company of Friendemann Schmidt provided zinc chloride ($ZnCl_2$) and potassium hydroxide (KOH). Hydrochloric acid (HCl) and N-Methyl-2-pyrrolidone (NMP) were purchased from Merck KGaA. All reagents were of analytical grade and used without further purification.

3.3 Methodology

3.3.1 Preparation of porous carbon

The collected PP was washed through under pipe water while shredded GW on the other used without washing. Both PP and GW were put in the oven at 110 ºC for 48 hours to get remove the moisture. PP and GW were then ground into powder and sieved with 300 μm siever. 10 g of sieved PP and GW were impregnated with 400 mL of 1M $ZnCl_2$ as activating agents. The mixture of precursor and acid were continuously stirred for 24 hours using magnetic stirrer and allowed for suspension at room temperature. Impregnated sample was dried at 100 °C followed by grinding into powder form. This was followed by carbonization via furnace equipped with nitrogen (N_2) flow with the rate of 1 L min^{-1} at 500 ºC under heating rate of 10 ˚C min^{-1} for 1 hour holding time. After heating, the sample was left cooled down in the furnace with N_2 flow until 80 ˚C. Sample was left overnight in the furnace until it reached room temperature. The cooled sample

was washed with 100 mL of 1 M HCl to ensure removal of ZnO (Li & Liu, 2014) and further washed with hot and cool distilled water until pH ~7 to remove volatile matter and ash. The washed sample was then dried with oven at 110 ºC. Porous carbon synthesized from pineapple peel (PP-C) and green waste (GW-C) were ready to be used.

3.3.2 Preparation of precursor for composite materials

Facile mixing method was used to prepare manganese carbonate ($MnCO_3$) and stannous carbonate ($SnCO_3$). Firstly, $MnSO_4$/$SnSO_4$ (1 mmol) and CH_5NO_3 (10 mmol) were dissolved individually in distilled water. When CH_5NO_3 was fully dissolve, it was added to the $MnSO_4$ solution with continuous stirring accompanied with ethanol according to the ratio of 1:10 with water. The colour alteration of solution indicating the formation of $MnCO_3$ (milky white) and $SnCO_3$ (light brownish). The mixture was allowed for precipitation at room temperature for 3 hours. The obtained $MnCO_3$ or $SnCO_3$ precipitate was isolated from the mixture using centrifugation at the speed of 5000 rpm for 5 mins. To remove the impurities, colloid was cleaned few times with water and ethanol. The collected $MnCO_3$/$SnCO_3$ precursor was dried in an oven at room temperature for 24 hours prior to be used.

3.3.3 Preparation of binary and ternary carbon composites

For binary carbon composite, both $ZnCl_2$ impregnated PP and GW were heated directly to obtain PP-ZnO and GW-ZnO. On the other hand, ternary carbon composites such as carbon/zinc manganese oxide (C/ZMO) and carbon/zinc tin oxide (C/ZTO) with a series of ratio were prepared by mixing impregnated PP and GW with $MnCO_3$/$SnCO_3$ prior for combustion. The composition of ternary carbon composites is listed in Table 3.1 and 3.2. Both binary and ternary carbon composites were synthesized via calcination with furnace as well at the temperature of 500 ºC for one hour holding time with the heating rate of 10 ˚C min^{-1} under N_2 atmosphere (1 $Lmin^{-1}$). The heating process is exactly like the

preparation of activated carbon; however, difference was observed during the washing process. In preparing binary and ternary carbon composites, lower molarity of HCl (0.05 M) was being used mainly due to higher molarity tends to wash away not only the impurities but also the composite materials. After washing with HCl, several washes with hot and cold distilled water until ~pH 7 was carried out before it was dried in an oven at 110 ºC.

Table 3.1: Weight percentage ratio of pineapple peel and green waste incorporated with $MnCO_3$.

Sample ID	Impregnated sample (%)	Manganese carbonate (%)
PP/GW-ZMO1	91	9
PP/GW-ZMO2	82	18
PP/GW-ZMO3	73	27
PP/GW-ZMO4	64	36

Table 3.2: Weight percentage ratio of pineapple peel and green waste incorporated with $SnCO_3$.

Sample ID	Impregnated sample (%)	Stannous carbonate (%)
PP/GW-ZTO1	91	9
PP/GW-ZTO2	82	18
PP/GW-ZTO3	73	27

3.3.4 Electrode preparation and supercapacitor fabrication

For the purpose of electrochemical measurement, electrode was prepared with slurry consists of carbon composite, super P and polyvinylidene fluoride (PvdF) binder in NMP which acts as solvent at the of ratio 9:1:1. The cut 4 cm^2 nickel foam was spreaded with carbon slurry (2cm^2) and heated in the furnace at 100 °C for 4 hours at the heating rate of 1 ˚C min^{-1}. The dried nickel foam was pressed at 200 kPa and further weight for the mass of active material for capacitance calculation purpose. A three-electrode set-up as seen in Figure 3.1 was carried out with all types of activated carbon and carbon composite

electrode, Pt and Ag/AgCl served as working, counter and reference electrode respectively in 6 M KOH to study the behavior of the active materials.

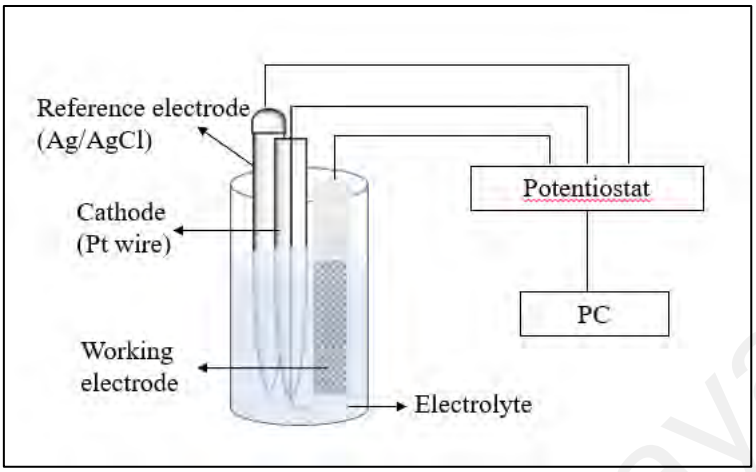

Figure 3.1: Schematic diagram of three-electrode system

After all the electrochemical studies were accomplished, supercapacitor was fabricated by preparing two similar electrodes with the size of 1 cm^2 pasted fully with slurry and microfibre filter which acts as separator and electrolyte. Microfibre filter was soaked in 6 M KOH for 3 hours to ensure the solution is fully absorbed. The symmetrical cell was then made up with the soaked filter sandwiched between two identical electrodes and placed in the battery holder prior to test the device performance as shown in Figure 3.2.

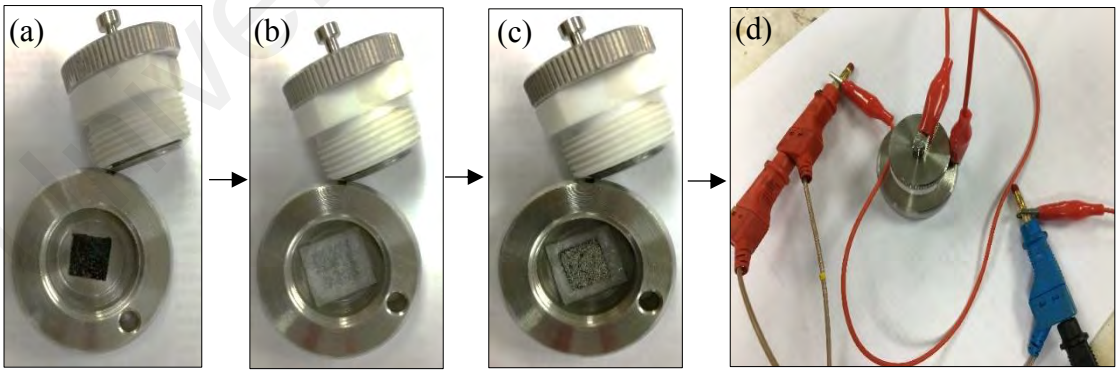

Figure 3.2: Sequence of supercapacitor fabrication in battery holder with (a) first electrode with active material faces upward (b) 6 M KOH soaked microfibre filter on top of first electrode (c) second electrode with active material placed on the filter and (d) battery holder is screwed and available for electrochemical testing

3.4 Binary and ternary carbon composite formation process

In this present work, simple combustion method was performed to synthesize binary and ternary carbon composites. Based on study conducted by Li and Liu (2014), $ZnCl_2$ can be transformed to ZnO under certain environment. Hydrothermal/solution heating is the most common method to produce ZnO. Equation below represents the synthesis of binary C/ZnO composite:

$$ZnCl_2 + H_2O + C \xrightarrow{\Delta} ZnO + C + 2HCl \uparrow \quad [3.1]$$

During combustion, the process of dehydration results in the aromatization of the carbon skeleton and release of volatile gas (Uçar et al., 2009). This process has led to the formation of pore structure to a porous material while ZnO formed under the thermal decomposition of hydrolyzate of $ZnCl_2$ (Li & Liu, 2014).

In ternary carbon composite, two types of composites such as C/ZMO and C/ZTO are included in this research. The addition of $MnCO_3$ and $SnCO_3$ to $ZnCl_2$ activated precursor which combusted in inert condition resulting in the formation of C/ZMO and C/ZTO composites following the equations:

$$ZnCl_2 + H_2O + 2MnCO_3 + C \xrightarrow{\Delta} ZnMn_2O_4 + C + 3CO \uparrow + 2HCl \uparrow \quad [3.2]$$

$$ZnCl_2 + H_2O + SnCO_3 + C \xrightarrow{\Delta} ZnSnO_3 + C + CO \uparrow + 2HCl \uparrow \quad [3.3]$$

Figure 3.3 demonstrated the schematic diagram on the synthesis of ternary C/ZMO and C/ZTO composites formation.

During the carbonization process, CO gas is emitted meanwhile gasification reaction between $ZnCl_2$ and surface carbon eventually lead to the volatile HCl being released. This devolatilization process further develops pores which improve the surface area and produces a porous carbon composite (Deng et al., 2010; Mopoung et al., 2015). The reaction is in agreement to the pore evolution theory whereby during decomposition, non-

carbonic elements will evolve to volatile and forms pressure inside the particle attributed to volatiles accumulation and subsequently create pores when the trapped volatiles are released (Ozdemir et al., 2014). The ZMO and ZTO are formed through the reaction of Zn from $ZnCl_2$ with the addition of $MnCO_3$ and $SnCO_3$.

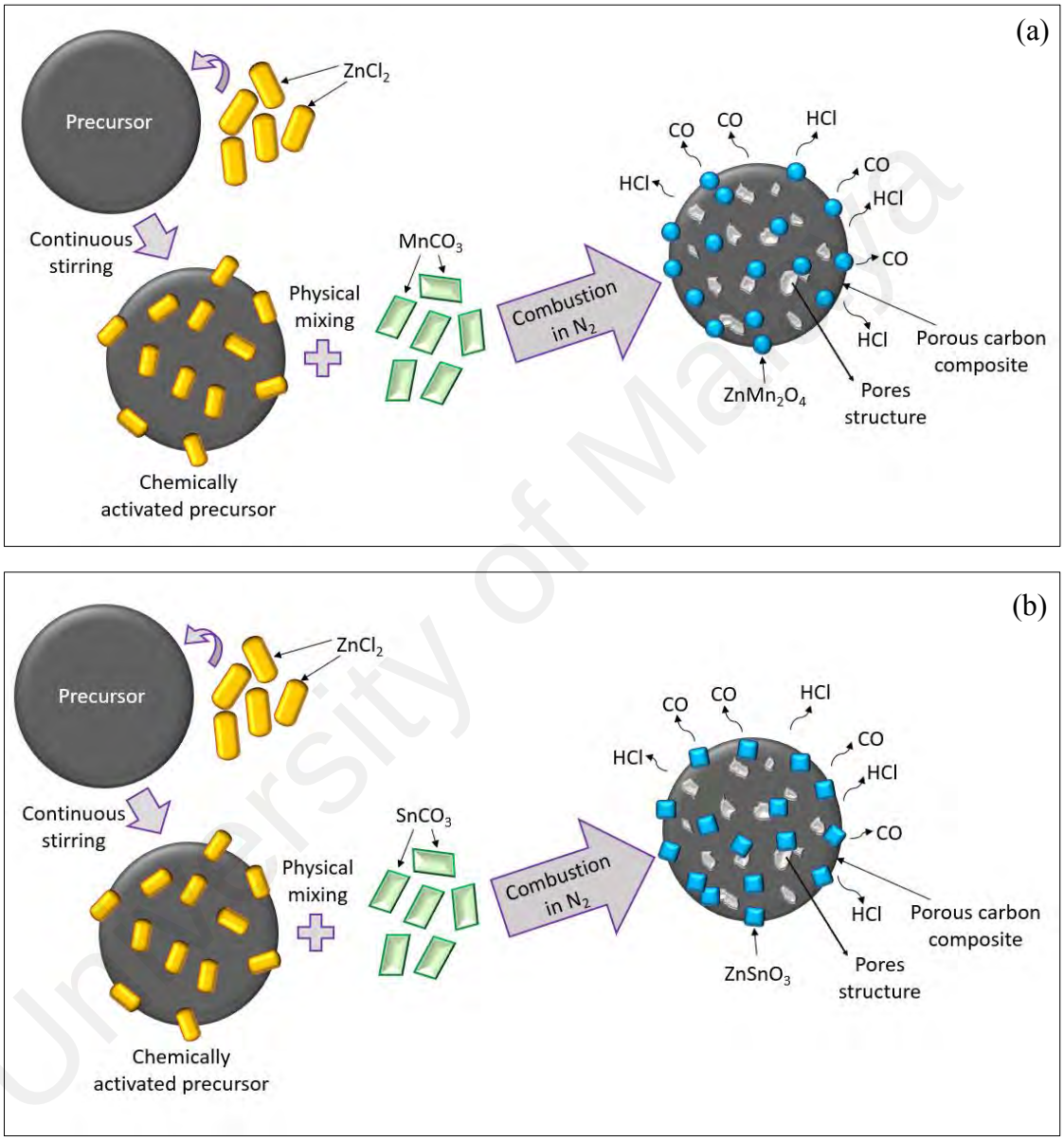

Figure 3.3: The schematic diagram on the process of synthesizing (a) C/ZMO (Sim et al., 2020) and (b) C/ZTO composites

3.5 Physical characterization

3.5.1 Thermogravimetric analysis

Thermogravimetric analysis (TGA) measurements were carried out using TA Instruments Q500 Thermogravimetric Analyzer. In this technique, the sample was carried out using the mode of Hi-Res, whenever there was mass change detected, the heating rate was altered to 50 ˚C min^{-1} and resolution of 5 °C in N_2 atmosphere. This analysis is widely used to study the thermal degradation of any organic matter (Baruah et al., 2018) and help to determine the combustion temperature. With this analytical tool, two types of graph can be plotted namely thermogravimetric (TG) and differential thermogravimetric (DTG) as illustrated in Figure 3.4. These graphs provide information including ignition temperature, burnout temperature, mass residue, maximum weight loss rate and corresponding temperature (Lang et al., 2019).

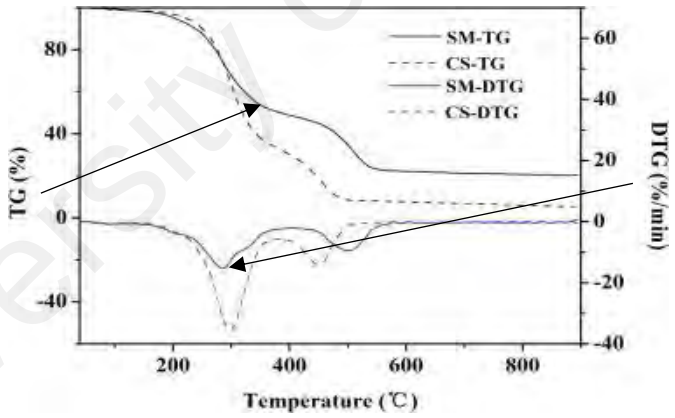

Figure 3.4: TG and DTG curves from swine manure and corn stalk (Lang et al., 2019)

3.5.2 Brunauer-Emmet-Teller

Micrometrics ASAP 2020 V4.00 was used to identify the specific surface area and textural properties of the samples from N_2 adsorption-desorption isotherm at 77 K. The software of MicroActive 2.00 was used to analyze the results obtained. The specific surface area was calculated using the conventional Brunauer-Emmet-Teller (BET) formula while micropore volume can be achieved with the t-plot method. Additionally,

textural properties such as pore size distribution, total pore volume and average pore width are investigated according to Barrett-Joyner-Halenda (BJH) method. For sample with mesopores, the mesopore volume was obtained by deducting the total pore volume to micropore volume.

The isotherm curve is plotted with relative pressure (P/P_0) against volume of adsorption (cm^3g^{-1} STP). The adsorption-desorption curves of activated carbon obtained from biomass (willow catkins) and dextrose with silica as template are shown in Figure 3.5(a) and (b) accordingly. Based on the curve, it can be observed that different types of curves are illustrated whereby the high uptake of gas absorption at low relative pressure as shown in Figure 3.5(a) indicating microporous sample while Figure 3.5(b) implying mesoporous characteristics due to the appearance of hysteresis loop at the middle of relative pressure. Hence, the isotherm curve helps to determine the textural properties through the behavior of the curve from initial, middle to the end of relative pressure.

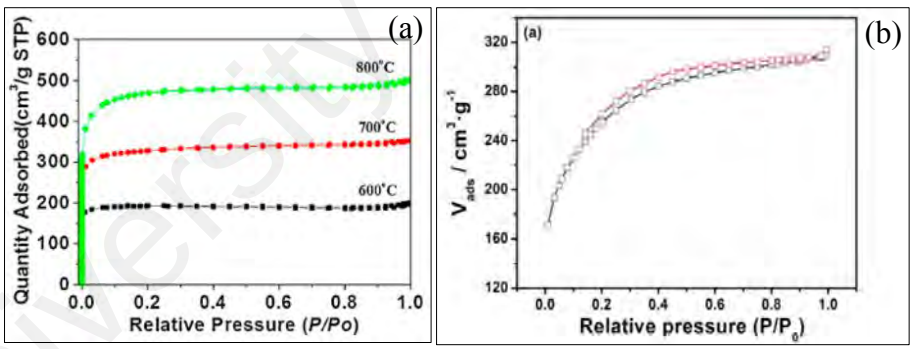

Figure 3.5: Nitrogen adsorption-desorption isotherm curve of (a) willow catkins (Wang et al., 2015) and (b) dextrose (Li et al., 2015b)

3.5.3 Field-emission scanning electron microscopy & energy dispersive x-ray spectroscopy

The morphology of carbon composites was observed under a FESEM equipped with EDX (JEOL-JSM-7600F) at 15 kV. Before imaging, the sample was placed on top of the adhesive carbon tape and insert into the microscopy. The image was then viewed directly

after the Wobbler and stigmatism effect was adjusted perfectly. According to FESEM image as display in Figure 3.6(a), we able to observe the porosity structure in term of sizes and shapes. The scale presents at the right bottom corner of the image assists in measuring the pore size. Another tool that connected to FESEM which is EDX allowed us to identify the element in our sample. As seen in Figure 3.6(b), EDX spectrum will list out the element of the sample along with its atomic percentage.

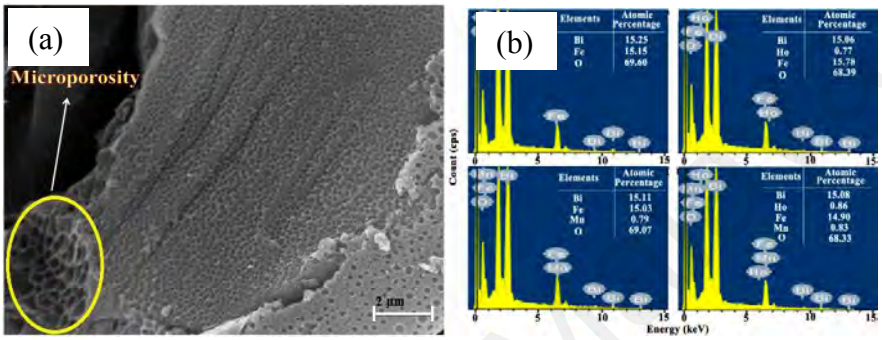

Figure 3.6: Images of (a) FESEM from activated commercial petcoke (Shree Kesavan et al., 2018) and (b) EDX spectrum of $BiFeO_3$ (Zhang et al., 2018d)

3.5.4 Transmission electron microscopy

The TEM is carried out to study the structure of the sample (Abbaslou et al., 2017). Figure 3.7 depicts the image of TEM that consists of both carbon and composite materials whereby carbon exhibits as blurry and non-uniformity while composite materials usually show lattice fringe at high magnification (800 K) with the d-spacing describes the type of element. The TEM images of the study was conducted using JEOL JEM-2100F.

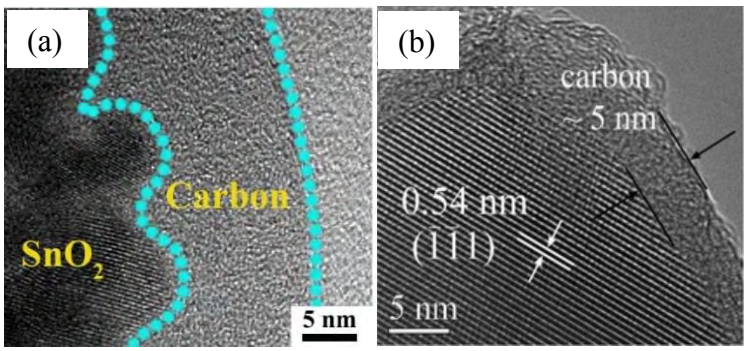

Figure 3.7: (a) TEM image of SnO_2/C (Zhang et al., 2018c) and (b) HRTEM of $Li_3V_2(PO_4)_3$/C (Sun et al., 2011)

3.5.5 X-ray diffraction

X-ray diffraction is a non-destructive analytical technique to identify the nature of material whether it is amorphous, crystalline or both structures. In this study, D8 Advance X-Ray Diffractometer-Bruker AXS with parameters such as 0.02˚ step size at 1 s as well as voltage and current of 40 kV and 40 mA at ambient temperature (Cu Kα monochromatized radiation) was used to anlayse the sample. Figure 3.8 depicts the typical spectra of different types of materials whereby small hump at low 2 theta represents amorphous while sharp peaks indicating crystalline structure. If both types of characteristics are existing in a spectrum implying that materials consist of both carbon and metal oxide/conducting polymer.

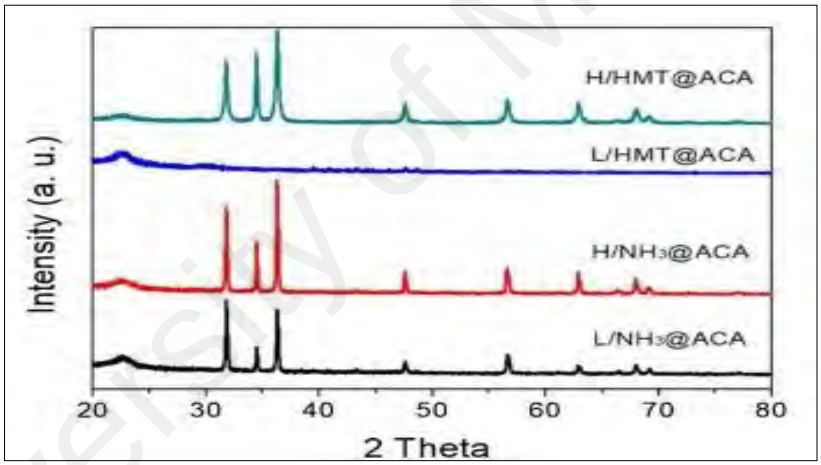

Figure 3.8: XRD spectrum of ZnO/AC derived from asphaltene (Lee et al., 2018b)

3.6 Electrochemical measurements

Cyclic voltammetry (CV), galvanostatic charge-discharge (GCD) and electrochemical impedance spectroscopy (EIS) were measured with Autolab electrochemical measurement unit (PGSTAT30, Germany).

3.6.1 Cyclic voltammetry

In this study, all the samples with three-electrode system were carried out in the voltage range of -0.3 to -1.0 V for activated carbon, binary composite and ternary composite of

series PP/GW-ZMO and 0 to -1.0 V for PP/GW-ZTO. In EDLC fabrication, CV was measured from 0 to 1.0 V. Various scan rates (3, 5, 10, 30, 50 and 100 mVs^{-1}) were conducted to investigate the rate capability. Cyclic voltammetry is one of the techniques to understand the qualitative information about electrochemical reaction between electrode and electrolyte.

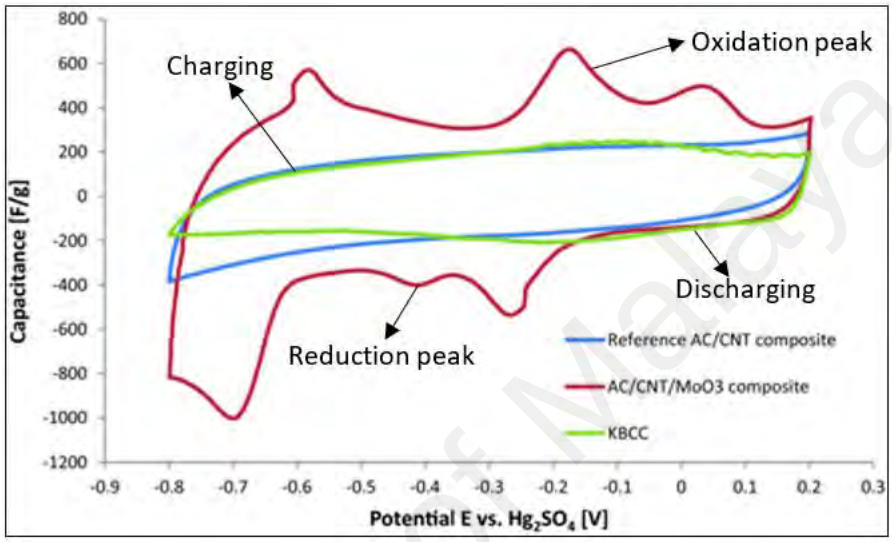

Figure 3.9: CV curves of activated carbon and carbon composites (Okashy et al., 2013)

Figure 3.9 illustrates both capacitive and pseudocapacitive curves which is symmetrical about the zero current. The curve with blue line is a typical rectangular curve for carbonaceous material while the red line curve showing oxidation and reduction peaks implying redox reactions are happening due to the transition metal oxide. The specific capacitance of the samples can be calculated by preforming formula as below:

$$\text{Specific capacitance } (C_{sp};\ Fg^{-1}) = \frac{\Delta i}{M_{ac} \times s} \qquad [3.4]$$

where Δi is average of discharge current, M_{ac} is the mass of active material, s (mVs^{-1}) is the scan rate.

3.6.2 Galvanostatic charge-discharge

GCD is a technique used to study the influence of ionic conductivity with electrode materials at the constant current charge and discharge characteristics (Sudhakar et al., 2018). Varies current densities such as 0.3, 0.5, 0.7, 1.0, 1.3 and 1.5 Ag^{-1} were applied during the three-electrode system. However, for rate capability test, current density such as 0.3, 0.7, 1.0, 0.7 and 0.3 Ag^{-1} were applied for 5000 cycles. In EDLC fabrication, the cells were tested with the selected current density such as 0.03, 0.05, 0.1, 0.3, 0.5 and 1.0 Ag^{-1}. Durability of the cell was applied with 0.1, 0.2 and 0.1 Ag^{-1} for 900 cycles whereas stability test of 5000 cycles was measured at 0.3 Ag^{-1}.

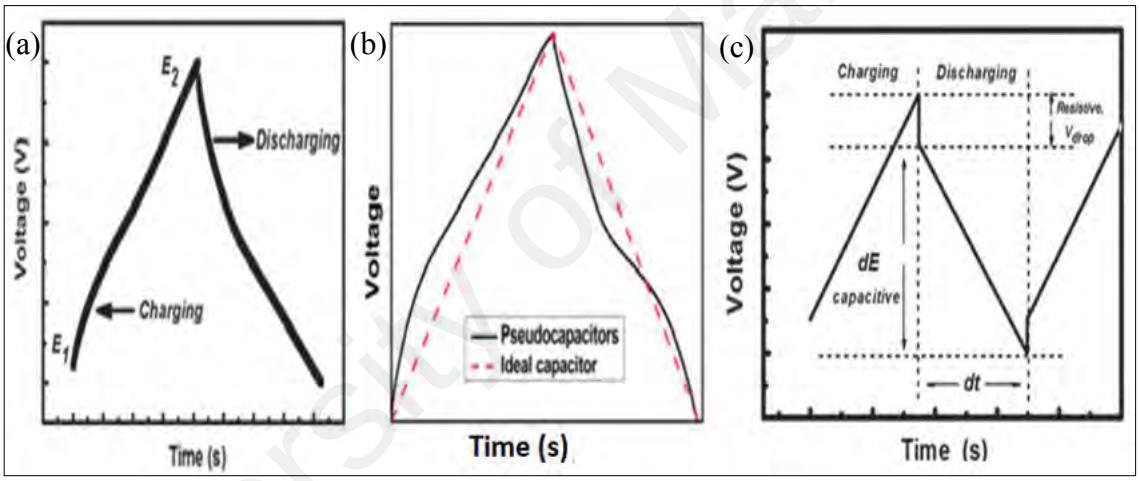

Figure 3.10: Galvanostatic CD of (a) carbonaceous capacitor, (b) pseudocapacitor and (c) capacitive and resistive part (Chen et al., 2014; Mahmoud et al., 2016)

Figure 3.10(a) and (b) show the typical triangular shape of carbonaceous materials while distorted triangular shape indicating the pseudo-characteristic accordingly. Figure 3.10(c) explains the details part of the CD curve whereby it comprises capacitive and resistive parts as well as voltage drop which also referring to iR drop. The capacitive refers to the part which is generated from voltage change originated on the energy change of the active materials while resistive part produced when there is voltage drop due to the voltage change of equivalent series resistance (ESR) (Mahmoud et al., 2016).

There is several information that able to obtain from CD curve such as specific capacitance, energy density and power density. Each of them can be calculated using equations as following:

$$\text{Specific capacitance } (C_{sp};\ Fg^{-1}) = \frac{(I \times \Delta t)}{\Delta V \times M_{ac}} \quad [3.5]$$

$$\text{Energy density } (E;\ Wh\ kg^{-1}) = \frac{C(\Delta V)^2}{2 \times 3.6} \quad [3.6]$$

$$\text{Power density } (P;\ W\ kg^{-1}) = \frac{E}{\Delta t} \times 3600 \quad [3.7]$$

where Δi is average of discharge current, M_{ac} is the mass of active material, s (mVs^{-1}) is the scan rate, I (A) is the discharge current, Δt (s) is the discharge time, ΔV represents the voltage change excluding the IR drop during the discharge process, C_{sp} is the specific capacitance of the single electrode, E is the energy density and P is power density

3.6.3 Electrochemical impedance spectroscopy

There appear to be different resistances in a single device which can be seen in Figure 3.11. These can be identified by employing EIS technique. All the EIS measurement in this study were conducted within a frequency range of 0.1 Hz to 10 kHz at 0 V of applied potential. As seen from the Nyquist plot displayed in Figure 3.10, R_A is formed due to the several factors such as (i) the bulk electrolyte resistance (R_s) or (ii) the total resistance of electrolyte, electrode and contact resistance of electrode and current resistance (Kang et al., 2014). The semicircle which resembled by R_{AB} is the charge transfer resistance (R_{ct}). It is mainly due to the ionic resistance referring to the mobility of electrolyte ions diffuse into the pores of the electrodes and electronic resistance which is the total of intrinsic of electrode material resistance and contact resistance (active material and current collector) (Yang et al., 2017). R_B is indicated as internal resistance which is the sum of R_s and R_{ct}. The deviated line BC, also known as Warburg impedance at the middle frequency is attributed to the pathway limitation or non-uniform of electrolyte ions in the porous

electrode structures (Coromina et al., 2016; Mei et al., 2018). Hence, R_{BC} is called as equivalent distribution resistance while R_C which is the intersection of the vertical line and Z_{re} axis are defined as equivalent series resistance (ESR) or overall resistance. At low frequency, the vertical line explains the dominant capacitive which is formed by the double layer ion adsorption at the electrode/electrolyte interface (Fang & Binder, 2006; Mei et al., 2018).

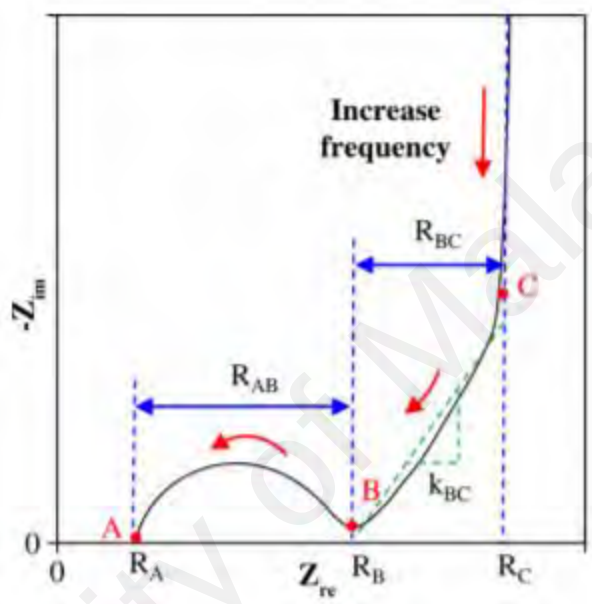

Figure 3.11: Schematic diagram of Nyquist plot of EDLC electrode of device (Mei et al., 2018)

3.7 Overview of the methodology

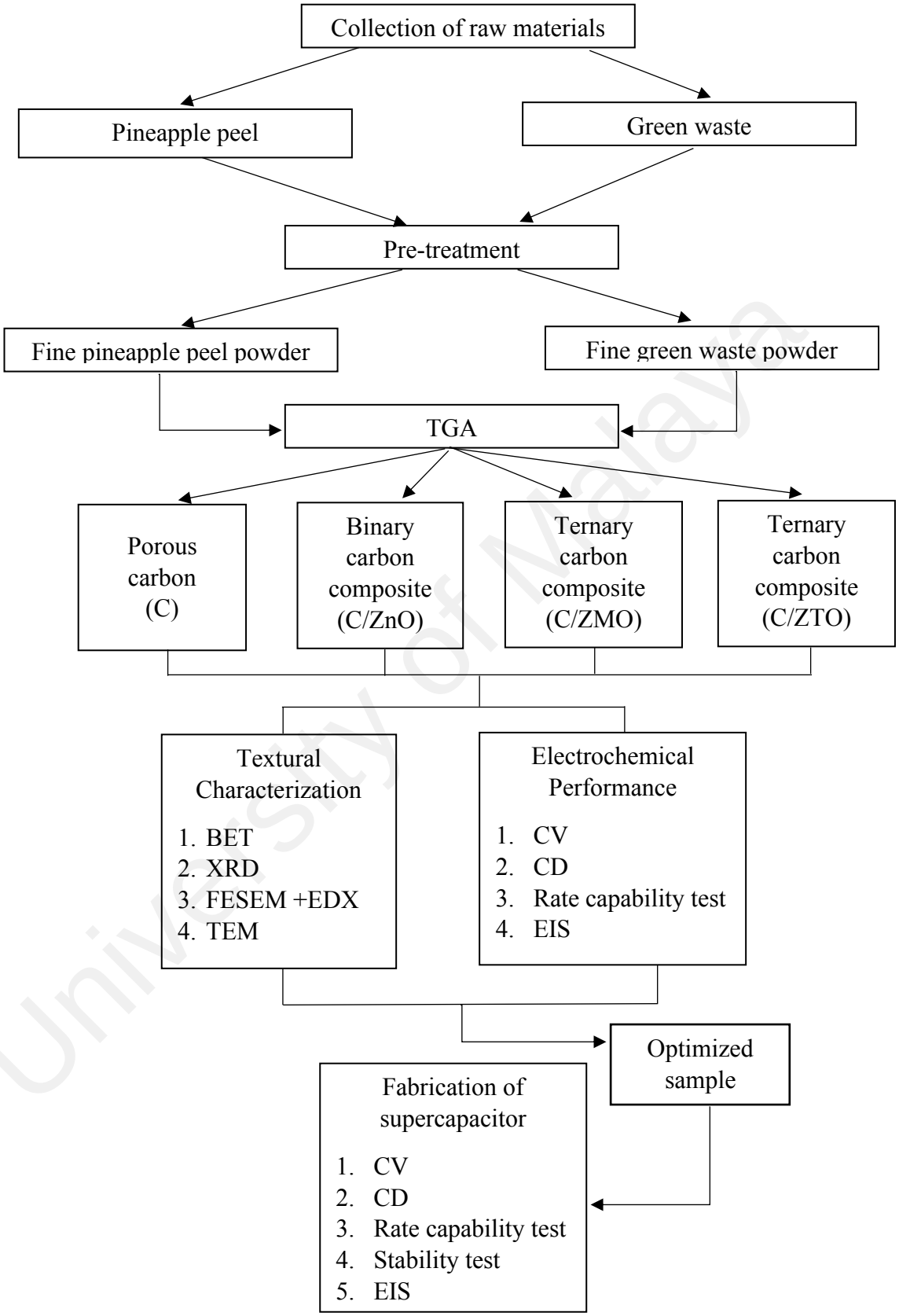

Figure 3.12: Flow chart of the project design

3.8 Summary

In this present work

- Pineapple peel and green waste were used as raw materials for carbon source while $ZnCl_2$, $MnCO_3$ and $SnCO_3$ were utilized as precursor for ZnO, ZMO and ZTO.
- All the activated carbon and carbon-based composite materials were calcined in tube furnace at 500 ºC for 1 hour under 1 $Lmin^{-1}$ nitrogen flow.
- Physical characterization of the synthesized materials was carried out by BET, XRD, FESEM, EDX and TEM.
- The electrochemical performance of the materials was examined using three-electrode system whereby the Ag/AgCl, Pt wire acted as reference and counter electrode accordingly and working electrode was synthesized materials with 6 M KOH as electrolyte medium.
- Symmetrical cell was fabricated to investigate its performance as in device for supercapacitor was conducted by CV and GCD from 0 - 1.0 V at varies scan rates and current densities.

CHAPTER 4: CHARACTERIZATION AND ELECTROCHEMICAL PERFORMANCE OF POROUS CARBON

4.1 Introduction

In this chapter, the results of characterization on textural properties such as the specific surface area, pore volume and pore size distribution of porous carbon derived from pineapple peel (PP) and green waste (GW) will be included. The thermal characteristics of both materials is discussed to understand the decomposition and suitable carbonization temperatures. The insight of porous carbon structure is determined by XRD to evaluate its amorphous properties and its morphology images are observed from FESEM. Supplementary to that images, EDX is carried out to identify the elements in PP-C and GW-C. PP-C and GW-C were synthesized to be the baseline of binary and ternary samples in this research. All the findings related to electrochemical performance of PP-C and GW-C including the durability test is conducted using three-electrode system configuration. The last part of this chapter is highlighted on the symmetrical cell of PP-C due to its better electrochemical behavior. Additional test on stability was performed for 5000 cycles at 0.3 Ag^{-1} while durability test was carried out at 0.1, 0.2 and 0.1 Ag^{-1} for 900 cycles.

4.2 Physical characterization

4.2.1 Thermogravimetric analysis

Figure 4.1 illustrates the profile of decomposition temperature up to 1000 ºC for PP. It is observed that the first weight loss of 10 % was assigned to water desorption. The second mass change of 23.91 wt.% at the range of 200 - 300 ˚C is attributed to the breakdown of organic substances (Sim et al., 2019). Temperature above 300 ˚C is due to the decomposition of main biomass components such as from 190 to 320 ˚C, breakdown of hemicellulose, while cellulose from 320 - 400 ˚C, and beyond 400 ˚C belong to lignin.

This pattern is in agreement to the research studied by Gutiérrez with his co-workers. PP has an average fiber content of 67.88% (including cellulose, hemicellulose, lignin and silica), making this type of biomass waste appropriate as carbonaceous material.

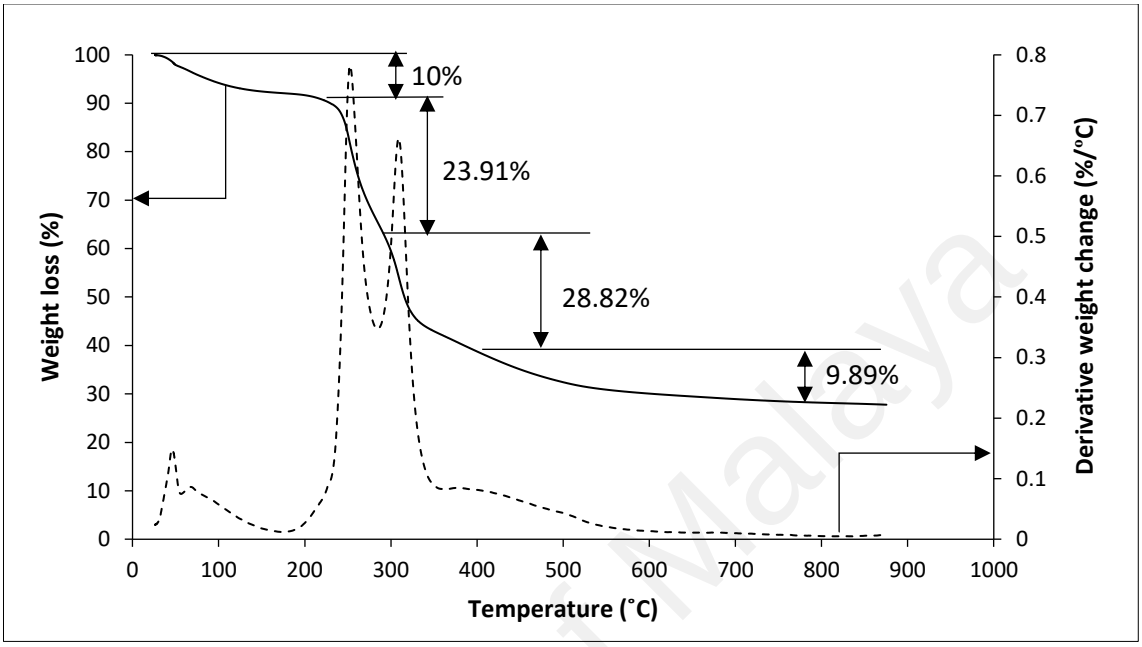

Figure 4.1: TG and DTG curves of pineapple peel

Figure 4.2 depicts the TGA pattern of GW from room temperature to 1000 ºC. The first weight loss below 100 ºC is attributed to the depletion of humidity content. The further 36.39 % reduction at 200 - 400 ºC showed the highest loss among all the stages and the highest peak attained in DTG was approximately 325 ºC. The process of carbonization takes place at this temperature range where leaves and wood elements which contain cellulose, hemicellulose and lignin are converted into heat, carbon dioxide, carbon monoxide, methane and wood tar (Liu et al., 2015b). At higher heating temperature, the weight loss of 14.46 % may be due to the branch decomposition (Liu et al., 2015b) while the remaining ~ 5 % is ascribed to ash and non-gasifiable components (Hilal-AlNaqbi et al., 2016).

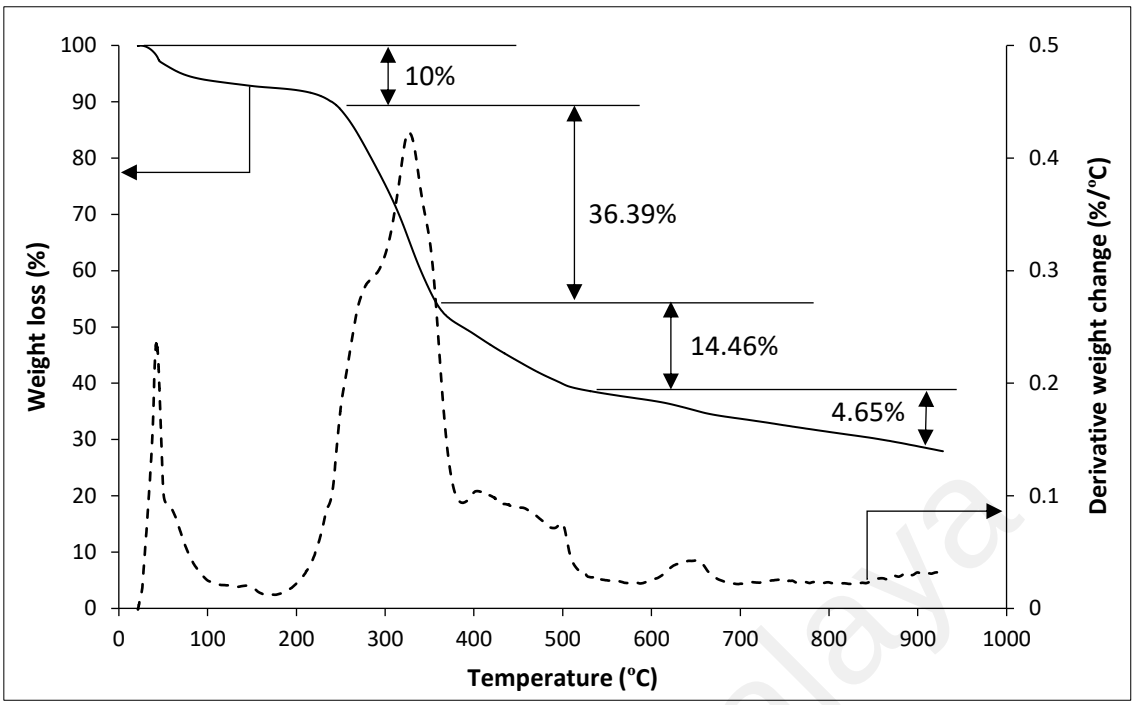

Figure 4.2: TG and DTG curves of green waste

As can be seen that both type of wastes showed insignificant weight loss after 500 ºC, thus, this temperature was determined to ensure the carbon is produced with maximum yield.

4.2.2 Adsorption-desorption isotherm

Figure 4.3 shows nitrogen adsorption-desorption curves of PP-C and GW-C.

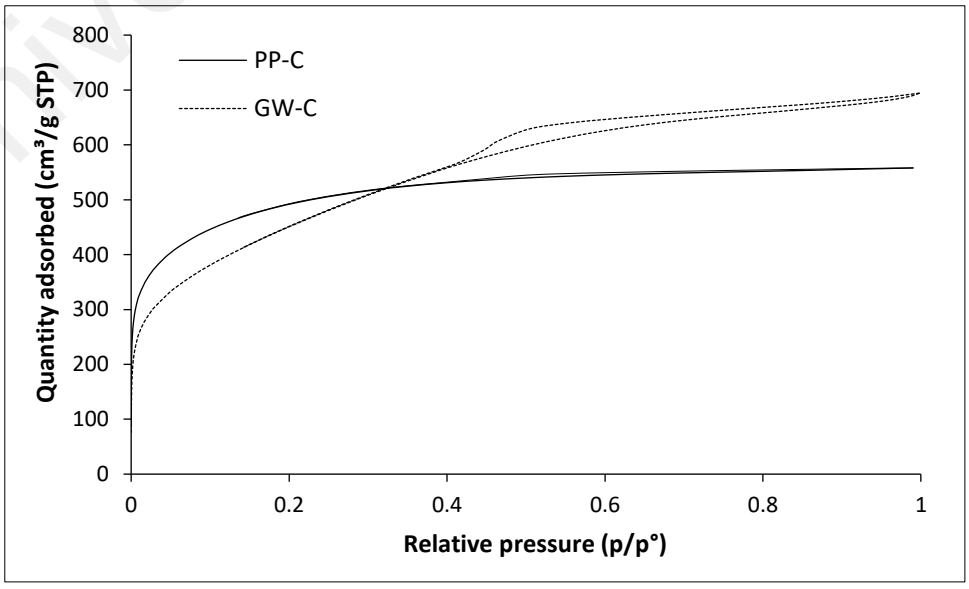

Figure 4.3: Adsorption-desorption isotherm for PP-C and GW-C

Both PP-C and GW-C exhibited type I and IV based on IUPAC classification. However, differences in PP-C and GW-C can be noticed. PP-C shows vertical absorption line at low relative pressure ≈ 0 due to the micropore filling. This usually happened when the sample has high micropores. In GW-C, high uptake of micropore filling can be noticed however, in lower steepness as compared to PP-C. This can be seen in Figure 4.3 which the quantity of N_2 absorbed by PP-C is ~ 300 cm^3g^{-1} STP while GW-C is ~ 200 cm^3g^{-1} STP. This value implying that PP-C has more microporous structure and higher specific surface area. At the further part after the steep absorption, inflection point was observed in both samples inferring the beginning of multilayer absorption. This process is followed by the gradual uprising along with hysteresis loop at p/p° ≈ 0.45 – 1.0. In PP-C, only tiny hysteresis loop can be observed indicating low and small mesopores structure. On the other hand, GW-C showed a noticeable hysteresis loop demonstrating higher and wider mesopores in the sample. In addition to the shape of hysteresis loop, both PP-C and GW-C are H4 type indicating the pore structure formed with slit-shaped pores (Cychosz et al., 2017).

4.2.3 BJH pore size distribution

Pore size distribution utilizing BJH theory for PP-C and GW-C is shown in Figure 4.4.

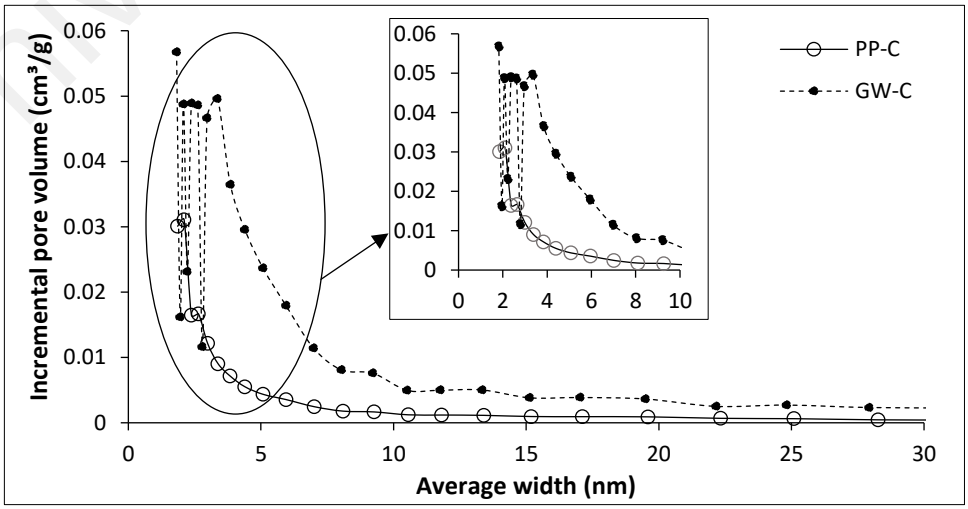

Figure 4.4: BJH pore size distribution of PP-C and GW-C

In Figure 4.4, it is clearly shown that both samples demonstrated mesoporous structure with the maximum peaks at the range of 2 - 4 nm. PP-C displayed narrower mesopore sizes which the highest peak appeared at ~2 nm and gradually reduced upon rising of the size range. This indicated that PP-C possessed small mesopore size which is consistent with the isotherm graph. In contrast, GW-C presented wider mesopores which the maximum peaks were accumulated at 2 - 4 nm. This phenomenon also in agreement with the hysteresis loop observed in Figure 4.3. Table 4.1 shows the data of surface area, micropore and mesopore volume, total pores volume and average pore width of PP-C and GW-C.

Table 4.1: Textural properties of porous carbon for PP-C and GW-C.

Sample	BET (m^2g^{-1})	t-plot micropore volume (cm^3g^{-1})	Mesopore volume (cm^3g^{-1})	Total pores volume (cm^3g^{-1})	Average pores width (nm)
PP-C	1765.92	0.33	0.53	0.86	2.69
GW-C	1613.92	0.043	1.03	1.07	3.09

According to the values tabulated in Table 4.1, both PP-C and GW-C exhibited high surface area, however, difference can be observed in term of the micropore and mesopore volume. GW-C showed 19.62 % higher total pore volume value than PP-C, though, it has much lower micropore volume than PP-C which lead to lower specific surface area. Besides that, the average width of PP-C and GW-C were tally with the BJH pore distribution plot in Figure 4.4.

4.2.4 X-ray diffraction

Figure 4.5 shows the XRD pattern of PP-C and GW-C. As seen from the figure, PP-C shows typical XRD pattern of the activated carbon where two broad peaks at ~ 24º and ~ 43º are detected which is corresponding to the (002) and (100) planes parallel-stacked graphene sheets (Chen et al., 2017). This pattern also indicated amorphous structure of

the samples. Alternatively, in GW-C, broad peak at ~ 24º can also be observed implied the amorphous characteristic. However, GW-C presented additional crystalline peaks at 2θ = 20.9º [100] and 26.8º [101] (Sim et al., 2015a) detected in GW-C which can be assigned to quartz element due to existence of tiny rock sand during green waste collection.

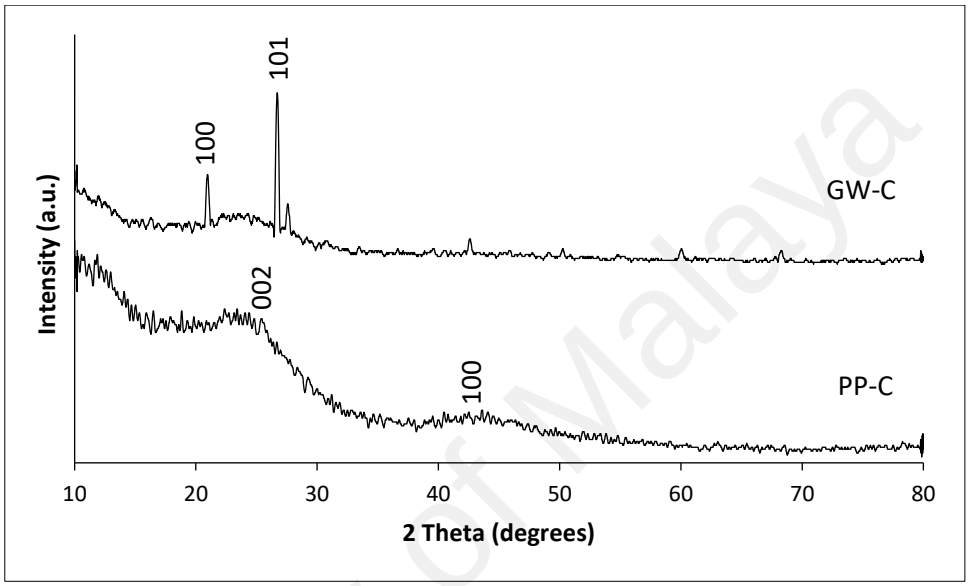

Figure 4.5: X-ray diffraction pattern of PP-C and GW-C

4.2.5 Field emission scanning electron microscopy & energy dispersive x-ray analysis

Figure 4.6 displays the FESEM images of PP-C and GW-C at the magnification of 100K.

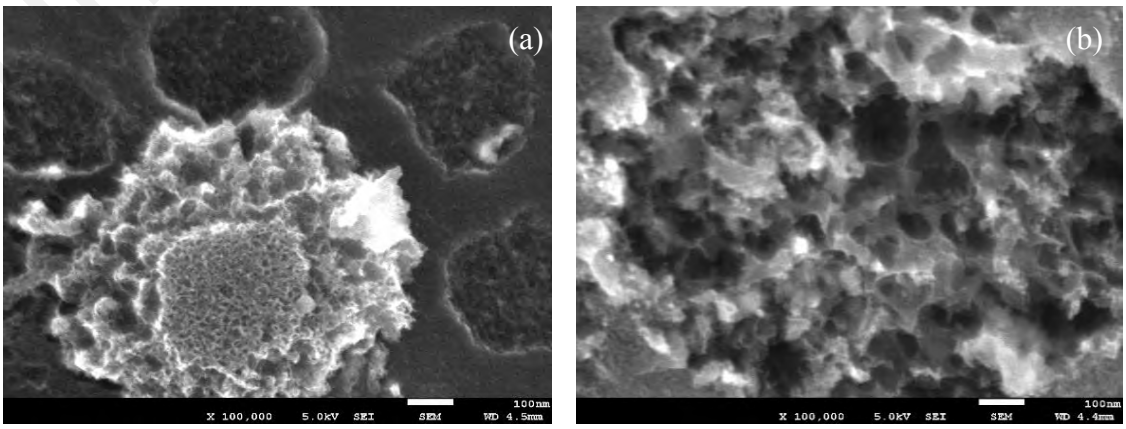

Figure 4.6: FESEM images of (a) PP-C and (b) GW-C

In Figure 4.6, images show both types of samples are porous materials. It is obvious that PP-C presented pores with smaller size homogenously distributed. On the other hand, GW-C illustrated larger pores equally formed with irregular shape. The FESEM image also further confirmed the result of average pore width as listed in Table 4.1 for PP-C (2.69 nm) and GW-C (3.09 nm).

EDX was carried out to identify the element of PP-C and GW-C as illustrated in Figure 4.7. The results showed that both samples had almost similar carbon and oxygen content. However, GW-C showed additional Si element in small percentage which is in agreement with the quartz peak appeared in XRD pattern as shown in Figure 4.5.

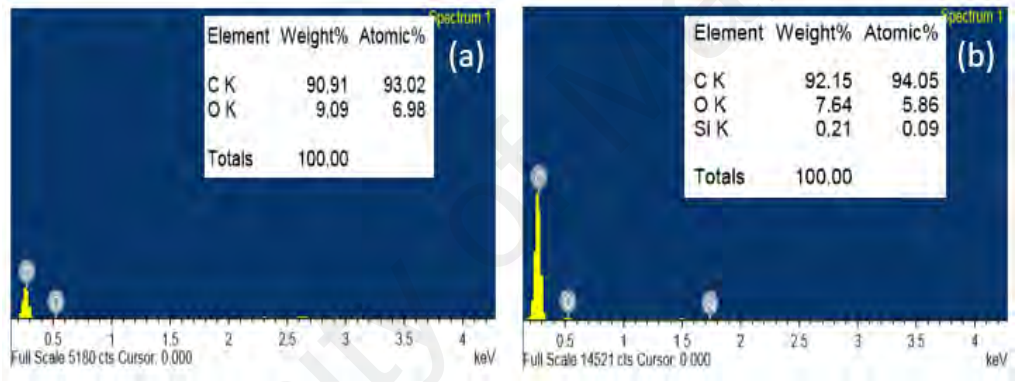

Figure 4.7: EDX of (a) PP-C and (b) GW-C

4.3 Electrochemical performance

In this electrochemical performance, both samples were conducted for CV, GCD in potential ranging from -0.3 to -1.0 V and EIS in three-electrode system. The durability was further carried out to select the optimized sample to be fabricated as a symmetrical cell. Three-electrode system was designed to study the electrode material behavior while symmetrical cell was made-up to examine the cell performance. The symmetrical cell was examined with CV, GCD from 0 to 1.0 V and EIS. Therefore, this section consists of electrochemical performance of both three-electrode system and symmetrical cell system.

4.3.1 Three-electrode system

4.3.1.1 Cyclic voltammetry

Cyclic voltammetry profile for PP-C and GW-C in the working potential range from -0.3 to -1.0 V is displayed in Figure 4.8.

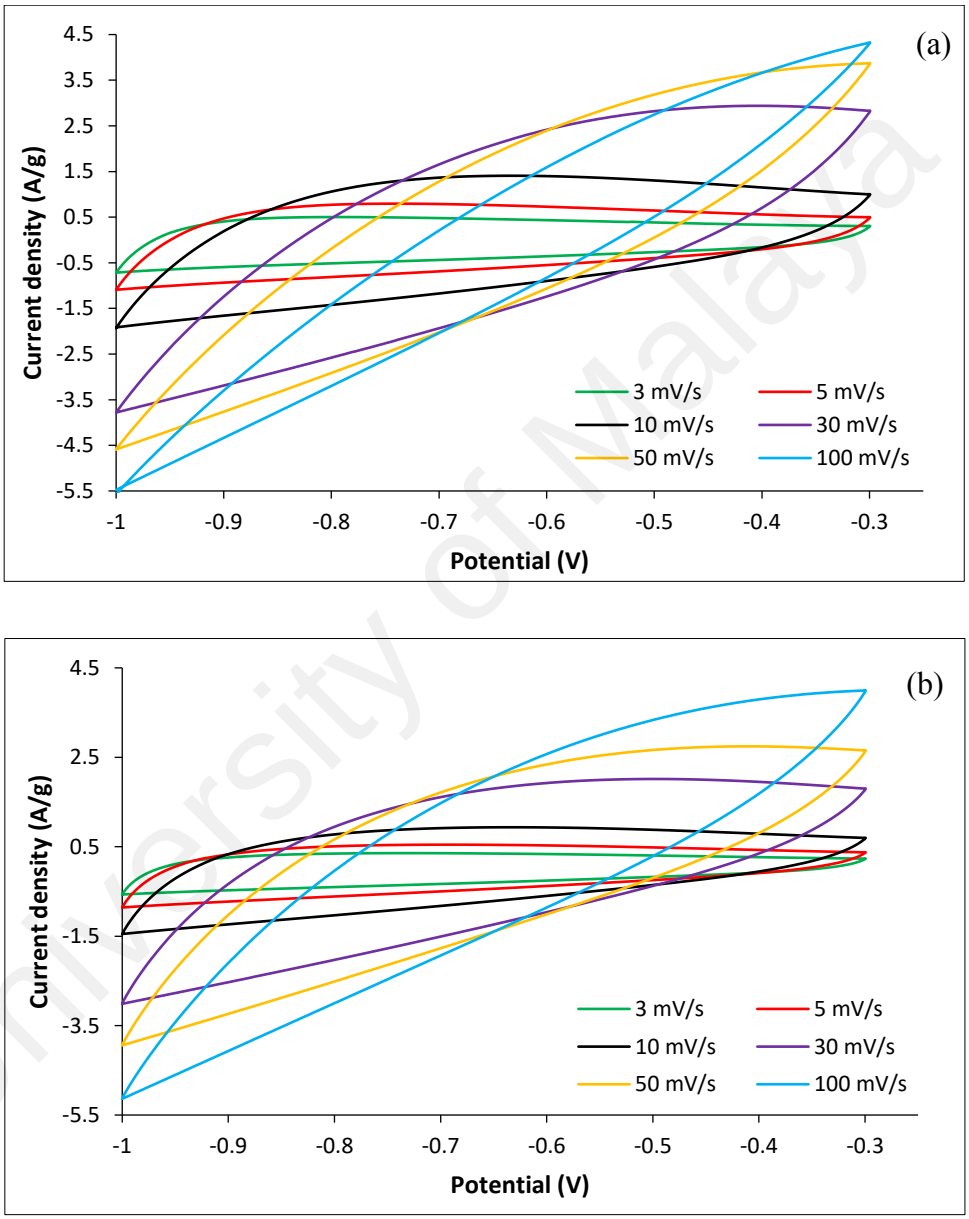

Figure 4.8: Cyclic voltammetry of (a) PP-C and (b) GW-C at various scan rates from -0.3 to -1.0 V

Both PP-C and GW-C exhibited the similar shape of CV curves at different scan rates. All the curves at lower scan rates preserved nearly rectangular shape indicated the good

conductivity of the electrode materials (Liu et al., 2015a). The distorted shape at higher scan rates can be explained by the existence of micropore which causing the difficulty of ions transportation at higher voltage scan rates (Liu et al., 2019). As calculated from the CV curves, highest capacitance was achieved from PP-C which was 128.94 Fg^{-1} at 3 mVs^{-1}. This is mainly due to higher specific surface area in PP-C (1765.92 m^2g^{-1}) than GW-C (1613.92 m^2g^{-1}). Table 4.2 tabulates the specific capacitance for sample PP-C and GW-C for the scan rate of 3 mVs^{-1}, 5 mVs^{-1}, 10 mVs^{-1}, 30 mVs^{-1}, 50 mVs^{-1} and 100 mVs^{-1}.

Table 4.2: Specific capacitance of PP-C and GW-C over scan rates.

Sample	Specific capacitance (Fg^{-1})					
	3 mVs^{-1}	**5 mVs^{-1}**	**10 mVs^{-1}**	**30 mVs^{-1}**	**50 mVs^{-1}**	**100 mVs^{-1}**
PP-C	128.94	119.70	101.81	61.97	44.15	25.11
GW-C	96.71	87.00	72.12	47.05	35.87	22.95

4.3.1.2 Galvanostatic charge-discharge

As shown in Figure 4.9, both samples illustrating similar charging and discharging time for all current densities. It is observed that all the curves were close to isosceles triangle shape demonstrating electrochemically stability and reversibility of the electrode material. The highest specific capacitance calculated from GCD was achieved by PP-C with 144.93 Fg^{-1} at 0.3 Ag^{-1}. The result from GCD is comparable to the specific capacitance calculated from CV which showing the similar trend of the higher the current density, the lower the specific capacitance. This is mainly due to shorter time reduce ion diffusion into the pores. Table 4.3 has listed out the specific capacitance of PP-C and GW-C from different current densities such as 0.3 Ag^{-1}, 0.5 Ag^{-1}, 0.7 Ag^{-1}, 1.0 Ag^{-1}, 1.3 Ag^{-1} and 1.5 Ag^{-1}.

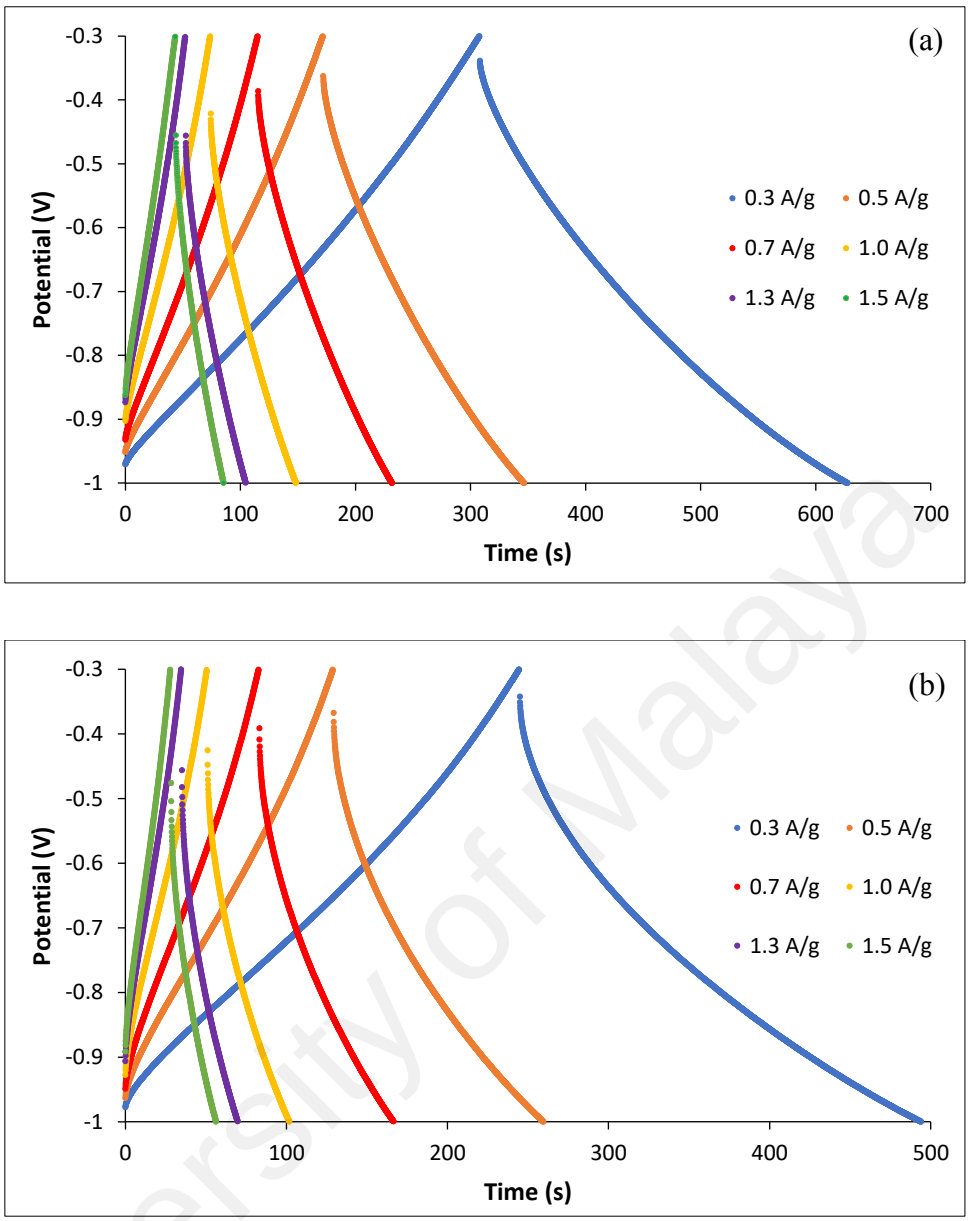

Figure 4.9: Galvanostatic charge-discharge of (a) PP-C and (b) GW-C at various current densities from -0.3 to -1.0 V

Table 4.3: Specific capacitance of PP-C and GW-C over current densities.

Sample	Specific capacitance (Fg^{-1})					
	0.3 Ag^{-1}	**0.5 Ag^{-1}**	**0.7 Ag^{-1}**	**1.0 Ag^{-1}**	**1.3 Ag^{-1}**	**1.5 Ag^{-1}**
PP-C	144.93	136.99	132.85	128.43	124.97	114.85
GW-C	113.64	103.07	95.96	88.64	83.25	80.49

In order to investigate the durability and stability of the electrode materials, PP-C and GW-C were applied with different current densities in the order of 0.3 Ag^{-1}, 0.7 Ag^{-1}, 1.0 Ag^{-1}, 0.7 Ag^{-1} and 0.3Ag^{-1}. Each respective current density was tested for 1000 cycles as depicted in Figure 4.10. Results showed that both samples performed outstandingly with capacitance retention achieved at 97.99 % from PP-C and 83.87 % from GW-C at the 5000th cycles as compared with the first 10th cycle. Nevertheless, based on Figure 4.10, it is clearly shown that PP-C displays a more stable trend along the 5000 cycles as compared to GW-C.

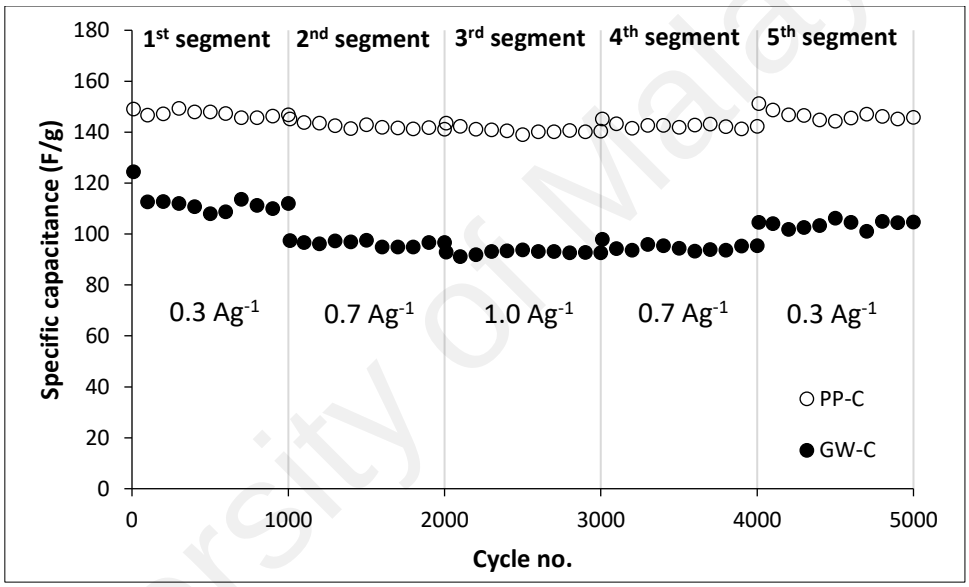

Figure 4.10: Rate capability performance of PP-C and GW-C at different current densities for 5000 cycles

A more detail calculation was carried out to analyses the rate capability and stability of the sample. As illustrated in Figure 4.11, PP-C maintain about 100 % when it was applied to higher current densities and adjusted back to lower current densities. Though, GW-C also performed a good rate capability at a minimum retention of ~ 87 %. In term of stability as shown in Figure 4.12, every 1000th cycle was compared with the first 10th cycles in respective segment. Both samples showed a promising result which retention for each segment were maintained at the range of 90 - 100 %.

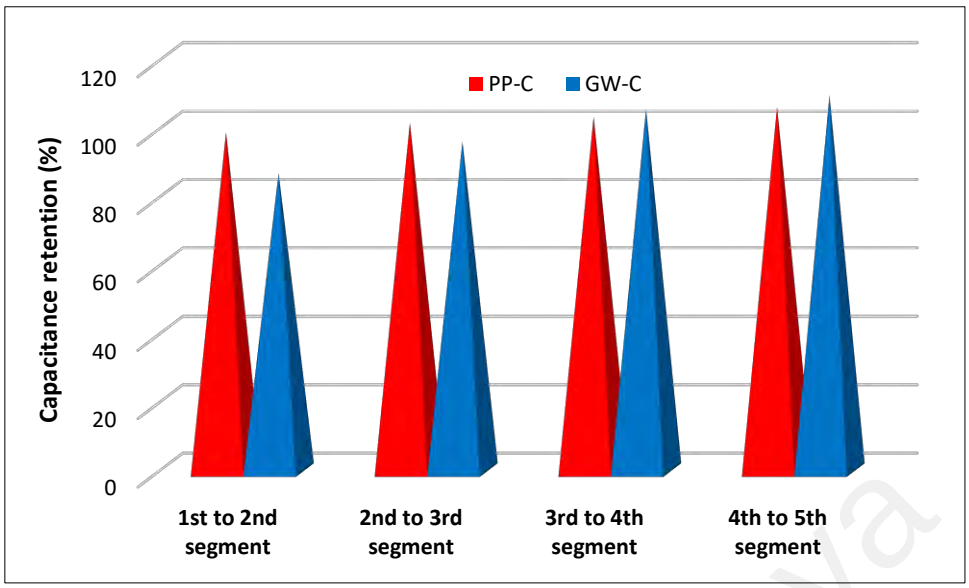

Figure 4.11: Rate capability of PP-C and GW-C from one to another segment across 5000 cycles

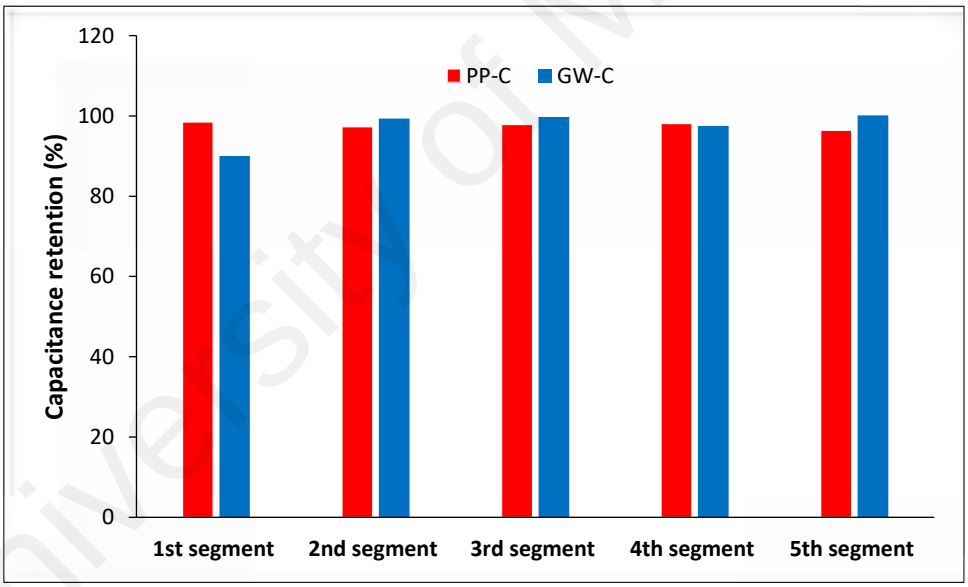

Figure 4.12: Stability of PP-C and GW-C at each segment across 5000 cycles

4.3.1.3 Electrochemical impedance spectroscopy

In Figure 4.13, the EIS of PP-C and GW-C is displayed with inset showing the zoom in of high frequency.

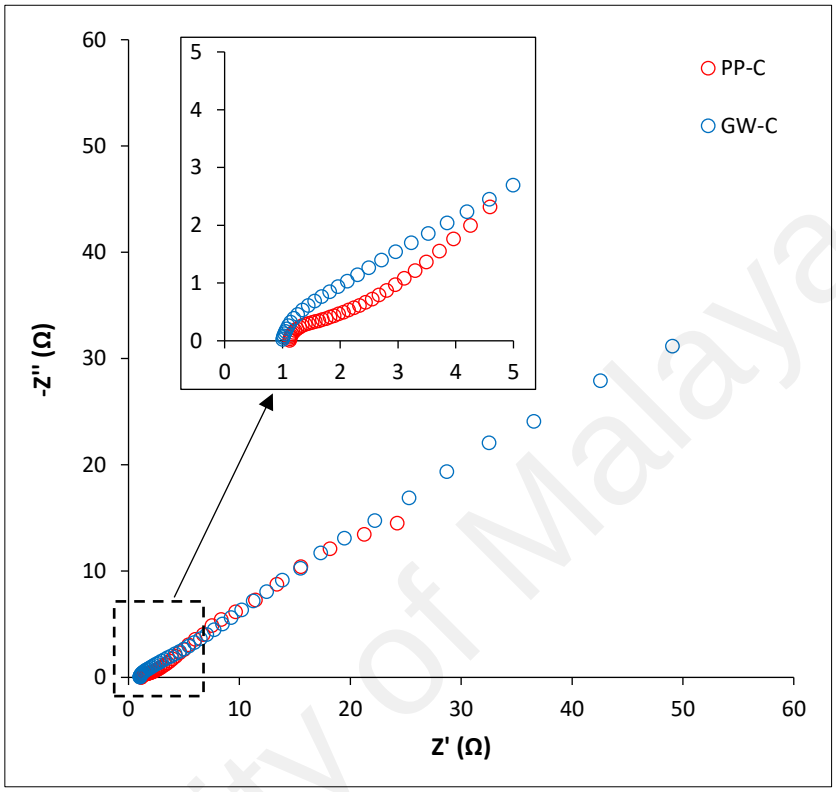

Figure 4.13: Nyquist plot of PP-C and GW-C with inset in high frequency range

Table 4.4 presents the value of bulk resistance and charge transfer resistance of PP-C and GW-C.

Table 4.4: Value of R_s and R_{ct} of PP-C and GW-C.

Sample	R_s (Ω)	R_{ct} (Ω)	$R_s + R_{ct}$ (Ω)
PP-C	1.11	1.00	2.11
GW-C	0.99	2.91	3.90

As seen in Figure 4.13, both samples almost same pattern Nyquist plot with semicircle at high frequency and 45º straight line over low frequency indicating ion diffusion process. According to Table 4.4, PP-C shows lower R_{ct} which can be explained with its optimum

pore size that allowed ions diffusion. This result also further clarified the higher specific capacitance achieved in PP-C.

4.3.2 Symmetrical cell system

In this system, PP-C was chosen over GW-C although they showed similar performance. This is mainly due to the performance of PP-C showed slightly better results as in specific capacitance and durability test.

4.3.2.1 Cyclic voltammetry

Figure 4.14 refers to the CV of PP-C fabricated as symmetrical cell at various scan rate from 0 to 1.0 V.

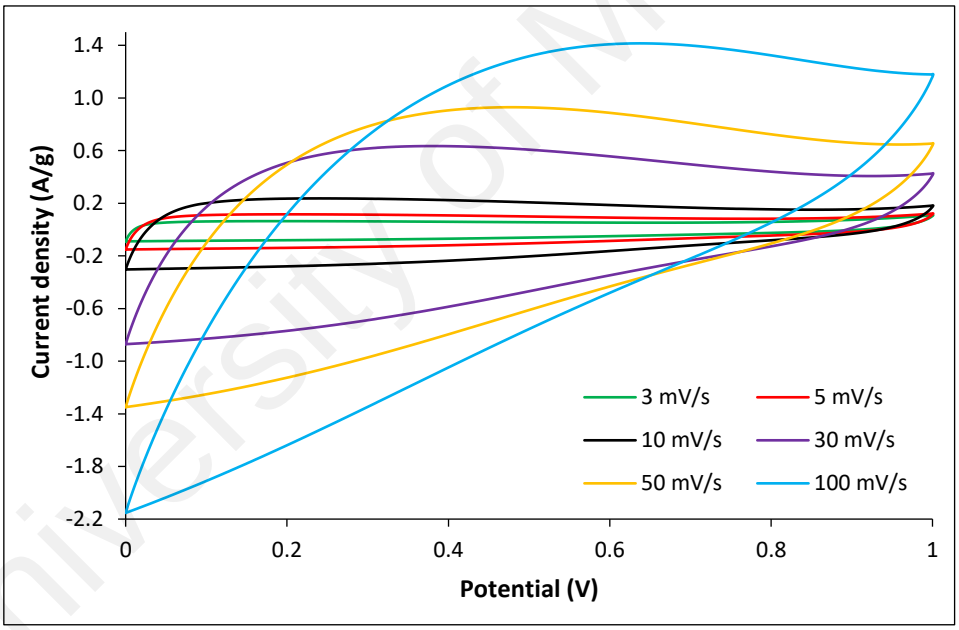

Figure 4.14: Cyclic voltammetry of PP-C with various scan rates in EDLC

Figure 4.14 depicts the similar shape as obtained in three-electrode system with nearly rectangular shape at lower scan rates indicating ideal capacitive behaviour. Nonetheless, the shape started to have distortion at scan rate beyond 50 mVs^{-1} which is due to higher resistance at higher scan rate. The highest specific capacitance was recorded at 18.89 Fg^{-1} in 3 mVs^{-1}. Table 4.5 tabulates the specific capacitance obtained over different scan rates in symmetrical cell.

Table 4.5: Specific capacitance of PP-C in EDLC at various scan rates.

Sample	Specific capacitance (Fg^{-1})					
	3 mVs^{-1}	**5 mVs^{-1}**	**10 mVs^{-1}**	**30 mVs^{-1}**	**50 mVs^{-1}**	**100 mVs^{-1}**
PP-C	18.89	19.11	18.60	15.53	13.14	11.36

4.3.2.2 Galvanostatic charge-discharge

Figure 4.15 depicts to the GCD of PP-C fabricated as symmetrical cell at various current densities. The GCD curves with nearly triangular shape indicated that the cell has good electrochemical reversibility. The charging and discharging time were almost similar indicated the cell had high coulombic efficiency. Across all the different current densities, 0.03 Ag^{-1} measurement recorded the highest specific capacitance at 24.61 Fg^{-1}. Table 4.6 tabulates the specific capacitance obtained over different scan rates in symmetrical cell.

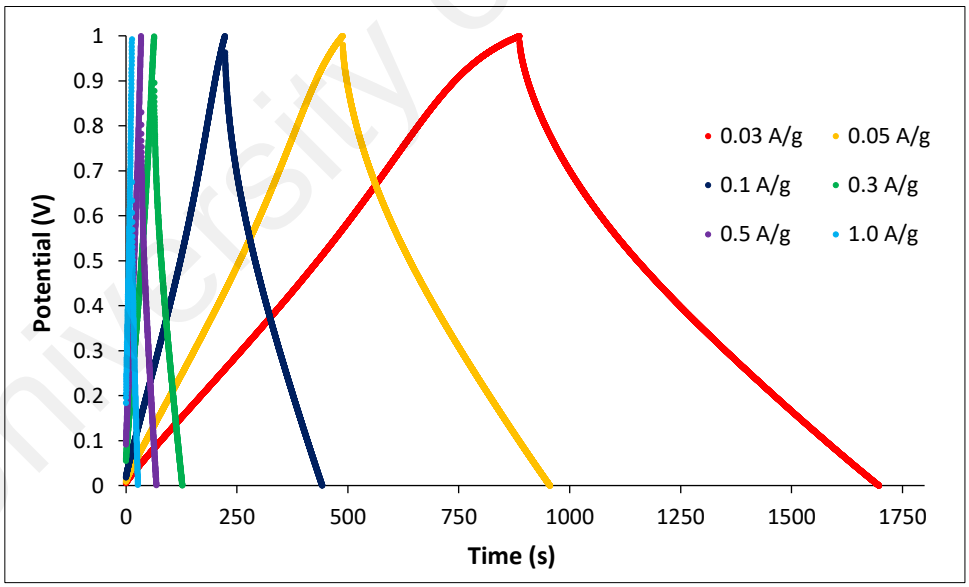

Figure 4.15: GCD of PP-C with various scan rates in EDLC

Table 4.6: Specific capacitance of PP-C in EDLC at various current densities.

Sample	Specific capacitance (Fg^{-1})					
	0.03 Ag^{-1}	**0.05 Ag^{-1}**	**0.1 Ag^{-1}**	**0.3 Ag^{-1}**	**0.5 Ag^{-1}**	**1.0 Ag^{-1}**
PP-C	24.61	23.82	22.74	21.18	20.53	19.80

The durability of the cell was examined by conducting 900 cycles of different current densities as illustrated in Figure 4.16.

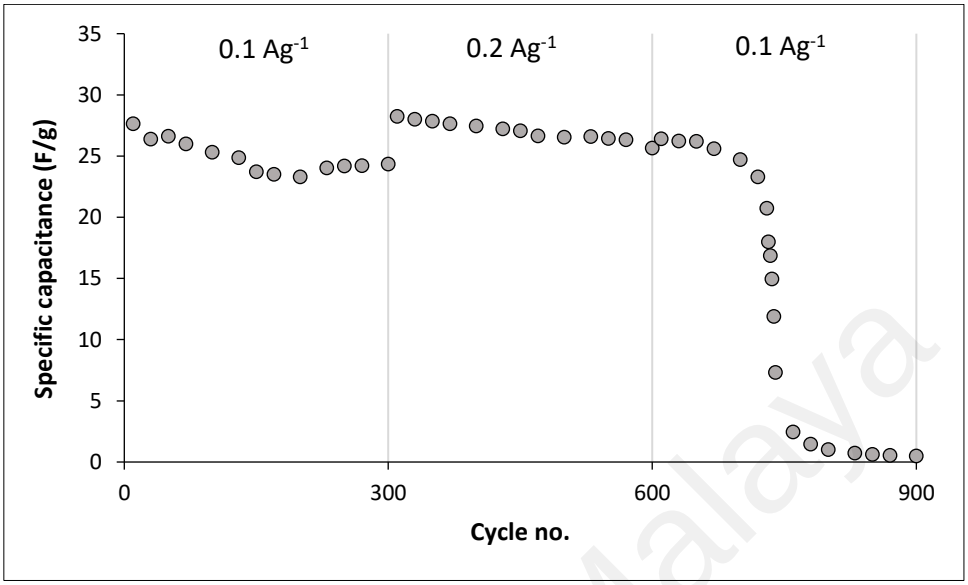

Figure 4.16: Rate capability test of PP-C at different current densities for 900 cycles in EDLC

As seen in the figure, the cell maintains quite stable at 87.52 % at the 300th cycle. When the cell was applied with 0.2 Ag^{-1}, better and stable performance were observed during that 300 cycles. However, drastic dropped was recorded after the cell was adjusted back to 0.1 Ag^{-1} started after the 600th cycle. The dropped continued until the 900th cycle which was nearly null capacitance value. This phenomenon might be due to the higher current density has caused the destruction of pores and lead to lesser active sites for ions diffusion and deteriorated charge transport (Li et al., 2019a).

In term of stability test, PP-C shows an outstanding performance over 5000 cycles at 0.3 Ag^{-1} as depicted in Figure 4.17. Throughout the whole cycling test, capacitance was maintained at above 98.88 %. At the 5000th cycles, 102.93 % of the capacitance was retained indicated that PP-C performed a better capacitance even after 5000 cycles. This result implied PP-C has high stability but poor durability. In overall, the cell was stable after many cycles of charge-discharge. However, the limitation of the cell was unable to

withstand different current loads for long cycling process. In addition, PP-C||PP-C cell hold an energy and power density of 1.43 Whkg^{-1} and 104.48 Wkg^{-1} at the 1000th cycle.

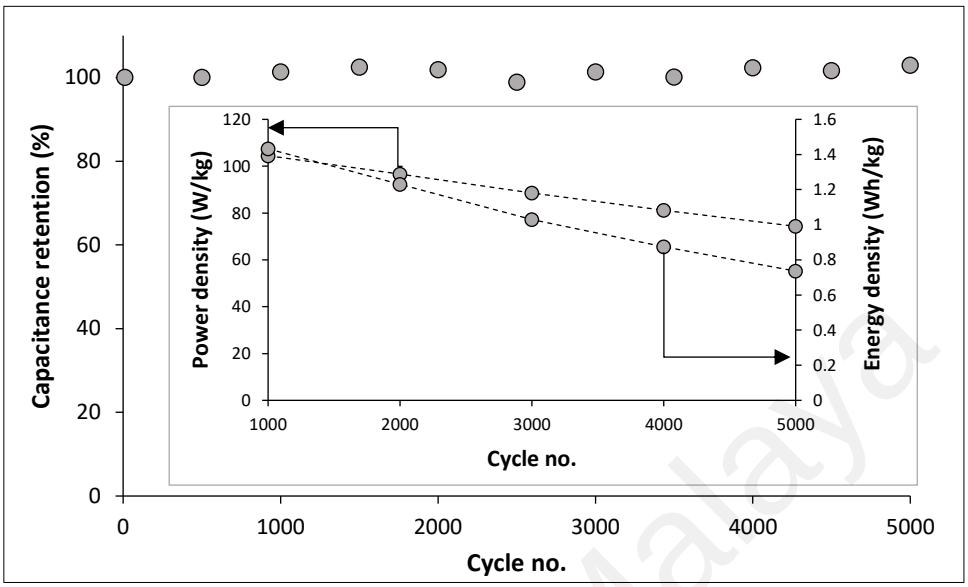

Figure 4.17: Stability test of PP-C at 0.3 Ag^{-1} for 5000 cycles in EDLC

4.3.2.3 Electrochemical impedance spectroscopy

Figure 4.18 shows the EIS of PP-C||PP-C symmetrical cell.

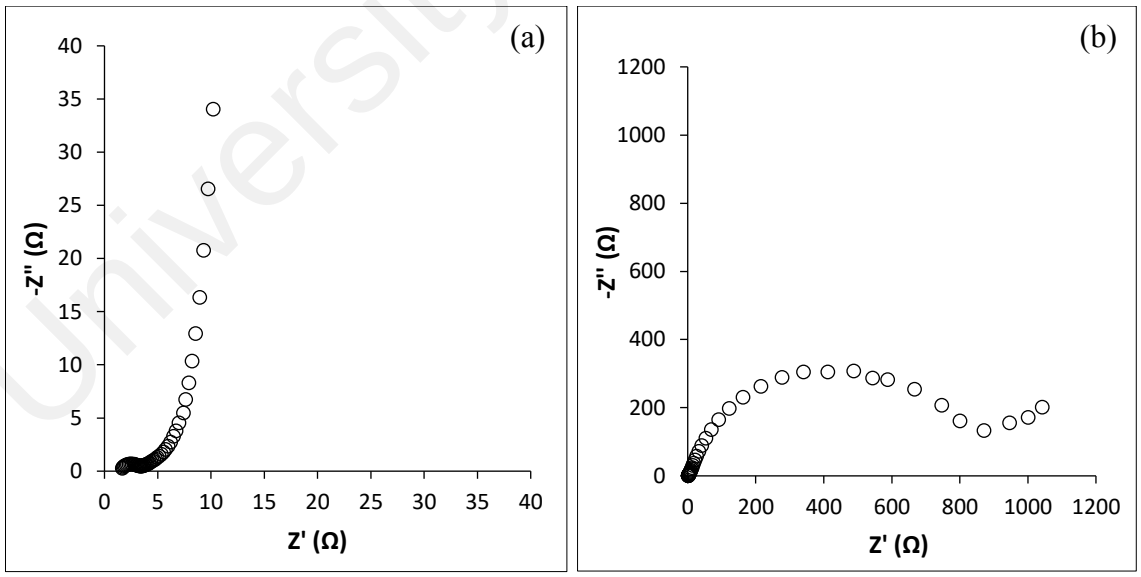

Figure 4.18: Nyquist plot of PP-C (a) before and (b) after cycle for rate capability test in EDLC

According to Figure 4.18, 1.42 Ω of R_s and 2.38 Ω of R_{ct} are detected before the cycling process started. The Nyquist plot of PP-C||PP-C cell demonstrated an ideal capacitor with a semicircle at high frequency and almost vertical straight line at low frequency region. The semicircle is due to the charge-transfer resistance of the capacitor while in low frequency region, the straight lines indicates better capacitive behavior with rapid ion diffusion (Chen et al., 2018b). However, after 900 cycles of rate capability test as depicted in Figure 4.16, high R_{ct} was recorded at 947.33 Ω while R_s showed 1.81 Ω. This is also the reason of drastic capacitance depletion as the device experienced obstacle during charging and discharging process. The ions were unable to diffuse to the active sites for charging leading to low capacitance which is highly due to the collapse of pores.

4.4 Summary

- Both PP-C and GW-C exhibited amorphous materials with high specific surface area of 1765.92 m^2g^{-1} and 1613.92 m^2g^{-1} respectively.
- PP-C achieved highest specific capacitance of 144.93 Fg^{-1} at 0.3 Ag^{-1} and 128.94 Fg^{-1} at 3 mVs^{-1}.
- PP-C||PP-C cell was fabricated and obtained highest specific capacitance of 24.61 Fg^{-1} at 0.03 Ag^{-1} and 18.89 Fg^{-1} at 3 mVs^{-1}.
- PP-C||PP-C cell performed high stability of 98.88 % over 5000 cycles at 0.3 Ag^{-1} but experienced poor durability which the capacitance dropped drastically to null after 900 cycles at 0.2 Ag^{-1}.

CHAPTER 5: CHARACTERIZATION AND ELECTROCHEMICAL PERFORMANCE OF BINARY C/ZNO COMPOSITES

5.1 Introduction

This chapter will discuss the results of binary carbon composite for PP-ZnO and GW-ZnO. Physical characterization consists of the textural properties, XRD, FESEM and accompanied with EDX. The electrochemical performance of PP-ZnO and GW-ZnO in three-electrode system based will be investigated by CV and GCD with different scan rates and current densities, respectively. The impedance will be identified by the EIS analysis. The durability of the materials was tested by rate capability study where different current densities are applied in the sequence of 0.3, 0.7, 1.0, 0.7 and 0.3 Ag^{-1} at 1000 cycles for each current density.

5.2 Physical characterization

5.2.1 Adsorption-desorption isotherm

Figure 5.1 shows the nitrogen adsorption-desorption isotherm of PP-ZnO and GW-ZnO.

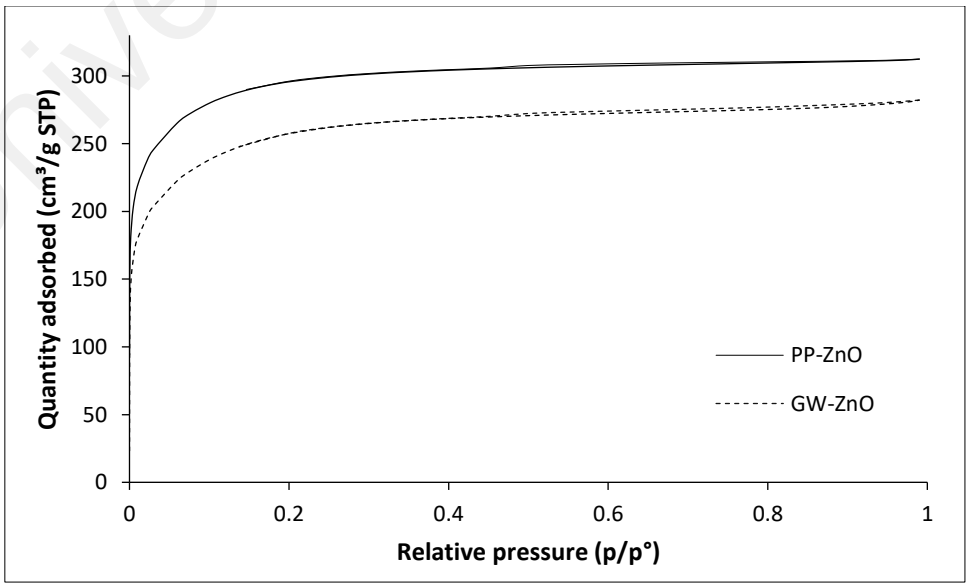

Figure 5.1: Adsorption-desorption isotherm for PP-ZnO and GW-ZnO

Both PP-ZnO and GW-ZnO showed the same trend of isotherm which belong to the combination of type I and type IV according to IUPAC classification. A vertical straight line parallel to y-axis at low relative pressure at $p/p^{\circ} \approx 0$ is attributed to high micropore volume which allow for rapid N_2 absorption. After low relative pressure was followed with an inflection point along with long plateau indicated multi-layer adsorption. The H4 type of hysteresis loop between the relative pressure of 0.45 to 1.0 indicating slit-shaped type of mesopore.

5.2.2 BJH pore size distribution

Figure 4.2 depicts the pore distribution obtained from BJH theory for PP-ZnO and GW-ZnO.

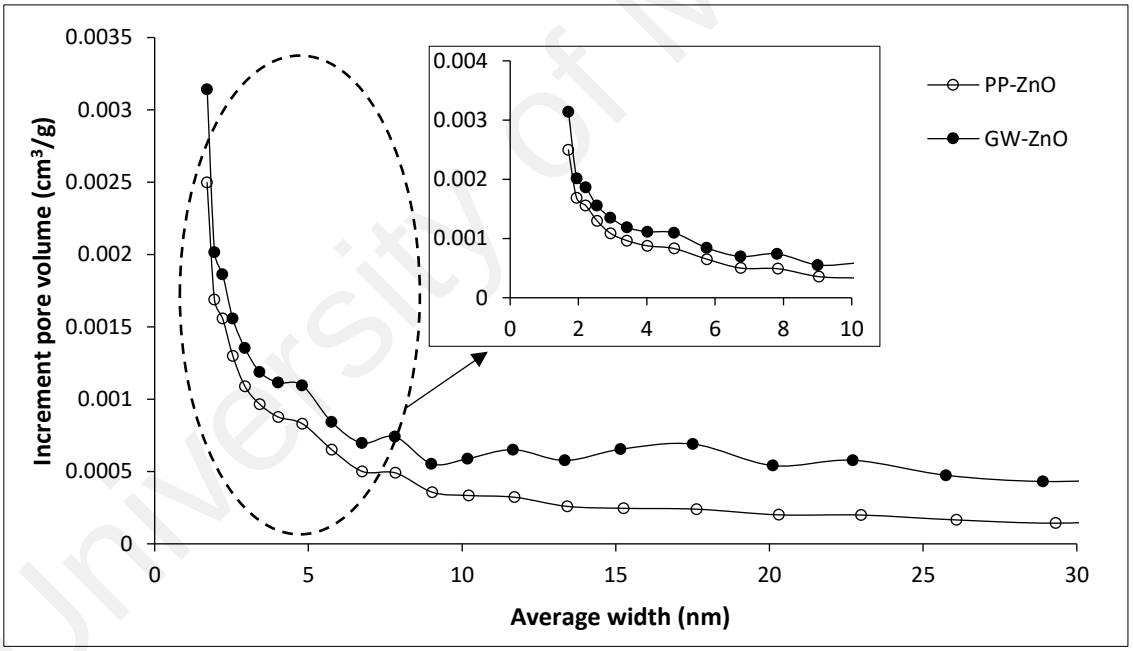

Figure 5.2: BJH pore size distribution of PP-ZnO and GW-ZnO

As seen in Figure 5.2, the highest peaks appear in pore size ~1.7 nm which is considered as micropore followed by accumulation of peaks around 2 to 4 nm. This result is tally with the isotherm stated that pore size existed in both micro and meso. After 5 nm, the peak reduced gradually implied lesser pore with bigger size.

Table 5.1 depicts the textural properties in term of specific surface area, micropore and mesopore volume, total pores volume and average pore width.

Table 5.1: Textural properties of PP-ZnO and GW-ZnO.

Sample	BET (m^2g^{-1})	t-plot micropore volume (cm^3g^{-1})	Mesopore volume (cm^3g^{-1})	Total pores volume (cm^3g^{-1})	Average pores width (nm)
PP-ZnO	1119.32	0.33	0.15	0.48	3.35
GW-ZnO	913.91	0.24	0.20	0.44	4.08

As expected, PP-ZnO possessed higher specific surface area due to its nature characteristic from PP-C. In binary carbon composites, it is observed that both PP-ZnO and GW-ZnO exhibited a more equivalent ratio of micropore and mesopore volume with total pore volume at 0.48 nm (PP-ZnO) and 0.44 nm (GW-ZnO). Both samples also showed a larger mesopore size which PP-ZnO was 3.35 nm and GW-ZnO was 4.08 nm. This is mainly due to guest molecules which will influence the pore width and pore volume significantly even at relatively low amount (Dong et al., 2006). The statement further explained the lower specific surface area obtained in PP-ZnO and GW-ZnO.

5.2.3 X-ray diffraction

Figure 5.3 displays the XRD of PP-ZnO and GW-ZnO. According to the figure, the combined features of the standard amorphous porous carbon and crystalline structure indexed to ZnO (JCPDS file no. 01-070-2551) in PP-ZnO and GW-ZnO are clearly demonstrated. This is due to the use of $ZnCl_2$ as an activating agent which resulted in the formation of ZnO in composite samples when heating is applied. The characteristic of amorphous graphitic carbon can be denoted by the broad diffraction peaks at around $2\theta = 24^{\circ}$ (002). Three well-resolved peaks in PP-ZnO and GW-ZnO can be indexed as 31.82º (100), 34.47º (002) and 36.30º (101) which is hexagonal ZnO pattern. The result has proved the existence of both carbon and ZnO in the sample.

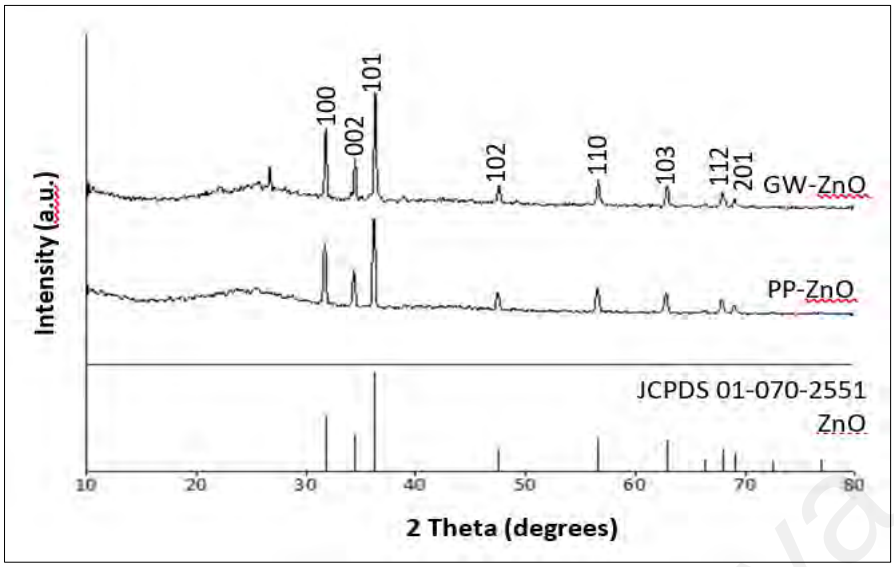

Figure 5.3: X-ray diffraction pattern of PP-ZnO and GW-ZnO

5.2.4 Field emission scanning electron microscopy & energy dispersive x-ray analysis

Figure 5.4 illustrates the FESEM images of PP-ZnO and GW-ZnO at 50k and 100k magnification.

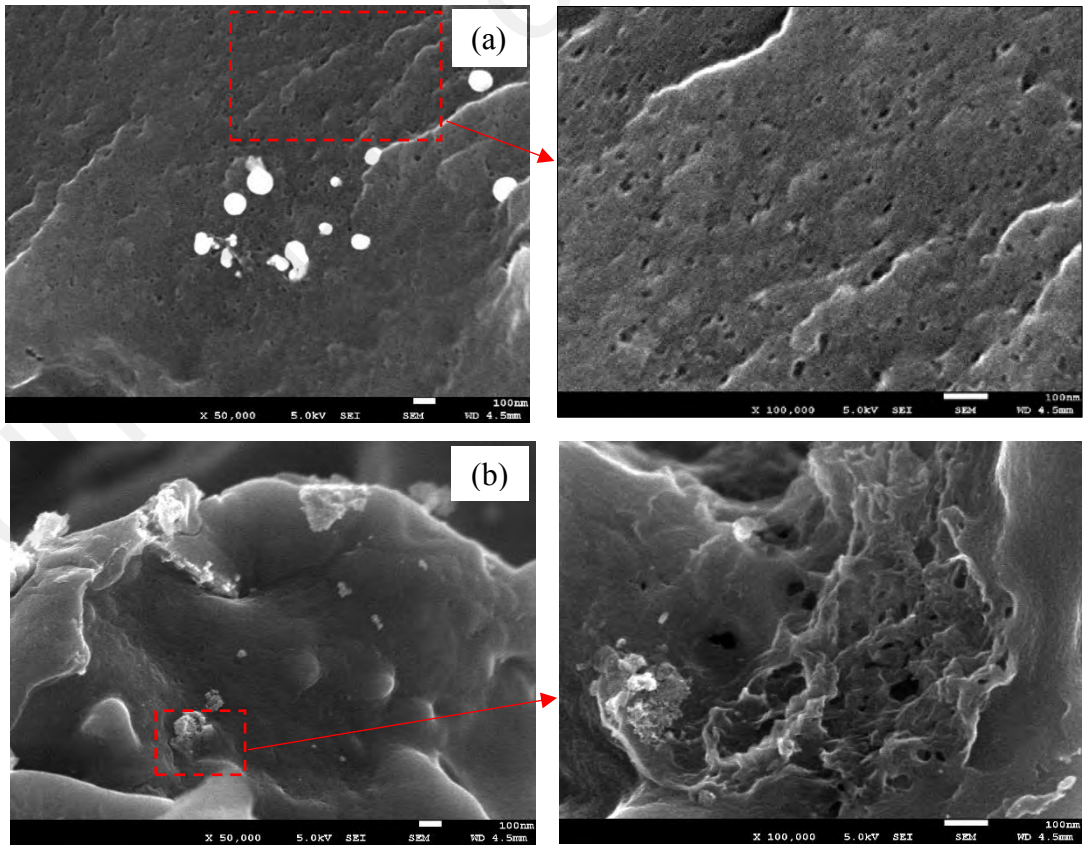

Figure 5.4: FESEM images of (a) PP-ZnO and (b) GW-ZnO with their enlarged view of circle box on the right

PP-ZnO and GW-ZnO showed a high porosity surface with pores of different sizes and irregular shape distributed homogenously. The pores are essential in offering more active sites for ion transfer and redox reaction. Additionally, it was observed that there were white spots scattered within the pore structure which can be assigned to ZnO according to EDX results. The images have verified that ZnO was successfully attached on the carbon surface. The EDX as depicted in Figure 5.5 further proved the existence of ZnO by the element of Zn detected in the test. The appeared of Cl element is mainly due to the residue of activating agent, $ZnCl_2$. This element cannot be successfully removed was attributed to the low molarity of HCl in order to maintain composites being washed away.

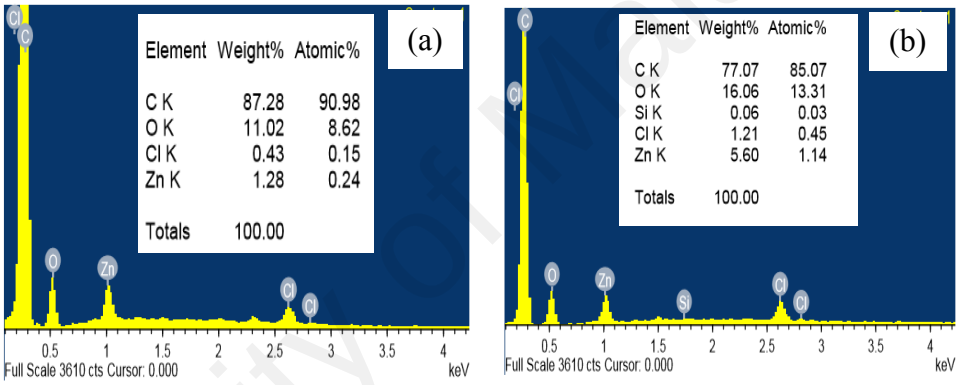

Figure 5.5: EDX of (a) PP-ZnO and (b) GW-ZnO

5.3 Electrochemical performance

In this chapter, only three-electrode system will be conducted for the binary carbon composite. This is mainly due to its electrochemical performance in terms of specific capacitance and durability demonstrated insignificant improvement which will be presented later as compared to porous carbon in previous chapter.

5.3.1 Cyclic voltammetry

Figure 5.6 illustrates CV curves with various scan rates 3 mVs^{-1}, 5 mVs^{-1}, 10 mVs^{-1}, 30 mVs^{-1}, 50 mVs^{-1} and 100 mVs^{-1}. The CV curves of both PP-ZnO and GW-ZnO showed nearly rectangular PP-ZnO and GW-ZnO up to 10 mVs^{-1} implying good conductivity of

the electrode material. Upon 10 mVs^{-1}, although the CV curves were distorted, the area under the curve still performed larger than the porous carbon. This can be explained by the larger pores size enhance the ion transportation at higher voltage scan rate. PP-ZnO achieved highest specific capacitance of 121.52 Fg^{-1} while GW-ZnO was 103.21 Fg^{-1} at 3 mVs^{-1}. Table 5.2 shows the specific capacitance for sample PP-ZnO and GW-ZnO for the scan rate of 3 mVs^{-1}, 5 mVs^{-1}, 10 mVs^{-1}, 30 mVs^{-1}, 50 mVs^{-1} and 100 mVs^{-1}.

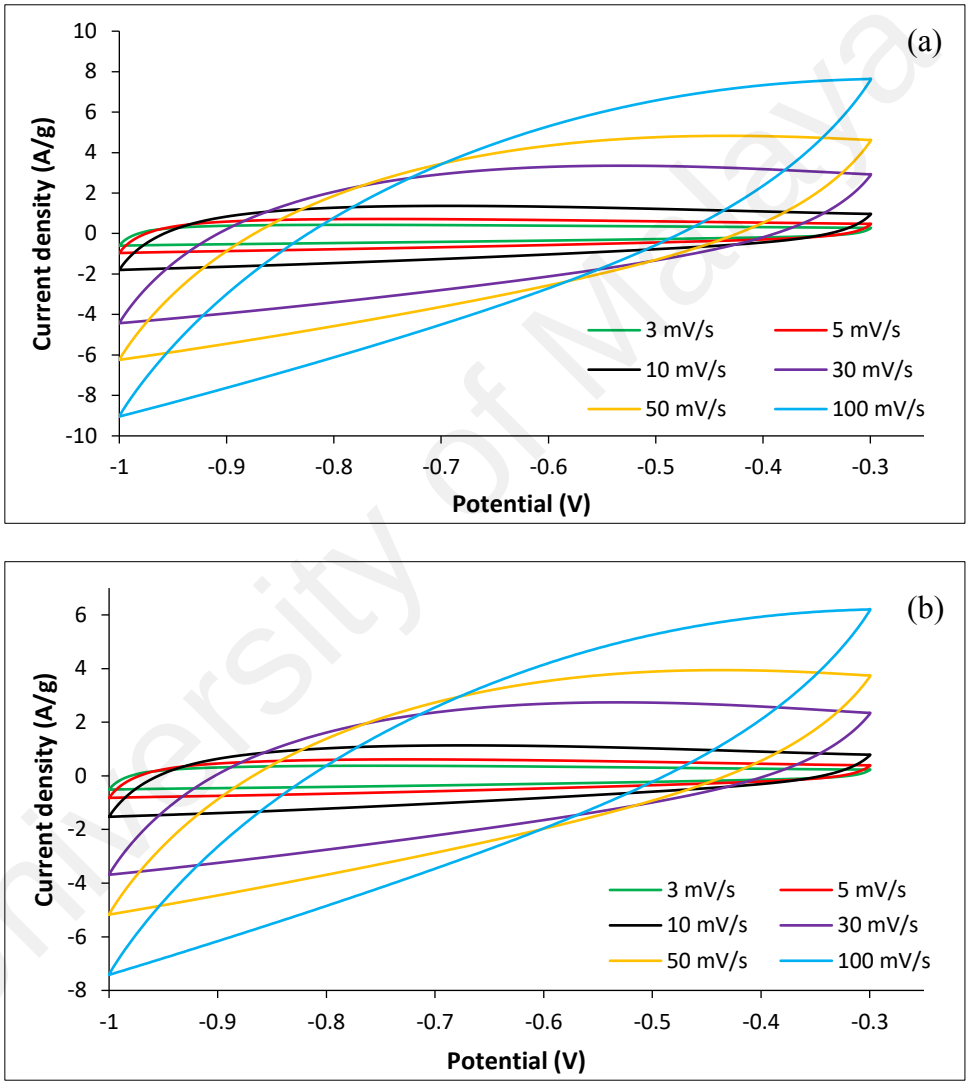

Figure 5.6: Cyclic voltammetry of (a) PP-ZnO and (b) GW-ZnO at various scan rates from -0.3 to -1.0 V

Table 5.2: Specific capacitance of PP-ZnO and GW-ZnO at various scan rates.

Sample	Specific capacitance (Fg^{-1})					
	3 mVs^{-1}	**5 mVs^{-1}**	**10 mVs^{-1}**	**30 mVs^{-1}**	**50 mVs^{-1}**	**100 mVs^{-1}**
PP-ZnO	121.52	118.67	108.67	81.05	65.31	45.01
GW-ZnO	103.21	98.92	88.85	65.25	52.58	35.96

5.3.2 Galvanostatic charge-discharge

Figure 5.7 displays the GCD curves of different current densities such as 0.3 Ag^{-1}, 0.5 Ag^{-1}, 0.7 Ag^{-1}, 1.0 Ag^{-1}, 1.3 Ag^{-1} and 1.5 Ag^{-1}. All GCD curves demonstrated nearly symmetrical triangle shape indicated the electrode material was electrochemical reversible. Based on the calculation from GCD, PP-ZnO and GW-ZnO obtained almost similar value of specific capacitance such as 119.03 Fg^{-1} and 117.06 Fg^{-1}, respectively. In term of the capability of retaining high energy storage, it was observed that only 63.32 % (PP-ZnO) and 68.24 % (GW-ZnO) of the capacitance retention was maintained along the increment of current densities. Table 5.3 illustrates the specific capacitance of PP-ZnO and GW-ZnO calculated from different current densities ranging from 0.3 to 1.5 Ag^{-1}.

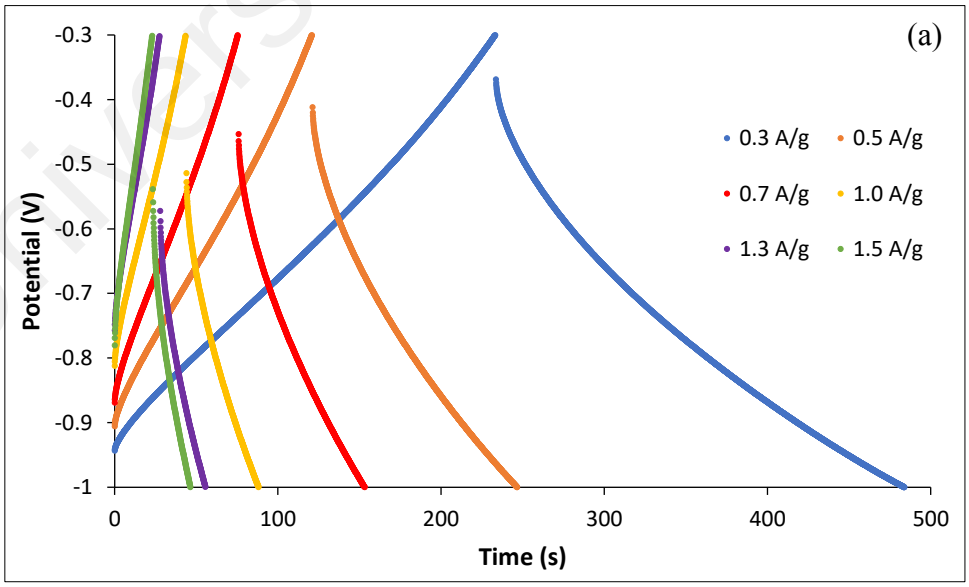

Figure 5.7: Galvanostatic charge-discharge of (a) PP-ZnO and (b) GW-ZnO at various current densities from -0.3 to -1.0 V

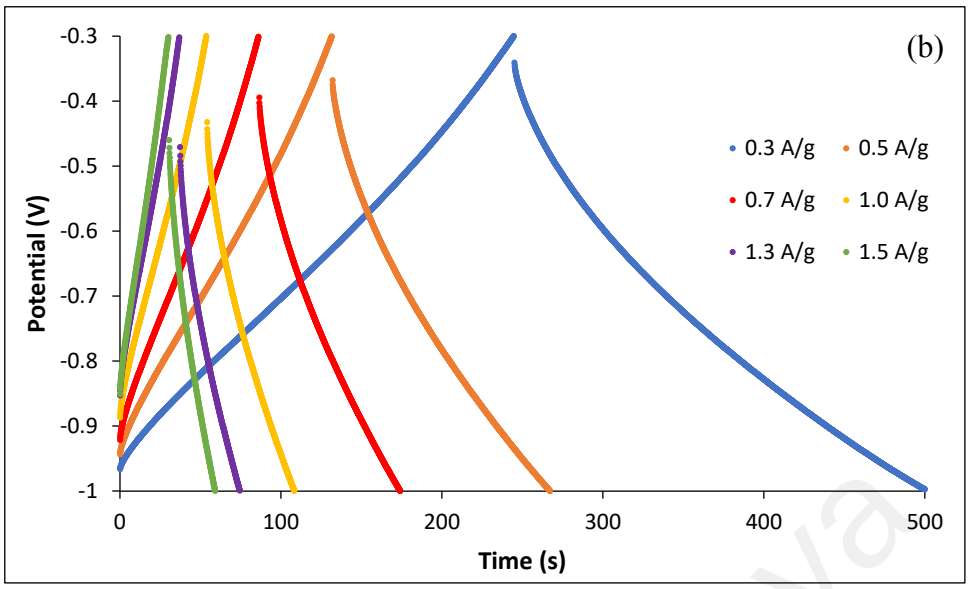

Figure 5.7, continued.

Table 5.3: Specific capacitance of PP-ZnO and GW-ZnO at various current densities.

Sample	Specific capacitance (Fg^{-1})					
	0.3 Ag^{-1}	**0.5 Ag^{-1}**	**0.7 Ag^{-1}**	**1.0 Ag^{-1}**	**1.3 Ag^{-1}**	**1.5 Ag^{-1}**
PP-ZnO	119.03	106.73	99.16	91.40	84.78	75.37
GW-ZnO	117.06	107.08	101.46	95.72	91.63	79.89

The durability and stability of the electrode materials were examined with profile study by different current densities in the order of 0.3 Ag^{-1}, 0.7 Ag^{-1}, 1.0 Ag^{-1}, 0.7 Ag^{-1} and 0.3Ag^{-1}. Based on the result presented in Figure 5.8, PP-ZnO exhibits stable cycling process up to 1.0 Ag^{-1} and started to have slight wobbly upon adjusted to 0.7 Ag^{-1}. PP-ZnO further confronted with a dropped in specific capacitance when applied back with 0.3 Ag^{-1} which only 74.74 % of capacitance is retained at the 5000th cycle as compared to the first 10th cycle. GW-ZnO, on the other hand performed a more stable rate capability with charge storage retained about 85.94 % at the last cycle of the initial capacitance.

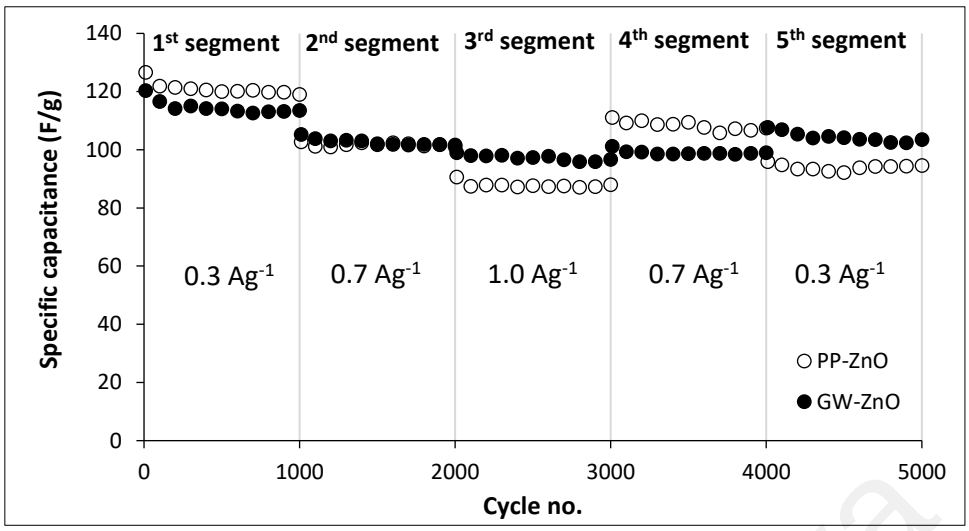

Figure 5.8: Durability performance of PP-ZnO and GW-ZnO at different current densities for 5000 cycles

Looking into the rate capability of individual adjustment of current density as in Figure 5.9, GW-ZnO shows a slightly better performance whereby a minimum of 92.72 % capacitance is retained while PP-ZnO demonstrated only 86.34 %. Figure 5.10 shows the stability of PP-ZnO and GW-ZnO for 1000 cycles with different current densities being applied. Result showed that both displayed a good stability electrode material which both electrode materials retained more than 90 % of the storage at each respective current density.

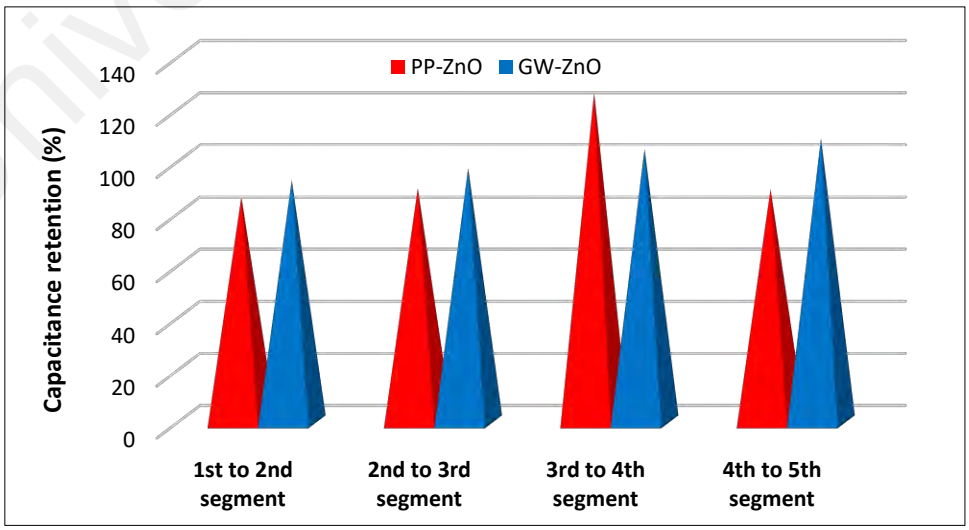

Figure 5.9: Rate capability of PP-ZnO and GW-ZnO from one to another segment across 5000 cycles

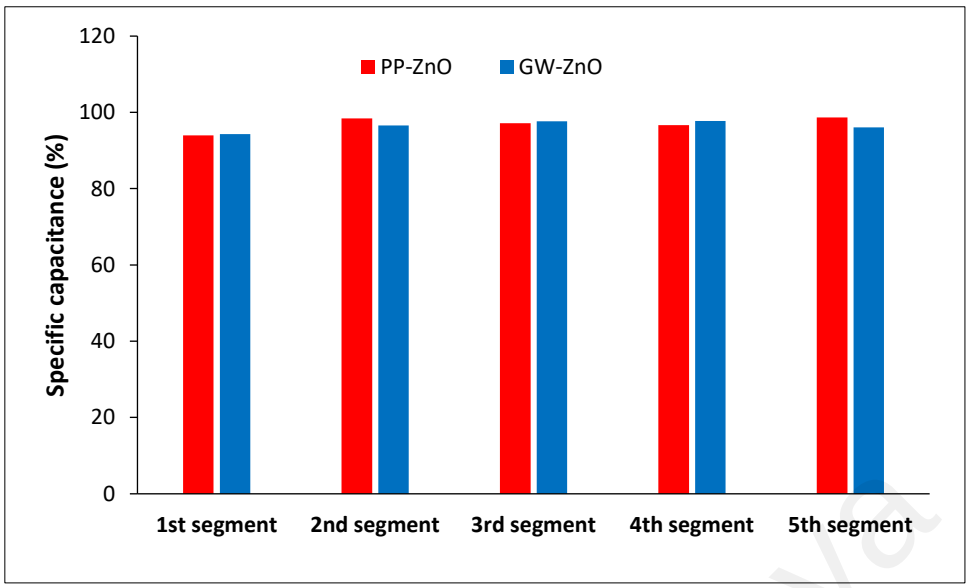

Figure 5.10: Stability of PP-ZnO and GW-ZnO at each segment across 5000 cycles

5.3.3 Electrochemical impedance spectroscopy

Figure 5.11 shows the Nyquist plot of PP-ZnO and GW-ZnO with the inset illustrating the high frequency region. As shown, both samples depicted the typical supercapacitor Nyquist plot with a semicircle at high frequency region and typical Warburg capacitive response at lower frequency region. It was observed that both samples demonstrated lower equivalent series resistance (ESR) value such as 0.35 Ω and 0.41 Ω for PP-ZnO and GW-ZnO, respectively indicated that the electrode materials having better conductivity with the electrolyte ions. Lower value of ESR can be explained with the contribution of the incorporation ZnO which assisted in developing larger mesopore and created a shorter diffusion pathway for electrons and ions charging process. Table 5.4 presents the value of R_s and R_{ct} of PP-ZnO and GW-ZnO.

Table 5.4: Value of R_s and R_{ct} of PP-ZnO and GW-ZnO.

Sample	R_s (Ω)	R_{ct} (Ω)	$R_s + R_{ct}$ (Ω)
PP-ZnO	0.35	0.38	0.73
GW-ZnO	0.41	0.30	0.71

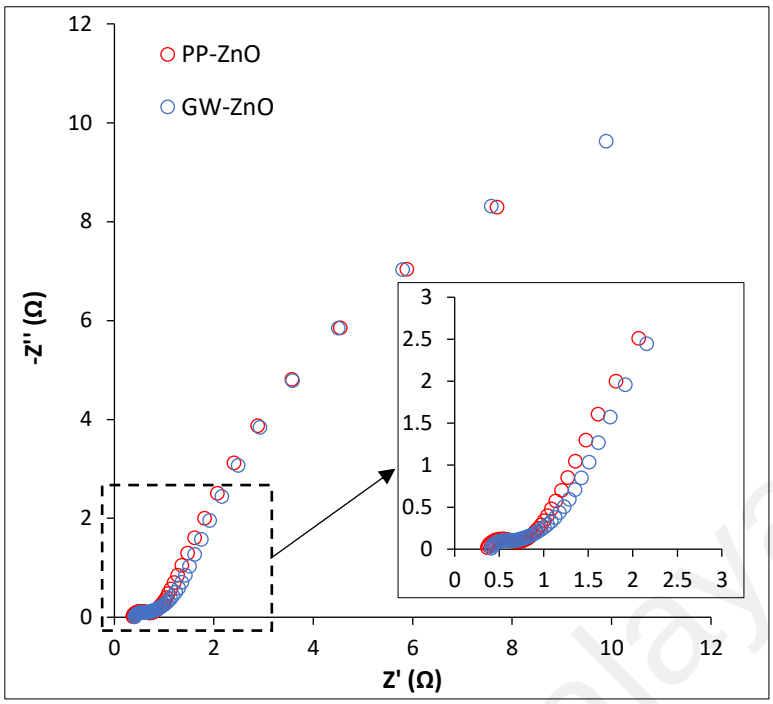

Figure 5.11: Nyquist plot of PP-ZnO and GW-ZnO with inset in high frequency range

5.4 Summary

- PP-ZnO and GW-ZnO behaved almost similar in term of textural properties and electrochemical performance.
- Both samples showed larger mesopore size which PP-ZnO was 3.35 nm and GW-ZnO was 4.08 nm as guest molecules (ZnO) will influence the pore width and pore volume significantly even at relatively small amount.
- Specific capacitance of 119.03 Fg^{-1} and 117.06 Fg^{-1} was obtained in PP-ZnO and GW-ZnO at 0.3 Ag^{-1} in three-electrode system.
- Durability test showed that PP-ZnO and GW-ZnO suffered from capacitance dropped of approximately 25 % and 14 %, respectively from its initial cycle after 5000 cycling process.
- PP-ZnO and GW-ZnO exhibited lower ESR value which is due to the incorporation ZnO which assisted in developing larger mesopore and created a shorter diffusion pathway for charge storage process.

CHAPTER 6: CHARACTERIZATION AND ELECTROCHEMICAL PERFORMANCE OF TERNARY C/ZMO COMPOSITES

6.1 Introduction

This chapter encompasses the results of ternary carbon with zinc dimanganese (ZMO) composite including the series of different ratios from PP-ZMO and GW-ZMO. The test for physical characterization includes the textural properties, XRD, FESEM images accompanied with EDX and TEM images. The electrochemical performance of PP-ZMO and GW-ZMO in three-electrode system is conducted along with the durability of materials examined by profile study with different current densities. Symmetrical cell was fabricated based on the optimum performance within the series of samples from PP-ZMO and GW-ZMO. The device stability test was performed for 5000 cycles at 0.3 Ag^{-1} while durability performance at 0.1, 0.2 and 0.1 Ag^{-1} for 900 cycles.

6.2 Physical characterization

6.2.1 Adsorption-desorption isotherm

Figure 6.1 displays the nitrogen adsorption-desorption isotherm of PP-ZMO and GW-ZMO series samples.

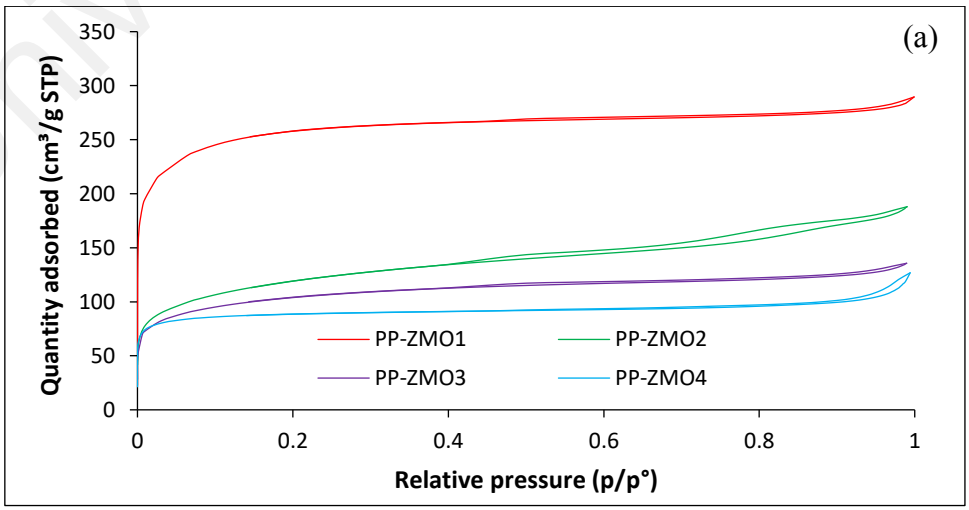

Figure 6.1: Adsorption-desorption isotherm for (a) PP-ZMO1, PP-ZMO2, PP-ZMO3, PP-ZMO4 and (b) GW-ZMO1, GW-ZMO2, GW-ZMO3, GW-ZMO4 samples

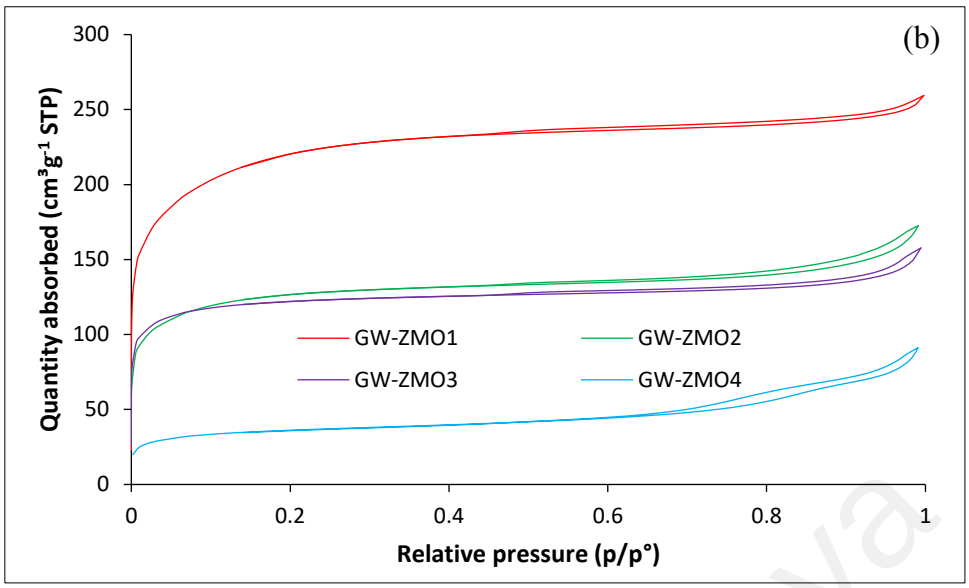

Figure 6.1, continued.

According to the isotherm depicted in Figure 6.1(a), all the curves show the mixture of type I and type IV as stated in IUPAC classification (Maarof et al., 2017). A high N_2 absorption was observed at low p/p° ≈ 0 illustrated high amount of micropore. As all the samples demonstrated type IV characteristic, the hysteresis loop between the relative pressure 0.4 to 1.0 suggesting the existence of mesopore. Nevertheless, they exhibited different types of hysteresis loop in which PP-ZMO1 and PP-ZMO2 were categorized as H4 type while PP-ZMO3 and PP-ZMO4 performed the type of H3. In fact, these two types of hysteresis loop are associated with slit-shaped pores, however, H3 are formed from aggregates of plate-like particles while H4 are pores with narrower sizes. As seen in Figure 6.1(e), the micropore volume is reduced as the ratio of ZMO is increased which can be observed by the reduction of quantity absorbed low relative p/p° ≈ 0.

Figure 6.1(b) also displays a combination of Type I and IV for samples GW-ZMO1, GW-ZMO2 and GW-ZMO3 indicating micro-mesoporous pore structure attributed to its high adsorption at low p/p° range (Maarof et al., 2017). On the other side, GW-ZMO4 exhibited Type II and IV isotherm due to its gradual increment in adsorption at relatively low p/p°. Hysteresis loop appeared in all samples indicating the presence of mesopores

with its significance being in accordance to the increasing weight ratio of ZMO. All samples demonstrated H4 type of hysteresis loop indicating slit-shaped pore with narrower size except for GW-ZMO4 depicted H3 type, a slit-shape pore that formed from cluster of plate-like particle.

6.2.2 BJH pore size distribution

Figure 6.2 illustrates the increment pore volume and pore size distribution curve obtained from BJH theory for a series of sample from PP-ZMO and GW-ZMO.

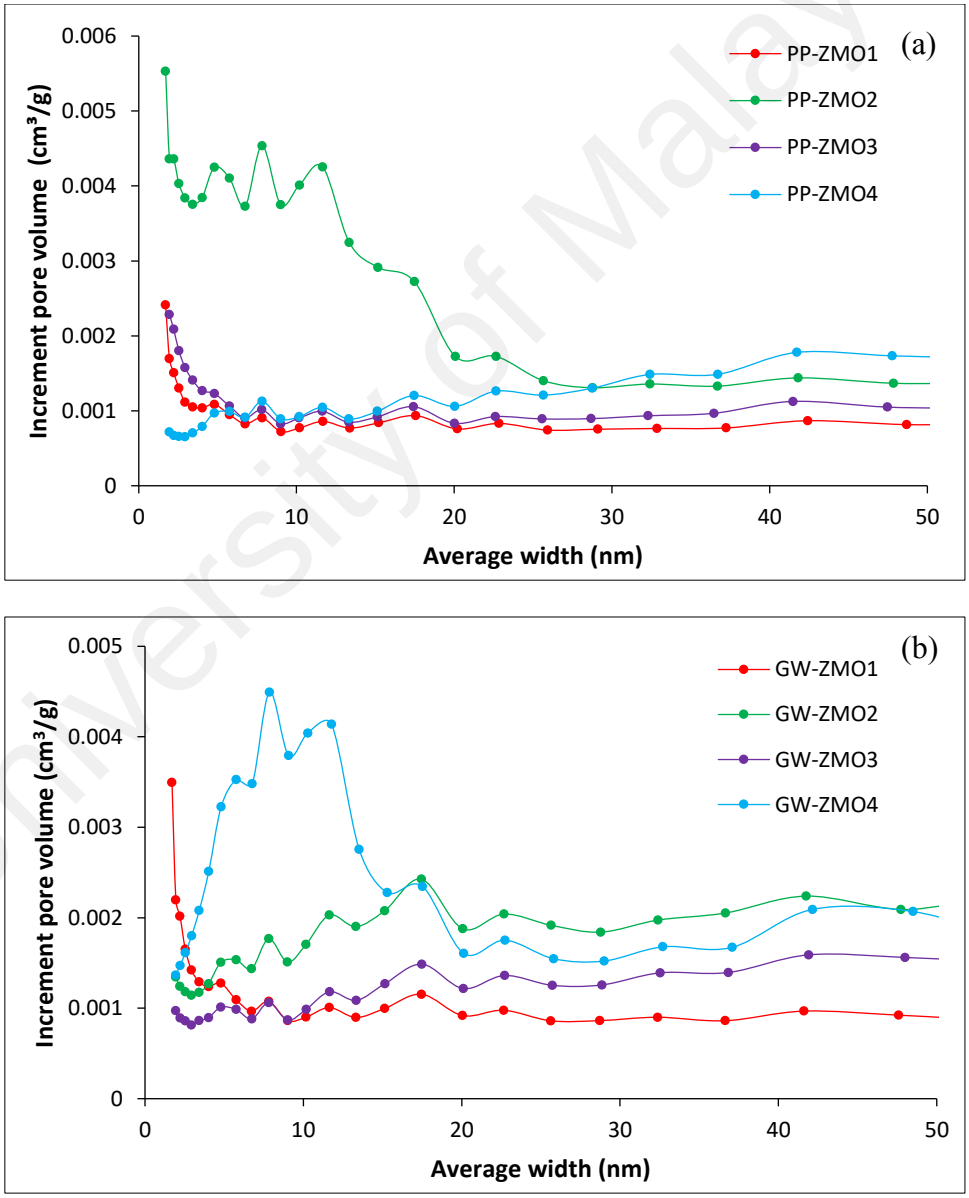

Figure 6.2: BJH pore size distribution for (a) PP-ZMO and (b) GW-ZMO samples with different ratios

Looking into the pore size distribution, it is clearly shown that both PP and GW samples show well-distributed mesopore. The highest peak at smaller pore size range around 1.7 to 2.5 nm can be observed in sample PP-ZMO1 and GW-ZMO1. However, increment of weight ratio in ZMO had caused several mesopore peaks with high density accumulated at 3 to 10 nm in PP-ZMO samples. On the other hand, GW-ZMO samples exhibited a larger mesopore size range which the peaks were gathered around 5 to 17 nm. This is normal as GW samples showed a wider pore size of its original characteristic. Towards 20 nm, a flat line can be observed in both PP-ZMO and GW-ZMO based samples indicated that no pore larger than 20 nm was developed.

Table 6.1 and 6.2 have illustrated all the textural properties such as surface area, micropore and mesopore volume, total pore volume and average pore width for PP-ZMO and GW-ZMO based samples. The specific surface area of both PP-ZMO and GW-ZMO based samples showed a similar trend which were inversely proportionate to weight ratio of ZMO. This result can be explained with two reasons, firstly is mainly due to the decrement of carbon and increment of non-porous materials, ZMO during synthesis that caused the reduction of surface area. Secondly is attributed to ZMO which has assisted in developing broader mesopore size, in which surface area reduces as pore size increases. The highest specific surface area was achieved from PP-ZMO1 and GW-ZMO1 which were 976.12 m^2g^{-1} and 794.94 m^2g^{-1}. Higher specific surface area in PP-ZMO1 is attributed to its higher micropore volume that contributed to the total surface area. Total pore volume also showed reduction in addition of ZMO which could due to the pore space occupied by ZMO. The results demonstrated that mass loading undeniably has caused significant influence in terms of the samples structure.

Table 6.1: Textural properties of PP-ZMO1, PP-ZMO2, PP-ZMO3 and PP-ZMO4.

Sample	BET (m^2g^{-1})	t-plot micropore volume (cm^3g^{-1})	Mesopore volume (cm^3g^{-1})	Total pores volume (cm^3g^{-1})	Average pores width (nm)
PP-ZMO1	976.12	0.30	0.15	0.45	7.06
PP-ZMO2	428.46	0.07	0.22	0.29	5.31
PP-ZMO3	377.53	0.08	0.13	0.21	6.75
PP-ZMO4	339.34	0.11	0.09	0.20	16.8

Table 6.2: Textural properties of GW-ZMO1, GW-ZMO2, GW-ZMO3 and GW-ZMO4.

Sample	BET (m^2g^{-1})	t-plot micropore volume (cm^3g^{-1})	Mesopore volume (cm^3g^{-1})	Total pores volume (cm^3g^{-1})	Average pores width (nm)
GW-ZMO1	794.94	0.20	0.20	0.40	6.40
GW-ZMO2	456.64	0.14	0.13	0.27	11.75
GW-ZMO3	460.49	0.15	0.09	0.24	13.40
GW-ZMO4	128.35	0.03	0.11	0.14	9.47

6.2.3 X-ray diffraction

Figure 6.3 displays the XRD pattern of a series of different ZMO weight ratio derived from PP and GW. It was observed that at lower ratio of ZMO, the characteristic of amorphous graphitic carbon denoted by the broad diffraction peaks at around $2\theta = 24^{\circ}$ (002) still can be detected. However, upon increasing ratio of ZMO, the characteristic of carbon was gradually suppressed by the crystalline peak of ZMO. Additionally, as the pattern of ZnO and ZMO are quite similar in certain range of 2θ, therefore peaks of ZMO are overlapped with ZnO pattern. Nevertheless, the distinguish peaks such as ~ 29º and 33º can be observed which belong to the pattern of ZMO. The x-ray diffraction pattern

peaks can be matched to tetragonal structure of ZMO. The peaks at 29.3˚, 31.2˚, 32.9˚, 36.4˚, 44.6˚, 54.3˚, 59, 60.5 and 64.9˚ are indexed to ZMO (JCPDS file no. 01-077-0470) which aligned to the plane of (112), (200), (103), (211), (220), (312), (321), (224) and (116) respectively (Zhang et al., 2016a). Thus, x-ray diffraction result has validated that ZMO is successfully synthesized on the carbon materials.

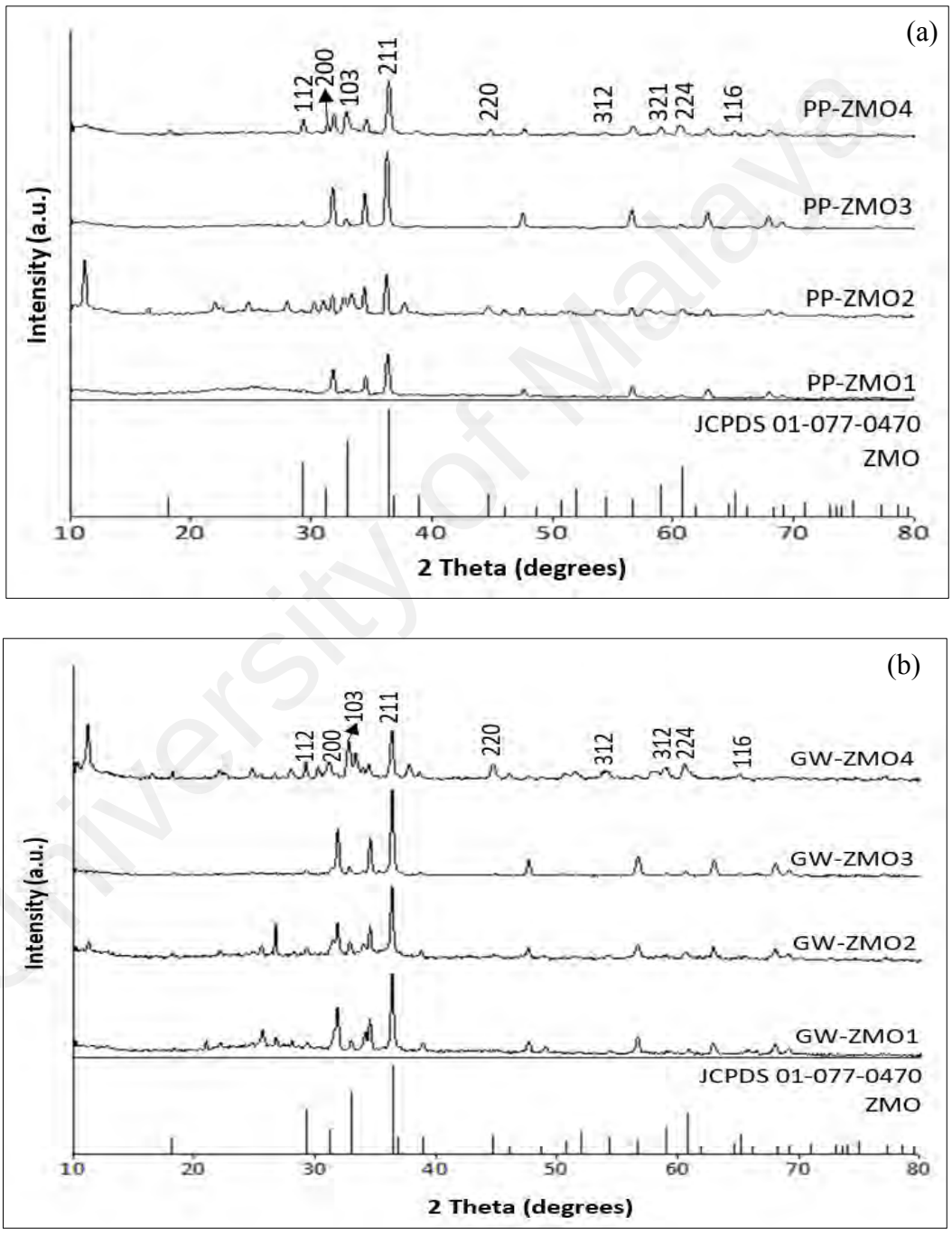

Figure 6.3: X-ray diffraction pattern of (a) PP-ZMO and (b) GW-ZMO series samples

6.2.4 Field emission scanning electron microscopy & energy dispersive x-ray analysis

Figure 6.4 and 6.5 demonstrating the morphology and elemental analysis of the ternary samples with different weight ratio of ZMO originates from PP.

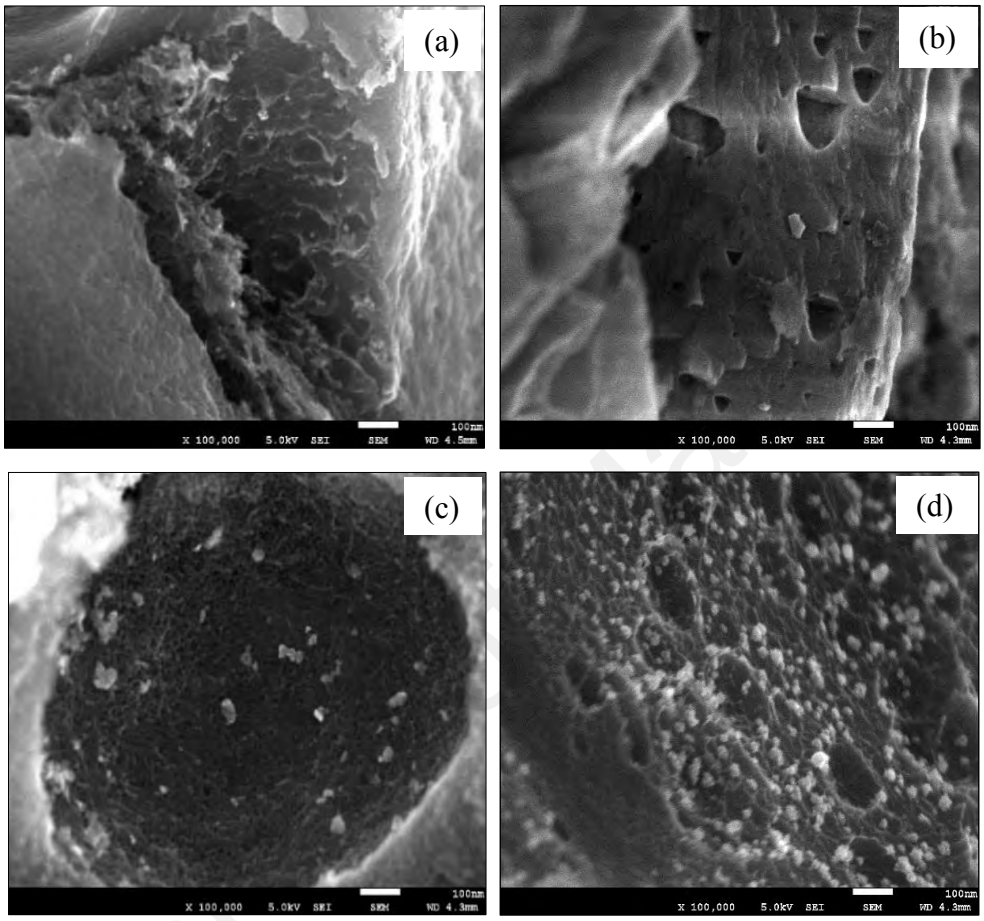

Figure 6.4: FESEM images at magnification of 100K for (a) PP-ZMO1, (b) PP-ZMO2, (c) PP-ZMO3 and (d) PP-ZMO4

According to the FESEM images as shown in Figure 6.4, it can be observed that samples exhibiting high porosity with pores evenly distributed that accords to the textural properties listed in Table 6.1. These numerous pores assist in providing more contact areas for the occurrence of ion transfer and redox reactions. Nevertheless, as the ZMO ratio increased, the pore size started to expand, as seen in PP-ZMO3 and PP-ZMO4, where mesopores were positioned next to each other. Higher weight ratio of ZMO enlarges the pore width which is also one of the factors that caused lower surface area as pore width is inversely proportionate to BET surface area.

Besides that, the density of white spot was proportionate to the ratio of ZMO which can be seen in the FESEM images. These white spots were denoted as ZMO that attached on the carbon surface. The attachment directly caused the pores being blocked which lead to the reduction in surface area and total pore volume. From the FESEM images, it further proved the synthesis of ZMO on carbon structure and the textural properties tabulated in Table 6.1.

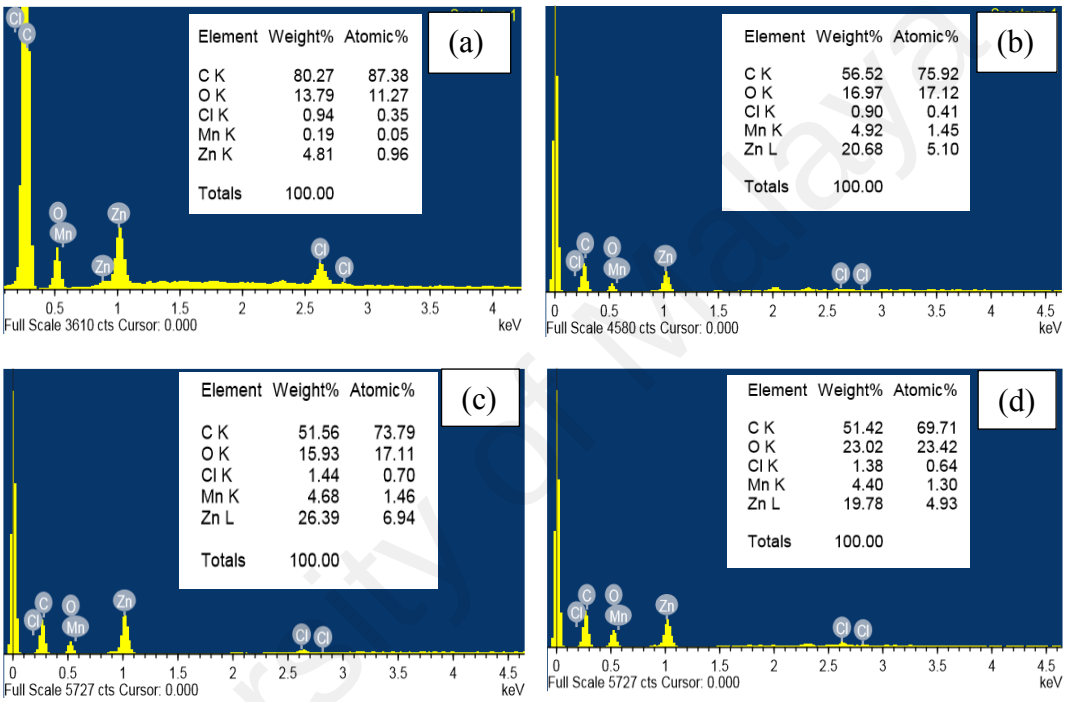

Figure 6.5: EDX of (a) PP-ZMO1, (b) PP-ZMO2, (c) PP-ZMO3 and (d) PP-ZMO4

To further identify the elements in the samples, EDX was conducted as shown in Figure 6.5. From the spectrum, it is obvious that element of C, Zn, Mn and O were spotted further proved that $ZnMn_2O_4$ was successfully integrated into the carbon. A small amount of Cl was observed maybe due to the residue of $ZnCl_2$ which is not clean during washing as only low molarity of HCl being used to ensure the ZMO is not remove.

Figure 6.6 displays the FESEM images of GW-ZMO series samples while Figure 6.7 shows the EDX spectrum of GW-ZMO based samples.

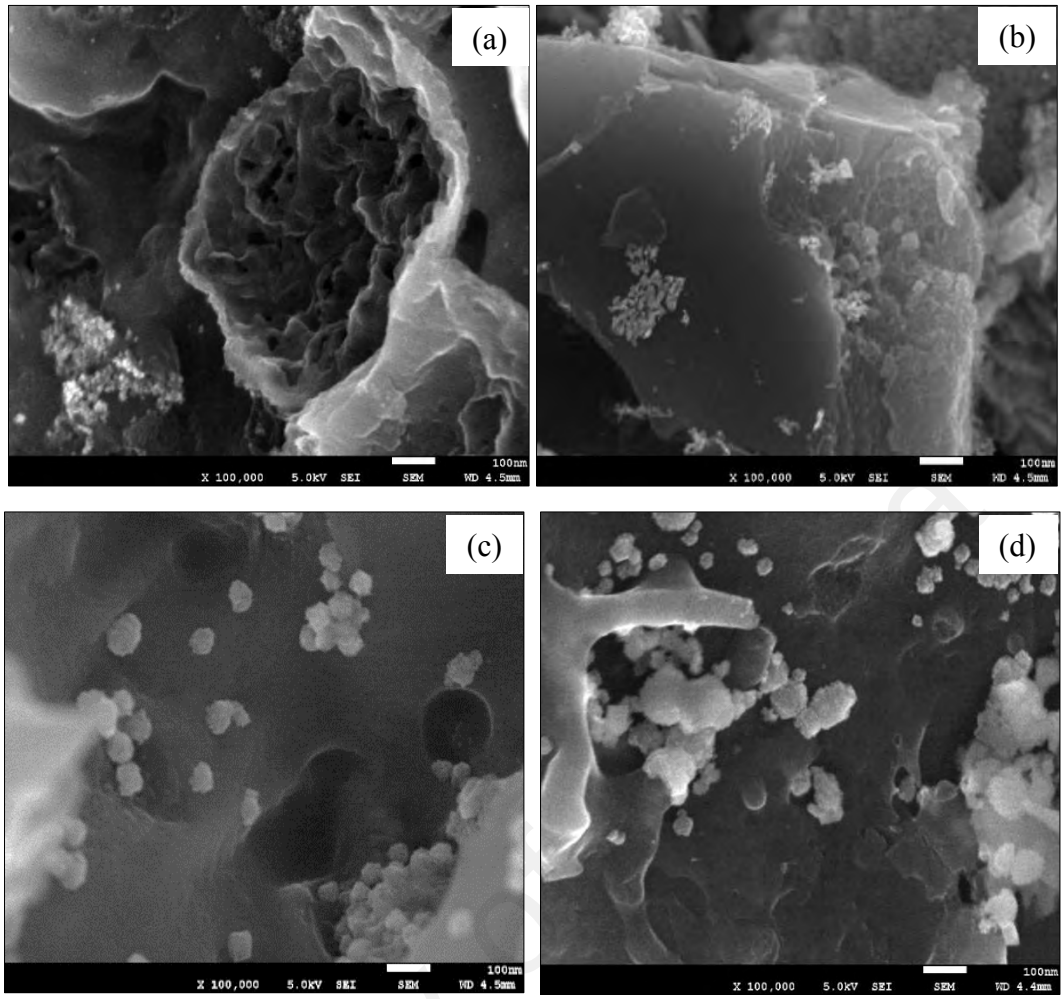

Figure 6.6: FESEM images at magnification of 100K for (a) GW-ZMO1, (b) GW-ZMO2, (c) GW-ZMO3 and (d) GW-ZMO4

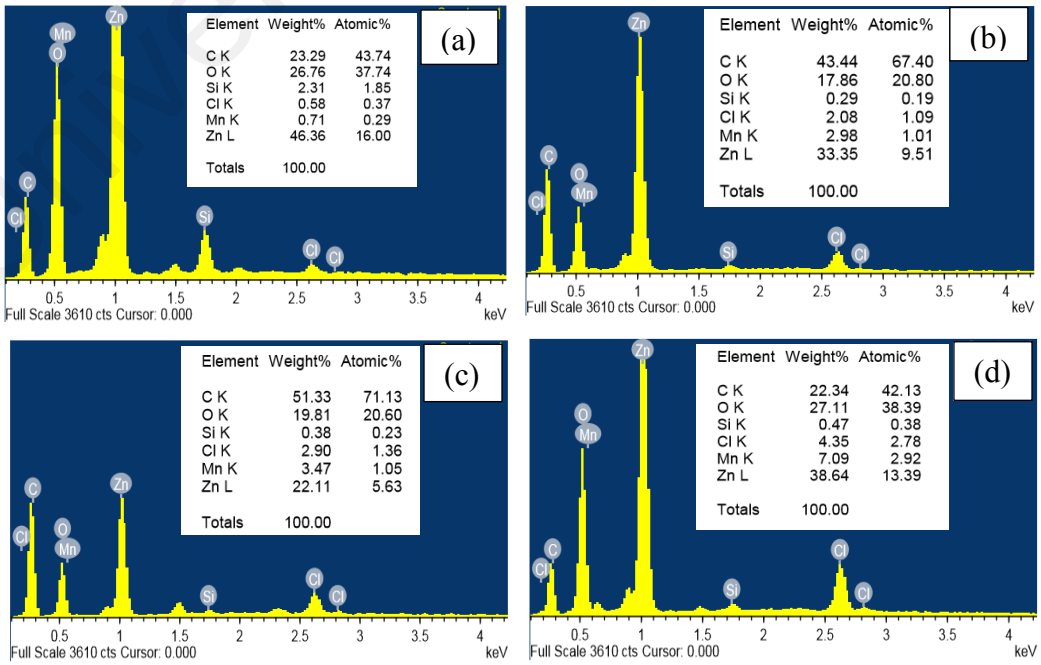

Figure 6.7: EDX of (a) GW-ZMO1, (b) GW-ZMO2, (c) GW-ZMO3 and (d) GW-ZMO4

As can be seen in Figure 6.6, the porosity is well distributed and developed. However, after $MnCO_3$ was added, the pore structure started to change as it got wider, thus reduced the total surface area. The porosity also started to be lessened along the increment of the ZMO ratio. This phenomenon is similar with PP-ZMO based samples. Another significance which can be seen is the pores developed were wider than the PP-ZMO series which is tally with the data in Table 6.1 and Table 6.2.

Another significant phenomenon that can be observed was the appearance of the increasing density of white spots as displayed across the Figure 6.6(a) to (d) that can be attributed to the ZMO. At higher ratio of ZMO, the white spots tend to fill the pores. This has led to the reduction in pore volume which explained the trend of total pore volume in Table 6.2. The FESEM images also proved that in GW-ZMO series samples, ZMO was successfully formed on the carbon surface.

Another evidence for the formation of ZMO can be identified in EDX analysis shown in Figure 6.7. The existence of Zn, Mn and O in all samples implied that ZMO has been formed in accordance with the XRD analysis. Additionally, the C element also detected in all samples implying the successful synthesis of carbon/ZMO composite material.

6.2.5 Transmission electron microscopy

Figure 6.8 and 6.9 depict the TEM and HRTEM images of PP-ZMO1 and GW-ZMO1 respectively. Based on the TEM image, irregular shape and size of the particle and amorphous structure can be observed. HRTEM image further revealed the crystallinity of ZMO. The structure in Figure 6.8(b) with d-spacing of 0.30 nm, 0.28 nm and 0.22 nm are corresponding to the (112), (200) and (004) plane of ZMO. On the other hand, the lattice fringe in Figure 6.10(b) shows the d-spacing of 0.24 and 0.27 nm that corresponds to the (202) and (103) plane of tetragonal ZMO. The HRTEM images further claimed the existence of ZMO on carbon surface is successfully synthesized.

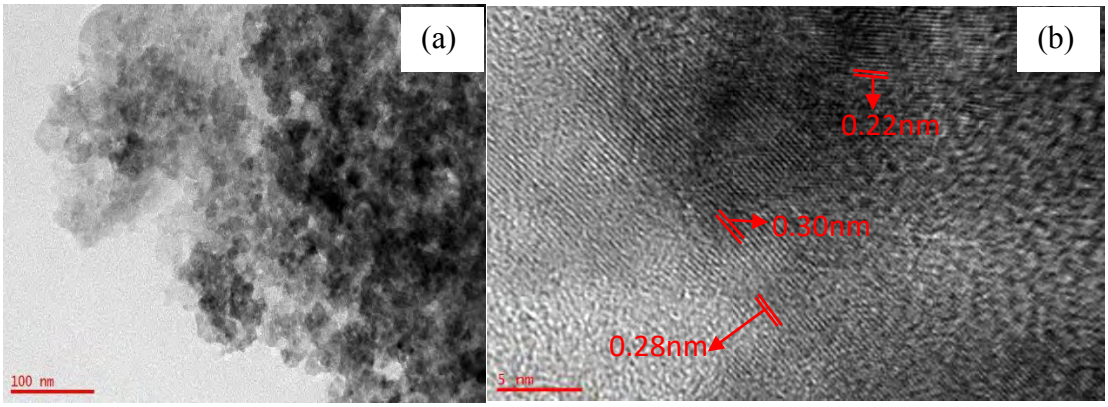

Figure 6.8: Images of (a) TEM and (b) HRTEM lattice fringe image of PP-ZMO1

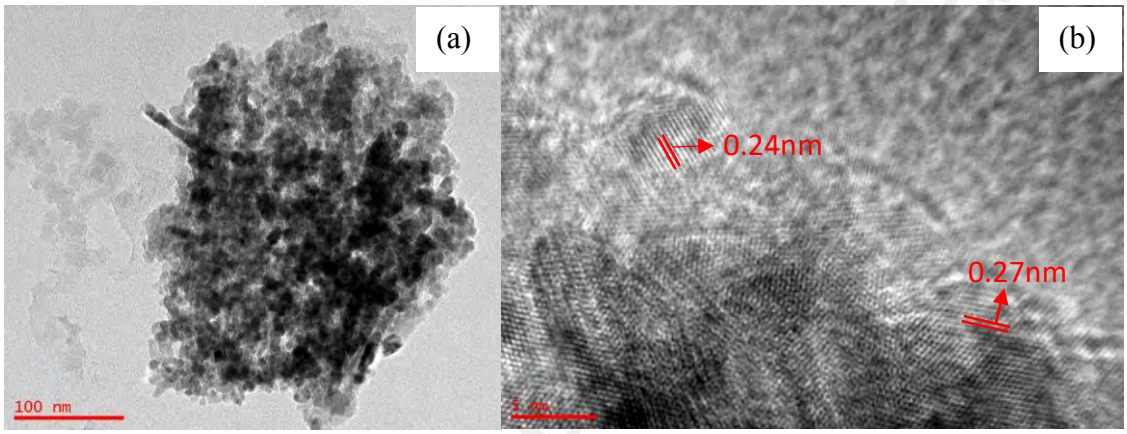

Figure 6.9: Images of (a) TEM and (b) HRTEM lattice fringe image of GW-ZMO1

6.3 Electrochemical performance

In this sub-chapter, electrochemical performance of both PP-ZMO and GW-ZMO with different ratio of ZMO will be first examined using three-electrode system to investigate its material behavior. After testing with durability test, the optimum samples from both PP-ZMO and GW-ZMO series was selected to be fabricated as symmetrical cell and further tested with CV, GCD and EIS to identify the cell performance. Thus, this section includes the electrochemical performance of both three-electrode system and symmetrical cell system.

6.3.1 Three-electrode system

6.3.1.1 Cyclic voltammetry

The CV with various scan rates (3 mVs^{-1}, 5 mVs^{-1}, 10 mVs^{-1}, 30 mVs^{-1}, 50 mVs^{-1} and 100 mVs^{-1}) of PP-ZMO1, PP-ZMO2, PP-ZMO3 and PP-ZMO4 from -0.3 to -1.0 V is depicted in Figure 6.10.

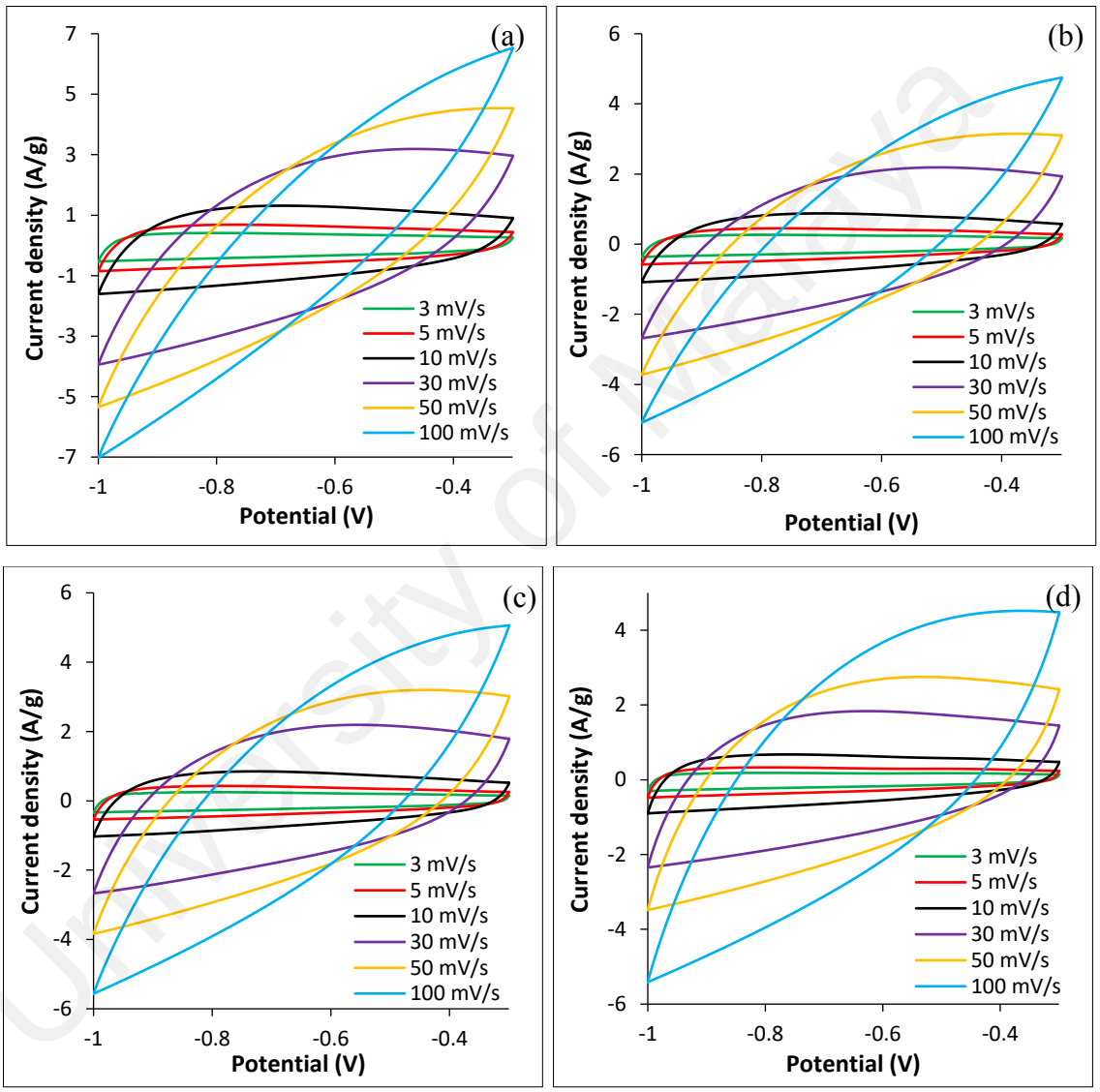

Figure 6.10: Cyclic voltammetry of (a) PP-ZMO1, (b) PP-ZMO2, (c) PP-ZMO3 and (d) PP-ZMO4 with various scan rates

Based on the curves, all the samples preserved nearly rectangular shape at lower scan rates indicated good conductivity of the electrode material. However, the shape of CV distorted to leaf shape at higher scan rates started 30 mVs^{-1} which was attributed to the

resistance when limited time was given for charging process. Though, it can be observed that as the ratio of ZMO increased, the rectangular shape was maintained and larger area under the curve at higher scan rates indicating ZMO assisted in enhancing the electrochemical performance. All the samples demonstrating highest specific capacitance achieved at the scan rate of 3 mVs^{-1}. This is mainly due to at low scan rate, ions have enough time to diffuse into the pores of ion adsorption which contribute to the total specific capacitance. The highest specific capacitance was achieved in PP-ZMO1 such as 113.44 Fg^{-1} at 3 mVs^{-1} due to the high surface area which helps in providing more active sites for ion adsorption. Table 6.3 tabulates the specific capacitance of PP-ZMO1, PP-ZMO2, PP-ZMO3 and PP-ZMO4 from different scan rates.

Table 6.3: Specific capacitance of PP-ZMO series samples at various scan rates.

Sample	Specific capacitance (Fg^{-1})					
	3 mVs^{-1}	**5 mVs^{-1}**	**10 mVs^{-1}**	**30 mVs^{-1}**	**50 mVs^{-1}**	**100 mVs^{-1}**
PP-ZMO1	113.44	110.29	101.01	72.57	55.51	34.64
PP-ZMO2	76.13	73.91	67.91	50.68	40.08	26.03
PP-ZMO3	70.92	70.05	66.08	52.19	42.66	29.11
PP-ZMO4	59.10	58.76	56.21	46.35	39.33	28.69

GW-ZMO series of samples were undergone for cyclic voltammetry of various scan rates (3 mVs^{-1}, 5 mVs^{-1}, 10 mVs^{-1}, 30 mVs^{-1}, 50 mVs^{-1} and 100 mVs^{-1}) as shown in Figure 6.11 to examine the electrochemical properties. The cyclic voltammetry in GW-ZMO series demonstrated the similar pattern as PP-ZMO series. All the samples behaved nearly rectangular shape of CV curves implying the good capacitive characteristic (Li et al., 2019b). The distortion at higher scan rates was due to the resistance of ion diffusion at shorter time given. Though, a larger area under the curve and rectangular shape at higher scan rates can be observed towards the sample of GW-ZMO4 indicating the contribution of ZMO in energy storage capability.

As listed in Table 6.4, lower scan rates having the highest capacitance for all GW-ZMO1, GW-ZMO2, GW-ZMO3 and GW-ZMO4. Among all the samples, GW-ZMO1 obtained the highest specific capacitance (111.30 Fg^{-1}) attributed to its higher specific surface which provide more active sites for ions adsorption. Lowest specific capacitance, on the other hand was observed in GW-ZMO4 which was only 28.51 Fg^{-1}.

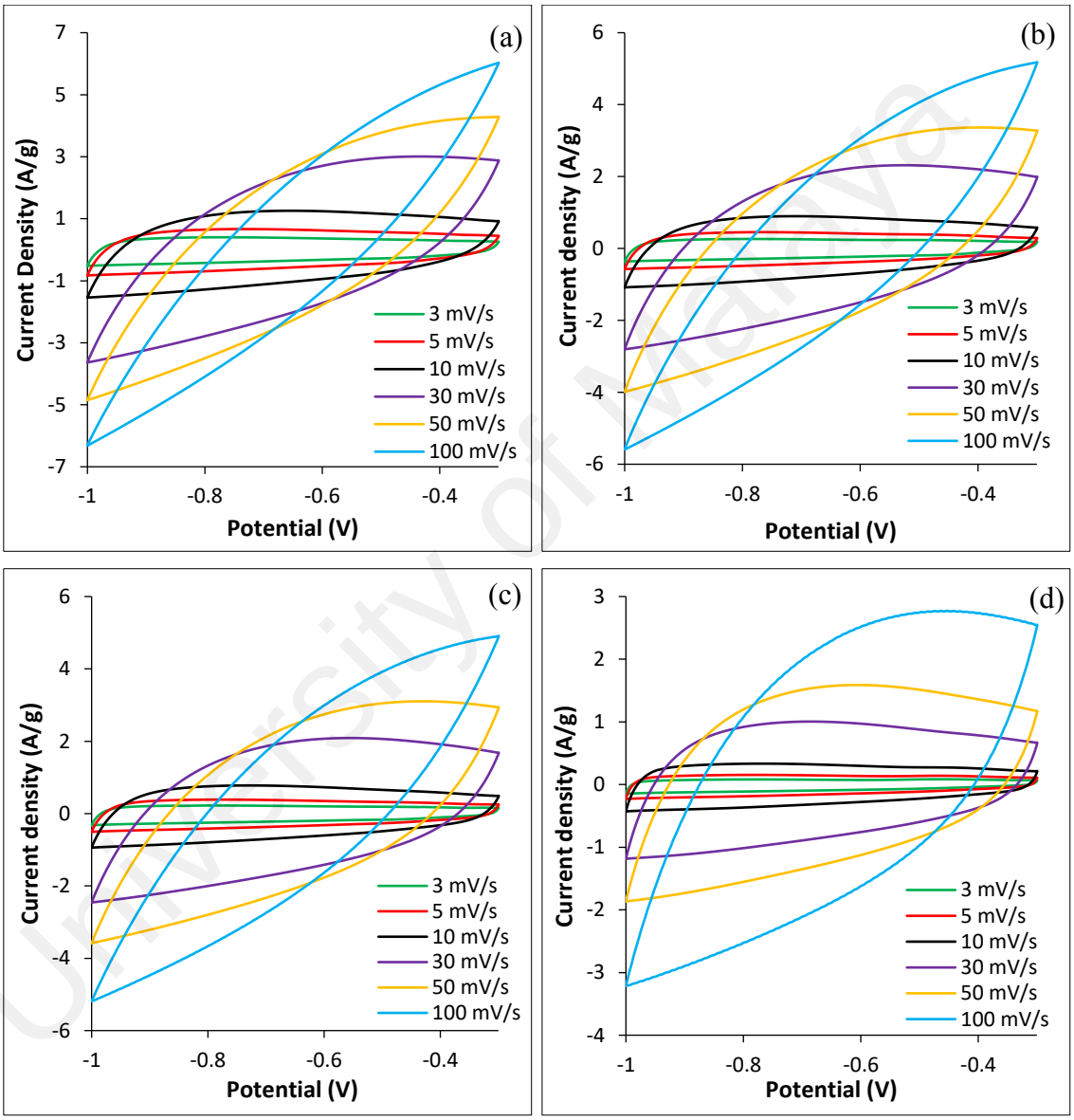

Figure 6.11: Cyclic voltammetry of (a) GW-ZMO1, (b) GW-ZMO2, (c) GW-ZMO3 and (d) GW-ZMO4 with various scan rates

Table 6.4: Specific capacitance of GW-ZMO series samples at various scan rates.

Sample	Specific capacitance (Fg^{-1})					
	3 mVs^{-1}	**5 mVs^{-1}**	**10 mVs^{-1}**	**30 mVs^{-1}**	**50 mVs^{-1}**	**100 mVs^{-1}**
GW-ZMO1	111.30	106.96	95.68	66.07	50.18	31.18
GW-ZMO2	77.06	75.24	70.28	54.47	43.71	28.78
GW-ZMO3	66.79	65.39	61.60	49.66	41.04	27.71
GW-ZMO4	28.51	28.88	28.41	25.80	23.27	18.49

6.3.1.2 Galvanostatic charge-discharge

Different current densities (0.3 Ag^{-1}, 0.5 Ag^{-1}, 0.7 Ag^{-1}, 1.0 Ag^{-1}, 1.3 Ag^{-1} and 1.5 Ag^{-1}) of PP-ZMO series measurement were recorded as depicted in Figure 6.12. All the GCD curves in Figure 6.12 showing slightly deviation of isosceles triangle shape indicating the pseudo reaction occurred. Additionally, a small hump at the voltage of -0.45 to -0.55 V during reduction in PP-ZMO3 and PP-ZMO4 implying intercalation process happened. This is noticeable in these two samples mainly due to their higher ratio of ZMO. Based on the calculation from GCD curves, the highest specific capacitance of 104.89 Fg^{-1} was obtained in PP-ZMO1 at 0.3 Ag^{-1}. The trend in GCD was tally with the analysis from scan rate which the specific capacitance reduced as current density increased attributed to limited time to access at the active sites. Additionally, all the GCD curves of any current density showed almost equal time of charging and discharging illustrating the electrode materials exhibited high coulombic efficiency. Table 6.5 shows the specific capacitance calculated from GCD of different current densities for PP-ZMO series.

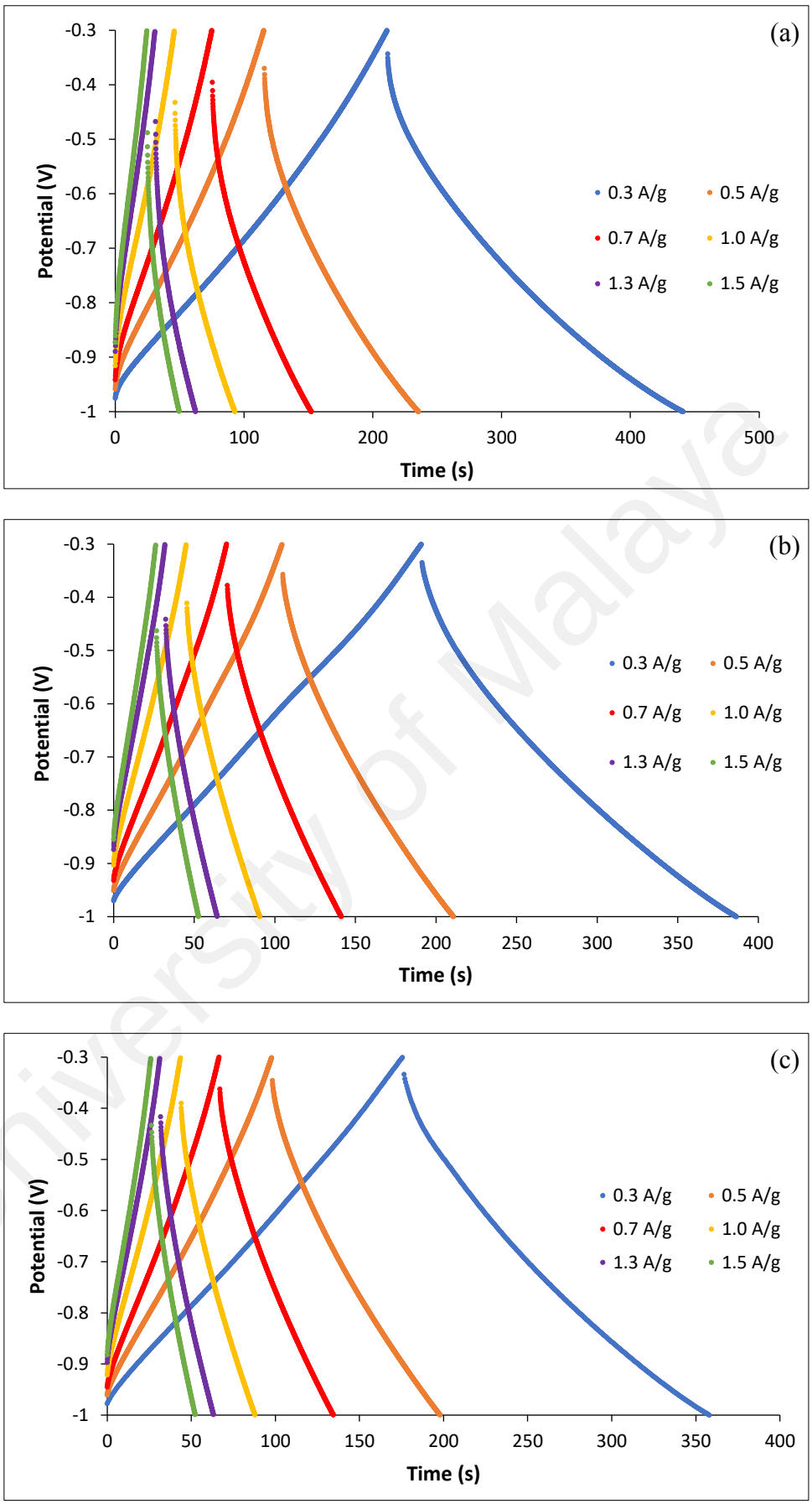

Figure 6.12: Galvanostatic charge-discharge curve of (a) PP-ZMO1, (b) PP-ZMO2, (c) PP-ZMO3 and (d) PP-ZMO4 with various current densities

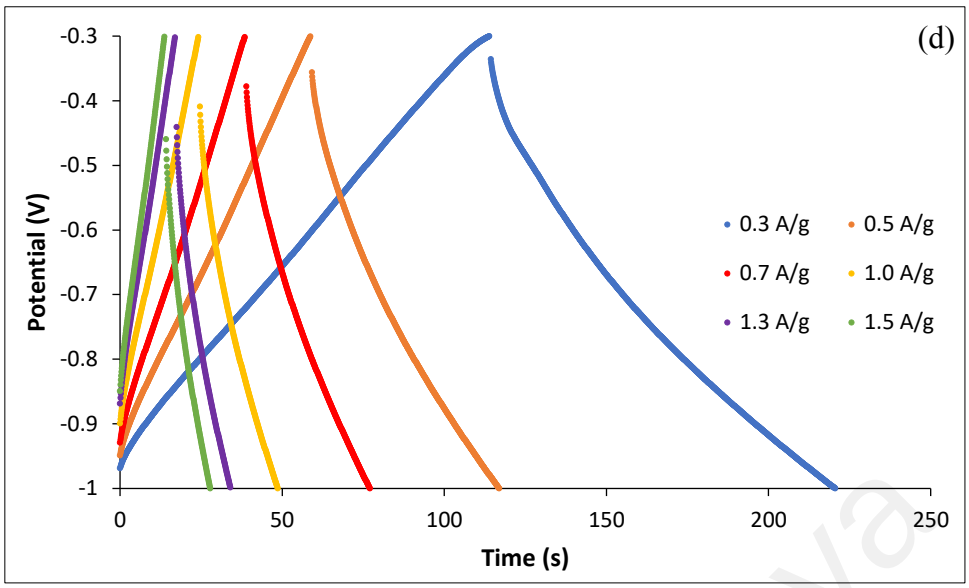

Figure 6.12, continued.

Table 6.5: Specific capacitance of PP-ZMO series samples at various current densities.

Sample	Specific capacitance (Fg^{-1})					
	0.3 Ag^{-1}	**0.5 Ag^{-1}**	**0.7 Ag^{-1}**	**1.0 Ag^{-1}**	**1.3 Ag^{-1}**	**1.5 Ag^{-1}**
PP-ZMO1	104.89	95.07	89.14	82.31	76.49	72.76
PP-ZMO2	87.99	82.46	79.68	76.97	74.63	73.31
PP-ZMO3	81.85	76.34	74.32	72.24	70.34	69.05
PP-ZMO4	48.03	44.91	43.03	40.89	39.02	38.16

In order to investigate the durability of the electrode materials, durability test with a profile study with various current densities was carried out as depicted in Figure 6.13. As this test was undergone with 1000 cycling process for each current density, the stability of the electrode was tested concurrently. Based on the Figure 6.13, the samples exhibited good cycling stability behavior with their respective current density for all the ratio of ZMO. Upon increasing the ratio of ZMO, the samples exhibited a stable specific capacitance value across the 5000 cycles of different current densities. PP-ZMO1 recorded a 92.26 % of capacitance retention at the last cycle as compared to the initial cycle while other samples were 84.05 %, 90.04 % and 101.98 % for PP-ZMO2, PP-ZMO3 and PP-ZMO4, respectively.

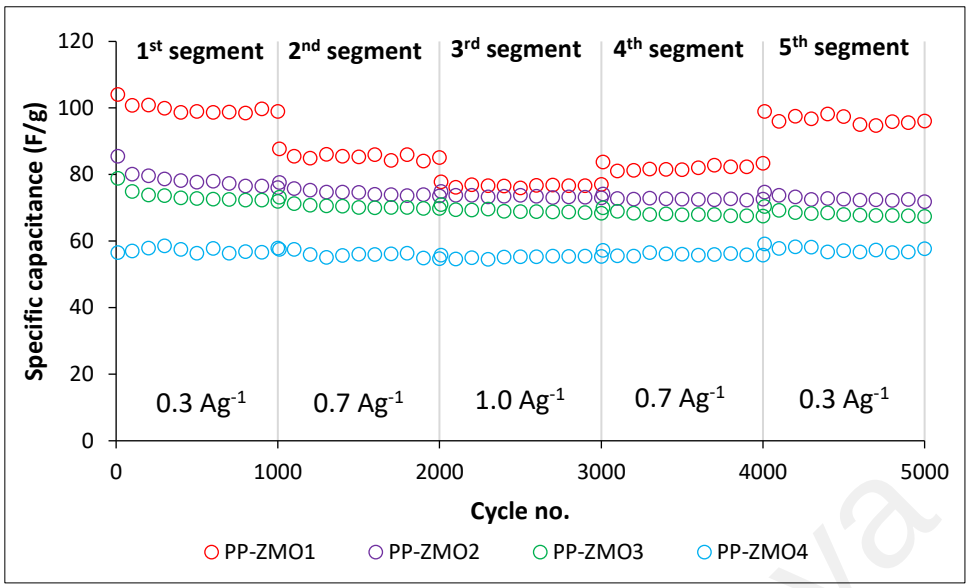

Figure 6.13: Durability performance of PP-ZMO series at different current densities for 5000 cycles

PP-ZMO1 demonstrates high durability behaviour in terms of rate capability as shown in Figure 6.14 where the capacity can sustain even the current density has been modified over long cycling. Other ternary composite samples also showed above 100% of capacitance retention whenever different current densities were applied. This trend implying that ZMO has helped in improving the rate capability. Furthermore, when analysing the capacitance of similar current density but different segments such as 0.3 Ag^{-1} at 1st and 5th segment as well as 0.7 Ag^{-1} at 2nd and 4th segment, the strength of the ternary sample was again demonstrated. For stability of each segment in Figure 6.15, all samples present exceptional stability as the percentage of retention was mostly above 90%, which means the samples capable to withstand long-term use with high stability.

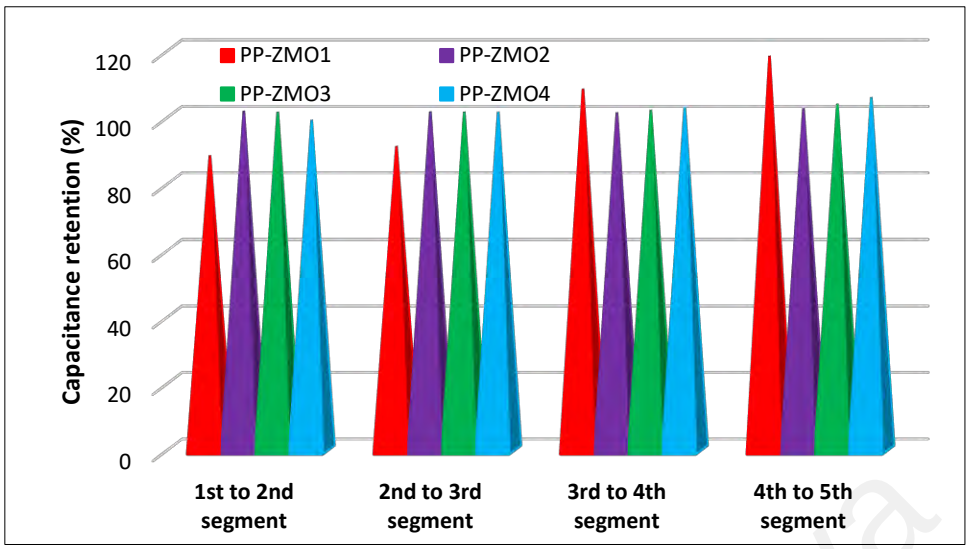

Figure 6.14: Rate capability of PP-ZMO series from one to another segment across 5000 cycles

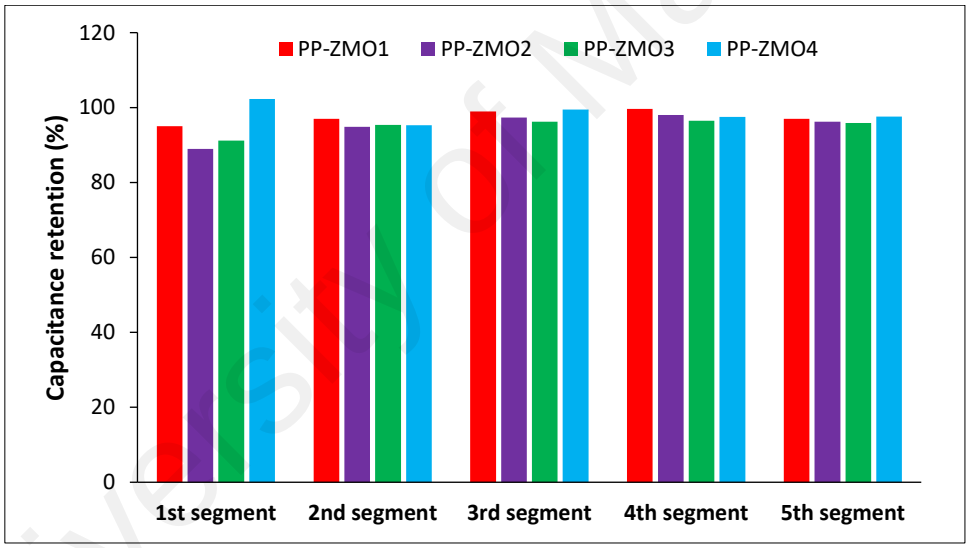

Figure 6.15: Stability of PP-ZMO series at each segment across 5000 cycles

Figure 6.16 as shown below indicates the measurement of GW-ZMO series for galvanostatic charge-discharge at different current densities. All the GCD curves showed slight deviation to linearlity indicating the existance of psuedocapacitance characteristic. Although distortion is formed, the GCD curves still demostrated the triangular shape revealing good electrochemical reversibility. As expected, the highest capacitance was achieved by GW-ZMO1 with 122.94 Fg^{-1} at the currenty density of 0.3 Ag^{-1}. Across different current densities, all the samples retained above 80 % of the capacitance up to

1.5 Ag^{-1}. This further explained that ZMO improved the rate capability of the supercapacitor through its pseudocapacitance characteristics. Table 6.6 shows the specific capacitance calculated from GCD at different current densities for GW-ZMO series.

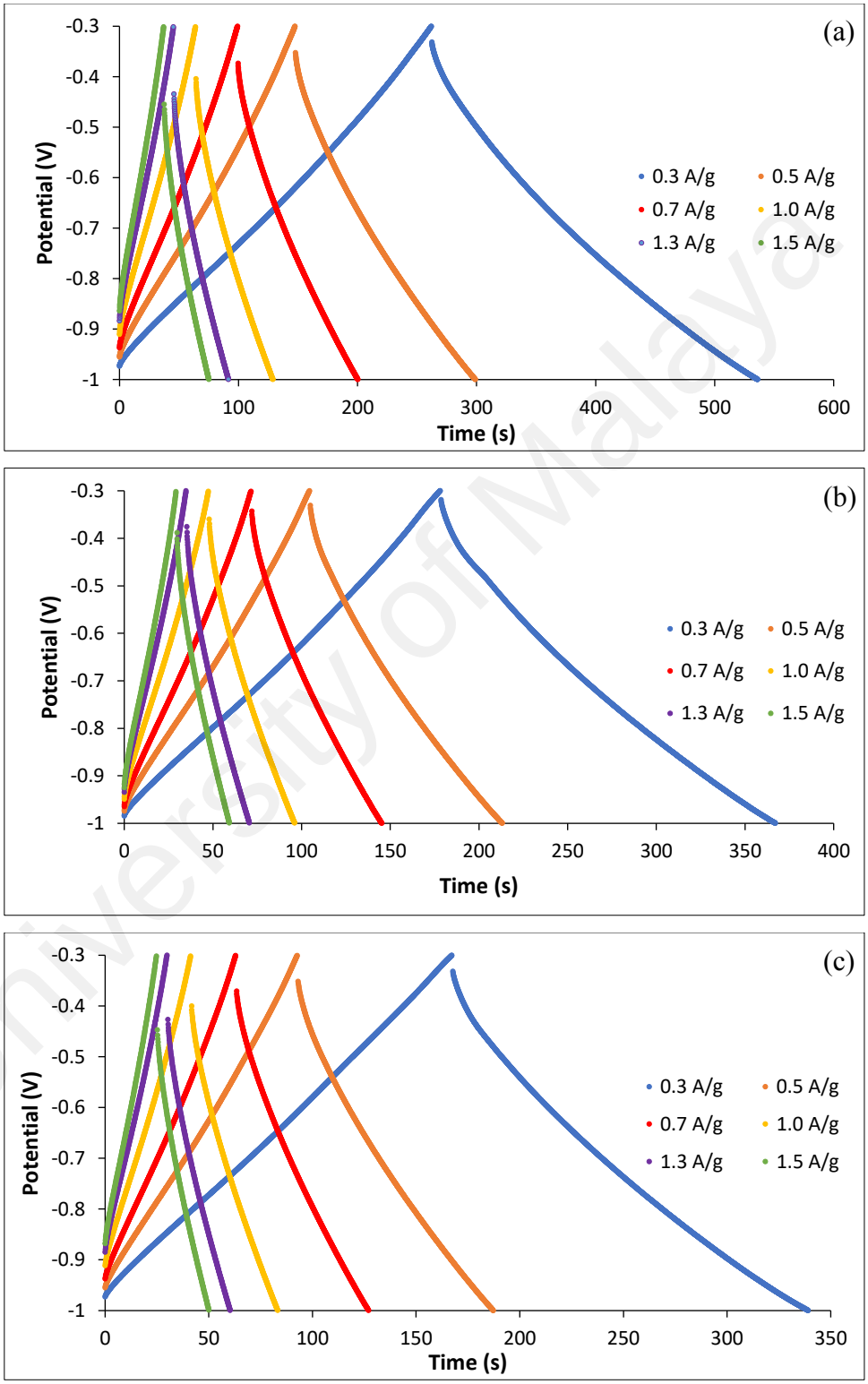

Figure 6.16: Galvanostatic charge-discharge curve of (a) GW-ZMO1, (b) GW-ZMO2, (c) GW-ZMO3 and (d) GW-ZMO4 with various current densities

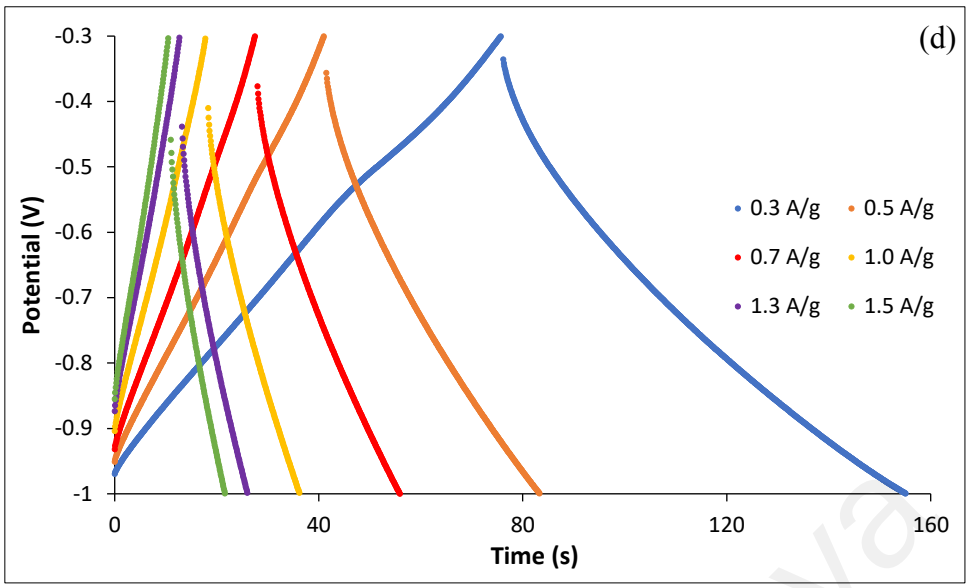

Figure 6.16, continued.

Table 6.6: Specific capacitance of GW-ZMO series samples at various current densities.

Sample	Specific capacitance (Fg^{-1})					
	0.3 Ag^{-1}	**0.5 Ag^{-1}**	**0.7 Ag^{-1}**	**1.0 Ag^{-1}**	**1.3 Ag^{-1}**	**1.5 Ag^{-1}**
GW-ZMO1	122.94	116.70	112.51	108.56	105.30	103.36
GW-ZMO2	83.11	81.02	78.20	75.47	73.70	72.74
GW-ZMO3	77.04	72.69	70.97	69.48	68.32	67.69
GW-ZMO4	35.74	32.62	31.49	30.63	29.99	29.72

The durability and stability of the samples are further evaluated at different current densities for 1000 cycles of charge-discharge. As shown in Figure 6.17, the measurement was conducted at 0.3 Ag^{-1} followed by 0.7 Ag^{-1} until 1.0 Ag^{-1} then reversed back to 0.7 Ag^{-1} and 0.3 Ag^{-1} for 1000 cycles at each current density. As seen GW-ZMO1 demonstrated good stability up to 0.7 Ag^{-1} and started to reduce gradually when it was applied with 1.0 Ag^{-1}. However, when it was adjusted back to 0.7 Ag^{-1} and 0.3 Ag^{-1}, the samples still showed good rate capability which will explain in Figure 6.18. Other samples such as GW-ZMO2, GW-ZMO3 and GW-ZMO4 exhibited a high rate capability and stability test mainly due to the higher ratio of ZMO in the composite materials that assisted in enhancing the electrochemical performance. The capacitance retention at the

5000th cycle as compared to initial cycle was 82.63 %, 82.59 %, 86.38 % and 84.88 % for GW-ZMO1, GW-ZMO2, GW-ZMO3 and GW-ZMO4, respectively.

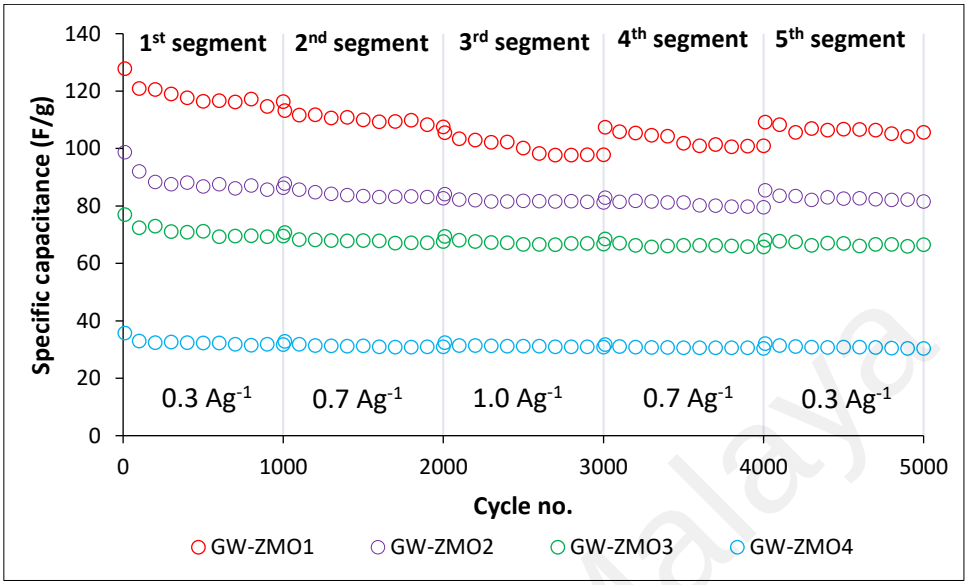

Figure 6.17: Durability performance of GW-ZMO series at different current densities for 5000 cycles

As seen in Figure 6.18, it was noted that samples able to obtain higher specific capacitance value even at higher current load which was from 1st to 2nd segment along with 2nd to 3rd segment. This proved that ZMO can withstand higher current load without any capacitance faded. Immediately upon 1.0 Ag^{-1} after 3000 cycles, the samples were analysed with lower load of current densities to inspect its durability and steadiness at the meantime. As calculated from the 5000th cycle, the capacitance retention as compared to the 1000th cycle for GW-ZMO1, GW-ZMO2, GW-ZMO3 and GW-ZMO4 were 90.77 %, 94.43 %, 95.61 % and 95.49 % respectively. The value increased gradually with the ZMO content mainly due to more electrochemically active sites on the surface of carbon. In term of stability for each segment as illustrated in Figure 6.19, all samples behaved outstanding stability of approximately 90 % and above of capacitance retention.

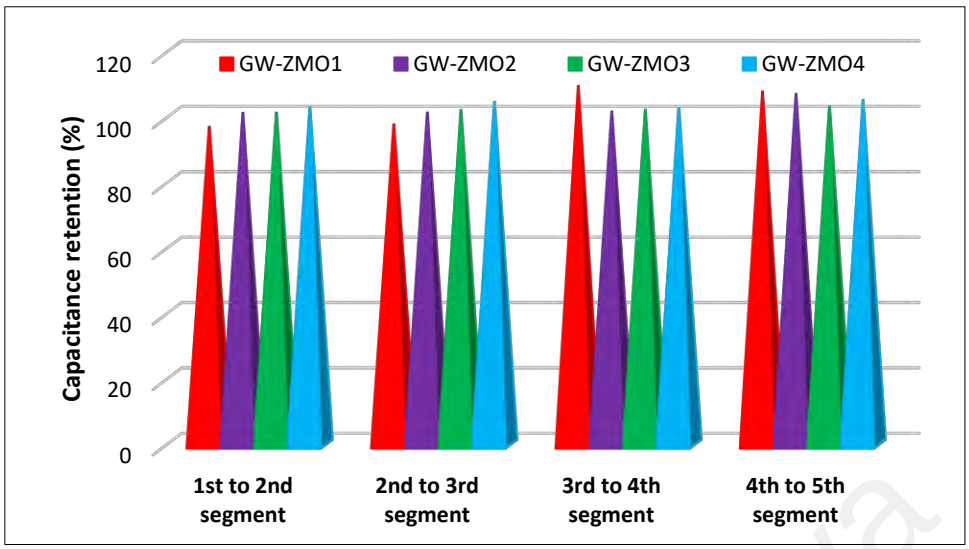

Figure 6.18: Rate capability of GW-ZMO series from one to another segment across 5000 cycles

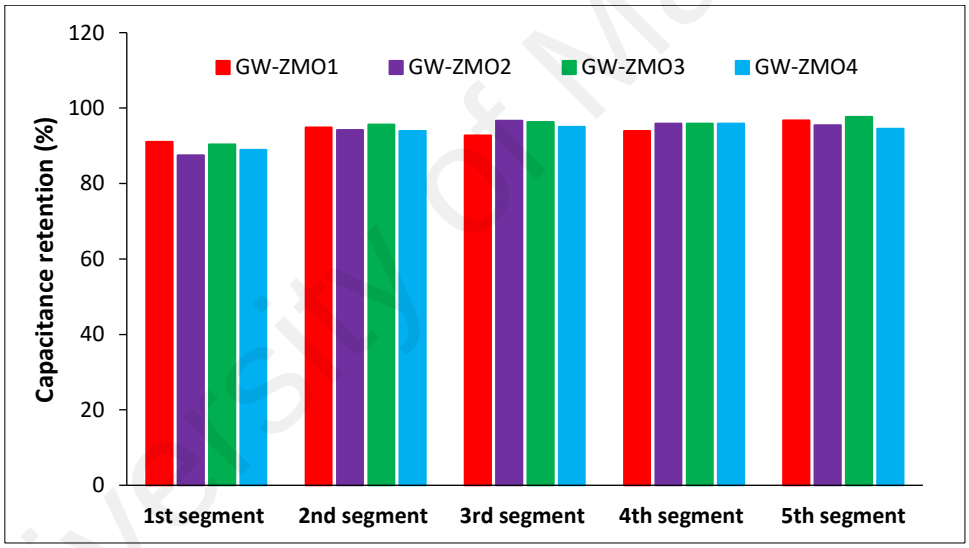

Figure 6.19: Stability of GW-ZMO series at each segment across 5000 cycles

6.3.1.3 Electrochemical impedance spectroscopy

In order to have a better understanding of electrochemical performance of the materials, EIS was employed to determine the kinetics and interfacial resistance of the samples. Figure 6.20 represents the bulk and charge-transfer resistance for the samples of PP-ZMO1, PP-ZMO2, PP-ZMO3 and PP-ZMO4. All the samples in PP-ZMO series demonstrated typical semicircle at the high frequency range and a 45º spike at low frequency range indicating capacitive behavior of the electrode materials. Nyquist plots

at Figure 6.20 shows that every sample having different R_s owing to different pore sizes of each samples creating varies contact resistance at the active materials. Table 6.7 has listed out the R_s and R_{ct} values of all electrodes. The lowest ESR in PP-ZMO1 might be one of the reasons for its high specific capacitance. In addition, R_{ct} increased up to PP-ZMO2 and reduced explained the improvement of PP-ZMO4 in stability test compared to other samples. Higher R_{ct} in PP-ZMO1 and PP-ZMO2 mainly due to lower ratio of ZMO in the samples which could provide a shorter ion diffusion pathway and intercalation process to happen.

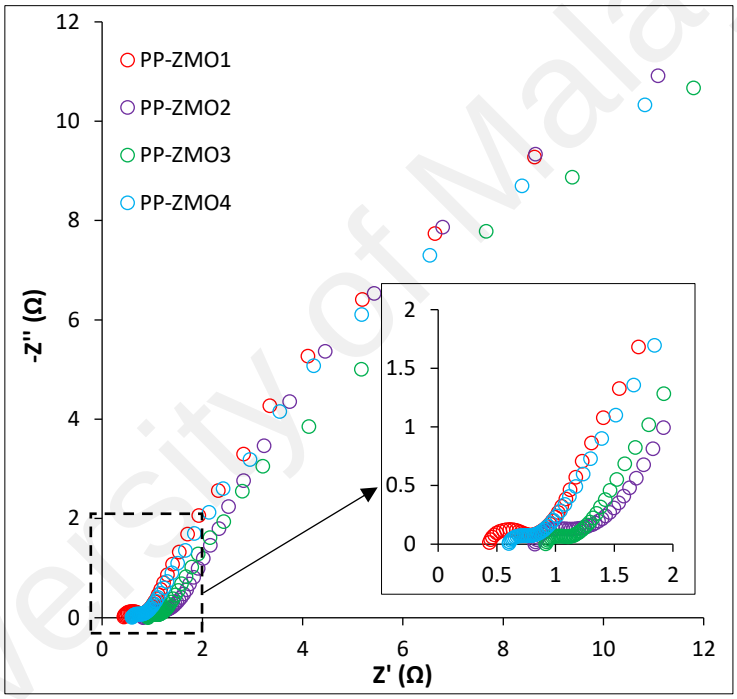

Figure 6.20: Nyquist plot of PP-ZMO series samples with inset in high frequency range

Table 6.7: Value of R_s and R_{ct} of PP-ZMO series.

Sample	R_s (Ω)	R_{ct} (Ω)	$R_s + R_{ct}$ (Ω)
PP-ZMO1	0.42	0.41	0.83
PP-ZMO2	0.81	0.47	1.28
PP-ZMO3	0.91	0.26	1.17
PP-ZMO4	0.59	0.29	0.88

Figure 6.21 shows the Nyquist plot of GW-ZMO series, similar with the result presented in PP-ZMO series, GW-ZMO1 also achieved the lowest ESR value that is

0.63 Ω which result in its highest specific capacitance. This ESR value was even lower as compared to PP-ZMO1 (104.89 Fg^{-1}) explained the better specific capacitance in GW-ZMO1 (122.94 Fg^{-1}). The highest R_{ct} in GW-ZMO4 can be attributed to lesser active sites for ion adsorption as it exhibited low specific surface area (128.35 m^2g^{-1}) and the ZMO tends to accumulate and block pore as shown in Figure 6.6(d). Apart from the R_{ct}, it is also observed that the slope at low frequency is deviated from the ideal vertical line which can be attributed to the pseudocapacitive characteristics leading to Warburg behavior. Table 6.8 presents the resistance value of GW-ZMO samples at a frequency range of 0.1 Hz to 10 kHz

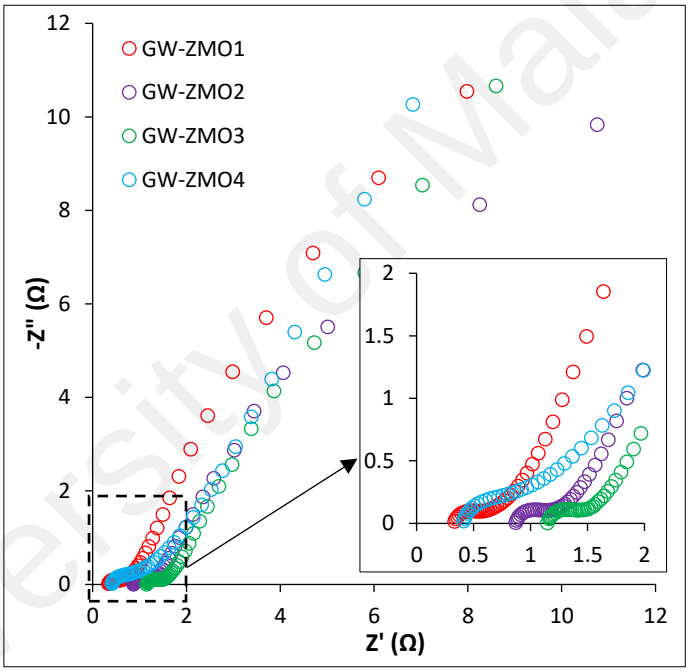

Figure 6.21: Nyquist plot of GW-ZMO series samples with inset in high frequency range

Table 6.8: Value of R_s and R_{ct} of GW-ZMO series.

Sample	R_s (Ω)	R_{ct} (Ω)	$R_s + R_{ct}$ (Ω)
GW-ZMO1	0.33	0.30	0.63
GW-ZMO2	0.87	0.34	1.21
GW-ZMO3	1.15	0.35	1.50
GW-ZMO4	0.41	0.61	1.02

6.3.2 Symmetrical cell system

In this system, PP-ZMO1 and GW-ZMO1 were selected for symmetrical cell fabrication due to their higher specific capacitance and good durability performance.

6.3.2.1 Cyclic voltammetry

Figure 6.22 depicts the CV curves of PP-ZMO1 and GW-ZMO1 symmetrical cells at different scan rates of 3 mVs^{-1} towards 100 mVs^{-1}. As shown in Figure 6.22, a distorted rectangular shape is depicted in both symmetrical cells of PP-ZMO1 and GW-ZMO1 indicating both EDLC and pseudo-capacitive behavior which is attributed to the elements of carbon and ZMO. The electrolyte ion adsorption on the active sites of the carbon during charging resulting in the rectangular shape of the CV curve. At the meantime, intercalation/de-intercalation between ZMO and K^+ electrolyte ions is the main reason of the distortion of CV curve as redox reaction is happening when the device is subjected to charge/discharge process. The appearance of two characteristics in a CV curve explains both elements are contributing in the overall performance of the supercapacitor. However, upon higher scan rates, it is observed that PP-ZMO1||PP-ZMO1 cell demonstrated major distortion of the CV curves implying the high resistance faced during charging and discharging process. On the other hand, the shape of the CV curves in GW-ZMO1||GW-ZMO1 cell retained almost alike representing low restriction during the movement of K^+ ions through the voids between adjacent nanopores at higher scan rates. This might be due to the equal ratio of micropore (0.20 cm^3g^{-1}) and mesopore (0.20 cm^3g^{-1}) volume appeared in GW-ZMO1||GW-ZMO1 that assisted in providing the optimum sites for ion diffusion and adsorption in both low and high scan rates. Table 6.9 shows the specific capacitance of symmetrical cell fabricated from PP-ZMO1 and GW-ZMO1 at different scan rates from 0 to 1.0 V. As presented in Table 6.9, GW-ZMO1||GW-ZMO1 cell obtained higher specific capacitance of 19.40 Fg^{-1} at 3 mVs^{-1} and retained 70 % of the capacitance up to 100 mVs^{-1} explained its high rate capability in supercapacitor.

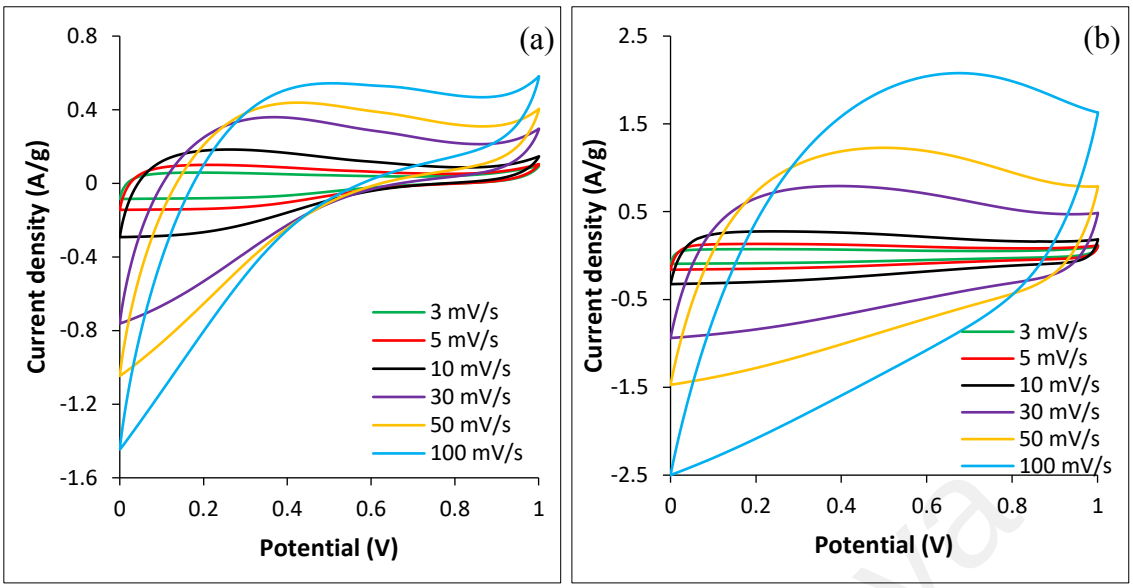

Figure 6.22: Cyclic voltammetry of (a) PP-ZMO1 and (b) GW-ZMO1 with various scan rates in EDLC

Table 6.9: Specific capacitance of PP-ZMO1 and GW-ZMO1 in EDLC at various scan rates.

Sample	Specific capacitance (Fg^{-1})					
	3 mVs^{-1}	**5 mVs^{-1}**	**10 mVs^{-1}**	**30 mVs^{-1}**	**50 mVs^{-1}**	**100 mVs^{-1}**
PP-ZMO1	15.38	15.24	14.27	10.82	8.66	5.88
GW-ZMO1	19.40	20.47	20.76	18.96	17.04	13.53

6.3.2.2 Galvanostatic charge-discharge

The Figure 6.23 illustrates the GCD curves of both PP-ZMO1||PP-ZMO1 and GW-ZMO1||GW-ZMO1 cell of different current densities. The GCD test was conducted with distorted triangular shape in both symmetrical cells of PP-ZMO1 and GW-ZMO1 explained the existence of ZMO. Moreover, the charging and discharging time are almost similar suggesting high coulombic efficiencies. As can be seen that, GW-ZMO1||GW-ZMO1 cell performed longer charging and discharging time suggesting higher specific capacitance in the supercapacitor. Additionally, it was observed that PP-ZMO1||PP-ZMO1 cell presented an iR drop and became more noticeable as the current density

signifying the internal resistance in the cell when it is charging and discharging. This phenomenon is tally which the result obtained in Figure 6.22(a) that the CV curves were distorted. On the other hand, symmetrical cell of GW-ZMO1 showed insignificant iR drop indicating low internal resistance and better electrochemical process. Based on the calculation of specific capacitance from GCD curves as listed in Table 6.10, 24.67 Fg^{-1} at 0.03 Ag^{-1} was achieved in symmetrical cell of GW-ZMO1 and retained 85 % of the capacitance at 1.0 Ag^{-1} while PP-ZMO1||PP-ZMO1 only able to retain 38 %.

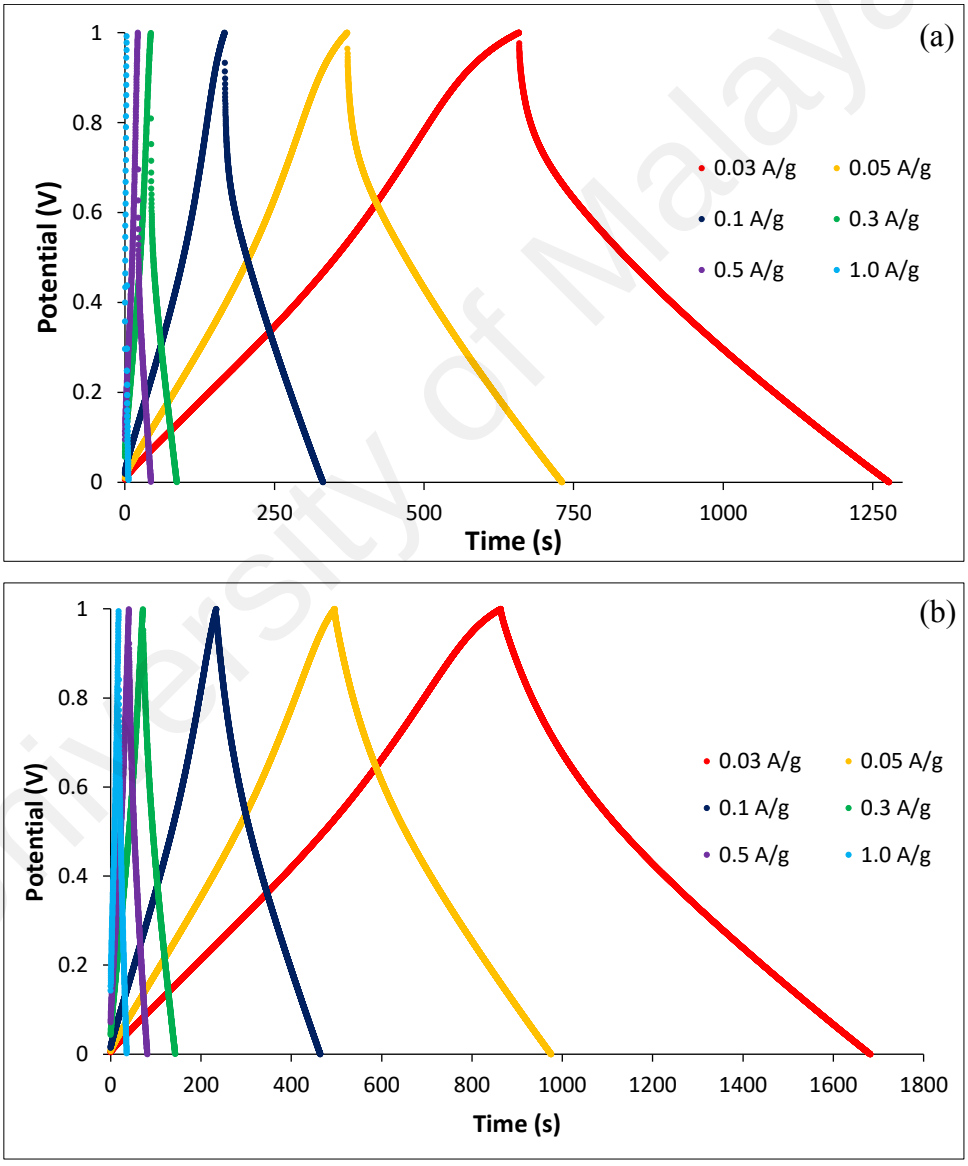

Figure 6.23: GCD of (a) PP-ZMO1 and (b) GW-ZMO1 with various current densities in EDLC

Table 6.10: Specific capacitance of PP-ZMO1 and GW-ZMO1 in EDLC at various current densities.

Sample	Specific capacitance (Fg^{-1})					
	0.03 Ag^{-1}	**0.05 Ag^{-1}**	**0.1 Ag^{-1}**	**0.3 Ag^{-1}**	**0.5 Ag^{-1}**	**1.0 Ag^{-1}**
PP-ZMO1	17.62	16.04	13.72	11.71	9.83	6.61
GW-ZMO1	24.67	24.16	23.39	22.43	21.87	20.92

In order to examine the durability of the cell, a profile study of different current densities for 900 cycles was carried out as shown in Figure 6.24 for both samples.

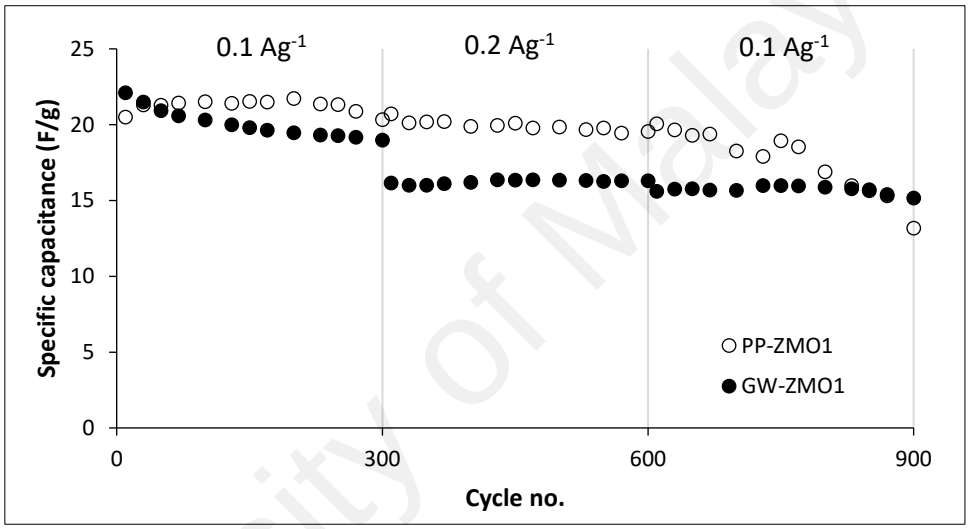

Figure 6.24: Durability performance of symmetrical cell at different current densities for 900 cycles in EDLC

The result showed that PP-ZMO1||PP-ZMO1 device performed an outstanding stability with capacitance retention of 95.32 % up to the 600th cycle. However, a gradual depletion and unstable condition were observed when the device was applied back to 0.1 Ag^{-1} with only 64.88 % of retention was achieved at the 900th cycle as compared with the 300th cycle. GW-ZMO1||GW-ZMO1 cell, on the other hand performed a quite stable condition at each current density. The capacitance retention showed 73.69 % at the 600th cycle and when it was applied back to 0.1 Ag^{-1} after 600th cycle, the cell retained 80 % of the capacitance at the last cycle as compared to the 300th cycle indicating GW-ZMO1||GW-ZMO1 cell exhibited a high durable supercapacitor.

Moreover, a stability test of 5000 cycles was also conducted for both symmetrical cell of PP-ZMO1 and GW-ZMO1 at 0.3 Ag^{-1} as shown in Figure 6.25. Based on the Figure 6.25(a), 83.89 % of the capacitance is retained after continuous 5000 cycles of charge and discharge implying good mechanical stability of the supercapacitor. The rise in capacitance retention was detected until 2500th cycle which might be due to the activation of the surface leading to a better pathway of electrolyte ions to the active sites of smaller mesopores. In GW-ZMO1||GW-ZMO1 cell, a retention of 84.81 % is attained at the 5000th cycle demonstrated a good long-term cycle stability. Both PP-ZMO1 and GW-ZMO1 exhibited almost similar strength of stability. In terms of energy and power density, GW-ZMO1||GW-ZMO1 cell displayed better power and energy density such as 129.43 Wkg^{-1} and 1.94 $Whkg^{-1}$, respectively. While PP-ZMO1||PP-ZMO1 cell only obtained power density of 37.62 Wkg^{-1} and energy density of 0.19 $Whkg^{-1}$ at 0.3 Ag^{-1}. This is mainly due to symmetrical cell of GW-ZMO1 provide an optimum pore size that allow ion to diffuse easily during charging and discharging that contribute to higher power and energy density.

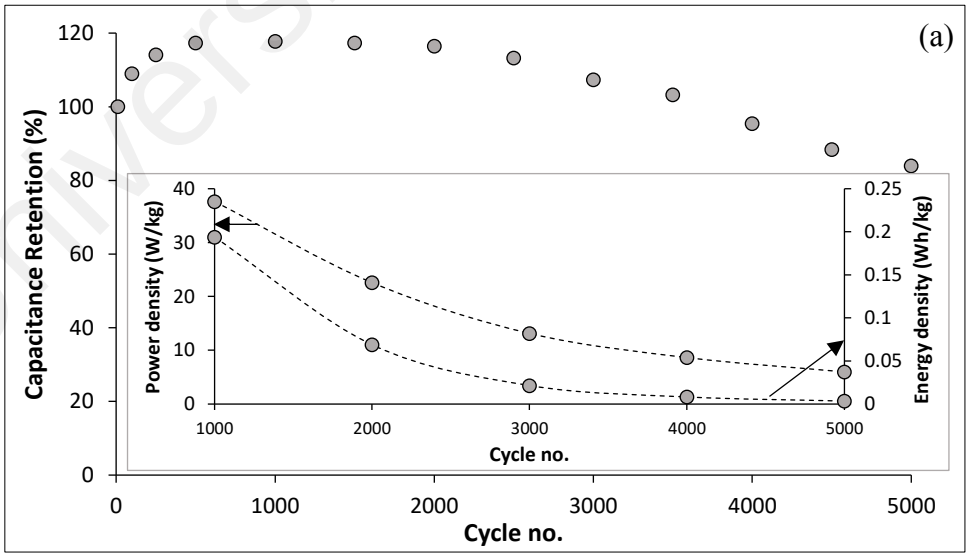

Figure 6.25: Stability test of (a) PP-ZMO1 and (b) GW-ZMO1 at 0.3 Ag^{-1} for 5000 cycles in EDLC

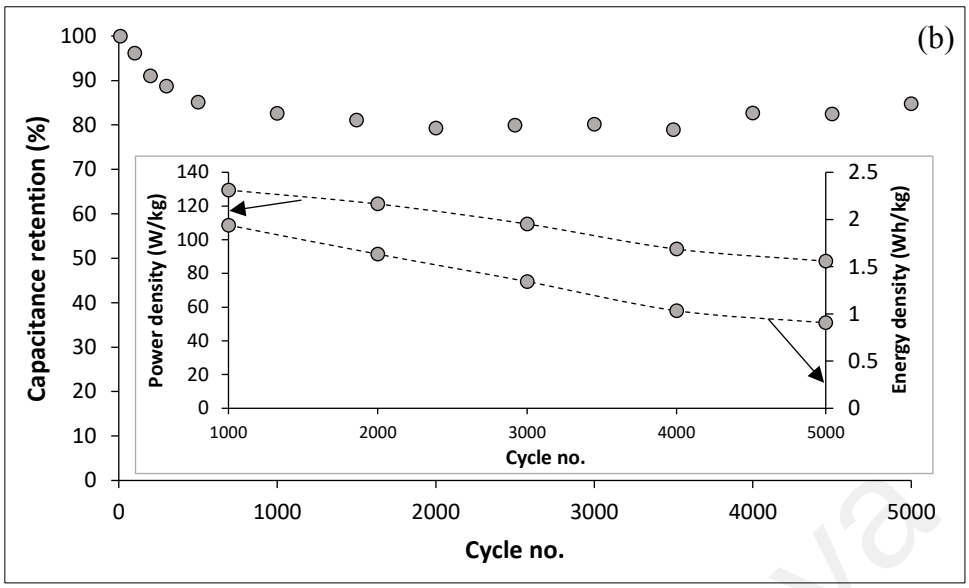

Figure 6.25, continued.

6.3.2.3 Electrochemical impedance spectroscopy

The Nyquist plot of PP-ZMO1 and GW-ZMO1 symmetrical cells are presented in Figure 6.26. Both symmetrical cells of PP-ZMO1 and GW-ZMO1 represent similar semicircle at high frequency region but different pattern of spike at low frequency region. Both cells exhibited about the same bulk resistance that is 1.49 Ω and 1.57 Ω indicating the device has good conductivity with the electrolyte. When looking into the diameter of the semicircle which represent the resistance during charge transfer, it can be seen that PP-ZMO1||PP-ZMO1 cells encountered higher obstacle during charging process which is 5.97 Ω as compared to the device of GW-ZMO1 (1.09 Ω). Additionally, the slope of the inclined line for GW-ZMO1 symmetrical cell was greater than PP-ZMO1 cell indicating rapid diffusion of electrolyte ion into GW-ZMO1 electrode (Wu et al., 2019a). The higher mesopore volume in GW-ZMO1 with the attachment of ZMO have shorten the transport pathway between electrode materials and electrolyte. Table 6.11 tabulates the bulk and charge-transfer resistance of PP-ZMO1 and GW-ZMO1 symmetrical cells.

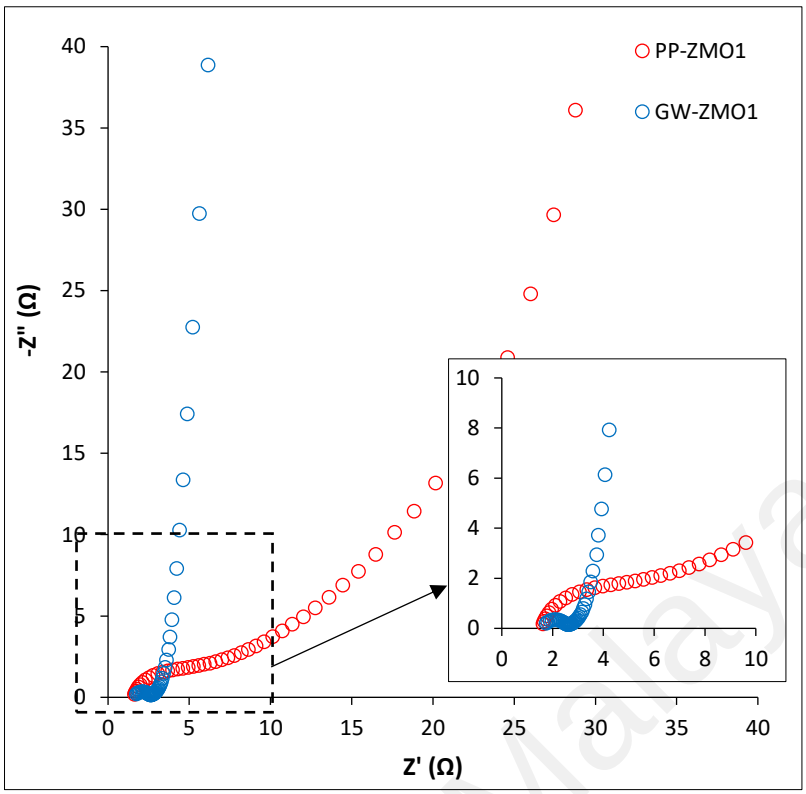

Figure 6.26: Nyquist plot of PP-ZMO1 and GW-ZMO1 in EDLC

Table 6.11: Value of R_s and R_{ct} for PP-ZMO1 and GW-ZMO1 in EDLC.

Sample	R_s (Ω)	R_{ct} (Ω)	$R_s + R_{ct}$ (Ω)
PP-ZMO1	1.49	5.97	7.46
GW-ZMO1	1.57	1.09	2.66

6.4 Summary

- Different ratio of ZMO into porous carbon has caused variety of pore textural properties to PP-ZMO and GW-ZMO series carbon composite.
- PP-ZMO1 and GW-ZMO1 achieved the specific capacitance of 104.89 Fg^{-1} and 122.94 Fg^{-1} at 0.3 Ag^{-1}, respectively.
- The durability of the materials is proportionate to the increment ratio of ZMO.
- Both PP-ZMO1 and GW-ZMO1 devices demonstrated almost similar specific capacitance such as 17.62 Fg^{-1} and 24.67 Fg^{-1} at 0.03 Ag^{-1}, respectively.

- In term of durability, GW-ZMO1 symmetrical cell demonstrated better capacitance retention of 80 % while PP-ZMO1 symmetrical cell showed 65 % at the 900th cycle as compared to the 300th cycle.
- GW-ZMO1||GW-ZMO1 cell showed smaller R_{ct} and vertical line at low frequency region indicating low internal resistance for electrochemical process and rapid diffusion of electrolyte ion into GW-ZMO1 electrode.
- Better capacitive performance in GW-ZMO1||GW-ZMO1 cell can be attributed to the equal ratio of micro-mesopore volume that provide optimum pore size and adequate active sites for energy storage process.

CHAPTER 7: CHARACTERIZATION AND ELECTROCHEMICAL PERFORMANCE OF TERNARY C/ZTO COMPOSITES

7.1 Introduction

In this chapter, the results of zinc tin oxide based ternary carbon composite derived from PP and GW are presented. The ratio for $ZnSnO_3$ was only synthesized up to 27 % of the total composite composition due to the result trend was similar to ZMO based composite. The physical characterization includes the specific surface area, pore size distribution, FESEM images, EDX and TEM image. The behavior of PP-ZTO and GW-ZTO are tested with three electrode system. Symmetrical cell was examined with stability test which performed for 5000 cycles at 0.3 Ag^{-1} while durability performance for 900 cycles was included.

7.2 Physical characterization

7.2.1 Adsorption-desorption isotherm

Figure 7.1 displays the nitrogen adsorption-desorption isotherm of PP-ZTO and GW-ZTO2 series samples.

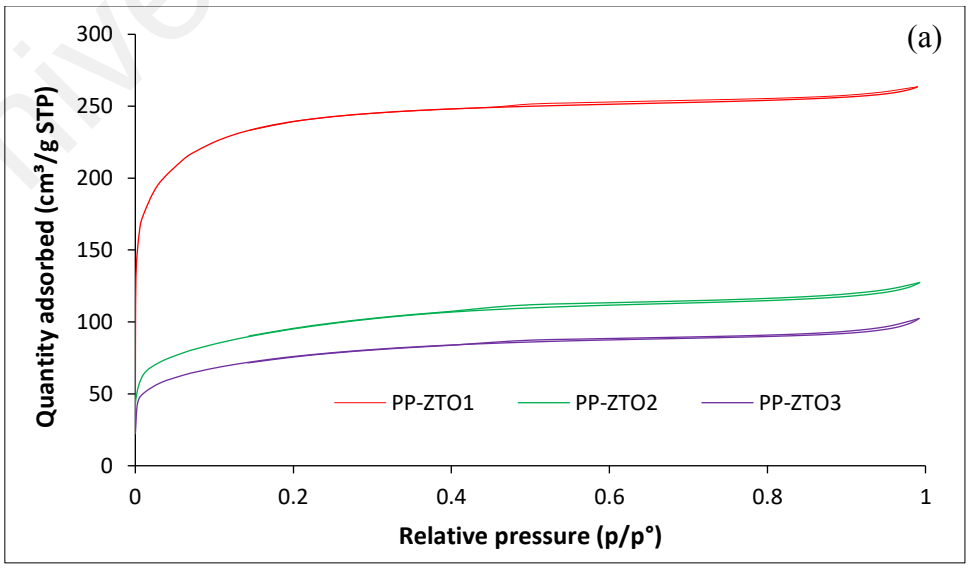

Figure 7.1: Adsorption-desorption isotherm for (a) PP-ZTO1, PP-ZTO2, PP-ZTO3 and (b) GW-ZTO1, GW-ZTO2, GW-ZTO3 samples

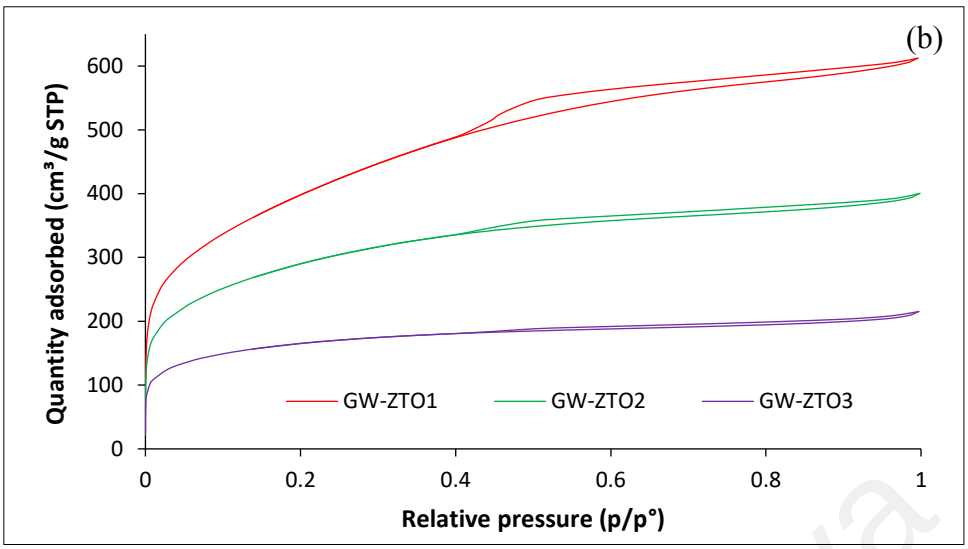

Figure 7.1, continued.

Figure 7.1(a) shows the combination isotherm curves of PP-ZTO1, PP-ZTO2 and PP-ZTO3. All the samples exhibited the pattern combination of Type I and IV according to IUPAC classification. High absorption of N_2 gas at low relative pressure indicated the presence of microporous. A gradual uprising with an inflection point after relative pressure > 0.1 along with hysteresis loop implied mesoporous structure. All hysteresis loop presented the H4 type with slit-shaped pore structure. As expected, higher ratio of ZTO showed reduction in quantity absorption. This phenomenon is mainly due to low micropores content.

Figure 7.1(b) illustrates the N_2 adsorption-desorption curves of GW-ZTO1, GW-ZTO2 and GW-ZTO3. All the curves represented the combination of Type I and Type IV. The initial part of the isotherm curve with significant uptake of N_2 gas is corresponded to the presence of microporous structure (Wei et al., 2019) as it provides higher surface area for gas absorption. An inflection point was observed right after the rapid N_2 gas uptake. This was followed with the hysteresis loop at the intermediate to high relative pressure (0.4 to 1.0 mmHg). The hysteresis loop in all samples indicated the carbon composites were occupied with mesopores structure. In overall, the trend of quantity absorption reduced as the ZTO amount in carbon composite increased.

7.2.2 BJH pore size distribution

Figure 7.2 illustrates the increment pore volume vs pore size distribution curve obtained from BJH theory for a series of sample from PP-ZTO and GW-ZTO.

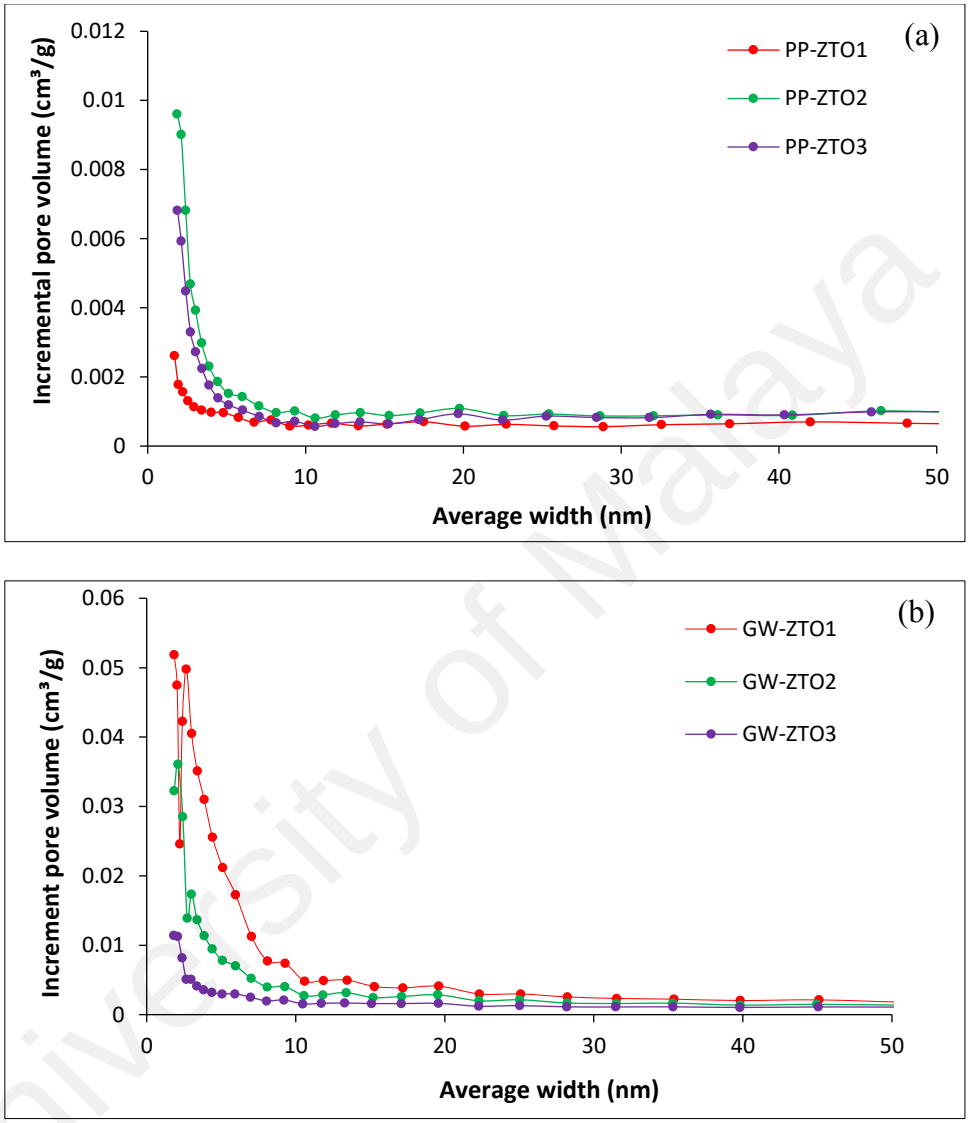

Figure 7.2: BJH pore size distribution for (a) PP-ZTO and (b) GW-ZTO samples with different ratios

From the pore size distribution plot, it can be observed that both PP-ZTO and GW-ZTO series samples consist of micro and mesoporous structure. In PP-ZTO series samples, the highest peak of pore volume which accumulated at ~1.7 nm and gradually reduced up to 5 nm indicating the materials favor to large micropores and moderate mesopores

structure. The existence of flat line in the plot further prove that there are no large mesopores structure in the materials.

GW-ZTO series samples in Figure 7.2(b) presented high density of pore size build up at 1.8 – 3.0 nm. This is followed by a progressive reduction and insignificant peak after 9 nm. On top of increasing weight ratio of ZTO, the trend of pore size distribution for both PP and GW samples remained similar. Table 7.1 and 7.2 have illustrated all the textural properties such as surface area, micropore and mesopore volume, total pore volume and average pore width for PP-ZTO and GW-ZTO based samples.

Table 7.1: Textural properties of PP-ZTO1, PP-ZTO2 and PP-ZTO3.

Sample	BET (m^2g^{-1})	t-plot micropore volume (cm^3g^{-1})	Mesopore volume (cm^3g^{-1})	Total pores volume (cm^3g^{-1})	Average pores width (nm)
PP-ZTO1	896.39	0.26	0.15	0.41	4.97
PP-ZTO2	337.45	0.05	0.15	0.20	3.66
PP-ZTO3	269.15	0.04	0.12	0.16	4.14

Table 7.2: Textural properties of GW-ZTO1, GW-ZTO2 and GW-ZTO3.

Sample	BET (m^2g^{-1})	t-plot micropore volume (cm^3g^{-1})	Mesopore volume (cm^3g^{-1})	Total pores volume (cm^3g^{-1})	Average pores width (nm)
GW-ZTO1	1446.41	0.04	0.91	0.95	3.19
GW-ZTO2	1040.37	0.08	0.54	0.62	3.31
GW-ZTO3	583.31	0.11	0.22	0.33	4.04

Both PP-ZTO and GW-ZTO showed a similar trend of inversely proportionate relationship between specific surface area and weight ratio of ZTO as discussed in subsection 6.2.2. This trend is mainly due to the low loading of carbon materials and

increase of guest materials, ZTO in developing wider mesopores structure. The highest specific surface area was achieved in PP-ZTO1 and GW-ZTO1 such as 896.39 m^2g^{-1} and 1446.41 m^2g^{-1}. The average pore width of PP-ZTO and GW-ZTO series samples also in agreement with the pore size distribution demonstrated in Figure 7.2.

7.2.3 X-ray diffraction

Figure 7.3 displays the XRD pattern of PP-ZTO and GW-ZTO series samples.

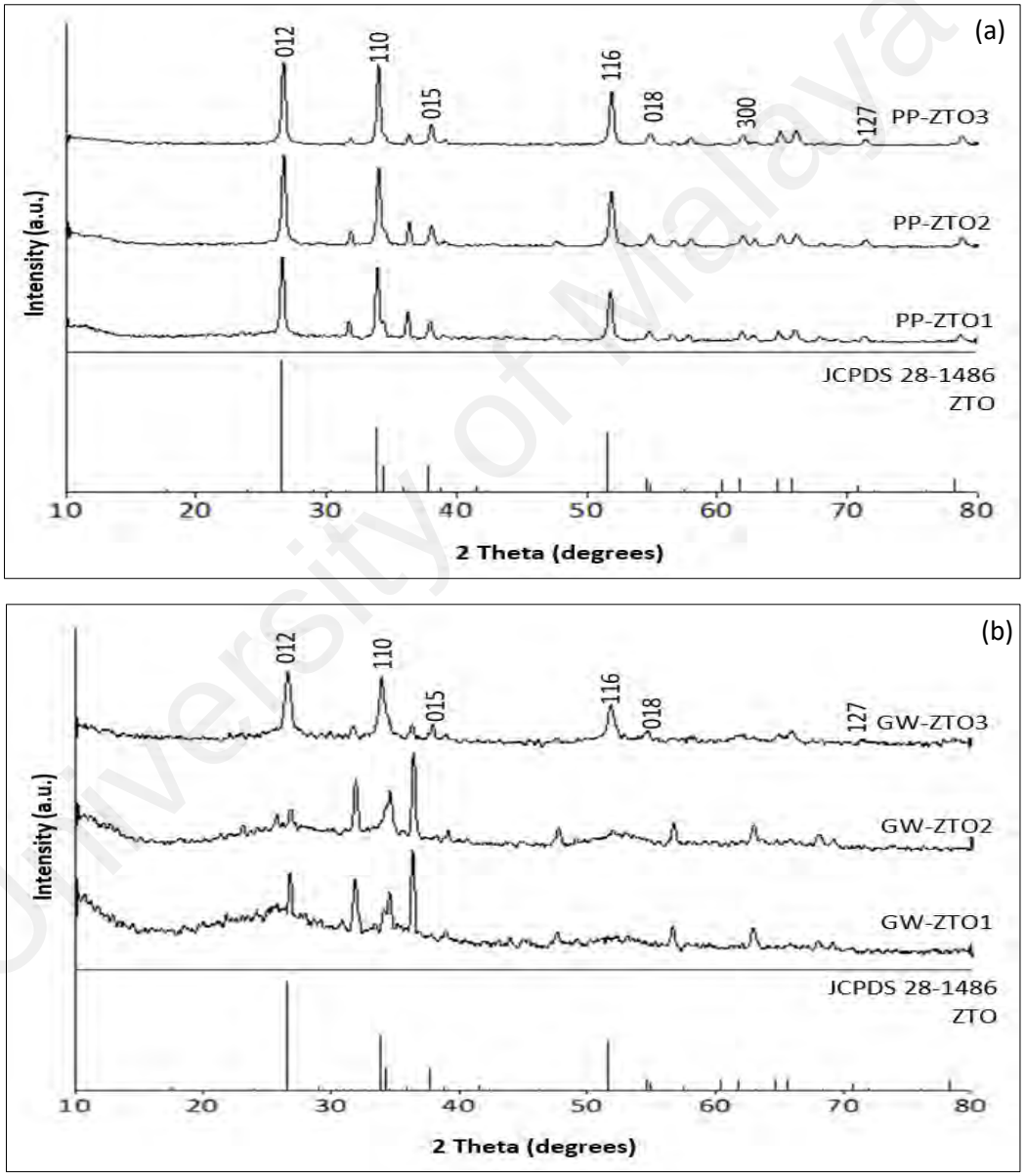

Figure 7.3: X-ray diffraction pattern of (a) PP-ZTO and (b) GW-ZTO series samples

Generally, the characteristic of amorphous graphitic carbon denoted by the broad diffraction peaks at around 2θ = 24º can be observed at lower weight ratio of ZTO.

However, the amorphous peak was suppressed by the crystalline structure when the weight ratio of ZTO increased. In PP-ZTO series samples, it is obvious that the peaks agreed well with the reported orthorhombic ZTO structure (Wang et al., 2014). Due to the similarity of peak position for ZTO and ZnO in 25º to 40º range, GW-ZTO1 and GW-ZTO2 exhibited several peaks overlapped with ZnO pattern. Though, the peaks located at 26.6º and 34.0º corresponded to ZTO pattern. Additionally, a small hump at ~ 52º indicating the formation of ZTO. The peaks at 26.6º, 34.0º, 38.0º, 51.8º, 54.9º, 62.0º and 71.3º can be indexed to ZTO (JCPDS file no. 28-1486) which is corresponding to the plane (012), (110), (015), (116), (018), (300) and (127) respectively (Chen et al., 2012; Siddiqui et al., 2017).

7.2.4 Field emission scanning electron microscopy & energy dispersive x-ray analysis

Figure 7.4 and 7.5 show the morphology and elemental analysis of PP-ZTO1, PP-ZTO2 and PP-ZTO3. Based on the FESEM images, it is noticeable that PP-ZTO1 possessed numerous small pores distributed uniformly. Upon increasing weight ratio of ZTO, the pores are enlarged while porosity reduced. The reduction of porosity is mainly due to the low loading of carbon content which is also one of the reasons in low specific surface area.

Additionally, all the FESEM images illustrated white spots with the density corresponding to the weight ratio of ZTO. These white spots can be designated as ZTO element. It is clearly seen that ZTO was attached on the carbon surface and partly block the porosity. This further explained the declining specific surface area and total pore volume tabulated in Table 7.1.

EDX was conducted to examine the element of PP-ZTO series samples as illustrated in Figure 7.5. From the spectrum, the element of C, O, Zn and Sn were detected further

confirm the existence of ZTO in the ternary carbon composite. The EDX results has demonstrated good agreement with the XRD pattern in Figure 7.3(a).

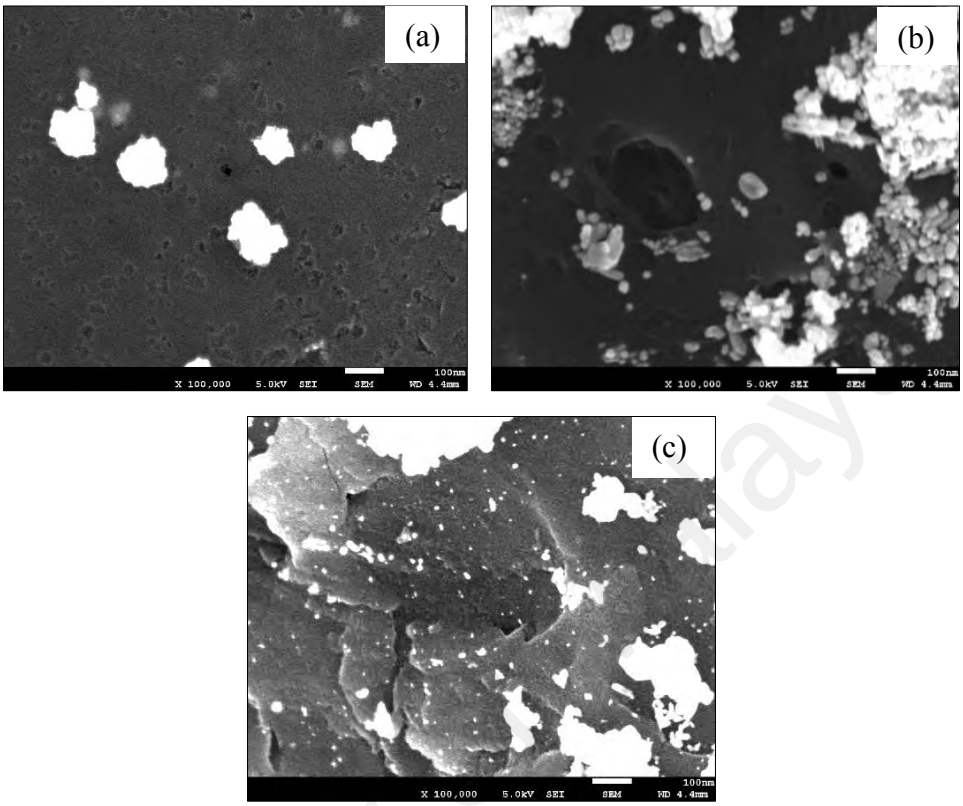

Figure 7.4: FESEM images at magnification of 100K for (a) PP-ZTO1, (b) PP-ZTO2 and (c) PP-ZTO3

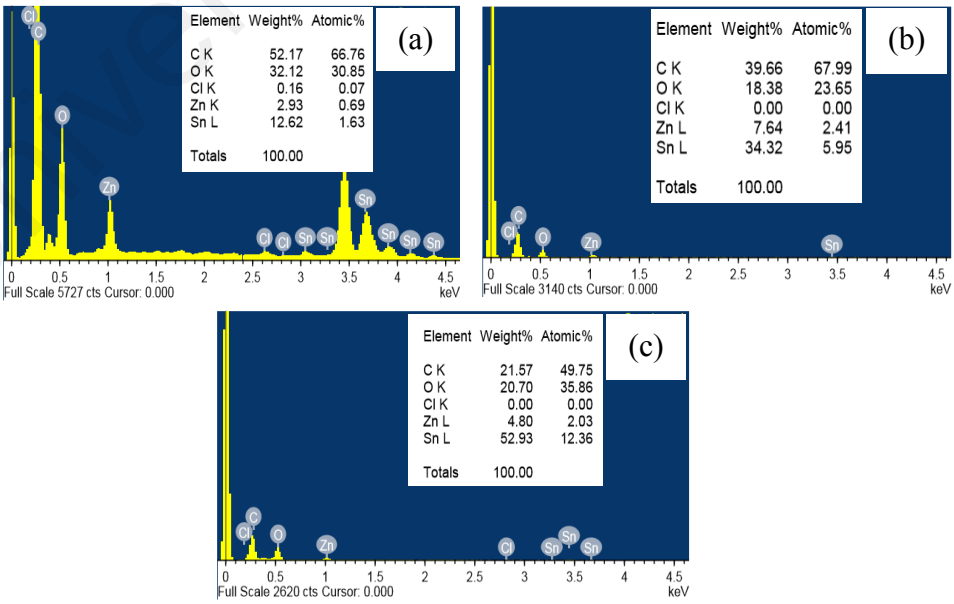

Figure 7.5: EDX of (a) PP-ZTO1, (b) PP-ZTO2 and (c) PP-ZTO3

Figure 7.6 presents the morphology of GW-ZTO1, GW-ZTO2 and GW-ZTO3. Similar with the PP-ZTO series samples, GW-ZTO1 exhibited higher porosity with irregular pore shape well-distributed. The mesopores were widen as the weight ratio of ZTO increased. Besides that, the white spots which is attributed to ZTO elements can be observed. The density trend exactly alike as demonstrated in this study. The direct attachment on the carbon surface and above or inside the pores has led to lower specific surface area.

Figure 7.7 displays the EDX spectrum of GW-ZTO series samples. It is obvious that element of C, O, Zn and Sn were spotted indicating the formation of C/ZTO composite. This result further verifies the XRD spectrum in Figure 7.3(b) which ZTO is successfully synthesized on the carbon material.

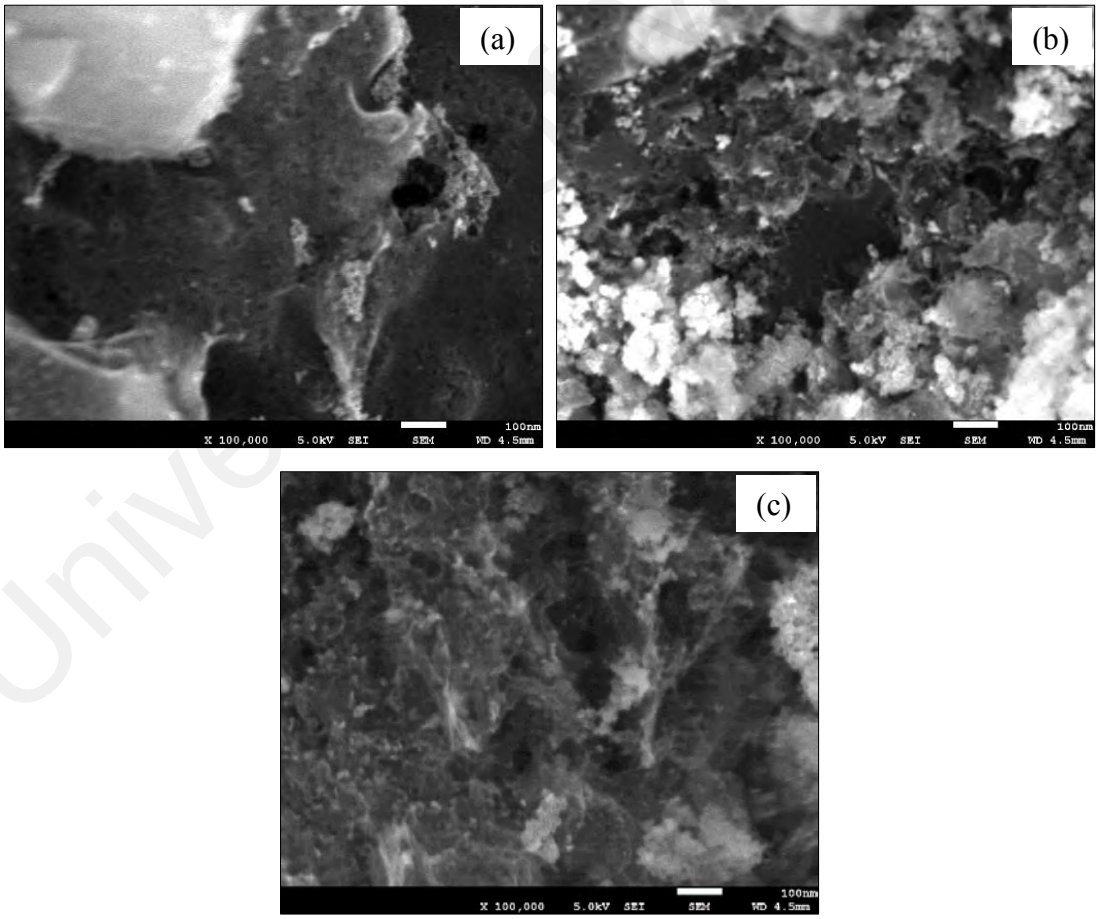

Figure 7.6: FESEM images at magnification of 100K for (a) GW-ZTO1, (b) GW-ZTO2 and (c) GW-ZTO3

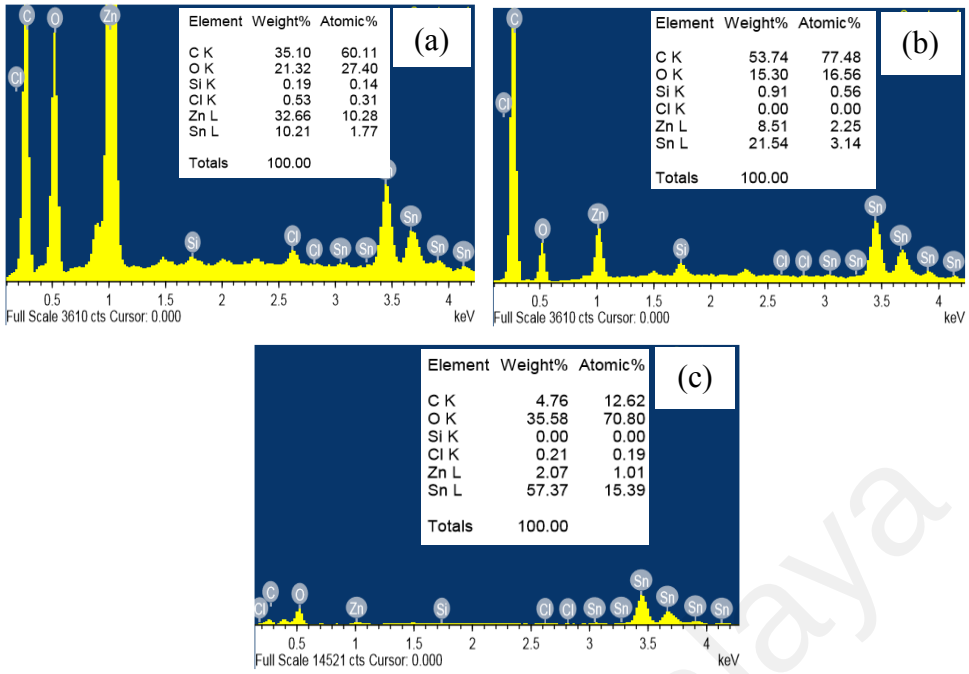

Figure 7.7: EDX of (a) GW-ZTO1, (b) GW-ZTO2 and (c) GW-ZTO3

7.2.5 Transmission electron microscopy

Figure 7.8 and 7.9 illustrate the images of TEM and HRTEM of PP-ZTO1 and GW-ZTO1 respectively. As presented in Figure 7.8(a) and 7.9(a), cubical shape of ZTO is successfully adhered to the amorphous carbon material. HRTEM further displayed the crystallinity and cubic shape of ZTO. In Figure 7.8(b), the lattice distance of 0.31 nm is corresponded to the (220) plane (Mayedwa et al., 2018). On the other hand, the HRTEM of GW-ZTO1 in Figure 7.9(b) shows the lattice spacing of 0.33 nm and 0.37 nm that is in good agreement to the crystal plane of (012) (Liang et al., 2014).

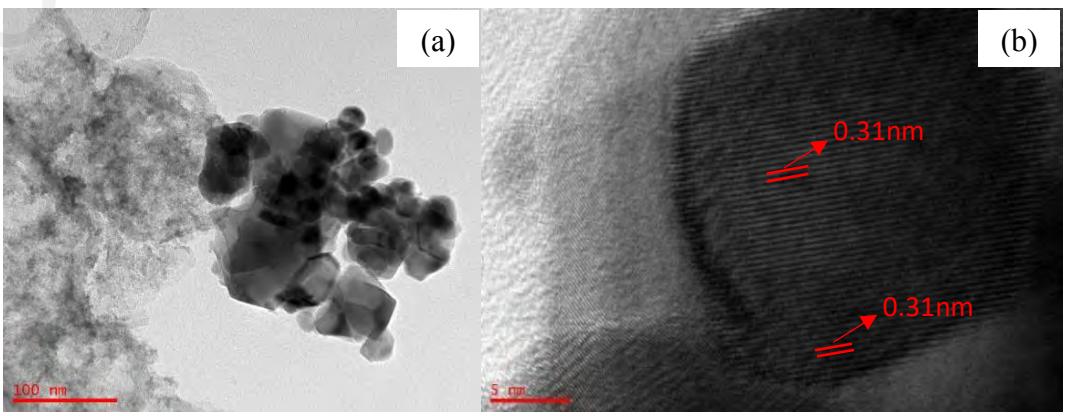

Figure 7.8: Images of (a) TEM and (b) HRTEM lattice fringe image of PP-ZTO1

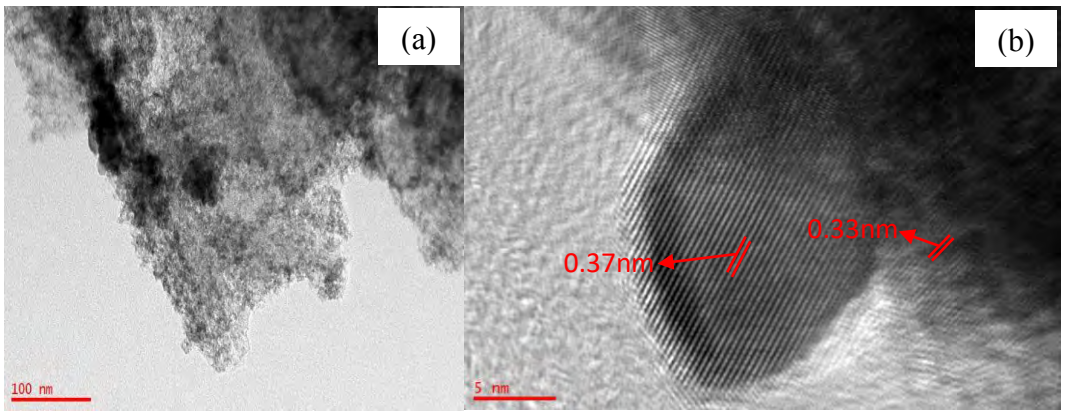

Figure 7.9: Images of (a) TEM and (b) HRTEM lattice fringe image of GW-ZTO1

7.3 Electrochemical performance

The electrochemical performance of all samples with different ratio for PP-ZTO and GW-ZTO was first tested with three-electrode system to analyze its behavior. Durability test was then carried out to select the optimum sample among the PP-ZTO and GW-ZTO series to be utilized for symmetrical cell fabrication. Thus, in this section will inclusive of electrochemical performance for both three-electrode system and symmetrical cell.

7.3.1 Three-electrode system

7.3.1.1 Cyclic voltammetry

Figure 7.10 displays the CV curves of various scan rates at the potential range from 0 to -1.0 V for PP-ZTO1, PP-ZTO2 and PP-ZTO3. As seen from the CV curves of all samples, a nearly rectangular shape was obtained at up to scan rate 50 mVs^{-1} indicating electrode materials has good intrinsic conductivity (Wei et al., 2019). Slight deviation from rectangular shape of CV curve is observed at 100 mVs^{-1} is mainly due to higher diffusion resistance and rapid ion transfer (Rajagopal & Ryu, 2019). The flat line in PP-ZTO2 is attributed to instrument limitation at high current measurement. Additionally, upon increasing of ZTO weight ratio, the rectangular shape is retained at 100 mVs^{-1}. This also explained the assistance of ZTO in improving the electrochemical performance of the electrode material. The highest specific capacitance calculated was obtained at the

scan rate of 3 mVs^{-1} as sufficient time are given during the ion diffusion. Among the samples, PP-ZTO1 delivered the highest specific capacitance such as 85.21 Fg^{-1}. Table 7.3 shows the specific capacitance of PP-ZTO1, PP-ZTO2 and PP-ZTO3 in all scan rates.

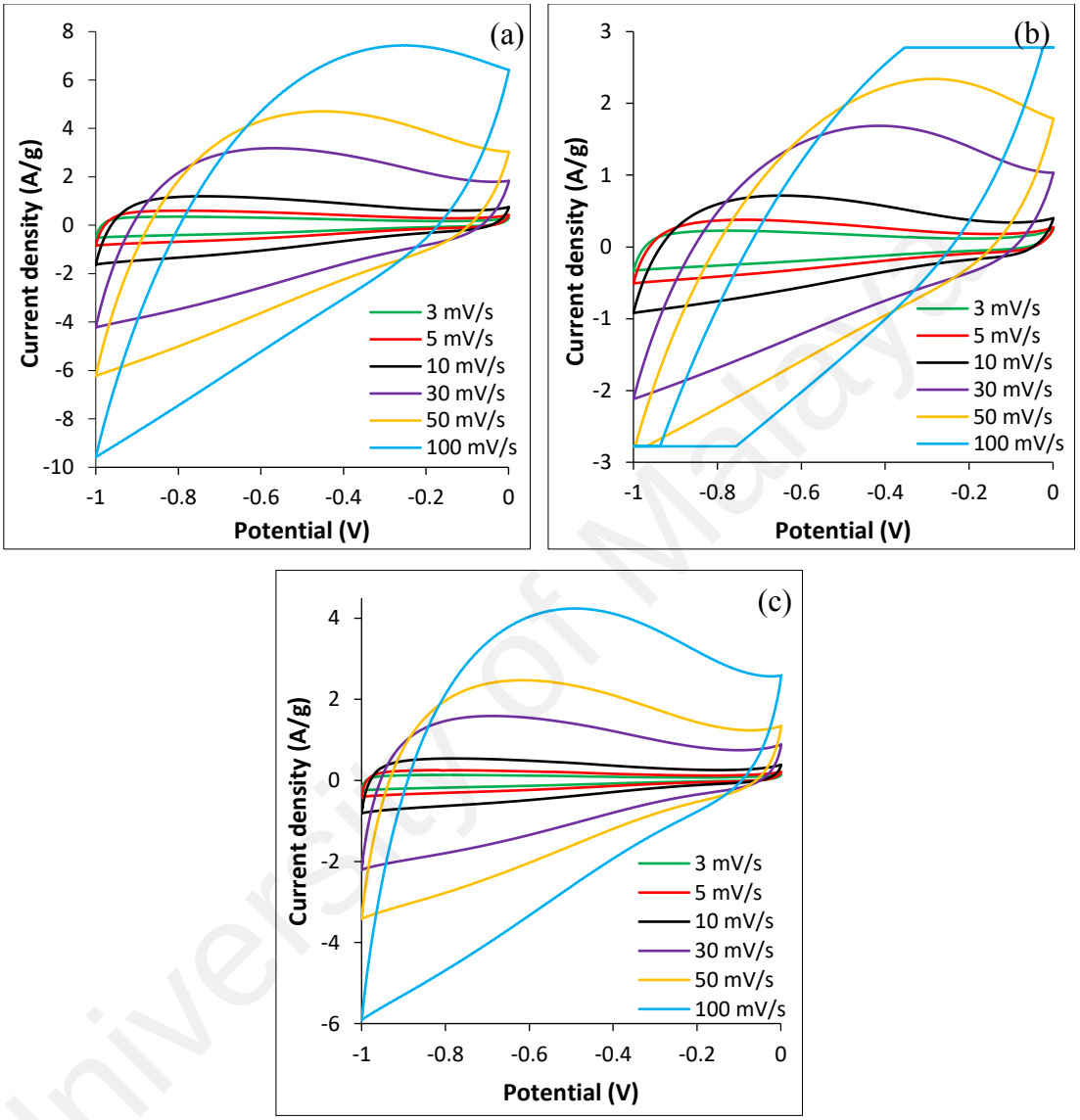

Figure 7.10: Cyclic voltammetry of (a) PP-ZTO1, (b) PP-ZTO2 and (c) PP-ZTO3 with various scan rates

Table 7.3: Specific capacitance of PP-ZTO series samples at various scan rates.

Sample	Specific capacitance (Fg^{-1})					
	3 mVs^{-1}	**5 mVs^{-1}**	**10 mVs^{-1}**	**30 mVs^{-1}**	**50 mVs^{-1}**	**100 mVs^{-1}**
PP-ZTO1	85.21	85.86	84.33	71.54	61.59	46.06
PP-ZTO2	54.24	51.47	46.79	34.62	27.74	17.66
PP-ZTO3	35.96	37.42	38.60	36.19	33.26	27.86

The CV curves of different scan rates (3 mVs^{-1}, 5 mVs^{-1}, 10 mVs^{-1}, 30 mVs^{-1}, 50 mVs^{-1} and 100 mVs^{-1}) for GW-ZTO1, GW-ZTO2 and GW-ZTO3 are illustrated in Figure 7.11. The shape and trend of the CV curves are of similar with PP-ZTO series samples. Distortion of the CV curve can be observed at high scan rates i.e. 30 mVs^{-1} to 100 mVs^{-1} resulting from diffusion resistance (Rajagopal & Ryu, 2019). However, this phenomenon is enhanced in GW-ZTO2 and GW-ZTO3 implying ZTO has improved the conductivity and rate capability of electrode materials in providing shorter diffusion pathway. As predicted, the highest specific capacitance was obtained in GW-ZTO1 with 90.99 Fg^{-1} at 3 mVs^{-1}. Table 7.4 tabulates the specific capacitance of different scan rates for GW-ZTO1, GW-ZTO2 and GW-ZTO3.

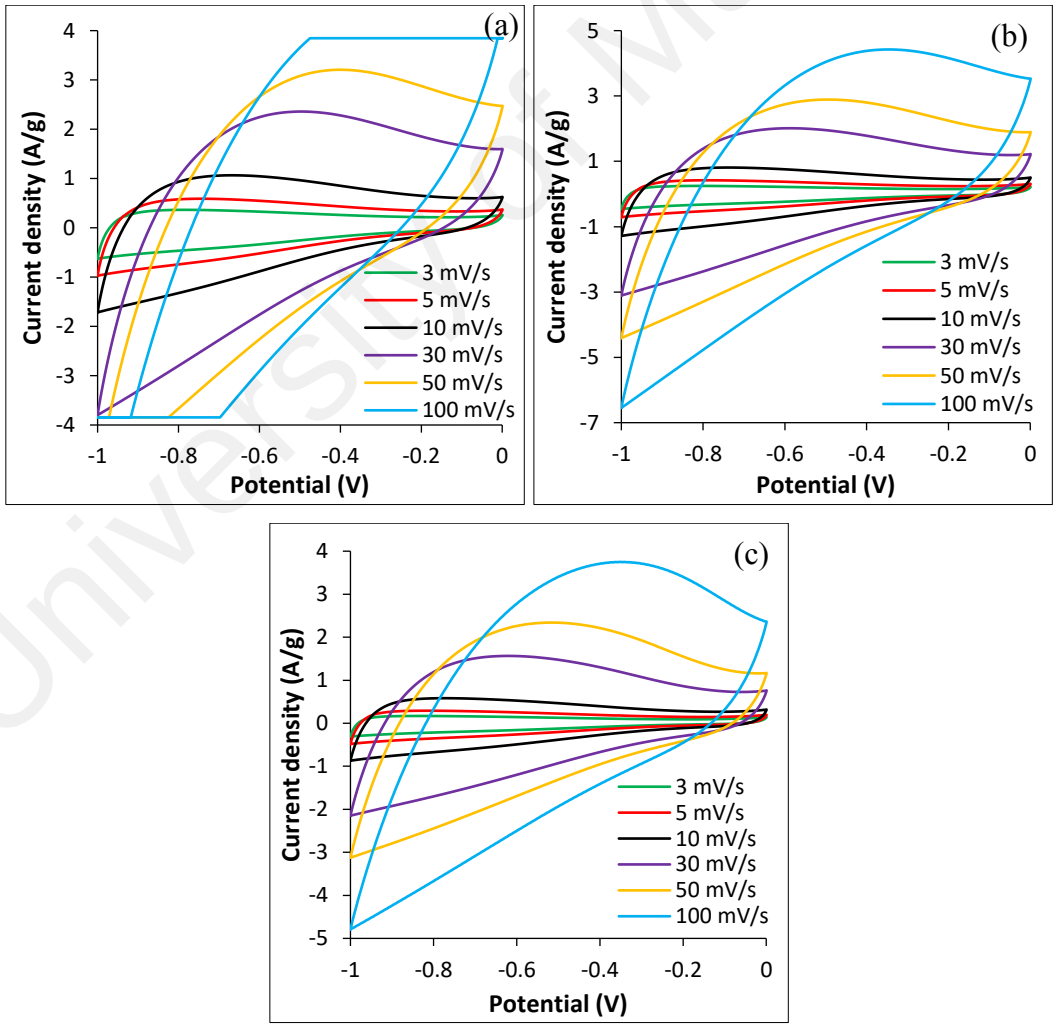

Figure 7.11: Cyclic voltammetry of (a) GW-ZTO1, (b) GW-ZTO2 and (c) GW-ZTO3 with various scan rates

Table 7.4: Specific capacitance of GW-ZTO series samples at various scan rates.

Sample	Specific capacitance (Fg^{-1})					
	3 mVs^{-1}	5 mVs^{-1}	10 mVs^{-1}	30 mVs^{-1}	50 mVs^{-1}	100 mVs^{-1}
GW-ZTO1	90.99	85.40	74.59	52.46	39.48	23.98
GW-ZTO2	64.47	62.03	57.29	45.19	37.89	27.88
GW-ZTO3	42.93	42.04	39.79	33.22	28.66	21.76

7.3.1.2 Galvanostatic charge-discharge

Different current densities of PP-ZTO series samples measurement performed at the potential range of 0 to -1.0 V are depicted in Figure 7.12. Based on the GCD curves, slight linear variation during charging and deviation from ideal triangular shape at discharging part representing the pseudocapacitive nature during ion diffusion at the interface of the electrode/electrolyte (Senthilkumar et al., 2019). Additionally, the almost similar charging and discharging time of various current densities indicating reversibility of the electrode materials. The calculated specific capacitance from GCD curves of different current densities is tabulated in Table 7.5. The highest specific capacitance was obtained in PP-ZTO1 (93.99 Fg^{-1}) followed by PP-ZTO2 (60.85 Fg^{-1}) and PP-ZTO3 (45.94 Fg^{-1}) attributed to the specific surface area provided as active site for ion adsorption and diffusion.

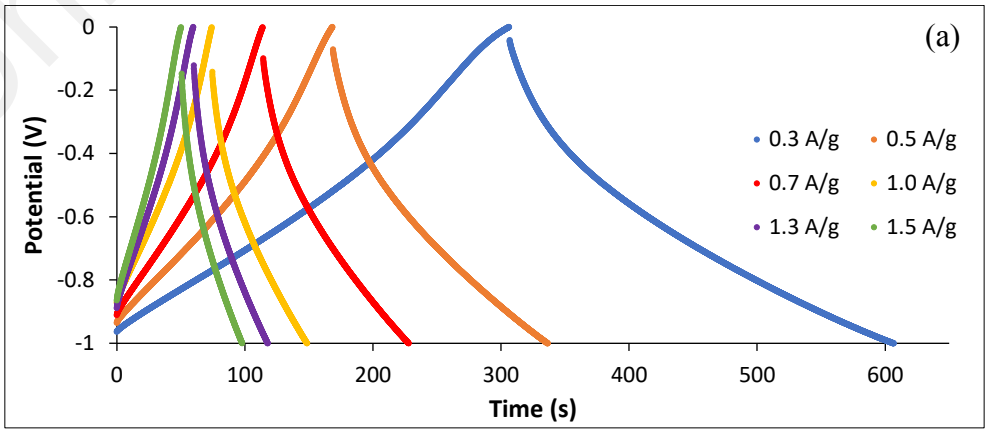

Figure 7.12: Galvanostatic charge-discharge curve of (a) PP-ZTO1, (b) PP-ZTO2 and (c) PP-ZTO3 with various current densities

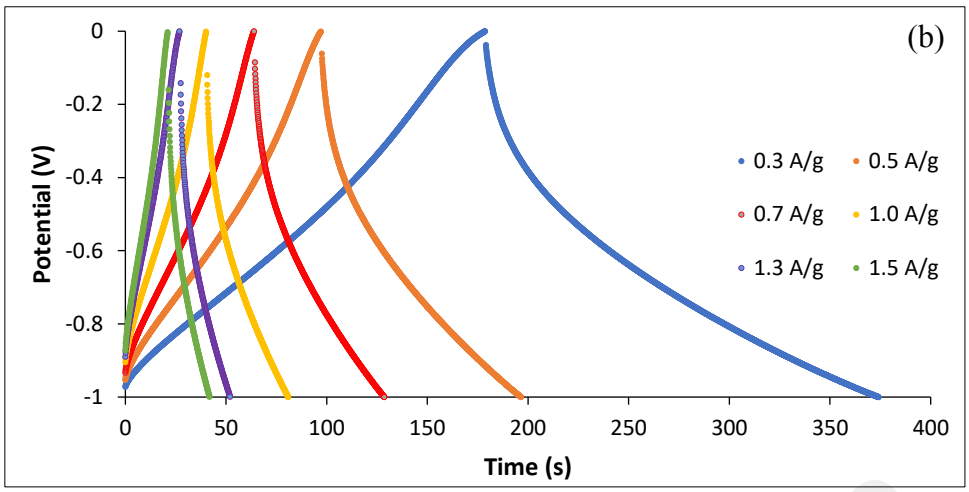

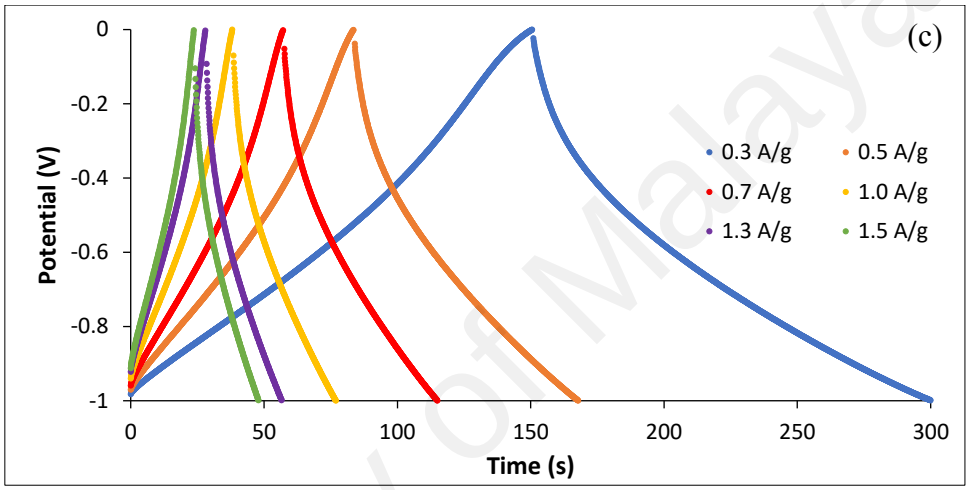

Figure 7.12, continued.

Table 7.5: Specific capacitance of PP-ZTO series samples at various current densities.

Sample	Specific capacitance (Fg^{-1})					
	0.3 Ag^{-1}	**0.5 Ag^{-1}**	**0.7 Ag^{-1}**	**1.0 Ag^{-1}**	**1.3 Ag^{-1}**	**1.5 Ag^{-1}**
PP-ZTO1	93.99	90.39	88.43	86.41	85.70	83.46
PP-ZTO2	60.85	52.78	49.34	46.05	37.62	36.66
PP-ZTO3	45.94	43.68	42.54	41.40	40.57	40.07

For the durability test as illustrated in Figure 7.13, different current densities were conducted for every 1000 cycles and run for 5000 cycles. This test allows both rate capability and stability to be examined concurrently. All the samples exhibited stable cycling response within the individual current density. In PP-ZTO series, the materials demonstrated good capacitance retention. As shown that PP-ZTO1 recorded a capacitance

retention of 85.06 % at the last cycle associated with the initial cycle while PP-ZTO2 and PP-ZTO3 were 82.98 % and 86.22 %.

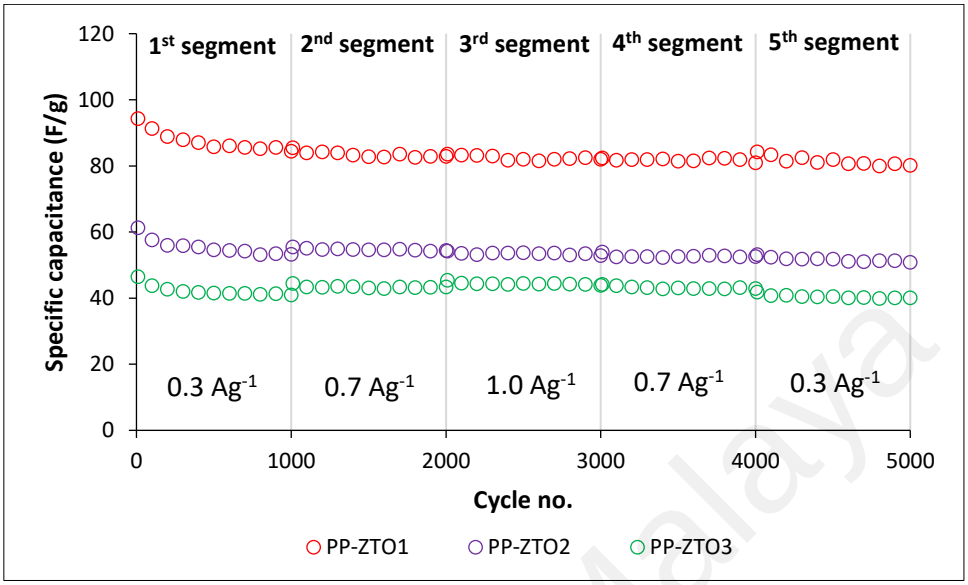

Figure 7.13: Durability performance of PP-ZTO series at different current densities for 5000 cycles

Figure 7.14 and 7.15 have further demonstrated the detail specific capacitance retention of across different current densities and within similar current density accordingly.

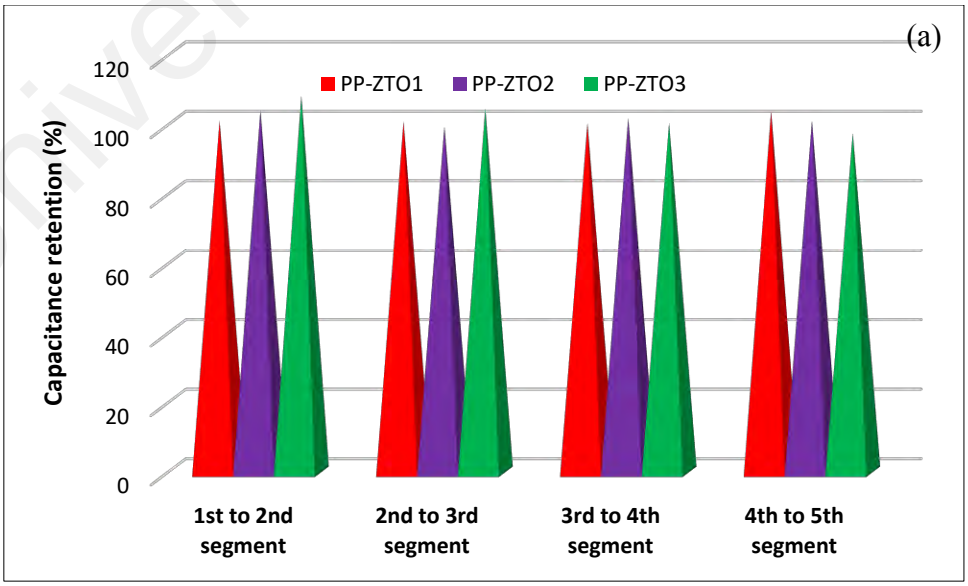

Figure 7.14: Rate capability of PP-ZTO series from one to another segment across 5000 cycles

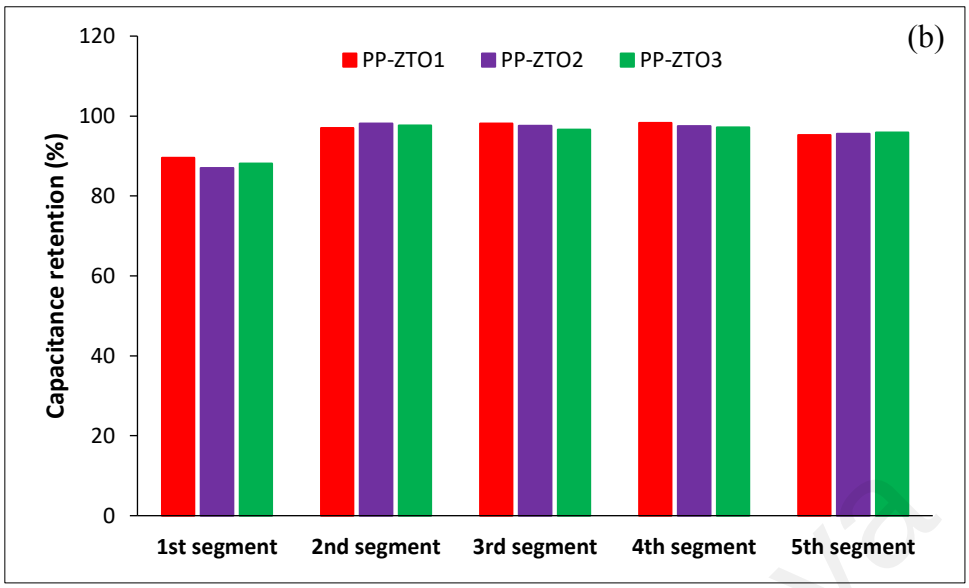

Figure 7.15: Stability of PP-ZTO series at each segment across 5000 cycles

Looking into the rate capability of each segment, the capacitance retention across different current densities for PP-ZTO1, PP-ZTO2 and PP-ZTO3 is presented in Figure 7.14. It is obvious that in term of rate capability, all the PP-ZTO series samples exhibited outstanding performance whereby capacitance retention of above 100 % was achieved for every adjustment of current density. Undeniably that ZTO has helped in developing a more durable materials for supercapacitor application. As in stability performance, Figure 7.15 has clearly shown that all the samples are performing steadily at each segment whereby a minimum of 87 % of capacitance retention are obtained at the 1st segment while other segments show more than 95 %.

Figure 7.16 shows the GCD curves of GW-ZTO series at different current densities (0.3 Ag^{-1}, 0.5 Ag^{-1}, 0.7 Ag^{-1}, 1.0 Ag^{-1}, 1.3 Ag^{-1} and 1.5 Ag^{-1}). As expected, the GCD curves demonstrated similar shape as presented in PP-ZTO series. All the curves exhibited an obvious deviation from isosceles triangle such as slight convex and concave during the charging and discharging respectively. This indicating the electrochemical pseudo-characteristic happened when ion diffusion is triggered. However, the shape of triangle still can be observed implying the materials behaved electrochemical reversibility.

Based on the GCD curves, the specific capacitance is calculated with the highest value achieved by GW-ZTO1 i.e. 104.02 Fg^{-1} followed by 73.65 Fg^{-1} and 47.50 Fg^{-1} from GW-ZTO2 and GW-ZTO3 at the current density of 0.3 Ag^{-1}. Table 7.6 tabulates the specific capacitance of all measured current densities for GW-ZTO series.

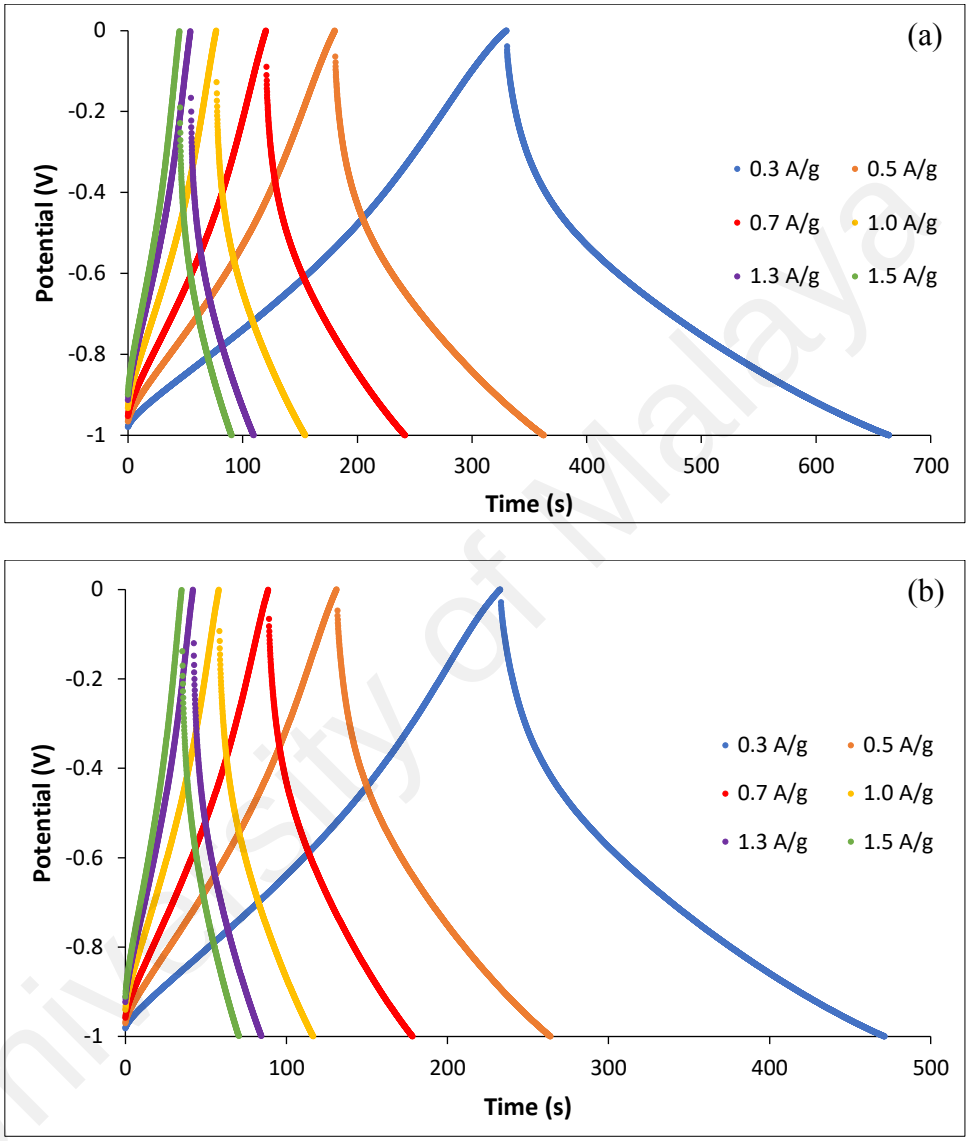

Figure 7.16: Galvanostatic charge-discharge curve of (a) GW-ZTO1, (b) GW-ZTO2, and (c) GW-ZTO3 with various current densities

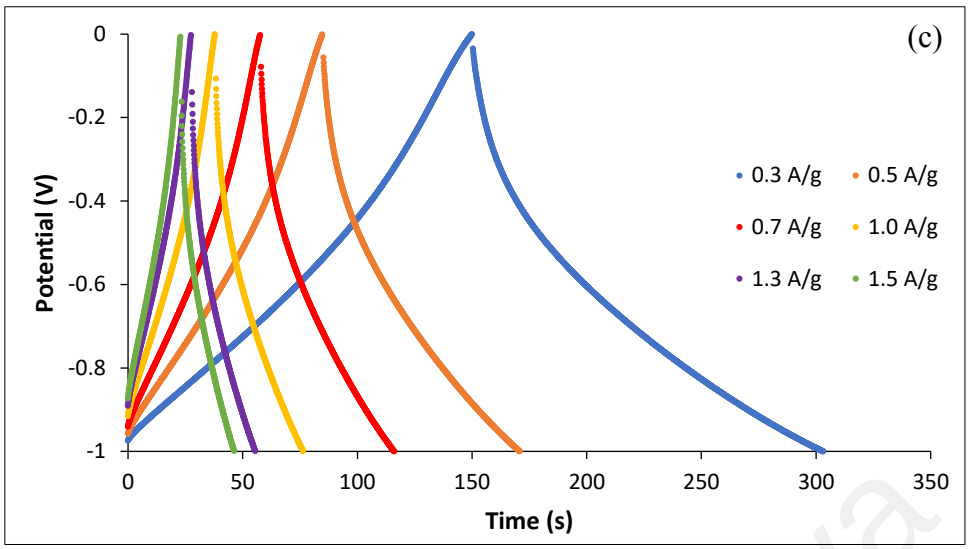

Figure 7.16, continued.

Table 7.6: Specific capacitance of GW-ZTO series samples at various current densities.

Sample	Specific capacitance (Fg^{-1})					
	0.3 Ag^{-1}	**0.5 Ag^{-1}**	**0.7 Ag^{-1}**	**1.0 Ag^{-1}**	**1.3 Ag^{-1}**	**1.5 Ag^{-1}**
GW-ZTO1	104.02	97.15	93.07	88.64	85.45	83.57
GW-ZTO2	73.65	69.56	67.04	64.42	62.43	61.37
GW-ZTO3	47.50	45.45	44.20	42.81	41.87	41.39

To further evaluate the durability of the GW-ZTO series materials, 5000 cycles with different current densities were conducted as shown in Figure 7.17.

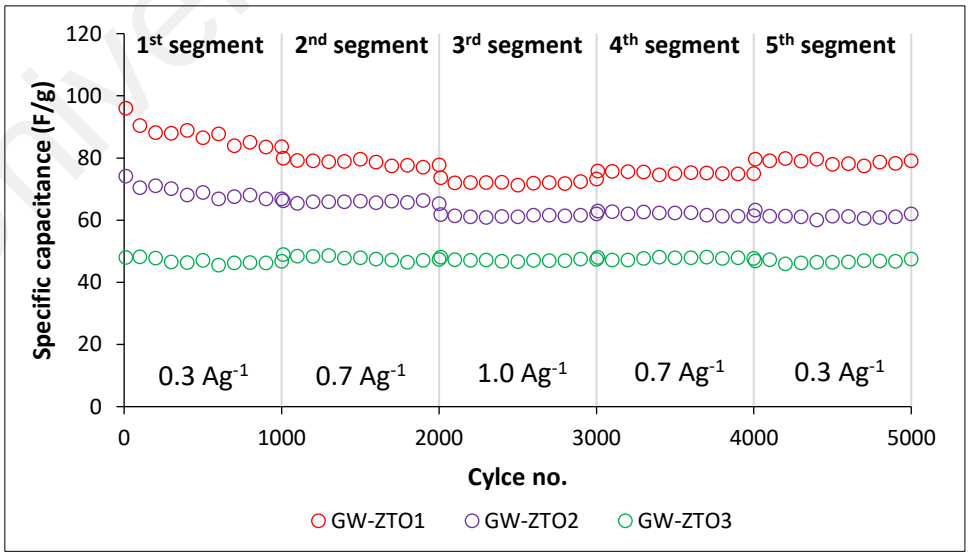

Figure 7.17: Durability performance of GW-ZTO series at different current densities for 5000 cycles

As presented in Figure 7.17, it is noticed that GW-ZTO1 experienced a slight reduction during the initial segment which might be due to very less micropore volume (0.04 cm^3g^{-1}) and low loading of ZTO ratio. However, the rate capability and stability are recovered once approaching 2nd segment. In overall, GW-ZTO1 has retained 82.44 % of the capacitance at the 5000th cycle as compared with the initial cycle. Upon increasing of the ZTO ratio, the capacitance retention is enhanced which 83.56 % and 98.98 % of the capacitance is maintained at the last cycle in GW-ZTO2 and GW-ZTO3 respectively. This result has further proved that ZTO has enhanced the electrochemical performance for long cycling and varies current densities test.

In Figure 7.18, the rate capability is further evaluated by calculating the capacitance retention when adjustment of current densities across different segments. As presented, all the GW-ZTO series achieved an outstanding capacitance retention whereby all the samples exhibited more than 96 % indicating good robustness in the samples. Additionally, the stability also included in this durability test as shown in Figure 7.19 that every samples reaching 100 % in every segment except for the first segment which has been explained earlier. Though, we can observe that the stability is improved as the ZTO ratio increased.

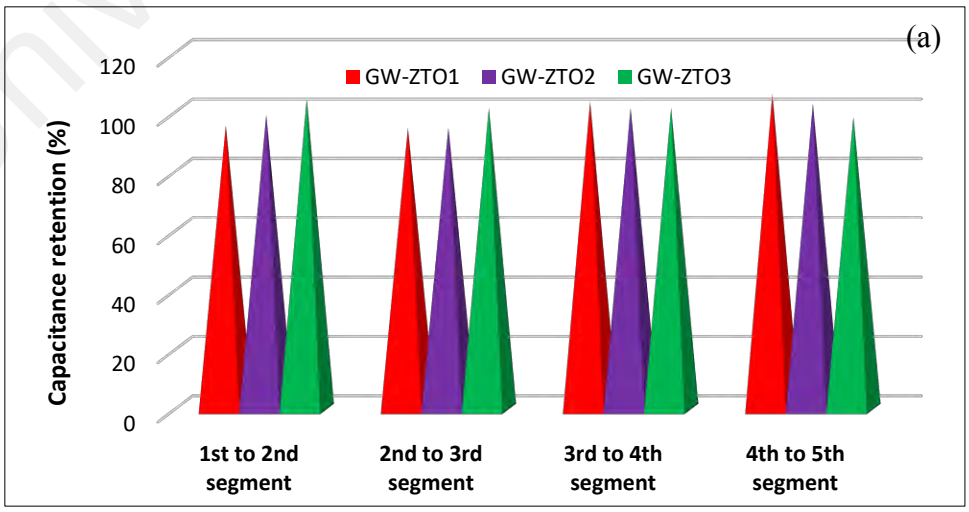

Figure 7.18: Rate capability of GW-ZTO series from one to another segment across 5000 cycles

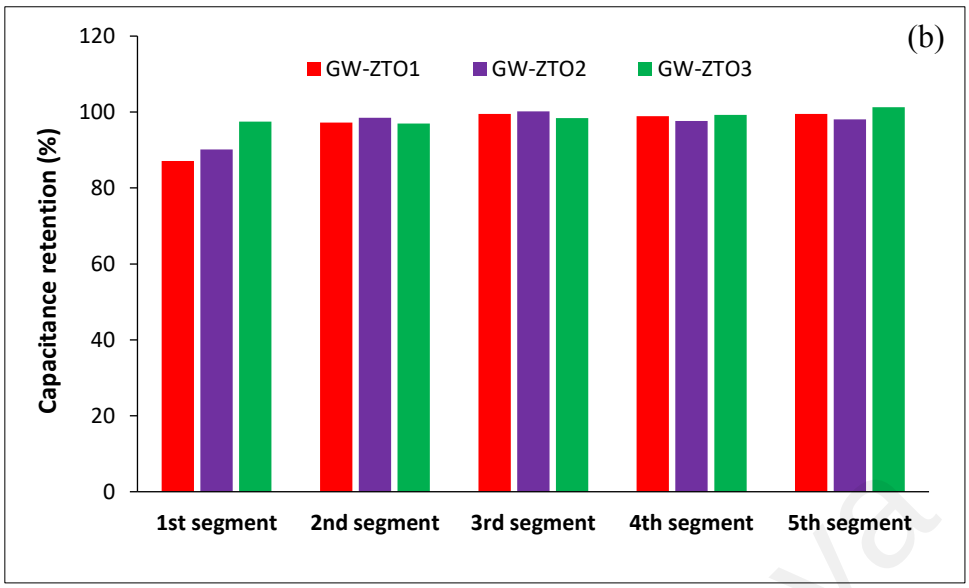

Figure 7.19: Stability of GW-ZTO series at each segment across 5000 cycles

7.3.1.3 Electrochemical impedance spectroscopy

The EIS assessment was conducted to determine the resistance of the samples to further understand the electrochemical performance of the materials. Figure 7.20 shows the detail insight of bulk and charge-transfer resistance. All the samples recorded the EIS spectra with small semicircle at high frequency region and 45º spike at low frequency region. The PP-ZTO series exhibited almost similar R_s and R_{ct} value owing to their pore size distribution which accumulated ~1.7 nm. Therefore, the different specific capacitance values in PP-ZTO series can be explained by the specific surface area provided while durability by the ratio of ZTO. Table 7.7 presents the value of R_s and R_{ct} for PP-ZTO1, PP-ZTO2 and PP-ZTO3.

Table 7.7: Value of R_s and R_{ct} of PP-ZTO series.

Sample	R_s (Ω)	R_{ct} (Ω)	$R_s + R_{ct}$ (Ω)
PP-ZTO1	0.44	0.18	0.63
PP-ZTO2	0.52	0.25	0.77
PP-ZTO3	0.54	0.21	0.75

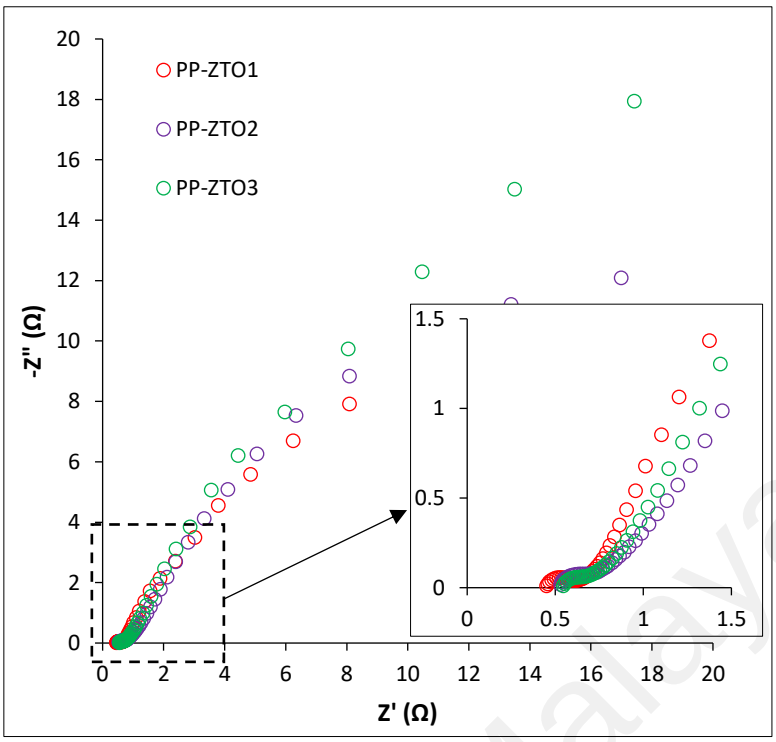

Figure 7.20: Nyquist plot of PP-ZTO series samples with inset in high frequency range

The Nyquist plot depicted in Figure 7.21 represents the EIS spectra of GW-ZTO series. Typical semicircle at high frequency region indicating the capacitive element followed by 45º slope due to Warburg element can be noticed. As can be seen, the trend of GW-ZTO series was unlike PP-ZTO series that GW-ZTO1 showed higher R_{ct} value such as 1.09 Ω as compared to GW-ZTO2 (0.43 Ω) and GW-ZTO3 (0.48 Ω). This is could be attributed to the imbalance ratio of micropore:mesopore volume in GW-ZTO1 which is 1:23 while GW-ZTO2 and GW-ZTO3 demonstrated a better ratio i.e. 1:7 and 1:2 respectively. Table 7.8 displays the detail values for R_s and R_{ct} of GW-ZTO series.

Table 7.8: Value of R_s and R_{ct} of GW-ZTO series.

Sample	R_s (Ω)	R_{ct} (Ω)	$R_s + R_{ct}$ (Ω)
GW-ZTO1	0.86	1.09	1.95
GW-ZTO2	0.80	0.43	1.23
GW-ZTO3	1.47	0.48	1.95

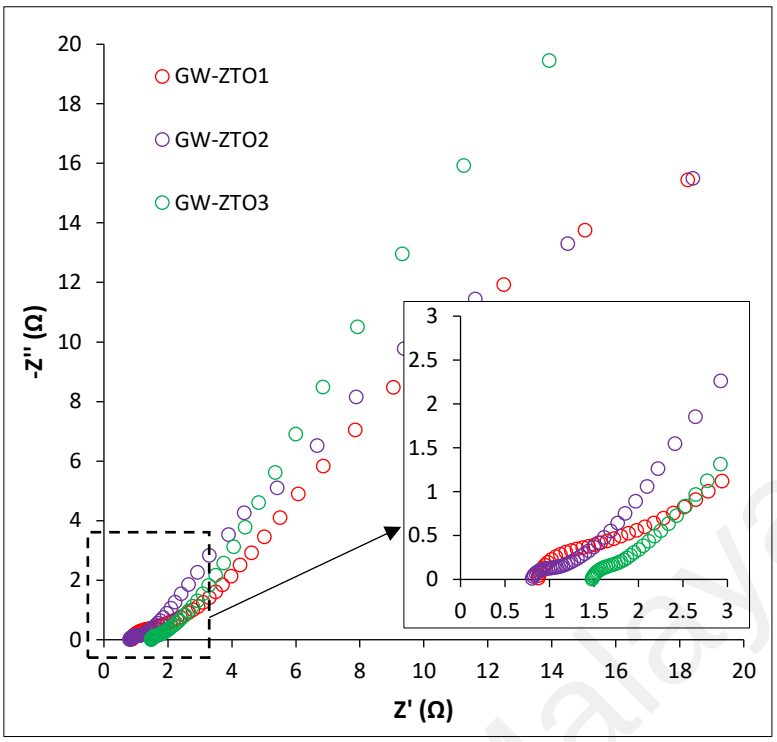

Figure 7.21: Nyquist plot of GW-ZTO series samples with inset in high frequency range

7.3.2 Symmetrical cell system

In this system, PP-ZTO1 and GW-ZTO1 were selected to assemble as symmetrical cell owing to their higher specific capacitance and good durability performance.

7.3.2.1 Cyclic voltammetry

The CV curves of PP-ZTO1||PP-ZTO1 and GW-ZTO1||GW-ZTO1 cells run from potential range of 0 to 1.0 V are illustrated in Figure 7.22. Both symmetrical cells exhibited slight deviation of rectangular shape implying the contribution of both EDLC and pseudo capacitance. The CV curves were well maintained up to 50 mVs^{-1} indicating the symmetrical cells performed ideal capacitive behavior. The distortion at highest scan rates (100 mVs^{-1}) is mainly due to the K^+ electrolyte ion only able to reach the outer surface of the electrode materials resulting in the limitation of effective interaction (Zhang et al., 2011). Additionally, it can be noticed that GW-ZTO1 symmetrical cell presented greater integrated area under CV curve indicating a faster electrons and ions diffusion rate (Xu et al., 2015) as well as good rate capability. Specific capacitance calculated from CV

showed PP-ZTO1 and GW-ZTO1 cells achieved 15.90 Fg^{-1} and 15.32 Fg^{-1} at 3 mVs^{-1} respectively. Table 7.9 displays the specific capacitance of respective scan rates for PP-ZTO1 and GW-ZTO1 symmetrical cells.

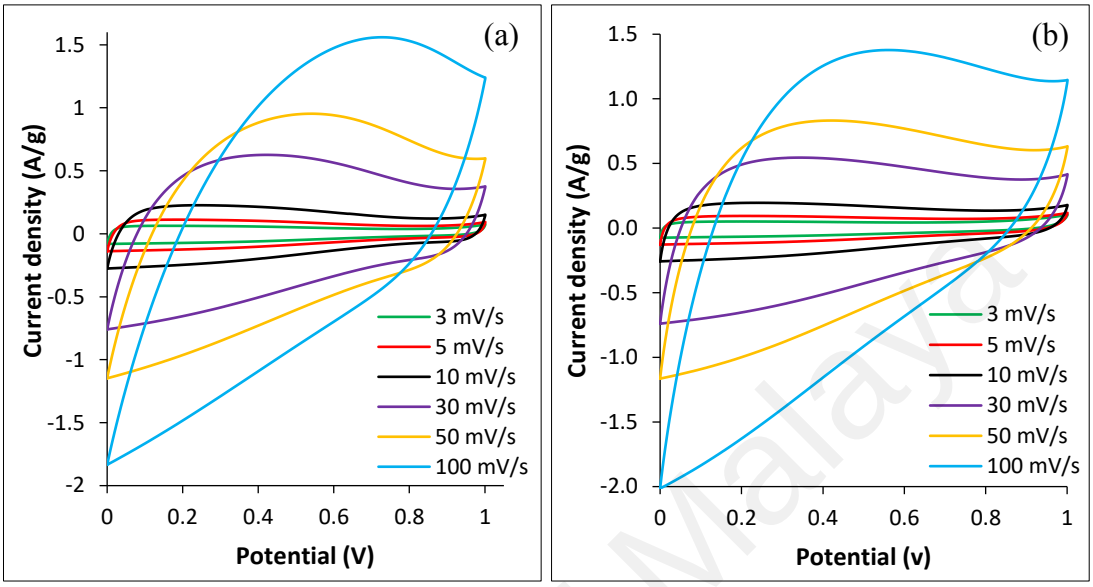

Figure 7.22: Cyclic voltammetry of (a) PP-ZTO1 and (b) GW-ZTO1 with various scan rates in EDLC

Table 7.9: Specific capacitance of PP-ZTO1 and GW-ZTO1 in EDLC at various scan rates.

Sample	Specific capacitance (Fg^{-1})					
	3 mVs^{-1}	**5 mVs^{-1}**	**10 mVs^{-1}**	**30 mVs^{-1}**	**50 mVs^{-1}**	**100 mVs^{-1}**
PP-ZTO1	15.90	16.47	16.30	14.19	12.41	9.47
GW-ZTO1	15.32	15.78	15.75	14.04	12.51	9.86

7.3.2.2 Galvanostatic charge-discharge

The GCD curves of various current densities for PP-ZTO1||PP-ZTO1 and GW-ZTO1||GW-ZTO1 cells are depicted in Figure 7.23. Both cells showing distorted triangular shape with slight concave at the charging region and convex at the discharging region indicating the pseudo capacitance of ZTO. Additionally, there is insignificant of iR drop in the GCD curves demonstrating the low internal resistance of the cells during

electrochemical process. All the GCD curves also illustrating symmetrical charge/discharge imply fine capacitive and reversible behavior. Both cells delivered almost identical specific capacitance such as 19.56 Fg^{-1} and 20 Fg^{-1} in PP-ZTO1||PP-ZTO1 and GW-ZTO1||GW-ZTO1 cells which was tally with the area under GCD curves.

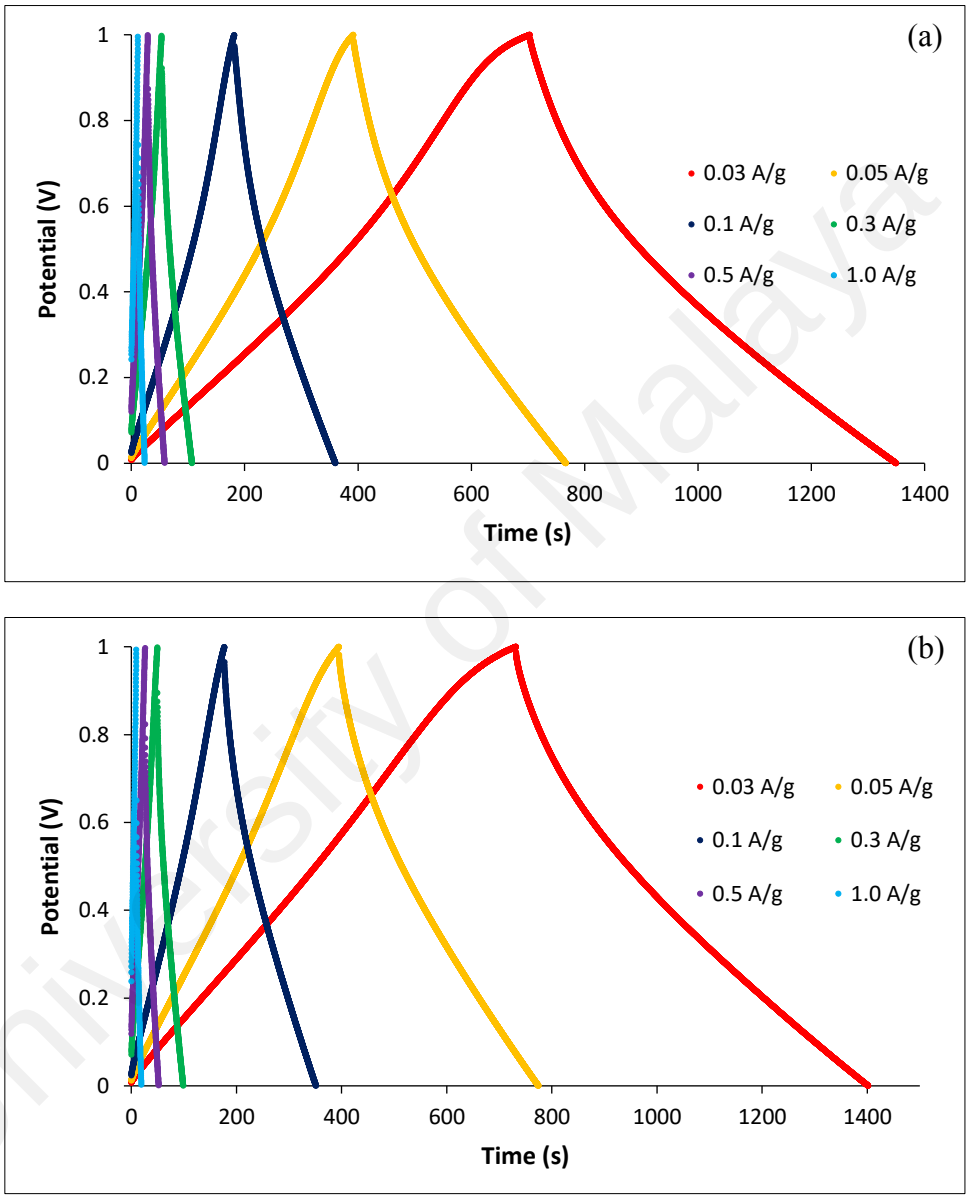

Figure 7.23: GCD of (a) PP-ZTO1 and (b) GW-ZTO1 with various current densities in EDLC

Table 7.10: Specific capacitance of PP-ZTO1 and GW-ZTO1 in EDLC at various current densities.

Sample	Specific capacitance (Fg^{-1})					
	0.03 Ag^{-1}	**0.05 Ag^{-1}**	**0.1 Ag^{-1}**	**0.3 Ag^{-1}**	**0.5 Ag^{-1}**	**1.0 Ag^{-1}**
PP-ZTO1	19.56	19.00	18.30	17.32	16.69	15.71
GW-ZTO1	20.00	19.00	18.04	16.44	15.64	14.28

The durability of the PP-ZTO1 and GW-ZTO1 symmetrical cells were further tested with different current densities for 900 cycles as shown in Figure 7.24. The result for both cells showed wobbly situation in maintaining the capacitance retention for the first 300 cycles. Though, the specific capacitance still at 87.63 % and 87.01 % for PP-ZTO1 and GW-ZTO1 cell at the 300^{th} cycle. When both cells were subjected to 0.2 Ag^{-1}, PP-ZTO1 cell experienced a sudden increase of 21.35 % of the specific capacitance which might due to the surface activation from earlier cycles allow more electrolyte ions to diffuse through the micropores (Zequine et al., 2016) and reduced progressively. GW-ZTO1 cells, on the other hand, with less micropore volume (0.04 cm^3g^{-1}) retained 83.91 % of the capacitance and gradually improved throughout the cycles of 0.2 Ag^{-1}.

When reversed back to the current density of 0.1 Ag^{-1}, both cells exhibited stable condition with PP-ZTO1 cells achieved the retention of 89.29 % at the 900^{th} cycle from the 300^{th} cycle. In similar condition, GW-ZTO1 cells displayed a more consistent and progressive improvement with better specific capacitance at the last cycle which was 107.59 % of the capacitance obtained from the 300^{th} cycle. From this durability test, we could observe the role of micropore and mesopore volume with incorporation of ZTO in retaining the energy storage.

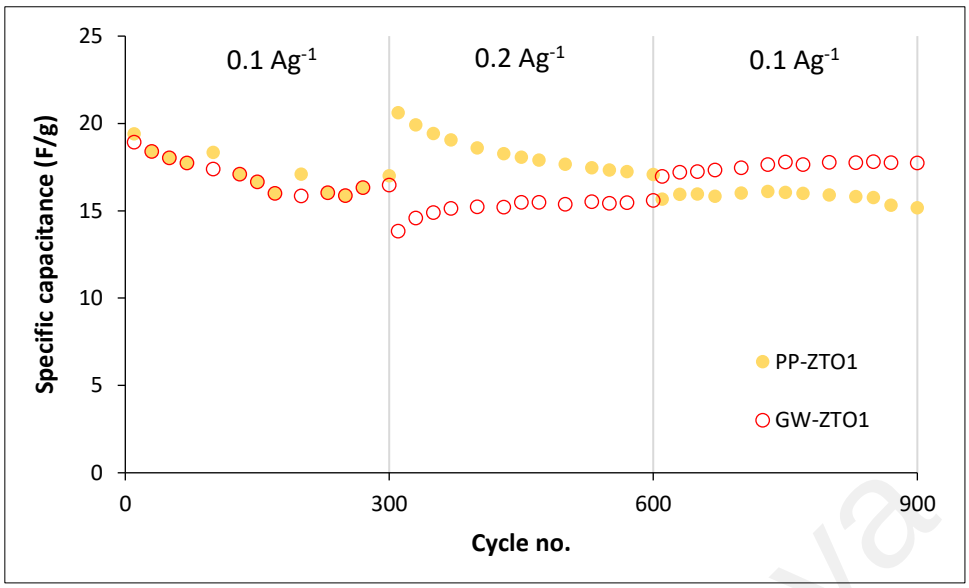

Figure 7.24: Durability performance of symmetrical cell at different current densities for 900 cycles in EDLC

Stability test was conducted for 5000 cycles at 0.3 Ag^{-1} to both PP-ZTO1||PP-ZTO1 and GW-ZTO1||GW-ZTO1 cells as depicted in Figure 7.25. As seen in Figure 7.25(a), PP-ZTO1 cell suffered from gradual depletion up to 2000 cycles followed by a steadier retention throughout the rest of the 5000 cycles (85.33 %). Nevertheless, GW-ZTO1 cell exhibited gradual enhancement after 1500 cycles and eventually retained the capacitance 111.45 % of the initial cycle indicating better capacitance obtained even after 5000 cycles. From the stability, both PP-ZTO1 and GW-ZTO1 symmetrical cells performed an outstanding stability supercapacitor. In term of energy and power density, both cells delivered about the similar value. PP-ZTO1||PP-ZTO1 cell has achieved the power density of 132.06 Wkg^{-1} and energy density of 1.79 $Whkg^{-1}$. For the cell of GW-ZTO1||GW-ZTO1, 101.74 Wkg^{-1} and 1.02 $Whkg^{-1}$ of the power and energy density were obtained.

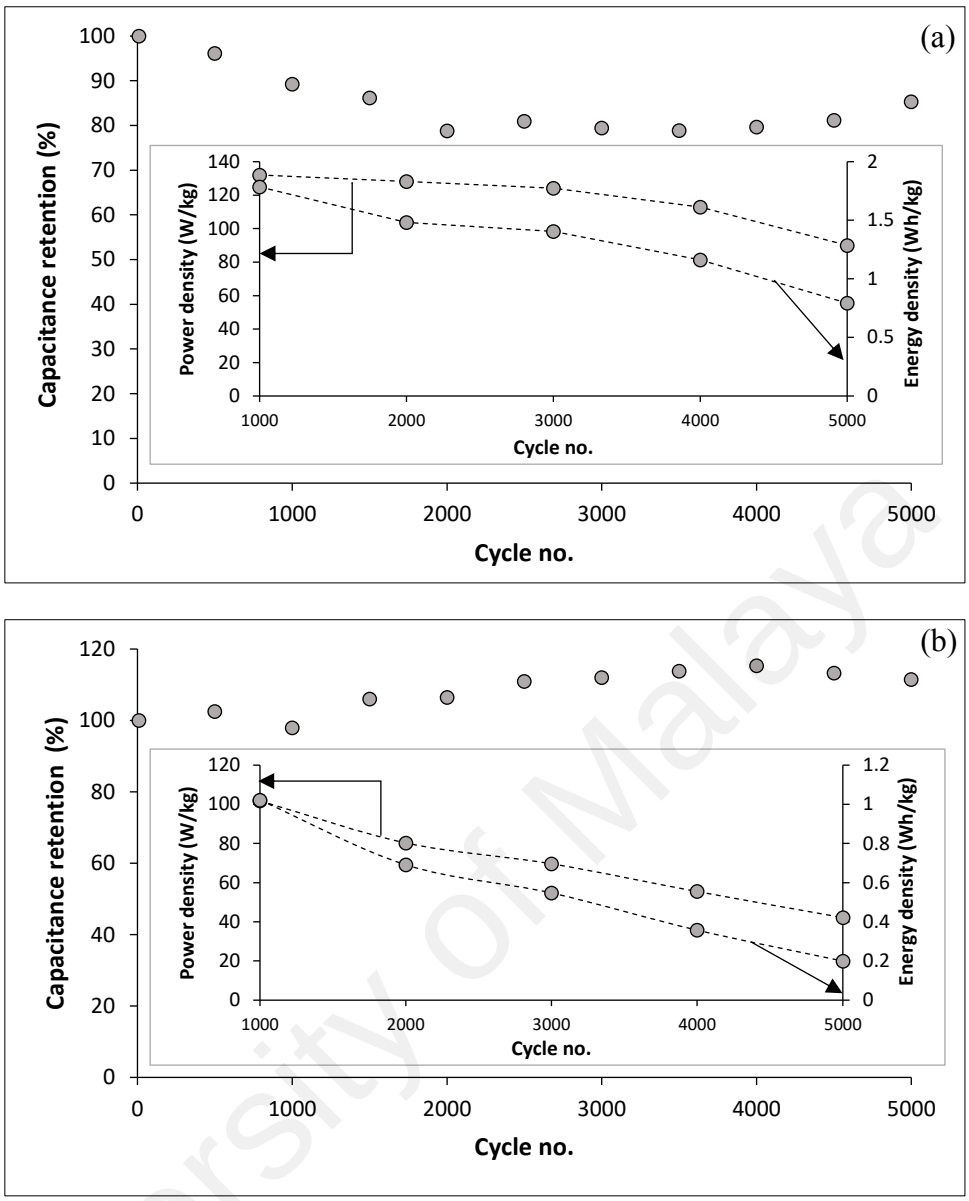

Figure 7.25: Stability test of (a) PP-ZTO1 and (b) GW-ZTO1 at 0.3 Ag^{-1} for 5000 cycles in EDLC

7.3.2.3 Electrochemical impedance spectroscopy

The EIS spectra of PP-ZTO1 and GW-ZTO1 symmetrical cells are illustrated in Figure 7.26. Both cells presented the typical semicircle at the high frequency region and almost vertical line with the Z imaginary axis at low frequency region. As shown, both cells recorded different bulk resistance with 3.64 Ω in PP-ZTO1 cell and 1.38 Ω for GW-ZTO1 cell. This could be attributed to the more mesopore volume (0.91 cm^3g^{-1}) in GW-ZTO1 cell which allow easier transport of ions between the interface of electrode and electrolyte.

However, the semicircle which represent the R_{ct} were almost identical to both cell such as 1.81 Ω and 1.58 Ω in PP-ZTO1 and GW-ZTO1 cells, respectively. Besides that, the vertical line in low frequency region implies that good rate of electrolyte ion diffusion and ideal capacitive behavior (Wu et al., 2019b). Table 7.11 shows the values of R_s and R_{ct} of PP-ZTO1 and GW-ZTO1 symmetrical cells.

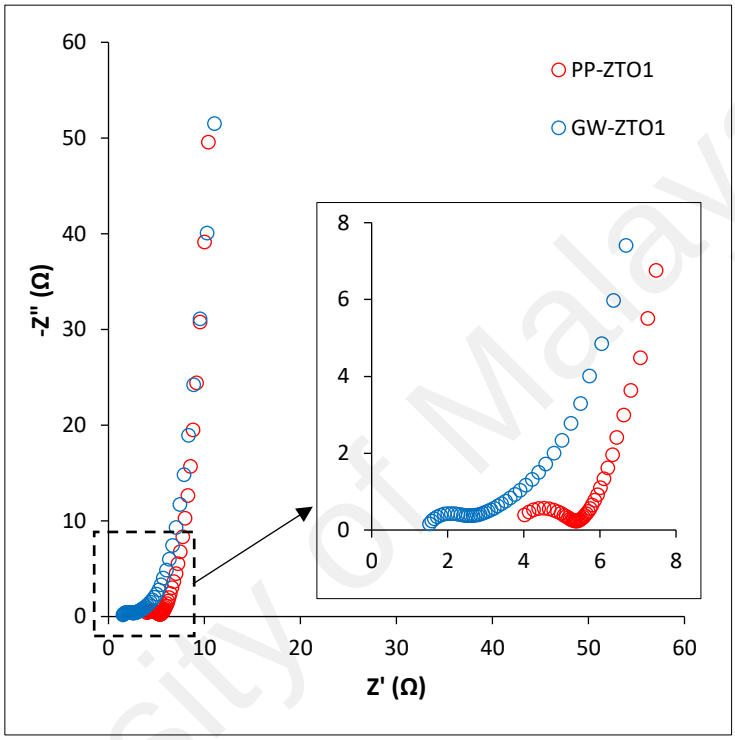

Figure 7.26: Nyquist plot of PP-ZTO1 and GW-ZTO1 in EDLC

Table 7.11: Value to R_s and R_{ct} for PP-ZTO1 and GW-ZTO1 in EDLC.

Sample	R_s (Ω)	R_{ct} (Ω)	$R_s + R_{ct}$ (Ω)
PP-ZTO1	3.64	1.81	5.45
GW-ZTO1	1.38	1.58	2.96

7.4 Summary

- Different ratio of ZTO into porous carbon has caused variety of pore textural properties to PP-ZTO and GW-ZTO series carbon composites.

- PP-ZTO1 and GW-ZTO1 delivered the specific capacitance of 93.99 Fg^{-1} and 104.02 Fg^{-1} at 0.3 Ag^{-1}, respectively.
- Outstanding durability performance is shown in both PP-ZTO and GW-ZTO series samples.
- PP-ZTO1||PP-ZTO1 and GW-ZTO1||GW-ZTO1 cells have achieved identical specific capacitance of 19.56 Fg^{-1} and 20 Fg^{-1} at 0.03 Ag^{-1}.
- Both symmetrical cells demonstrated as promising candidates for durable device with capacitance retention at 89.29 % (PP-ZTO1 cell) and 107.59 % (GW-ZTO1 cell) at the 900^{th} cycle as compared to the 300^{th} cycle.
- In Nyquist plot, PP-ZTO1 and GW-ZTO1 symmetrical cells behaved a good rate of ion diffusion and ideal capacitive behavior through the reflection vertical line at low frequency region.

CHAPTER 8: DISCUSSION

8.1 Introduction

In this chapter, the process formation of ZnO, ZMO and ZTO through calcination treatment are firstly discussed. The reaction of raw material and guest material are explained in the schematic diagram along with the equation. This is followed by the discussion on the influence of guest materials (ZnO, ZMO and ZTO) towards textural properties. For instance, the effect of guest materials in specific surface area, pore size and volume and morphology transformation. Lastly, the discussion includes the effect of textural properties and guest materials towards the electrochemical and durability performance.

8.2 Physical characterization

In this research, all the samples were activated using $ZnCl_2$, this activating agent was selected due to its low cost, high porous structure, good yields and minor erosion (Pezoti et al., 2014; Zhang et al., 2015). Most importantly, $ZnCl_2$ used to produce small mesopores which is beneficial towards energy storage performance, unlike other activating agents such as KOH and H_3PO_4 which generates wide micropore and heterogenous pore size respectively (Uçar et al., 2009).

Based on the results presented in previous chapters, both PP and GW based porous carbon and carbon composites demonstrate insignificant difference in specific surface area but the ratio of micro-mesopore volume. It is observed that PP-C produced mostly micropores while GW-C is towards mesopores. This is a typical phenomenon as numerous studies have been conducted that different precursor with similar synthesizing method will give rise to diverse textural properties owing to their structure and composition of the waste precursor (Abioye & Ani, 2015; Temesgen et al., 2018).

In PP-ZnO and GW-ZnO, the specific surface area is reduced at 36.62 % and 43.34 % as compared to PP-C and GW-C, respectively mainly due to ZnO has occupied. For the ternary carbon composites, specific surface area also experienced decrement (45 % to 92 %). This is attributed to the reduction in carbon source and pore-filling by ZMO/ZTO. These results are in agreement with the work carried out by Yumak and his co-researchers (2019) that once the loading amount of metal oxide increased, the specific surface area and total pore volume are reduced. Besides that, literature reviews have claimed that guest molecules will significantly influence the pore size and pore volume of the materials even at relatively low amount (Dong et al., 2006; Li et al., 2004) which can be seen that the pore size distribution of binary and ternary carbon composites with different weight ratio presenting pore size ranges.

The XRD pattern for porous carbon derived from PP and GW have shown a typical amorphous carbon structure. In binary C/ZnO samples, three well-resolved peaks are detected at 2θ = 31.82º (100), 34.47º (002) and 36.30º (101) can be indexed to ZnO (JCPDS file no. 01-070-2551). For samples of C/ZMO, the peaks at 29.3˚, 31.2˚, 32.9˚, 36.4˚, 44.6˚, 54.3˚, 59, 60.5 and 64.9˚ are in good agreement to ZMO (JCPDS file no. 01-077-0470) which aligned to the plane of (112), (200), (103), (211), (220), (312), (321), (224) and (116). In ternary C/ZTO samples, the peaks at 26.6º, 34.0º, 38.0º, 51.8º, 54.9º, 62.0º and 71.3º can be matched to ZTO (JCPDS file no. 00-028-1486) which correspond to the plane (012), (110), (015), (116), (018), (300) and (127), respectively. Based on the XRD pattern, the one-step combustion method has successfully synthesized porous carbon, binary and ternary porous carbon composites.

The FESEM images shown in previous chapters have clearly presented the different structures due to the addition of guest materials. The ZnO, ZMO and ZTO have partly participated in pore-filling especially when the weight ratio is increased. Attributable to this condition, the surface area and total pore volume are further decreased which is tally

with the textural properties demonstrated. Besides that, comparison also can be made for the morphology (Figure 4.6) in PP-C and GW-C whereby pure carbon allows more pores development, unlike samples in C/ZMO and C/ZTO series when the weight ratio of the carbon reduced. According to the FESEM images, we also observed the composites materials were attached on the carbon surface. The HRTEM images with individual lattice spacing and the EDX also further confirmed the element of ZnO, ZMO and ZTO which adhered on porous carbon were successfully synthesized.

8.3 Electrochemical performance

According to the results presented in sub-chapters of 4.3, 5.3, 6.3 and 7.3, it can be claimed that the textural properties and addition of guest materials have greatly influenced in the electrochemical performance. In this work, all the testing for three-electrode and symmetrical cell systems were conducted in electrolyte with 6 M KOH. The selection of KOH is mainly due to its higher ionic conductivity and ideal electrolyte for porous carbon -based electrode materials (Barzegar et al., 2015).

In the three-electrode system, PP-C and GW-C presented an ideal rectangular shape up to 10 mVs^{-1} but distortion of CV profile happened upon higher scan rates. Binary and ternary carbon composites, on the other hand, demonstrating a better rate capability whereby the shape of CV curves is almost identical from low to high scan rates. This phenomenon can be observed clearer in ternary carbon composites under the different weight ratio of carbon and metal oxide. The retention of CV shape is mainly due to the existence of ZMO and ZTO in contributing pseudo-capacitance through intercalation/deintercalation with K^+ electrolyte ions. The process of the redox reaction can be explained with the equations below (Sahoo & Sharma, 2015a):

(a) <u>System ZMO</u>

$$(ZMO)_{surface} + K^+ + e^- \leftrightarrow [KZMO]_{surface} \quad [8.1]$$

$$ZMO + K^+ + e^- \leftrightarrow [ZMO]K \quad [8.2]$$

(b) System ZTO

$$(ZTO)_{surface} + K^+ + e^- \leftrightarrow [KZTO]_{surface} \quad [8.3]$$

$$ZTO + K^+ + e^- \leftrightarrow [ZTO]K \quad [8.4]$$

As the surface of the carbon is greatly exposed with ZMO or ZTO, shorter transportation path during rapid ion diffusion at higher scan rates allow good electrochemical stability. This can be seen that when rate capability test was conducted, the samples with higher ratio of ZMO or ZTO exhibit higher capacitance retention. This is mainly due to ZMO or ZTO having the characteristic of greater electronic conductivity and electrochemical which allow the participation of different metallic oxides and eventually enhance the faradic pseudo-capacitance with rich redox reaction compared to single metallic oxides (Huang et al., 2017). This also explained the reason of lower capacitance retention during rate capability test in binary carbon composites.

In term of specific capacitance, Figure 8.1 displays the specific capacitance of C/ZMO and C/ZTO series samples. It is obvious that sample with lowest weight ratio of ZMO and ZTO achieved higher specific capacitance among other samples. However, porous carbon (144.93 Fg^{-1}) and C/ZnO (119.03 Fg^{-1}) exhibited slightly higher specific capacitance at 0.3 Ag^{-1}. This is attributed to higher specific surface area which provide more active sites for ion diffusion. Besides that, as samples with higher weight ratio of ZMO or ZTO system, content of carbon is lesser, therefore the role of carbon which serves as support or matrix in stress relaxation is not fully function. In this condition, metal oxide nanoparticles might tend to undergo aggregation and pulverization which limit the electrochemical performance (Li et al., 2015a).

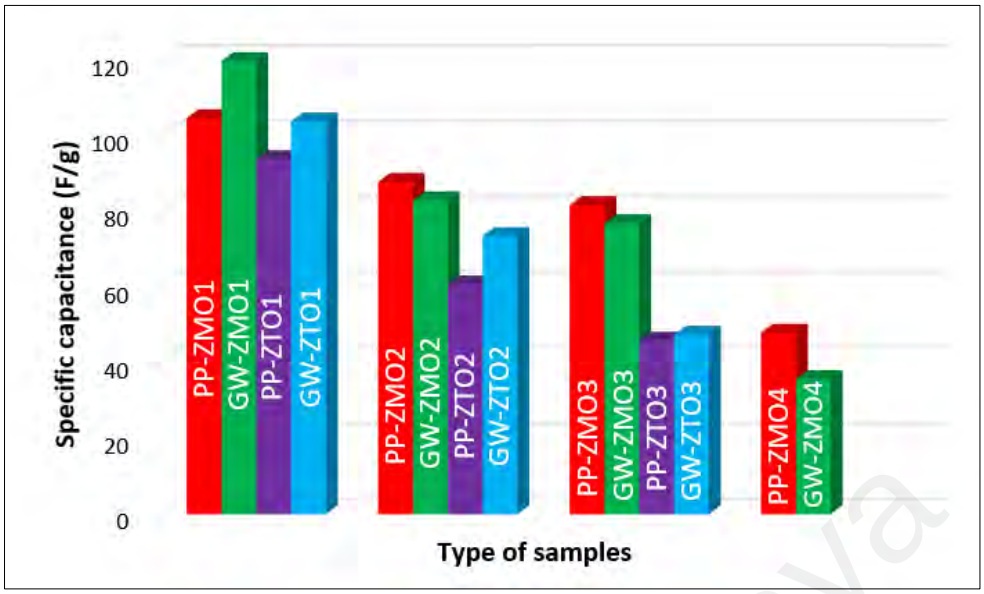

Figure 8.1: Specific capacitance of all ternary carbon composites at the current density of 0.3 Ag^{-1} in three-electrode system

Two-electrode system was also conducted to investigate the cell performance, thus, sample such as PP-C, PP-ZMO1, GW-ZMO1, PP-ZTO1 and GW-ZTO1 were selected for fabrication as devices. All the cells presented about the similar specific capacitance, for instance PP-C (24.61 Fg^{-1}), PP-ZMO1 (17.62 Fg^{-1}), GW-ZMO1 (24.67 Fg^{-1}), PP-ZTO1 (19.56 Fg^{-1}) and GW-ZTO1 (20 Fg^{-1}) at the current density of 0.03 Ag^{-1}. As compared to commercial activated carbon which showed 22 Fg^{-1} (Sim et al. 2015b), the performance from synthesized samples were comparable to the commercial product. The CV curves of GW-ZMO1, PP-ZTO1 and GW-ZTO1 cells exhibited almost identical shape from low to high scan rates indicating the devices possess good rate capability. Though the cell of PP-C (2.69 nm) and PP-ZMO1 (7.06 nm) experience shape distortion at higher scan rate which is mainly due to small and too large pore size create higher resistance for ion diffusion especially during limited time at high scan rates. Report has claimed that supercapacitor with mesopore between the range of 3 to 5 nm favors high energy and power density (Zhi et al., 2014).

In terms of rate capability test, all the symmetrical cells performed good stability results among different current densities except for PP-C||PP-C which the capacitance suffered from drastic dropped to null value. According to Figure 4.18 high R_{ct} after charge and discharge is observed indicating electrolyte ions are difficult or block to diffuse through the pores. This might be due to the pore destruction after exposed with different current load over long cycling. Another reason could be due to the lack of metal oxide as the combination of both metal oxide and carbon will bring synergistic effect in enhancing the intrinsic properties such as ionic conductivity, mechanical stability and electrochemical performance (Jiang et al., 2012). This is mainly due to carbon allows more active sites which improve the electrical conductivity and metal oxide decreases the ionic resistance by enhancing the homogeneity in oxidation-reduction reaction (Dong et al., 2006).

8.4 Summary

- Different raw materials with similar synthesizing method will give rise to diverse textural properties owing to their structure and composition of the waste precursor.
- Guest molecules will significantly influence the pore size and pore volume of the materials even at relatively low amount.
- Electrode materials with mesopores size from 3 to 5 nm favors high energy and power density.
- ZMO or ZTO allowed the participation of different metallic oxides enhanced the faradic pseudo-capacitance with rich redox reaction.
- The incorporation of both metal oxide and carbon will bring synergistic effect in enhancing the intrinsic properties such as ionic conductivity, mechanical stability and electrochemical performance.

CHAPTER 9: CONCLUSIONS & RECOMMENDATIONS

9.1 Conclusions

In this study, the porous carbon, binary and ternary porous carbon composites have been successfully produced utilizing the similar synthesizing route. All the samples were synthesized through simple combustion method under inert condition at 500 ºC for one hour holding time. Based on the results, the addition of ZnO, ZMO and ZTO showed significant influence towards the textural properties. The highest specific surface area was obtained in porous carbon such as 1765.92 m^2g^{-1} and 1613.92 m^2g^{-1} in PP-C and GW-C, respectively. The specific surface area reduced to 1119.32 m^2g^{-1} (PP-ZnO) and 913.91 m^2g^{-1} (GW-ZnO) and the pattern appeared to be the same in C/ZMO and C/ZTO composites samples whereby a progressively reduction shown upon increasing weight ratio of ZMO or ZTO. From the FESEM images, it can be clearly seen that ZnO, ZMO and ZTO were attached on the carbon surface that have partially blocked the pores and participated in pore filling which reduced the specific surface area. Besides that, the pore sizes were enlarged upon addition of guest materials resulting in different pore size distribution. In the XRD spectra, PP-C and GW-C demonstrated significant amorphous structure. While in the samples of binary and ternary carbon composites, crystalline peaks were observed indicating the synthesized materials such as ZnO, ZMO and ZTO. Other characterization tests for instance, lattice spacing of HRTEM and EDX analysis further support the result obtained in XRD diffraction pattern.

In order to investigate the electrochemical behavior of the samples, three-electrode system was carried out. We found out that the highest specific capacitance was achieved by PP-C (144.93 Fg^{-1}) owing to its highest specific surface area which provide more active sites for ion adsorption. Besides that, when looking into ternary carbon composites, the specific capacitance reduced as weight ratio of ZMO/ZTO increased while carbon content decreased. This is due to metal oxide nanoparticles might tend to suffer

aggregation and pulverization when there is lack of carbon which serves as support for stress relaxation. However, in term of rate capability, ZMO or ZTO has clearly shown an outstanding stability even applied with different current densities explained the role of composites in enhancing the overall performance through pseudo-capacitance. This also can be seen in CV curves with various scan rates such as improvement on the shape of CV curves and area under the curves especially at high scan rates indicating good rate capability.

To further determine the device performance, the samples within its category with optimum electrochemical behavior were selected for supercapacitor. The device such as PP-C||PP-C, PP-ZMO1||PP-ZMO1, GW-ZMO1||GW-ZMO1, PP-ZTO1||PP-ZTO1 and GW-ZTO1||GW-ZTO1 were successfully fabricated. All the symmetrical cells exhibited identical shape of CV curves from low to high scan rates excluding the cell of PP-C and PP-ZMO1 due to the small and too large pore sizes which creating higher resistance when the cell is applied at high scan rate. In term of specific capacitance, all the symmetrical cells demonstrated almost similar performance in the range of 17 to 25 Fg^{-1} at 0.03 Ag^{-1}. In term of rate capability test, all the ternary composites symmetrical cells exhibited good rate capability performance (65 % to 108 %) due to the ZMO or ZTO which has provided a shorter pathway for ion diffusion and greater electronic conductivity. However, PP-C||PP-C cell suffered from drastic drop in capacitance retention due to its high R_{ct} implying electrolyte ions are difficult to diffuse through the pores. The two reasons that have caused this high resistance are (i) pore destruction after applied high current density for long cycling and (ii) non-existance of metal oxide in providing the sygnergistic effect with carbon to enhance the ionic conductivity and mechanical stability. For stability, all symmetrical cells were steady with the capacitance retention above 80 % implying good materials for long lifespan device.

At the end of this research, we have created a novel synthesis route of generating eco-friendly porous carbon composite materials through single carbonization method in which there yet any research reporting on the use of biomass as raw materials to produce carbon composite materials. The synthesized sustainable biomass exhibited a promising candidate as precursor for electrode materials in energy storage device. Besides that, contribution also goes towards waste to energy. From here, we can see that the study has provide a new alternative of managing waste volume to landfill and the meantime turning it into valuable product and gain revenue. It also creates socio-economic benefits in terms of investment in energy storage system, education and environmental dimension such as greenhouse gas emission and materials consumption. Lastly is the aspect of durability, we have proved that the addition of metal oxide has further enhanced the durability through the synergistic effect between carbon and composite by allowing it to hold with different current loads over long cycle process. Durability test also seldom reported by researchers which has highlighted the importance of this study as the baseline for future experiments being carried out.

9.2 Recommendations

The overview of the study provided a positive outcome for biomass to be utilized in energy storage device and solution to manage the agricultural wastes. Though, future work can focus on various electrolytes such as saturated sodium perchlorate aqueous solution, $NaClO_4$ (3 V) or ionic liquid likewise N, N-propylmethylpyrrolidinium hexafluorophosphate (7.2 V), which have larger potential window to achieve higher energy and power densities of the device. Besides that, the addition of guest materials with higher electronegativity values would be another study whereby it can attract more electrons for redox reaction hence it is expected to have higher specific capacitance. Other than that, different synthesis methods such as metal–organic framework, in-situ electrodeposition, emulsion polymerization, solvothermal, hydrothermal or sol-gel will

produce materials with different surface morphologies which can be spherical, tubular, core-shell etc. The various shapes and sizes of material will then be applied in diverse fields not only energy storage but medical biotechnology, catalyst and so on. This will be an interesting topic to explore the materials for more applications.

REFERENCES

Abbaslou, R. M., Vosoughi, V., & Dalai, A. K. (2017). Comparison of nitrogen adsorption and transmission electron microscopy analyses for structural characterization of carbon nanotubes. *Applied Surface Science, 419*, 817-825.

Abdollahifar, M., Huang, S.-S., Lin, Y.-H., Lin, Y.-C., Shih, B.-Y., Sheu, H.-S., Liao, Y.-F., & Wu, N.-L. (2018). High-performance carbon-coated $ZnMn_2O_4$ nanocrystallite supercapacitors with tailored microstructures enabled by a novel solution combustion method. *Journal of Power Sources, 378*, 90-97.

Abdollahifar, M., Huang, S.-S., Lin, Y.-H., Sheu, H.-S., Lee, J.-F., Lu, M.-L., … Wu, N.-L. (2019). Tetragonal $LiMn_2O_4$ as dual-functional pseudocapacitor-battery electrode in aqueous Li-ion electrolytes. *Journal of Power Sources, 412*, 545-551.

Abdullah, & Mat, H. B. (2017). The Characteristic of Pineapple Waste from Canning Industry. *Advanced Science Letters, 23*(6), 5691-5693.

Abioye, A. M., & Ani, F. N. (2015). Recent development in the production of activated carbon electrodes from agricultural waste biomass for supercapacitors: A review. *Renewable and Sustainable Energy Reviews, 52*, 1282-1293.

Adeyi, O. (2010). Proximate composition of some agricultural wastes in Nigeria and their potential use in activated carbon production. *Journal of Applied Sciences and Environmental Management, 14*(1), 55-58.

Ahmad, M. A., Ahmad Puad, N. A., & Bello, O. S. (2014). Kinetic, equilibrium and thermodynamic studies of synthetic dye removal using pomegranate peel activated carbon prepared by microwave-induced KOH activation. *Water Resources and Industry, 6*, 18-35.

Alam, M. M., Ghosh, S. K., Sultana, A., & Mandal, D. (2015). Lead-free $ZnSnO_3$/MWCNTs-based self-poled flexible hybrid nanogenerator for piezoelectric power generation. *Nanotechnology, 26*(16), Article#165403.

Ao, W., Fu, J., Mao, X., Kang, Q., Ran, C., Liu, Y., … Dai, J. (2018). Microwave assisted preparation of activated carbon from biomass: A review. *Renewable and Sustainable Energy Reviews, 92*, 958-979.

Ashar, A., Iqbal, M., Bhatti, I. A., Ahmad, M. Z., Qureshi, K., Nisar, J., & Bukhari, I. H. (2016). Synthesis, characterization and photocatalytic activity of ZnO flower and pseudo-sphere: Nonylphenol ethoxylate degradation under UV and solar irradiation. *Journal of Alloys and Compounds, 678*, 126-136.

Bagheri, N., & Abedi, J. (2011). Adsorption of methane on corn cobs based activated carbon. *Chemical Engineering Research and Design, 89*(10), 2038-2043.

Barbieri, O., Hahn, M., Herzog, A., & Kötz, R. (2005). Capacitance limits of high surface area activated carbons for double layer capacitors. *Carbon, 43*(6), 1303-1310.

Barkhordari, H., Heydari, H., Nosrati, A., & Mohammadi, J. (2019). Facile synthesis of $ZnMn_2O_4$ nanosheets via cathodic electrodeposition: characterization and supercapacitor behavior studies. *Ionics, 25*(1), 275-285.

Baruah, B., Tiwari, P., Thakur, P., & Kataki, R. (2018). TGA-FTIR analysis of Upper Assam oil shale, optimization of lab-scale pyrolysis process parameters using RSM. *Journal of Analytical and Applied Pyrolysis, 135*, 397-405.

Barzegar, F., Momodu, D. Y., Fashedemi, O. O., Bello, A., Dangbegnon, J. K., & Manyala, N. (2015). Investigation of different aqueous electrolytes on the electrochemical performance of activated carbon-based supercapacitors. *RSC Advances, 5*(130), 107482-107487.

Baytar, O., Şahin, Ö., & Saka, C. (2018). Sequential application of microwave and conventional heating methods for preparation of activated carbon from biomass and its methylene blue adsorption. *Applied Thermal Engineering, 138*, 542-551.

Bhagwan, J., Kumar, N., Yadav, K. L., & Sharma, Y. (2018). Probing the electrical properties and energy storage performance of electrospun $ZnMn_2O_4$ nanofibers. *Solid State Ionics, 321*, 75-82.

Biswal, M., Banerjee, A., Deo, M., & Ogale, S. (2013). From dead leaves to high energy density supercapacitors. *Energy & Environmental Science, 6*(4), 1249-1259.

Bondavalli, P. (2018). Graphene and related nanomaterials: Properties and application (1st ed.). Oxford, United Kingdom: Matthew Deans.

Bora, T., Al-Hinai, M. H., Al-Hinai, A. T., & Dutta, J. (2015). Phase Transformation of Metastable $ZnSnO_3$ Upon Thermal Decomposition by In-Situ Temperature-Dependent Raman Spectroscopy. *Journal of the American Ceramic Society, 98*(12), 4044-4049.

BP Statistical Review of World Energy (2017). Retrieved on March 1, 2018 from https://www.connaissancedesenergies.org/sites/default/files/pdf-actualites/bp-statistical-review-of-world-energy-2017-full-report.pdf

Cagnon, B., Py, X., Guillot, A., Stoeckli, F., & Chambat, G. (2009). Contributions of hemicellulose, cellulose and lignin to the mass and the porous properties of chars and steam activated carbons from various lignocellulosic precursors. *Bioresource Technology, 100*(1), 292-298.

Cao, W., & Yang, F. (2018). Supercapacitors from high fructose corn syrup-derived activated carbons. *Materials Today Energy, 9*, 406-415.

Chang, S.-K., & Zainal, Z. (2019). Activated carbon for supercapacitors. In S. A. Rashid, R. N. I. Raja Othman, & M. Z. Hussein (Eds.), Synthesis, technology and applications of carbon nanomaterials (pp. 309-334). United Kingdom: Matthew Deans.

Chen, F., Wang, Z., Huo, S., Ji, S., Wang, H., & Zhou, P. (2019a). Cubic $CoMn_2O_4$ particles directly grown on Ni foam as binder-free electrode for asymmetric supercapacitors. *Materials Letters, 237*, 209-212.

Chen, K. F., Yang, Y. Y., Li, K. Y., Ma, Z. S., Zhou, Y. C., & Xue, D. F. (2014). $CoCl_2$ designed as excellent pseudocapacitor electrode materials. *ACS Sustainable Chemistry & Engineering, 2*(3), 440-444.

Chen, M., Yan, D., Zhang, X., Yu, Z., Zhu, G., Zhao, Y., … Yu, A. (2017). Activated carbons by a hydrothermal-assisted activated method for Li-ion batteries. *Materials Letters, 196*, 276-279.

Chen, Q., Pu, W., Hou, H., Hu, J., Liu, B., Li, J., … Yang, J. (2018a). Activated microporous-mesoporous carbon derived from chestnut shell as a sustainable anode material for high performance microbial fuel cells. *Bioresource Technology, 249*, 567-573.

Chen, S., Yao, M., Wang, F., Wang, J., Zhang, Y., & Wang, Y. (2019b). Facile microemulsion synthesis of mesoporous $ZnMn_2O_4$ submicrocubes as high-rate and long-life anodes for lithium ion batteries. *Ceramics International, 45*(5), 5594-5600.

Chen, X., Liu, X., Liu, Y., Zhu, Y., Zhuang, G., Zheng, W., … Yang, P. (2018b). Advanced binder-free electrodes based on $CoMn_2O_4$@Co_3O_4 core/shell nanostructures for high-performance supercapacitors. *RSC Advances, 8*(55), 31594-31602.

Chen, Y., Yu, L., Li, Q., Wu, Y., Li, Q., & Wang, T. (2012). An evolution from 3D face-centered-cubic $ZnSnO_3$ nanocubes to 2D orthorhombic $ZnSnO_3$ nanosheets with excellent gas sensing performance. *Nanotechnology, 23*(41), Article#415501.

Coromina, H. M., Adeniran, B., Mokaya, R., & Walsh, D. A. (2016). Bridging the performance gap between electric double-layer capacitors and batteries with high-energy/high-power carbon nanotube-based electrodes. *Journal of Materials Chemistry A, 4*(38), 14586-14594.

Cychosz, K. A., Guillet-Nicolas, R., García-Martínez, J., & Thommes, M. (2017). Recent advances in the textural characterization of hierarchically structured nanoporous materials. *Chemical Society Reviews, 46*(2), 389-414.

Dai, C., Wan, J., Yang, J., Qu, S., Jin, T., Ma, F., & Shao, J. (2018). H_3PO_4 solution hydrothermal carbonization combined with KOH activation to prepare argy wormwood-based porous carbon for high-performance supercapacitors. *Applied Surface Science, 444*, 105-117.

Danish, M., & Ahmad, T. (2018). A review on utilization of wood biomass as a sustainable precursor for activated carbon production and application. *Renewable and Sustainable Energy Reviews, 87*, 1-21.

Demiral, H., Demiral, İ., Karabacakoğlu, B., & Tümsek, F. (2011). Production of activated carbon from olive bagasse by physical activation. *Chemical Engineering Research and Design, 89*(2), 206-213.

Deng, H., Li, G., Yang, H., Tang, J., & Tang, J. (2010). Preparation of activated carbons from cotton stalk by microwave assisted KOH and K_2CO_3 activation. *Chemical Engineering Journal, 163*(3), 373-381.

Deng, H., Yang, L., Tao, G., & Dai, J. (2009). Preparation and characterization of activated carbon from cotton stalk by microwave assisted chemical activation—Application in methylene blue adsorption from aqueous solution. *Journal of Hazardous Materials, 166*(2), 1514-1521.

Diallo, A., Ngom, B. D., Park, E., & Maaza, M. (2015). Green synthesis of ZnO nanoparticles by Aspalathus linearis: Structural & optical properties. *Journal of Alloys and Compounds, 646*, 425-430.

Dong, X., Shen, W., Gu, J., Xiong, L., Zhu, Y., Li, H., & Shi, J. (2006). MnO_2-embedded-in-mesoporous-carbon-wall structure for use as electrochemical capacitors. *The Journal of Physical Chemistry B, 110*(12), 6015-6019.

Duan, X. H., Srinivasakannan, C., Peng, J. H., Zhang, L. B., & Zhang, Z. Y. (2011). Preparation of activated carbon from Jatropha hull with microwave heating: optimization using response surface methodology. *Fuel Processing Technology, 92*, 394-400.

Elmouwahidi, A., Bailón-García, E., Pérez-Cadenas, A. F., Maldonado-Hódar, F. J., & Carrasco-Marín, F. (2017). Activated carbons from KOH and H_3PO_4-activation of olive residues and its application as supercapacitor electrodes. *Electrochimica Acta, 229*, 219-228.

Fang, B., & Binder, L. (2006). A modified activated carbon aerogel for high-energy storage in electric double layer capacitors. *Journal of Power Sources, 163*(1), 616-622.

Foo, K. Y., & Hameed, B. H. (2012). Porous structure and adsorptive properties of pineapple peel based activated carbons prepared via microwave assisted KOH and K_2CO_3 activation. *Microporous and Mesoporous Materials, 148*(1), 191-195.

Frackowiak, E., Lota, G., Machnikowski, J., Vix-Guterl, C., & Béguin, F. (2006). Optimisation of supercapacitors using carbons with controlled nanotexture and nitrogen content. *Electrochimica Acta, 51*(11), 2209-2214.

Fu, K., Yue, Q., Gao, B., Wang, Y., & Li, Q. (2017). Activated carbon from tomato stem by chemical activation with $FeCl_2$. *Colloids and Surfaces A: Physicochemical and Engineering Aspects, 529*, 842-849.

Gao, Y., Zheng, M., & Pang, H. (2015). Achieving high-performance supercapacitors by constructing porous zinc–manganese oxide microstructures. *Energy Technology, 3*(8), 820-824.

Georgin, J., Dotto, G. L., Mazutti, M. A., & Foletto, E. L. (2016). Preparation of activated carbon from peanut shell by conventional pyrolysis and microwave irradiation-pyrolysis to remove organic dyes from aqueous solutions. *Journal of Environmental Chemical Engineering, 4*(1), 266-275.

Gidwani, M., Bhagwani, A., & Rohra, N. (2014). Supercapacitors: The near future of batteries. *International Journal of Engineering Inventions, 4*(5), 22-27.

Gonçalves, G. d. C., Pereira, N. C., & Veit, M. T. (2016). Production of bio-oil and activated carbon from sugarcane bagasse and molasses. *Biomass and Bioenergy, 85*, 178-186.

González-García, P. (2018). Activated carbon from lignocellulosics precursors: A review of the synthesis methods, characterization techniques and applications. *Renewable and Sustainable Energy Reviews, 82*, 1393-1414.

Guan, T., Zhao, J., Zhang, G., Zhang, D., Han, B., Tang, N., … Li, K. (2018). Insight into controllability and predictability of pore structures in pitch-based activated carbons. *Microporous and Mesoporous Materials, 271*, 118-127.

Guan, Y., Feng, Y., Mu, Y., Fang, L., Zhang, H., & Wang, Y. (2016). Ultra-tiny $ZnMn_2O_4$ nanoparticles encapsulated in sandwich-like carbon nanosheets for high-performance supercapacitors. *Nanotechnology, 27*(47), Article#475402.

Guo, N., Wei, X. Q., Deng, X. L., & Xu, X. J. (2015). Synthesis and property of spinel porous $ZnMn_2O_4$ microspheres. *Applied Surface Science, 356*, 1127-1134.

Han, D., Xu, P., Jing, X., Wang, J., Yang, P., Shen, Q., … Zhang, M. (2013). Trisodium citrate assisted synthesis of hierarchical NiO nanospheres with improved supercapacitor performance. *Journal of Power Sources, 235*, 45-53.

Han, F., Li, W. C., Lei, C., He, B., Oshida, K., & Lu, A. H. (2014). Selective formation of carbon-coated, metastable amorphous $ZnSnO_3$ nanocubes containing mesopores for use as high-capacity lithium-ion battery. *Small, 10*(13), 2637-2644.

Hernandez, J. H., Barocio, E., & Messina, A. R. (2007, 24-28 June 2007). Nonlinear Modal Identification of Power System Response Signals Using Higher Order Statistics. Paper presented at the 2007 IEEE Power Engineering Society General Meeting.

Hilal-AlNaqbi, A., Al-Omari, S. B., & Selim, M. Y. E. (2016). Assessment of tree leaves flakes mixed with crude glycerol as a bioenergy source. *BioMed Research International*, *2016*, 1-10.

Hoel, C. A., Amores, J. M. G., Morán, E., Álario-Franco, M. A., Gaillard, J.-F., & Poeppelmeier, K. R. (2010). High-Pressure Synthesis and Local Structure of Corundum-Type $In_{2-2x}Zn_xSn_xO_3$ ($x \leq 0.7$). *Journal of the American Chemical Society, 132*(46), 16479-16487.

Huang, T., Zhao, C., Qiu, Z., Luo, J., & Hu, Z. (2017). Hierarchical porous $ZnMn_2O_4$ synthesized by the sucrose-assisted combustion method for high-rate supercapacitors. *Ionics, 23*(1), 139-146.

Hulicova-Jurcakova, D., Seredych, M., Lu, G. Q., Kodiweera, N. K. A. C., Stallworth, P. E., Greenbaum, S., & Bandosz, T. J. (2009). Effect of surface phosphorus functionalities of activated carbons containing oxygen and nitrogen on electrochemical capacitance. *Carbon, 47*(6), 1576-1584.

International Energy Outlook (2017). Retrieved on March 5, 2018 from https://www.eia.gov/outlooks/ieo/pdf/0484(2017).pdf

Ioannidou, O., & Zabaniotou, A. (2007). Agricultural residues as precursors for activated carbon production-A review. *Renewable and Sustainable Energy Reviews, 11*(9), 1966-2005.

Jagadeesan, D., & Eswaramoorthy, M. (2010). Functionalized carbon nanomaterials derived from carbohydrates. *Chemistry – An Asian Journal, 5*(2), 232-243.

Jiang, J., Li, Y., Liu, J., Huang, X., Yuan, C., & Lou, X. W. D. (2012). Recent advances in metal oxide-based electrode architecture design for electrochemical energy storage. *Advanced Materials, 24*(38), 5166-5180.

Jibril, B., Houache, O., Al-Maamari, R., & Al-Rashidi, B. (2008). Effects of H_3PO_4 and KOH in carbonization of lignocellulosic material. *Journal of Analytical and Applied Pyrolysis, 83*(2), 151-156.

Kalpana, D., Omkumar, K. S., Kumar, S. S., & Renganathan, N. G. (2006). A novel high power symmetric ZnO/carbon aerogel composite electrode for electrochemical supercapacitor. *Electrochimica Acta, 52*(3), 1309-1315.

Kang, J., Wen, J., Jayaram, S. H., Yu, A., & Wang, X. (2014). Development of an equivalent circuit model for electrochemical double layer capacitors (EDLCs) with distinct electrolytes. *Electrochimica Acta, 115*, 587-598.

Kazmierczak-Razna, J., Nowicki, P., Wiśniewska, M., Nosal-Wiercińska, A., & Pietrzak, R. (2017). Thermal and physicochemical properties of phosphorus-containing activated carbons obtained from biomass. *Journal of the Taiwan Institute of Chemical Engineers, 80*, 1006-1013.

Kesavan, T., Partheeban, T., Vivekanantha, M., Kundu, M., Maduraiveeran, G., & Sasidharan, M. (2019). Hierarchical nanoporous activated carbon as potential electrode materials for high performance electrochemical supercapacitor. *Microporous and Mesoporous Materials, 274*, 236-244.

Khedkar, M. A., Nimbalkar, P. R., Kamble, S. P., Gaikwad, S. G., Chavan, P. V., & Bankar, S. B. (2018). Process intensification strategies for enhanced holocellulose solubilization: Beneficiation of pineapple peel waste for cleaner butanol production. *Journal of Cleaner Production, 199*, 937-947.

Kılıç, M., Apaydın-Varol, E., & Pütün, A. E. (2012). Preparation and surface characterization of activated carbons from Euphorbia rigida by chemical activation with $ZnCl_2$, K_2CO_3, NaOH and H_3PO_4. *Applied Surface Science, 261*, 247-254.

Kwaghger, A., & Ibrahim, J. S. (2013). Optimization of conditions for the preparation of activated carbon from mango nuts using HCl. *American Journal of Engineering Research, 2*(7), 74-85.

Lang, Q., Zhang, B., Liu, Z., Chen, Z., Xia, Y., Li, D., Ma, J., & Gai, C. (2019). Co-hydrothermal carbonization of corn stalk and swine manure: Combustion behavior of hydrochar by thermogravimetric analysis. *Bioresource Technology, 271*, 75-83.

Lee, J.-S. M., Briggs, M. E., Hu, C.-C., & Cooper, A. I. (2018a). Controlling electric double-layer capacitance and pseudocapacitance in heteroatom-doped carbons derived from hypercrosslinked microporous polymers. *Nano Energy, 46*, 277-289.

Lee, K. S., Park, C. W., & Kim, J.-D. (2017). Electrochemical properties and characterization of various ZnO structures using a precipitation method. *Colloids and Surfaces A: Physicochemical and Engineering Aspects, 512*, 87-92.

Lee, K. S., Park, C. W., & Kim, J.-D. (2018b). Synthesis of ZnO/activated carbon with high surface area for supercapacitor electrodes. *Colloids and Surfaces A: Physicochemical and Engineering Aspects, 555*, 482-490.

Lee, K. S., Shin, M. J., Park, C. W., & Kim, J.-D. (2018c). Simple and direct synthesis of ZnO decorated multi-walled carbon nanotube for supercapacitor electrodes. *Colloids and Surfaces A: Physicochemical and Engineering Aspects, 538*, 23-27.

Li, H., Zhao, Y., Liu, S., Li, P., Yuan, D., & He, C. (2019a). Hierarchical porous carbon monolith derived from lignin for high areal capacitance supercapacitors. *Microporous and Mesoporous Materials*, *297*, Article#109960.

Li, L., Shi, J. L., Zhang, L. X., Xiong, L. M., & Yan, J. N. (2004). A novel and simple in-situ reduction route for the synthesis of an ultra-thin metal nanocoating in the channels of mesoporous silica materials. *Advanced Materials, 16*(13), 1079-1082.

Li, P., Liu, J., Liu, Y., Wang, Y., Li, Z., Wu, W., … Qiu, J. (2015a). Three-dimensional $ZnMn_2O_4$/porous carbon framework from petroleum asphalt for high performance lithium-ion battery. *Electrochimica Acta, 180*, 164-172.

Li, X., Meng, X., Liu, J., Geng, D., Zhang, Y., Banis, M. N., … Verbrugge, M. W. (2012). Tin oxide with controlled morphology and crystallinity by atomic layer deposition onto graphene nanosheets for enhanced lithium storage. *Advanced Functional Materials, 22*(8), 1647-1654.

Li, X.-S., Xu, M.-M., Yang, Y., Huang, Q.-B., Wang, X.-Y., Ren, J.-L., & Wang, X.-H. (2019b). MnO_2@corncob carbon composite electrode and all-solid-state supercapacitor with improved electrochemical performance. *Materials, 12*(15), Article#2379.

Li, Y., & Liu, X. (2014). Activated carbon/ZnO composites prepared using hydrochars as intermediate and their electrochemical performance in supercapacitor. *Materials Chemistry and Physics, 148*(1), 380-386.

Li, Y., Li, C., Qi, H., Yu, K., & Liang, C. (2018). Mesoporous activated carbon from corn stalk core for lithium ion batteries. *Chemical Physics, 506*, 10-16.

Li, Z.-Y., Akhtar, M. S., & Yang, O. B. (2015b). Supercapacitors with ultrahigh energy density based on mesoporous carbon nanofibers: Enhanced double-layer electrochemical properties. *Journal of Alloys and Compounds, 653*, 212-218.

Liang, D., Wu, S., Wang, P., Cai, Y., Tian, Z., Liu, J., & Liang, C. (2014). Recyclable chestnut-like Fe_3O_4@C@$ZnSnO_3$ core–shell particles for the photocatalytic degradation of 2,5-dichlorophenol. *RSC Advances, 4*(50), 26201-26206.

Liu, D., Zhang, W., & Huang, W. (2019). Effect of removing silica in rice husk for the preparation of activated carbon for supercapacitor applications. *Chinese Chemical Letters, 30*(6), 1315-1319.

Liu, J., Liu, B., Wang, C., Huang, Z., Hu, L., Ke, X., … Guo, Z. (2017). Walnut shell – derived activated carbon: Synthesis and its application in the sulfur cathode for lithium–sulfur batteries. *Journal of Alloys and Compounds, 718*, 373-378.

Liu, Y., Wang, Y., Zhang, G., Liu, W., Wang, D., & Dong, Y. (2016). Preparation of activated carbon from willow leaves and evaluation in electric double-layer capacitors. *Materials Letters, 176*, 60-63.

Liu, Y., Weng, B., Razal, J. M., Xu, Q., Zhao, C., Hou, Y., … Chen, J. (2015a). High-performance flexible all-solid-state supercapacitor from large free-standing graphene-PEDOT/PSS films. *Scientific Reports, 5*, 17045-17045.

Liu, Z., Qi, N., Luan, Y., & Sun, X. (2015b). Thermogravimetry-infrared spectroscopy analysis of the pyrolysis of willow leaves, stems, and branches. *Advances in Materials Science and Engineering, 2015*, Article#303212.

Luo, P., Zhang, H., Liu, L., Fang, L., & Wang, Y. (2016). Sandwich-like nanostructure of amorphous $ZnSnO_3$ encapsulated in carbon nanosheets for enhanced lithium storage. *Electrochimica Acta, 219*, 734-741.

Ma, Y. (2017). Comparison of Activated Carbons Prepared from Wheat Straw via $ZnCl_2$ and KOH Activation. *Waste and Biomass Valorization, 8*(3), 549-559.

Maarof, H. I., Ajeel, M. A., Daud, W. M. A. W., & Aroua, M. K. (2017). Electrochemical properties and electrode reversibility studies of palm shell activated carbon for heavy metal removal. *Electrochimica Acta, 249*, 96-103.

Mahmoud, M., Maher, F. E.-K., Zhiheng, Z., Peter, M., & Jun, M. (2016). Recent progress and performance evaluation for polyaniline/graphene nanocomposites as supercapacitor electrodes. *Nanotechnology, 27*(44), Article#442001.

Mayedwa, N., Mongwaketsi, N., Khamlich, S., Kaviyarasu, K., Matinise, N., & Maaza, M. (2018). Green synthesis of zin tin oxide ($ZnSnO_3$) nanoparticles using Aspalathus Linearis natural extracts: Structural, morphological, optical and electrochemistry study. *Applied Surface Science, 446*, 250-257.

McQuillan, R. V., Stevens, G. W., & Mumford, K. A. (2018). The electrochemical regeneration of granular activated carbons: A review. *Journal of Hazardous Materials, 355*, 34-49.

Mei, B. A., Munteshari, O., Lau, J., Dunn, B., & Pilon, L. (2018). Physical interpretations of nyquist plots for EDLC electrodes and devices. *Journal of Physical Chemistry C, 122*(1), 194-206.

Molina-Sabio, M., & Rodríguez-Reinoso, F. (2004). Role of chemical activation in the development of carbon porosity. *Colloids and Surfaces A: Physicochemical and Engineering Aspects, 241*(1-3), 15-25.

Mopoung, S., Moonsri, P., Palas, W., & Khumpai, S. (2015). Characterization and properties of activated carbon prepared from tamarind seeds by KOH activation for Fe(III) adsorption from aqueous solution. *The Scientific World Journal, 2015*, 415961-415961.

Moreno, N., Caballero, A., Hernán, L., & Morales, J. (2014). Lithium–sulfur batteries with activated carbons derived from olive stones. *Carbon, 70*, 241-248.

Nabais, J. M. V., Laginhas, C. E. C., Carrott, P. J. M., & Ribeiro Carrott, M. M. L. (2011). Production of activated carbons from almond shell. *Fuel Processing Technology, 92*(2), 234-240.

Nahil, M. A., & Williams, P. T. (2012). Pore characteristics of activated carbons from the phosphoric acid chemical activation of cotton stalks. *Biomass and Bioenergy, 37*, 142-149.

Nayak, A., Bhushan, B., Gupta, V., & Sharma, P. (2017). Chemically activated carbon from lignocellulosic wastes for heavy metal wastewater remediation: Effect of activation conditions. *Journal of Colloid and Interface Science, 493*, 228-240.

Okashy, S., Noked, M., Zimrin, T., & Aurbach, D. (2013). The study of activated carbon/CNT/MoO_3 electrodes for aqueous pseudo-capacitors. *Journal of the Electrochemical Society, 160*(9), A1489-A1496.

Othman, A. F. (2017,). Pineapples new source of wealth for Malaysia. Retrieved on April 18, 2019 from https://www.nst.com.my/news/nation/2017/12/313347/pineapples-new-source-wealth-malaysia

Ozdemir, I., Şahin, M., Orhan, R., & Erdem, M. (2014). Preparation and characterization of activated carbon from grape stalk by zinc chloride activation. *Fuel Processing Technology, 125*, 200-206.

Pallarés, J., González-Cencerrado, A., & Arauzo, I. (2018). Production and characterization of activated carbon from barley straw by physical activation with carbon dioxide and steam. *Biomass and Bioenergy, 115*, 64-73.

Pezoti, O., Cazetta, A. L., Souza, I. P. A. F., Bedin, K. C., Martins, A. C., Silva, T. L., & Almeida, V. C. (2014). Adsorption studies of methylene blue onto $ZnCl_2$-activated carbon produced from buriti shells (*Mauritia flexuosa L.*). *Journal of Industrial and Engineering Chemistry, 20*(6), 4401-4407.

Prahas, D., Kartika, Y., Indraswati, N., & Ismadji, S. (2008). Activated carbon from jackfruit peel waste by H_3PO_4 chemical activation: Pore structure and surface chemistry characterization. *Chemical Engineering Journal, 140*(1-3), 32-42.

Purnomo, C. W., Kesuma, E. P., Perdana, I., & Aziz, M. (2018). Lithium recovery from spent Li-ion batteries using coconut shell activated carbon. *Waste Management, 79*, 454-461.

Qin, Z., Chang, P., Ma, L., Bu, L., & Song, Z. (2019). Preparation and modulation of a novel thin-walled carbon foam. *International Journal of Mining Science and Technology, 29*(2), 281-287

Rajagopal, R., & Ryu, K.-S. (2019). Synthesis of MnO_2 nanostructures with MnS-deposits for high performance supercapacitor electrodes. *New Journal of Chemistry, 43*, 12987-13000.

Ray, A., Roy, A., Ghosh, M., Alberto Ramos-Ramón, J., Saha, S., Pal, U., Bhattacharya, S. K., & Das, S. (2019). Study on charge storage mechanism in working electrodes fabricated by sol-gel derived spinel $NiMn_2O_4$ nanoparticles for supercapacitor application. *Applied Surface Science, 463*, 513-525.

Research, T. M. (2013). Activated carbon market (powdered, granular) for liquid phase and gas phase applications - Global industry analysis, size, share, growth, trends and Forecast, 2013 - 2019. Retrieved on May 10, 2019 from https://www.slideshare.net/tmrreport/activated-carbon-market-powdered-granular-for-liquid-phase-and-gas-phase-applications-global-industry-analysis-size-share-growth-trends-and-forecast-2013-2019

Rodrigues, L. A., da Silva, M. L. C. P., Alvarez-Mendes, M. O., Coutinho, A. d. R., & Thim, G. P. (2011). Phenol removal from aqueous solution by activated carbon produced from avocado kernel seeds. *Chemical Engineering Journal, 174*(1), 49-57.

Sahoo, A., & Sharma, Y. (2015). Synthesis and characterization of nanostructured ternary zinc manganese oxide as novel supercapacitor material. *Materials Chemistry and Physics, 149-150*, 721-727.

Sasirekha, C., Arumugam, S., & Muralidharan, G. (2018). Green synthesis of ZnO/carbon (ZnO/C) as an electrode material for symmetric supercapacitor devices. *Applied Surface Science, 449*, 521-527.

Saucerman, L. (2004). Carbon (1st ed.). New York, United States: The Rosen Publishing Group.

Selvakumar, M., Krishna Bhat, D., Manish Aggarwal, A., Prahladh Iyer, S., & Sravani, G. (2010). Nano ZnO-activated carbon composite electrodes for supercapacitors. *Physica B: Condensed Matter, 405*(9), 2286-2289.

Senthilkumar, N., Venkatachalam, V., Kandiban, M., Vigneshwaran, P., Jayavel, R., & Vetha Potheher, I. (2019). Studies on electrochemical properties of hetarolite ($ZnMn_2O_4$) nanostructure for supercapacitor application. *Physica E: Low-Dimensional Systems and Nanostructures, 106*, 121-126.

Shahzad, S., Shah, A., Kowsari, E., Iftikhar, F. J., Nawab, A., Piro, B., … Zou, Y. (2019). Ionic liquids as environmentally benign electrolytes for high-performance supercapacitors. *Global Challenges, 3*(1), Article#1800023.

Shandle, J. (2019). Supercapacitors find applications in hybrid vehicles, smartphones, and energy harvesting. Retrieved on May 21, 2019 from https://my.mouser.com/applications/new-supercapacitor-applications/

Shree Kesavan, K., Surya, K., & Michael, M. S. (2018). High powered hybrid supercapacitor with microporous activated carbon. *Solid State Ionics, 321*, 15-22.

Siddiqui, G. U., Rehman, M. M., & Choi, K. H. (2017). Resistive switching phenomena induced by the heterostructure composite of $ZnSnO_3$ nanocubes interspersed ZnO nanowires. *Journal of Materials Chemistry C, 5*(22), 5528-5537.

Sim, C.-K., Majid, S. R., & Mahmood, N. Z. (2015a). Electrochemical performance of activated carbon derived from treated food-waste. *International Journal of Electrochemical Science, 10*(12), 10157-10172.

Sim, C.-K., Majid, S. R., & Mahmood, N. Z. (2015b). *Potential of vermicompost as carbonaceous material for electrical double layer capacitors* (Unpublished master's thesis). Universiti Malaya, Kuala Lumpur, KL.

Sim, C.-K., Majid, S. R., & Mahmood, N. Z. (2019). Durable porous carbon/$ZnMn_2O_4$ composite electrode material for supercapacitor. *Journal of Alloys and Compounds, 803*, 424-433.

Sim, C. K., Razali, S. A., Majid, S. R., & Mahmood, N. Z. (2020). Synthesis and Characterization of Ternary Mesoporous Carbon/$ZnMn_2O_4$ for Supercapacitor Application. *Journal of Electronic Materials, 49*(2), 1024-1035.

Sudhakar, Y. N., Selvakumar, M., & Bhat, D. K. (2018). Biopolymer electrolytes: Fundamentals and applications in energy storage (1st ed.). Oxford, United Kingdom: Susan Dennis.

Sun, C., Rajasekhara, S., Dong, Y., & Goodenough, J. B. (2011). Hydrothermal synthesis and electrochemical properties of $Li_3V_2(PO_4)_3$/C-based composites for lithium-ion batteries. *ACS Applied Materials & Interfaces, 3*(9), 3772-3776.

Sun, K., Leng, C.-y., Jiang, J.-c., Bu, Q., Lin, G.-f., Lu, X.-c., & Zhu, G.-z. (2017). Microporous activated carbons from coconut shells produced by self-activation using the pyrolysis gases produced from them, that have an excellent electric double layer performance. *New Carbon Materials, 32*(5), 451-459.

Temesgen, F., Gabbiye, N., & Sahu, O. (2018). Biosorption of reactive red dye (RRD) on activated surface of banana and orange peels: Economical alternative for textile effluent. *Surfaces and Interfaces, 12*, 151-159.

Tham, Y. J., Latif, P. A., Abdullah, A. M., Shamala-Devi, A., & Taufiq-Yap, Y. H. (2011). Performances of toluene removal by activated carbon derived from durian shell. *Bioresource Technology, 102*(2), 724-728.

The Nature Conservancy (2017). Retrieved on February 27, 2018 from https://www.nature.org/en-us/what-we-do/our-insights/perspectives/the-biggest-environmental-challenges-of-2017/

Tran, M.-H., & Jeong, H. K. (2017). Ternary carbon composite films for supercapacitor applications. *Chemical Physics Letters, 684*(Supplement C), 1-7.

Uçar, S., Erdem, M., Tay, T., & Karagöz, S. (2009). Preparation and characterization of activated carbon produced from pomegranate seeds by $ZnCl_2$ activation. *Applied Surface Science, 255*(21), 8890-8896.

Üner, O., & Bayrak, Y. (2018). The effect of carbonization temperature, carbonization time and impregnation ratio on the properties of activated carbon produced from *Arundo donax*. *Microporous and Mesoporous Materials, 268*, 225-234.

Wang, K., Zhao, N., Lei, S., Yan, R., Tian, X., Wang, J., … Liu, L. (2015). Promising biomass-based activated carbons derived from willow catkins for high performance supercapacitors. *Electrochimica Acta, 166*, 1-11.

Wang, Y., Gao, P., Bao, D., Wang, L., Chen, Y., Zhou, X., … Zhang, M. (2014). One pot, two phases: Individual orthorhombic and face-centered cubic $ZnSnO_3$ obtained synchronously in one solution. *Inorganic Chemistry, 53*(23), 12289-12296.

Wei, H., Wang, X., Zhang, D., Du, W., Sun, X., Jiang, F., & Shi, T. (2019). Facile synthesis of lotus seedpod-based 3D hollow porous activated carbon/manganese dioxide composite for supercapacitor electrode. *Journal of Electroanalytical Chemistry, 853*, Article#113561.

Weng, Y.-T., Pan, H.-A., Lee, R.-C., Huang, T.-Y., Chu, Y., Lee, J.-F., … Wu, N.-L. (2015). Spatially confined MnO_2 nanostructure enabling consecutive reversible charge transfer from Mn(IV) to Mn(II) in a mixed pseudocapacitor-battery electrode. *Advanced Energy Materials, 5*(18), Article#1500772.

Wong, S., Lim, Y., Ngadi, N., Mat, R., Hassan, O., Inuwa, I. M., … Low, J. H. (2018). Removal of acetaminophen by activated carbon synthesized from spent tea leaves: Equilibrium, kinetics and thermodynamics studies. *Powder Technology, 338*, 878-886.

Wu, G., Song, Y., Wan, J., Zhang, C., & Yin, F. (2019a). Synthesis of ultrafine ZnO nanoparticles supported on nitrogen-doped ordered hierarchically porous carbon for supercapacitor. *Journal of Alloys and Compounds, 806*, 464-470.

Wu, X., Yang, F., Dong, H., Sui, J., Zhang, Q., Yu, J., Zhang, Q., & Dong, L. (2019b). Controllable synthesis of MnO_2 with different structures for supercapacitor electrodes. *Journal of Electroanalytical Chemistry, 848*, Article#113332.

Wu, Z., Zhu, Y., Ji, X., & Banks, C. E. (2016). Transition metal oxides as supercapacitor materials. In K. I. Ozoemena & S. Chen (Eds.), Nanomaterials in advanced batteries and supercapacitors (pp. 317-344). Cham, Switzerland: Springer International Publishing.

Xia, Y., Yang, Z., & Mokaya, R. (2010). Templated nanoscale porous carbons. *Nanoscale, 2*(5), 639-659.

Xiao, X., Han, B., Chen, G., Wang, L., & Wang, Y. (2017). Preparation and electrochemical performances of carbon sphere@ZnO core-shell nanocomposites for supercapacitor applications. *Scientific Reports, 7*, Article#40167.

Xie, Q., Ma, Y., Zhang, X., Guo, H., Lu, A., Wang, L., … Peng, D.-L. (2014). Synthesis of amorphous $ZnSnO_3$-C hollow microcubes as advanced anode materials for lithium ion batteries. *Electrochimica Acta, 141*, 374-383.

Xu, G.-r., Wen, Y., Min, X.-p., Dong, W.-h., Tang, A.-p., & Song, H.-s. (2015). Construction of MnO_2/3-dimensional porous crack Ni for high-performance supercapacitors. *Electrochimica Acta, 186*, 133-141.

Yahya, M. A., Al-Qodah, Z., & Ngah, C. W. Z. (2015). Agricultural bio-waste materials as potential sustainable precursors used for activated carbon production: A review. *Renewable and Sustainable Energy Reviews, 46*, 218-235.

Yan, J., Huang, Y., Han, X., Gao, X., & Liu, P. (2019a). Metal organic framework (ZIF-67)-derived hollow CoS_2/N-doped carbon nanotube composites for extraordinary electromagnetic wave absorption. *Composites Part B: Engineering, 163*, 67-76.

Yan, S., Yu, Y., & Cao, Y. (2019b). Synthesis of porous $ZnMn_2O_4$ flower-like microspheres by using MOF as precursors and its application on photoreduction of CO_2 into CO. *Applied Surface Science, 465*, 383-388.

Yan, Y., Liu, J., Zhang, H., Song, D., Li, J., Yang, P., … Wang, J. (2019c). One-pot synthesis of cubic $ZnSnO_3$/ZnO heterostructure composite and enhanced gas-sensing performance. *Journal of Alloys and Compounds, 780*, 193-201.

Yang, I., Kim, S.-G., Kwon, S. H., Kim, M.-S., & Jung, J. C. (2017). Relationships between pore size and charge transfer resistance of carbon aerogels for organic electric double-layer capacitor electrodes. *Electrochimica Acta, 223*, 21-30.

Yang, J., Yang, X., Zhong, Y. L., & Ying, J. Y. (2015). Porous MnO/Mn_3O_4 nanocomposites for electrochemical energy storage. Nano Energy, 13, 702-708.

Yu, K., Li, J., Qi, H., & Liang, C. (2018). High-capacity activated carbon anode material for lithium-ion batteries prepared from rice husk by a facile method. *Diamond and Related Materials, 86*, 139-145.

Yumak, T., Bragg, D., & Sabolsky, E. M. (2019). Effect of synthesis methods on the surface and electrochemical characteristics of metal oxide/activated carbon composites for supercapacitor applications. *Applied Surface Science, 469*, 983-993.

Zanella, O., Tessaro, I. C., & Féris, L. A. (2014). Desorption- and decomposition-based techniques for the regeneration of activated carbon. *Chemical Engineering & Technology, 37*(9), 1447-1459.

Zeng, L., Lou, X., Zhang, J., Wu, C., Liu, J., & Jia, C. (2019). Carbonaceous mudstone and lignin-derived activated carbon and its application for supercapacitor electrode. *Surface and Coatings Technology, 357*, 580-586.

Zequine, C., Ranaweera, C. K., Wang, Z., Singh, S., Tripathi, P., Srivastava, O. N., … Gupta, R. K. (2016). High performance and flexible supercapacitors based on carbonized bamboo fibers for wide temperature applications. *Scientific Reports, 6*, Article#31704.

Zhai, Y., Dou, Y., Zhao, D., Fulvio, P. F., Mayes, R. T., & Dai, S. (2011). Carbon materials for chemical capacitive energy storage. *Advanced Materials, 23*(42), 4828-4850.

Zhang, G., Chen, Y., Chen, Y., & Guo, H. (2018a). Activated biomass carbon made from bamboo as electrode material for supercapacitors. *Materials Research Bulletin, 102*, 391-398.

Zhang, L. L., Wei, T., Wang, W., & Zhao, X. S. (2009). Manganese oxide–carbon composite as supercapacitor electrode materials. *Microporous and Mesoporous Materials, 123*(1), 260-267.

Zhang, L., & Sun, X. (2018b). Effects of bean dregs and crab shell powder additives on the composting of green waste. *Bioresource Technology, 260*, 283-293.

Zhang, N., Cheng, F., Liu, Y., Zhao, Q., Lei, K., Chen, C., Liu, X., & Chen, J. (2016a). Cation-deficient spinel $ZnMn_2O_4$ cathode in $Zn(CF_3SO_3)_2$ electrolyte for rechargeable aqueous Zn-ion battery. *Journal of the American Chemical Society, 138*(39), 12894-12901.

Zhang, R., Liu, X., Zhou, T., Wang, L., & Zhang, T. (2018c). Carbon materials-functionalized tin dioxide nanoparticles toward robust, high-performance nitrogen dioxide gas sensor. *Journal of Colloid and Interface Science, 524*, 76-83.

Zhang, Y., Gao, S., & Xing, H. (2019). Reduced graphene oxide wrapped cube-like $ZnSnO_3$: As a high-performance microwave absorber. *Journal of Alloys and Compounds, 777*, 544-553.

Zhang, Y., Gao, Z., Song, N., & Li, X. (2016b). High-performance supercapacitors and batteries derived from activated banana-peel with porous structures. *Electrochimica Acta, 222*, 1257-1266.

Zhang, Y., Li, G.-y., Lv, Y., Wang, L.-z., Zhang, A.-q., Song, Y.-h., & Huang, B.-l. (2011). Electrochemical investigation of MnO_2 electrode material for supercapacitors. *International Journal of Hydrogen Energy, 36*(18), 11760-11766.

Zhang, Y., Wang, Y., Qi, J., Tian, Y., Sun, M., Zhang, J., … Yang, J. (2018d). Enhanced magnetic properties of $BiFeO_3$ thin films by doping: Analysis of structure and morphology. *Nanomaterials, 8*(9), Article#711.

Zhang, Z. J., Dong, C., Ding, X. Y., & Xia, Y. K. (2015). A generalized $ZnCl_2$ activation method to produce nitrogen-containing nanoporous carbon materials for supercapacitor applications. *Journal of Alloys and Compounds, 636*, 275-281.

Zhi, J., Wang, Y., Deng, S., & Hu, A. (2014). Study on the relation between pore size and supercapacitance in mesoporous carbon electrodes with silica-supported carbon nanomembranes. *RSC Advances, 4*(76), 40296-40300.

Zhi, M., Xiang, C., Li, J., Li, M., & Wu, N. (2013). Nanostructured carbon-metal oxide composite electrodes for supercapacitors: A review. *Nanoscale, 5*(1), 72-88.

Zhou, C., Chen, S., Lou, J., Wang, J., Yang, Q., Liu, C., Huang, D., & Zhu, T. (2014). Graphene's cousin: The present and future of graphane. *Nanoscale Research Letters, 9*(1), Article#26.

Zhu, X., Wei, Z., Zhao, W., Zhang, X., Zhang, L., & Wang, X. (2018a). Microstructure and electrochemical properties of $ZnMn_2O_4$ nanopowder synthesized using different surfactants. *Journal of Electronic Materials, 47*(11), 6428-6436.

Zhu, X., Yu, S., Xu, K., Zhang, Y., Zhang, L., Lou, G., … Fu, S. (2018b). Sustainable activated carbons from dead ginkgo leaves for supercapacitor electrode active materials. *Chemical Engineering Science, 181*, 36-45.

Zhu, Z., Wang, Z., Yan, Z., Zhou, R., Wang, Z., & Chen, C. (2018c). Facile synthesis of MOF-derived porous spinel zinc manganese oxide/carbon nanorods hybrid materials for supercapacitor application. *Ceramics International, 44*(16), 20163-20169.

LIST OF PUBLICATIONS AND PAPERS PRESENTED

PUBLICATIONS

1. **Sim, C.-K.**, Majid, S. R., & Mahmood, N. Z. (2019). Durable porous carbon/$ZnMn_2O_4$ composite electrode material for supercapacitor. *Journal of Alloys and Compounds, 803*, 424-433.

2. **Sim, C.-K.**, Razali, S. A., Majid, S. R., & Mahmood, N. Z. (2019). Synthesis and characterization of ternary mesoporous carbon/$ZnMn_2O_4$ for supercapacitor application. *Journal of Electronic Materials, 49*(2), 1-12.

3. **Sim, C.-K.**, Majid, S. R. & Mahmood, N. Z. (2018). Development of mesoporous biocarbon from treated spent mushroom substrate for supercapacitor application. *AIP Conference Proceedings, 2030*, Article#020229.

4. Rusi, **Sim, C.-K.**, & Majid, S. R. (2017). Morphology-controlled PANI nanowire electrode by using deposition scan rate in H_2SO_4/PVA polymer electrolyte for electrochemical capacitor. *Ionics, 23*(5), 1219-1227.

5. **Sim, C.-K.**, Bakar, A. A., Mahmood, N. Z., & Abdullah, N. (2016). Heavy metal contaminated soil bioremediation via vermicomposting with spent mushroom compost. *ScienceAsia, 42*(6), 367-374.

PAPER PRESENTED

1. **Sim, C.-K.**, Majid, S. R., & Mahmood, N. Z. (2017). *Green waste derived activated carbon doped with manganese oxide for supercapacitor application.* Paper presented at the 6th International Conference on Functional Materials & Devices 2017, 15-18th August 2017, Melaka, Malaysia.